LIFE IN THE OUTER LIMITS: INSIGHTS ON HIERARCHICAL ASSEMBLY FROM STELLAR HALOES IN THE LOCAL UNIVERSE

Rachael L. Beaton
Brights, Virginia

B.A., University of Virginia, 2007

M.A., University of Virginia, 2008

A Dissertation Presented to the Graduate
Faculty of the University of Virginia
in Candidacy for the Degree of
Doctor of Philosophy

Department of Astronomy

University of Virginia
Dec, 2014

Dr. Steven R. Majewski

Dr. Kelsey E. Johnson

Dr. D. Mark Whittle

Dr. Gabriel Robins

Dr. R. Craig Group

Abstract

Owing to their large dynamical timescales, the stellar haloes of Milky Way (MW) sized galaxies represent ideal environments to test modern theories of galaxy formation within the Λ-CDM paradigm. Only in stellar haloes can the remnants of hierarchical accretion both be preserved over long timescales as in-tact dwarf satellites or as tidal debris and be easily distinguished from the underlying smooth structure. Stellar haloes, however, remain some of the most difficult galactic structures to study due to their large angular extent (to R_{virial}) and extremely low surface brightness ($\sim>$ 30 mag arcsec^2). Thus, the basic properties of stellar haloes – the overall stellar distribution, substructure fraction, global kinematics and detailed stellar content – remain relatively unconstrained.

First, we revisit the development of the modern theory of stellar evolution — in particular, the visualization of this evolution from the Hertzsprung-Russell diagram. Key to this understanding was the proper placement of the star cluster stellar sequences in order of their age, a task accomplished in the realization of the evolutionary link between the well known dwarf and giant sequences: the subgiant branch. We show that the Mt. Wilson spectroscopic program of the early 20th century discovered the subgiant sequence in their 1935 catalog of stellar absolute magnitudes derived from the technique of spectroscopic parallax — several decades before they were to be discovered within the stellar sequences of nearby star clusters.

Second, we present the Spectroscopic and Photometric Landscape of the Andromeda Stellar Halo (SPLASH) project, a decade long observational campaign to understand the current structure and the the formation of the Andromeda (M 31) stellar halo. The halo of M 31 remains the only extragalactic stellar halo whose resolved stellar content is within reach of current ground based facilities on the large scale required to constrain its basic properties. The combination of Washington+$DDO51$

imaging to isolate red giant candidates and moderate resolution spectroscopy has allowed the SPLASH project to identify bone fide M 31 halo member stars at 32 mag arcsec^{-2}, which are buried beneath a Galactic foreground of many times higher surface brightness. This thesis presents a campaign that has resulted in the largest sample of stellar halo member stars beyond $R_{proj} \sim 120$ kpc ($\sim$1/3 R$_{virial}$) in any galaxy. We utilize the large angular extent of these member stars on the sky ($R > 8°$) to measure the transverse motion of the M 31 system, using the variable projection of this motion onto its member stars at large angular separations. The technique is found to be comparable in precision to other statistical and direct proper motion studies and this effort is the first step to a global kinematical modelling of the halo using this unique kinematic sample.

Third, we use deep imaging to 29 mag arcsec^{-2} to reveal merger debris NGC 5387, an edge-on disk disk galaxy similar to the Milky Way. The debris are found to be consistent with the merger of a dwarf satellite galaxy at a 1:10 mass ratio. The progenitor of the tidal debris is identified as a relatively compact ($\sim$1 kpc) region undergoing extreme star formation at a rate of 2 M$_\odot$ year^{-1}, consistent with a massive star density of 1200 stars kpc^{-1} — making it similar to the conditions observed in super star clusters typically identified in more massive mergers. Despite showing chemical properties consistent with a galaxy of its original mass, we show that this galaxy is unique among samples of nearby dwarf galaxies regardless of environment, both in its integrated colors and in its star forming properties. From comparison to detailed numerical modelling, we infer the extreme star formation was induced by a recent passage through the NGC 5387 disk and that the satellite remnant could continue forming stars through an additional disk passage. We show that were this galaxy undisturbed, i.e., had its stellar halo not been stripped, it would have colors

consistent with those objects in the "green valley" for dwarf satellites, suggesting opportunities to probe extreme star formation environments need not only occur on the 'star forming sequence'. Lastly, we apply a set of non-parametric morphology metrics to our imaging for NGC 5387, which suggest it would be identified as a 1:1 merging system in 'blind' morphological surveys in rest-frame UV.

Acknowledgements

A person is truly the sum of their experiences and there are far too many that have influenced me to detail here. First and foremost, I have to thank my immediate family for their unwavering support of my ethereal pursuits – my father: Richard C. Beaton, my brother: Mathew Beaton, my maternal grandmother: Nancy Hicks, and an assortment of aunts, uncles, and cousins, who are too many to list by name and yet too few to avoid offense in even an accidential omission. I wish to acknowledge the incredible influence of my late mother: Lynn H. Beaton, my late maternal grandfather: Roy Lynwood Hicks, both of whom passed during my graduate career, and my paternal grandmother: Elgie L. Beaton. Not a decision is made in which I do not consider their reaction to the matter. Lastly, I wish to thank Charles Romero for reminding me to eat, sleep, and exercise, and for providing a general clear headed balance to my anxious chaos.

I wish to acknowledge the mentorship of the late Deborah J. Mason and the late Edwin Temples, both of whom spent countless hours training me to speak in public, discussing leadership, and being honest givers of advice. I wish to acknowledge Audrey Powell and Jerry Boteler, both of whom encouraged me to think and whose constant love of knowledge for the pure sake of knowledge remains inspirational. I thank Thomas Morgan for finding and convincing F. Jay Lockman to mentor me for my junior high school research project and Steve Howard for teaching me how to troubleshoot technical matters with humor and class.

I thank the late Robert Rood for changing my course schedule during my first week at UVa and forcibly enrolling me in the College Science Scholars Program, which propelled me into research as a first year student. I wish to acknowledge my past and current research adviser, Steven R. Majewski, for first raising me in the spirit of hands-on astronomical observation as an undergraduate and then his tolerance of

my independence as a graduate student. I thank Richard J. Patterson for answering a list of questions that could wrap round the Earth. I thank Puragra GuhaThakurta for his enthusiasm, support, and thoughtful advise. I thank Kelsey E. Johnson for her mentorship, particularly as a role model in her tireless efforts to support strong role models for local K-12 students — an effort that reminds me constantly of how lucky I have been to have the mentors listed here. Moreover, I thank Shannon Beasley for her insatiable energy while being that mentor out in, what now seem to be quite distant, trenches of high school science education.

I thank the telescope operators, night assistants, and general observing staff at the LBT, MMT, KPNO, and Keck observatories — who on many occasions kept me awake (if not alert) and not crushed by a telescope. In particular, I thank those staff that helped me retrieve my car keys from the base of the elevator shaft at the Mayall 4-meter. I thank Barbara Johnson, Janice Dean, Howard Powell, Whitney Richardson, C. David Rigby, and Jackie Harding for their behind the scenes work that kept this graduate student afloat on numerous misadventures. I further thank my older research siblings, Co-Is, and collaborators, whom I am pleased to formally embrace as colleagues.

Table of contents

List of Figures

List of Tables

Chapter 1

Introduction and Overview

Owing to their large dynamical timescales, the stellar haloes of Milky Way (MW) sized galaxies represent ideal environments to test theories of galaxy formation within the Λ-CDM paradigm. Only in stellar haloes can the remnants of hierarchical accretion be preserved over long timescales as in-tact dwarf satellites or as tidal debris, both of which can be easily distinguished from the underlying smooth structure. Theoretical explorations of stellar haloes come in two classes: (i) those at a cosmological scale that make predictions of generic processes of galaxy formation, and (ii) those that simulate the formation of an individual galaxy. The former has revealed the large-scale process of hierarchical formation, that galaxies form via the accumulation of mass cannibalized from its companion galaxies, where as the latter better informs how, at the individual galaxy level, the accretion process can be viewed observationally. Both the global, generalized view and the specific predictions are fundamental to drive appropriate observational probes of these structures.

Despite the vast theoretical framework underpinning hierarchical formation, stellar haloes, however, remain the most difficult galactic structure to constrain observationally due to their intrinsically low surface brightness (e.g., low stellar density) and to their large extent relative to the higher surface brightness disk and bulge (e.g., hundreds of kpc). Thus, the even the most basic properties of stellar haloes – the overall stellar distribution, substructure fraction, global kinematics and detailed stellar content – remain relatively unprobed observationally even for the most well-studied local galaxies. Furthermore, a statistical characterization of these properties across a large sample of galaxies, e.g., a sample that averages over discrete accretion histories and (potentially) variations in local baryon density, is nearly impossible given the current state of observations. This thesis aim to add to our observational understanding of stellar halos as a probe of galaxy formation and evolution within

the Λ-CDM paradigm.

There are two observational approaches to the study of stellar halos: (i) highly detailed kinematical and photometric portraits of the resolved stellar content, and (ii) global views of halo substructure in integrated light. We present both a detailed, star-by-star characterization of the Andromeda (M 31) stellar halo — the only stellar halo besides our own accessible with current facilities — that extends to a truly "global" scale by the use of specialized observational techniques and a global or 'birds-eye' view of the sub-structure within the halo of the distant edge-on spiral, NGC 5387. In this chapter, we briefly motivate the study of stellar haloes in relation to the larger goal of deciphering the phases of galaxy formation and evolution.

1.1 The Λ-CDM Paradigm

The notion that there was more mass in the Universe than could be accounted for from a characterization of luminous matter is not a new one. As early as Zwicky (1933), it was noted that the intra-cluster line-of-sight velocities within galaxy clusters were too large to be supported from a mass follows light approach for modelling the mass structure of the cluster. More conclusive evidence came from Rubin & Ford (1970) whose observations of HII regions in the M 31 disk demonstrated a flat rotation curve, suggesting that additional unseen mass must exist at large radii (∼10 kpc). Roberts & Rots (1973) found similar results for a sample of three spiral galaxies. Both Ostriker et al. (1974) and Einasto et al. (1974) used motions of satellite galaxies around larger hosts to demonstrate additional dark mass was required to keep said satellites bound to their parent. Later results based on samples of tens of galaxies of different morphological types in Rubin et al. (1980) and Rubin et al. (1985) made it clear that a significant portion of the matter in galaxies was dark.

In these early studies the term 'dark matter' generically referred to any matter whose existence could only be inferred by its gravitational effect, whereas today the term generically refers to a class of yet undetermined subatomic particles. Thus, initial efforts also explored the potential of "baryonic dark matter" to account for the gravitational effects, the most likely being very low mass stars. As demonstrated in Peacock (1999), boosting the faint end of the stellar initial mass function to include more objects in the mass range from Jupiter to brown dwarfs can only account for 20% more mass than observed (and still not violate existing limits on the number of such objects), falling far short of that anticipated from the aforementioned gravitational studies. Thus, there was no 'faint' astrophysical object capable of boosting the mass to its requisite levels.

Efforts then focused on a search for additional fundamental particles, yet undiscovered or known, that could provide the missing mass on galaxy-scales. Moreover, the baryon fraction in the early Universe is fixed by observations of big bang nucleosynthesis (Peacock 1999) and any massive particles would distort those ratios — albeit even a large number of the nearly massless neutrinos (or any particle with similar properties) would not affect the nucleosythetic yields given that such particles were still ultra-relativistic at the timescale when baryons become locked in. Thus, the observed properties of baryonic matter do not support a 'matter like' particle; more specifically, any other particle must be weakly coupled to baryonic matter. This class of particles is referred to as a weakly interacting massive particle (WIMP) and they come in three classes, as follows:

1. Hot Dark Matter (HDM) — very low mass particles that have relativistic speeds even at $z = 0$ (m_v10-100 eV);

2. Warm Dark Matter (WDM) — intermediate mass particles ($m_v \sim$ 0.5-2.0 keV);

3. Cold Dark Matter (CDM) — massive particles that decouple while non-relativistic ($m_v >$ few keV);

At recombination the "speed" of the particle determines its effective horizon or mixing length within the primordial Universe. This "wavelength" for the particle at early times can be described as:

$$\lambda_c = 41(\frac{m_v}{30eV})^{-1} Mpc, \tag{1.1}$$

and gives a back of the envelope estimate of the approximate minimum distance scale at $z = 0$ for dark matter clustering (Bond & Szalay 1983). Even in the pre-Degree Field Galaxy and pre-Sloan Digital Sky Survey era, it was apparent that galaxies clustered on ∼few Mpc scales and galaxies themselves are clusters of mass at ∼Mpc in scale (Binney & Tremaine 2008, and references therein). Thus, dark matter must cluster at, at least, for all spatial scales larger than normal galaxies, which places a limit on the mass of the dark matter particle. Moreover, systematically decreasing the thermal velocity results in particles able to cluster spatial scales as small as the diameter of the Earth (Mo et al. 2010).

Insertion of the HDM mass scale into Equation 1.1 result in co-moving wavelengths (λ_c) for an m_v=10 (100) eV is 120 (20) Mpc, a scale far larger than the observed galaxy clustering (Bond & Szalay 1983) and flat rotation curves in spirals (Rubin & Ford 1970; Rubin et al. 1980, 1985). Thus, "hot" particles were insufficient to explain the large scale distribution of matter in the universe, which was confirmed in early simulations using HDM that resulted in a Universe without *any* large scale clustering (White et al. 1984). Thus, other efforts proceeded using WDM, CDM, or combinations thereof, with strong constraints on exotic models coming from the COBE results (see discussion in Mo et al. 2010). At the time of the COBE results,

CDM was able to produce reasonable clustering results (albeit at low particle resolution) and was adopted, along with a 'cosmological constant' (Λ) to accommodate for the accelerating Universe, as a part of the "concordance" cosmological model that was supported by numerous works (see summary in Mo et al. 2010).

Despite its wide adoption, Λ-CDM is not without its problems, though these appeared as both simulations and observations were able to better probe smaller mass scales. These criticisms are as follows:

1. the angular momentum problem (AMP);
2. the core-cusp problem (CCP); and
3. the missing satellites problem (MSP).

The AMP refers to over-cooling that occurs for baryons in cosmological simulations of Milky Way sized galaxies, which results in ultra-compact galaxies, instead of the large ($R \sim$10's kpc) disk galaxies observed. The AMP is driven physically by gas falling into the parent halo that cools quickly to form dense subunits. These subunits are acted upon by a combination of dynamical friction and gravitational torques to transfer their angular momentum to the dark matter halo and thereby move into the central regions of galaxies (Navarro & Benz 1991; Navarro & White 1994). Often framed as the "angular momentum catastrophe", three solutions were posited: (i) an increase in numerical resolution, (ii) feedback capable of putting energy back into the gas from astrophysical processes, and (iii) warmer dark matter. The insertion of baryon processes at higher numerical resolution (i and ii) have, at least partially, solved the AMP and reasonable Milky Way sized galaxies can be produced in simulations (see discussion in Mo et al. 2010), albeit the formalized prescriptions for these processes are simplistic.

The CCP relates the 'internal' structure of the dark matter halo. Navarro et al. (1996a) and Navarro et al. (1997) demonstrated a 'universal' profile for dark matter halos of all masses, commonly referred to as the NFW profile. This profile contains a steeper inner region termed a cusp. Despite over a decade of effort (see detailed summary in Mo et al. 2010, Section 11.1.2), no galaxy has yet been observed to have a cusp-y inner dark matter profile, though such observations are difficult because the inner regions of galaxies can be baryon dominated (e.g., the disk-halo degeneracy) or have non-axis-symmetric potentials (e.g., V_{ROT} is not proportional to R). It is possible both that observations are incomplete or that cusps could be destroyed due to secular galaxy evolution. Nevertheless, the striking inability to find cusps in nature cause serious problems for CDM.

Lastly, the MSP refers to the over prediction of dark matter structure at the smallest scales, those of the the dwarf satellites (Moore et al. 1999). While hundreds, if not thousands, of dark matter substructures are predicted by CMD models to exist in the stellar haloes of Milky Way sized galaxies, only a few dozen are known at the limits of current surveys (Bullock 2010). Though extrapolation from current survey footprints to the 'all sky' surveys of the next decade suggest that many more dwarf satellites will be discovered around the Milky Way, it remains to be seen if a sufficient number can be found (Bullock 2010). Moreover, Boylan-Kolchin et al. (2011) and Boylan-Kolchin et al. (2012) have indicated that even the known satellites pose problems for CDM; more specifically, those well studied satellites have dark matter haloes that are not as dense as their counterparts in simulations. Known as 'too big to fail,' this problem suggests a near complete failure of Λ-CDM for the most massive dwarf satellites, that are too massive for various astrophysical phenomena (i.e., feedback) to have significantly altered their underlying dark matter halo.

The combination of these criticisms and the lack of viable solutions from CDM have re-invigorated the notion of WDM models, which were initially given less attention than CDM due to concerns over super-symmetry for particle species (Peacock 1999). While early efforts are able to produce realistic dwarf satellites (Lovell et al. 2012) and solve the 'Too Big To Fail' problem (Lovell et al. 2014), the galaxies still contain cuspy profiles. Thus, the ultimate solution must fall in a "Goldilocks" zone of solving problems on both galaxy and satellite galaxy scales, that remains elusive. However, the observational record at the mass regime where criticisms of Λ-CDM are applicable are far from complete.

1.2 Motivation:

Halo Formation in the Λ-CDM Paradigm

Cold dark matter (CDM) structure formation models make specific predictions about the shape, extent and smoothness of halos, but few stellar halos outside the Milky Way have been explored for even the most basic, global properties. The Milky Way halo presents serious challenges for study from within, paramount among them being the Milky Way halo covers the *entire* sky — and homogeneous study requires sister telescope+instrumentation with large etandue in both the Northern and Southern hemispheres. M31 offers a global external perspective and yet is close enough for us to resolve individual stars. Until relatively recently, however, observations had indicated that the stellar "halo" of M31 was markedly different from that of the Milky Way, and implied *unexpected* diversity for galaxy formation paths. Milky Way halo stars are old, metal-poor, and have a power-law radial surface brightness profile ($R^{-2.5}$, in projection), whereas two decades of comparable M 31 studies had established its

"halo" to be an extension of its inner bulge: a metal-rich population of [Fe/H]=−0.7 (Durrell et al. 2004; Mould & Kristian 1986) with an exponential decline out to a radius of $R_{\rm proj}$ = 20-30 kpc from M31's center (Pritchet & van den Bergh 1994).

The Spectroscopic and Photometric Landscape of the Stellar Halo (SPLASH) has contributed to a revision of this traditional picture of M 31. Using a powerful combination of KPNO/4m+Mosaic optical photometry and Keck/DEIMOS spectroscopy, SPLASH has identified pure samples of M 31 stars at large projected radii from the galaxy's center, which permits study the *global* properties of a stellar halo using a single tracer population. It was discovered that, like the Milky Way, M 31 indeed possesses a metal-poor ([Fe/H]=−1.5), power-law (R^{-2}, in projection) stellar halo that extends to beyond 150 kpc (Gilbert et al. 2012, 2006; Guhathakurta et al. 2005; Kalirai et al. 2006; Ostheimer 2003). The *true* M31 halo begins to dominate over the inner metal-rich spheroid population beyond $R \sim$ 20-30 kpc. Other projects (Irwin et al. 2005; Chapman et al. 2006; Ibata et al. 2007, 2014) have reached similar conclusions about M31's metal-poor halo based on a combination of wide-field imaging and deep spectroscopy as part of the Pan-Andromeda Archaeological Survey (PAndAS). Thus, the *true* structural disparity between the Milky Way and M 31 stellar halos appears to lie in *the relative sizes of their inner spheroid populations*, a difference easily explained by comparing the orbital properties of the most recent accretions in either galaxy (Sagittarius in the Milky Way and the Great Southern Stream in M 31).

The discovery of a metal-poor stellar halo in M31 resolved a long-standing mystery and provided an important clue to indicate overall similar evolutionary paths for M31 and the Milky Way. This alone, however, does not tell the entire story, nor does this provide a fully comprehensive global picture of halo formation — a question that still remains unanswered even for our own Milky Way, where multiple scenarios

for producing halo stars are actively discussed (e.g., Sheffield et al. 2012). Recent simulations that follow the evolution of baryons *as well as dark matter* imply that the inner regions of stellar halos may include stars arising from three distinct origins:

1. stars from **accreted** dwarf satellite galaxies (Bullock & Johnston 2005),

2. stars formed deep within the potential well of the host galaxy in either the disk or bulge that were subsequently **kicked-out** into the halo (McCarthy et al. 2012; Purcell et al. 2010; Zolotov et al. 2009), and

3. stars formed **in situ** during the early, monolithic collapse phase for the main halo (Eggen et al. 1962; Samland & Gerhard 2003).

However, there is sufficient uncertainty in the simulations that it is unclear which of these mechanisms is *most important* for halo formation. While observations support accretion as the dominant mode for the formation of the outer halo, observations in the Milky Way inner halo have been largely inconclusive. Evidence for the presence of a significant fraction of *in situ* or kicked out stars has been claimed based on apparent transitions in the metallicity distributions for local stars in low versus high eccentricity orbits (Carollo et al. 2007, 2010) and based on transitions between the orbital properties of local stars with low and high α-abundance (Nissen & Schuster 2011, 2010; Schuster et al. 2012). However, a recent survey of M-giants within 10 kpc of the Sun found α-element distributions that suggest dominance by accreted stars even within the innermost regions of the halo (Sheffield et al. 2012).

Studies of these sorts in the Milky Way are beset by several problems. The first is that our location in the Milky Way makes it difficult to identify, and cleanly distinguish, the various populations of ancient, low-metallicity stars whose tenuous densities are swamped by the much higher density stellar disk. To overcome this, one

typically resorts to winnowing out samples of easily recognizable stellar tracers, but

1. a comprehensive analysis of the halo requires an *all-sky* survey of such tracers,

2. one needs to have relatively precise line-of-sight distances to the tracers to formulate their 3-D distribution, and

3. it is now recognized that our view of the stellar halo changes according to what tracer is adopted (Bell et al. 2010; Sharma et al. 2011) (e.g., M giants, K giants, MSTO stars, RR Lyrae, BHB stars, etc.),

the latter *could explain* why descriptions of the local stellar halo differ across the various studies noted above. In addition, one of the most fundamental properties that could help elucidate origin scenarios — the ages of halo stars — is extremely difficult to establish, *even in a statistical sense.* Presently, our most reliable means by which to measure the ages of intermediate and old stellar populations is through analysis of color-magnitude diagrams (CMDs — e.g., via the position of the main sequence turn-off), which, however, are only sensibly interpretable when the CMD can be created for stars at a common distance. It is not clear how much the above-enumerated observational challenges have contributed to uncertainties in our theoretical understanding of how stellar halos form. For example, ΛCDM-based numerical simulations predict outer stellar halos to be lumpy, flattened, and coursed by streams from satellite accretion (Bullock & Johnston 2005), but these predictions are virtually untested at large Galactocentric distances due to the limited ability for current large-area photometric surveys to map standard halo tracers beyond 100 kpc (MSTO, BHB's, RR Lyraes, M giants). Meanwhile, even the reality of the "dual halo" used to argue for multiple origin mechanisms by Carollo et al. (2007) has been challenged (Schönrich et al. 2011).

Recent large area (Downes et al. 2004; Green 2013, e.g., SDSS:) and *all-sky* surveys (Mauron et al. 2004, e.g., 2MASS:) have, however, provided *some* access to the intermediate stellar content of the Milky Way, discovering hundreds of second ascent, asymptotic giant branch (AGB) stars (often identified as "carbon stars"). In both the optical and near-infrared, AGB stars are particularly luminous and it is feasible to sample AGB stars with these surveys to $\sim$150 kpc for non-pulsating stars and $>$150 kpc for *rare* variable-type carbon stars (Groenewegen 2005) — though a large fraction of the known AGB halo population are associated with a *single* halo substructure, the Sagittarius stellar stream (Majewski et al. 2003; Ibata et al. 2002). While these stars have been discovered, their variability (even in NIR) makes spectrophotometrically estimated distances from their theoretical mean magnitudes challenging, and *severely* limits their use as tracers of halo structure.

In the near future, however, highly-sensitive, *all-sky* observational programs will come online with the potential to respond to traditional limitations to studying the large-scale structure of the Milky Way stellar halo. LSST and PAN-STARRS, capable of imaging the entire sky to greater photometric depths than SDSS, will permit photometric identification of stellar populations to much greater distances in the Milky Way halo. GAIA will obtain high-precision distances to one billion stars in the Milky Way, greatly reducing one of the greatest limitations of global Milky Way work. Complementary to these efforts, APOGEE, APOGEE-II, and APOGEE-S will obtain high-resolution ($R \sim 22,500$) H-band spectra for over 10^5 RGB candidates in the disk(s), bar, bulge, and halo of the Milky Way (Zasowski et al. 2013) to produce a *uniform* database of high-precision radial velocities and chemical abundances (Eisenstein et al. 2011). In fact, even in its early phase, APOGEE has already serendipitously discovered hundreds of AGB stars (Zasowski et al. 2013) in the northern hemisphere,

suggesting that this program has great potential to study both old and intermediate age populations. While these future datasets will increase access to stellar tracers in the Milky Way halo and, *to a degree*, alleviate many of the inherent complications to backing out Milky Way halo structure, this approach still lacks two components to translate detailed Milky Way studies into a generalizable form: (i) an *unambiguous* global perspective of the halo, and (ii) a comparison system measured at equal detail to understand galaxy-to-galaxy variation (i.e., cosmic variance).

On the other hand, despite the greater distance to M31 (780 kpc Freedman & Madore 1990), study of *its* stellar halo does confer several advantages:

1. large fractions of the halo can be surveyed with limited sky coverage (approximately 22° in diameter),

2. clean samples of halo stars can be extracted, free of disk contamination (M 31 disk inclination i= 77°),

3. a different, external perspective of a spiral galaxy halo is afforded, with different dependencies/degeneracies of line-of-sight differences with galactocentric radius,

4. we can confidently identify stars in the outer halo of M31 — to beyond 100 kpc — a regime presently poorly traced around the Milky Way, and

5. the limited variation of line-of-sight distances to M31 halo stars empowers all of the tools we have for stellar population analysis of CMDs of field halo stars, and in particular, the opportunity to use CMDs to gauge the distributions of stellar *ages* within the M31 halo becomes possible.

This advantage was exploited in the groundbreaking, deep, optical Hubble Space Telescope (HST) imaging studies by Brown et al. (2008, 2006b,a) from which access

to the very faint magnitudes of the M31 MSTO revealed that there are stars covering a range of ages in M31's stellar halo (Brown et al. 2008). In particular, the deep HST fields on a strong tidal debris feature in M31 (the GSS) and associated debris (in the H11, H13s fields) show conclusive evidence for intermediate-age populations (Brown et al. 2006b,a). Unfortunately, these studies demand *enormous* investments of HST orbits, and, to date, cover only several very narrow pencil-beams. This is not presently a viable path for a comprehensive assessment of the properties of the M31 halo [1]

While large-area (SPLASH) and panoramic (PAndaS) views of the M31 halo now exist, these optical data sets only reach a few magnitudes down the luminosity function and are beset by the insidious metallicity-age degeneracy of the RGB. Thus, we are unable to infer stellar ages from SPLASH or PAndaS imaging data alone. Instead, this degeneracy can only be broken through expensive spectroscopic metalicities that are able to measure not just [Fe/H], but also [α/Fe] — which also *strongly* contributes to the shape of the corresponding isochrones. As a result, the only observational evidence in M31 that can be brought to bear on the question of *in situ*/accreted/kicked-out formation mechanisms in M31 are global metallicity profiles and gross structural properties (e.g., the change in surface brightness profile from Sersic to power-law). While these crude constraints compare favorably to the results of hydrodynamical ΛCDM simulations, they are of insufficient detail to provide precision measurements or sufficient constraints to adapt simulation techniques (McCarthy et al. 2012). And while the inner halo of M31 does contain abundant evidence for accretion by way of substructure, including the *spectacular*, high-surface brightness GSS (Ibata et al. 2001), most of M31's halo remains unexplored to the depths nec-

[1]The Pan-Chromatic Hubble Andromeda Treasury (PHAT), though vast in area, only images a portion of the disk and bulge and is insufficient for study of the questions raised here.

essary to detect more tenuous substructure. Therefore, our view of the M31 inner halo is dominated by the extensive GSS, whereas a more comprehensive understanding of the merger history — including less dramatic, older, and even more recent accretion events — remains largely unknown. Thus, there are potentially many more stellar streams yet to be discovered, with implications for the hierarchical formation of galaxy halos and missing satellite problem (Klypin et al. 1999; Moore et al. 1999; Simon & Geha 2007). Naively we would expect to see more structure in intermediate age stars (assumed to be accreted, with possible contributions from kicked-out stars) compared to older populations (which could be a mixture of *in situ*, accreted and kicked out stars). Moreover, we anticipate that the total count of substructure should decrease systematically from the outer halo (dominated by accretion) to the inner halo (a mixture of all three mechanisms).

1.3 Expected Properties for Halo Formation Mechanisms

Stellar halos provide unique opportunities to probe the overall formation of galaxies, which is both imprinted on the halo populations and still recoverable due to the long dynamical timescales. Broadly, this theme has deep roots in the traditional formulation of galaxy formation as "Eggen, Lynden-Bell & Sandage 'in-situ formation' (Eggen et al. 1962) versus Searle & Zinn (1978) 'accretion' "; the primary datum that Searle & Zinn used to suggest that the Milky Way experienced late-infall inconsistent with formation solely by early, *in situ* formation was a spread in halo age — estimated to be at least several Gyr — as evidenced by variations in the horizontal branch morphologies of Milky Way halo globular clusters. Our modern understanding of halo

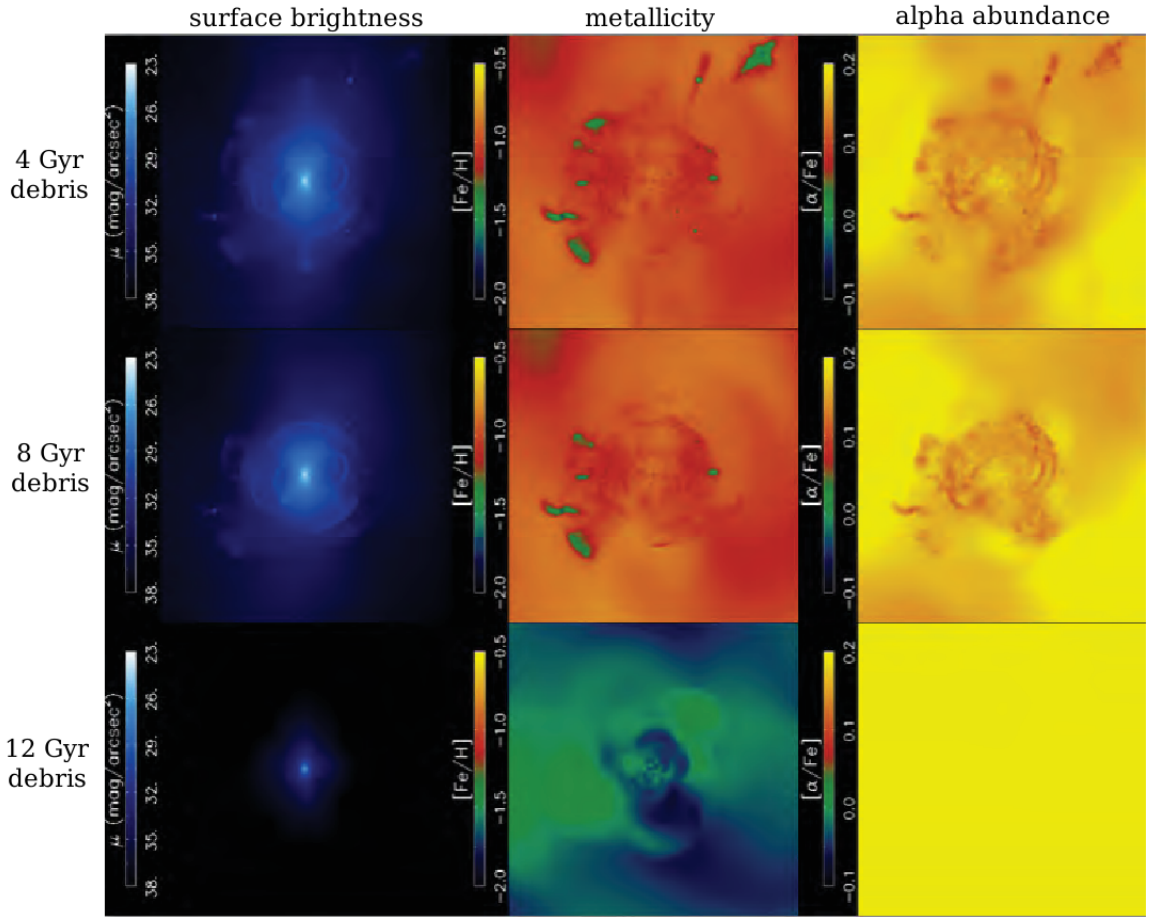

Fig. 1.1.— Model of the formation of a stellar halo in several observational phase spaces adapted from Johnston et al. (2008). The rows (top to bottom) illustrate the present contributions to a model stellar halo that were accreted more than 4, 8, and 12 Gyrs ago, respectively. The columns show projections in surface brightness (left), metallicity (center) and [α/Fe] (right). Current observational work on nearby stellar haloes with resolved stars are focused on revealing the surface brightness substructure (left). While there are some differences in the debris accreted 4, 8 and 12 Gyr ago, the most striking contrast occurs in the metallicity and [α/Fe] spaces and it is this contrast that can help detangle the relevance of the three halo formation models discussed here.

formation lends more sophistication to this basic framework, but still strives to realize the relative contributions from these two disparate portraits of galaxy formation.

In the **accreted** scenario, for example, it is generally assumed that when a gas-rich satellite with (hitherto) continuous star-formation is accreted, star formation ceases through some combination of gas loss via ram pressure stripping by the parent galaxy's hot gaseous halo and blow-out (e.g., Grcevich & Putman 2009, and references therein) or exhaustion of that fuel by acute star formation enhancement incited by tidal shocking (as observed in NGC 5387; Chapters 4 and 5; Beaton et al. 2014). These processes lead to specific expectations for trends in properties of different stellar populations in galaxy halos, as is illustrated in Figure 1.1.

Each column in Figure 1.1 represents the portion of the stellar halo and satellite systems that were accreted more than 4, 8, and 12 Gyrs ago in one of the Bullock & Johnston (2005) model halos, which were built via the superposition of many N-body simulations of individual satellite disruption. The columns of Figure 1.1 show surface brightness, metallicity and [α/Fe], where the observed quantities were calculated using associated semi-analytical work combined with the simulations (Robertson et al. 2005; Font et al. 2006a) A comparison of the rows shows that: (1) the earliest-accreted stars form a smooth, inner, metal poor and α-rich component; (2) high-surface-brightness spatial substructures (streams and shells) are accreted more recently, more spatially extended, and generally more α-poor and metal-rich (Font et al. 2006b, 2008); and (3) satellites are the most-recently accreted population, with a range of metalicities, but overall α-poor (Font et al. 2006a), consistent with observations (Venn et al. 2004). While compelling, previous comparisons between the stellar population variations predicted in the models and observed in M 31 are limited to a few, small-area lines-of-sight (Gilbert et al. 2009a) and to only the inner portions of the Milky Way's stellar

halo (tens of kpc, Bell et al. 2010). The work described in this Thesis (Chapter 3) — the secure identification of M 31 halo populations at a global level — is the first step toward measuring stellar ages and chemistries *over a larger range of radii* and is complementary to current work in the Milky Way. Moreover, detailed study of M 31 on par with those studies of the Milky Way provide data for a second real halo against which to compare the models — and a halo that already demonstrates the striking structural differences discussed previously. In the case of M 31, identifying intermediate age stars will not only *indicate* the presence of recently accreted material but also, allow estimates of the range of infall times of disrupted satellites (Chapter 6). Moreover, if the intermediate age populations show *increasing* dominance in the outer halo, the outer halo can be inferred to be composed of more recent accretion events. If there are trends in mean satellite populations with galactic radius, then there is an implied systematic change in the accretion timescale with the orbital energy of the satellite (Rocha et al. 2012).

Stars formed within the main halo progenitor (and not accreted from other objects) can be created not only *in situ* during the primordial collapse of the halo (see below), but also within the main galaxy's bulge or disk and later **kicked-out** onto higher energy orbits. This halo-formation mechanism has been illustrated with both N-body (Purcell et al. 2010) and hydrodynamical simulations (McCarthy et al. 2012; Zolotov et al. 2009). At present, these simulations are unable to predict firmly the importance of this contribution to the halo given the difficulty of forming simulated galaxies with realistic sizes and star formation histories. In this case, rather than confirming predictions of the simulations, identifying a kicked-out population yields an important constraint on this phase of halo formation. The simulations *are* able to give valuable insight into our expectations of where to find and how to identify these

stars observationally. For example, Zolotov et al. (2010) see an inner halo in their simulations that is dominated by such kicked-out stars (out to a few tens of kpc) and that it is possible to distinguish these stars from those that had been accreted by looking in abundance space: *kicked out stars are metal rich and α-enhanced compared to the accreted population.* If such kicked-out stars form a significant part of M31's stellar halo, our surveys would identify them as a large, intermediate-age population at small radii, which would be hard to explain in purely accreted models.

The remaining **in situ** component of a stellar halo, thought to form in the primordial collapse as the main halo progenitor first forms, has been seen in the hydrodynamical simulations of Samland & Gerhard (2003). These stars would form an ancient, metal-poor, and [α]-rich population in the inner halo. It would be hard to separate these stars either from an ancient accreted or a kicked-out population. Rather, the presence of these stars could be inferred if our accounting of accreted and kicked-out stars falls short of the populations actually observed in the inner halo.

1.4 Overview

The unifying theme of the work presented within this thesis is that of using stellar populations to prove the stellar halos of Milky Way sized galaxies. As motivated in previous sections, the observational census of stellar halo structures even for the most accessible galaxies — the Milky Way and M 31 — is relatively sparse compared to our modern understanding (albeit a complex one) of other galaxy structures. Of the questions posed in the preceding sections, the most compelling can only be answered with the more detailed "phase space" probes (Figure 1.1) that are not currently feasible on the global scale required to address them. Present efforts to study stellar haloes, however, are still focused on their basic characterization — the overall size, shape

and kinematical properties — and it is this effort to which this work contributes. The ordering of topics proceeds from the properties of the very nearby stars, to the samples of stars in M 31, and out to study the stellar populations of distant galaxies in resolved light. The progression is meant to demonstrate the complementary nature of each in obtaining a full portrait of galaxy formation; more specifically, while the nearby objects permit study in high detail, we are fundamentally limited to only a handful of galaxies, and *only* with the acquisition of statistical samples can the we begin to understand the level of cosmic variation inherent to this aspect of galaxy formation. Each chapter addresses independent questions using different observational techniques and technical analyses and, as such, introductory material is provided for each individual study.

1.4.1 Stellar Evolution: The Unnoticed Discovery of Subgiants in 1935

In Chapter 2, we present a historical study into the discovery of subgiant stars by the early 20th century Mt. Wilson spectroscopic campaign. While the overt subject matter deviates strongly from the other chapters, the role of subgiant stars in our modern understanding of stellar evolution, and by extension the power of color-magnitude diagrams to identify stellar populations, can not be overstated. In the early 20th century, the astronomical community was focused on the formidable challenge posed by the questions of how stars are structured, powered and evolve. Key to this understanding was appropriate placement of stars on the Hertzsprung-Russell diagram and the measurement of absolute luminosities (and thus distances) for large samples of stars spanning each phase of evolution. The technique of spectroscopic parallaxes — determination of absolute magnitudes from luminosity sensitive spectral

lines — had great potential to generate large samples of stars without the severely limiting restrictions and biases of other geometric parallax techniques. In a seminal 1935 catalog, the Mount Wilson Observatory spectroscopists produced an H-R diagram for 4,179 stars using this method, and identified a distinct grouping of "90 stars of intermediate luminosity" lying between the already known giant and dwarf sequences. Currently known as subgiants, these stars provided a crucial, and hitherto missing, evolutionary link between the dwarf and giant phases of evolution and could have definitively ruled out the prevailing giant-to-dwarf contraction hypothesis postulated by Henry Russell. What caused a several decade delay in the appreciation of the transitionary role of these stars in stellar evolution? We review the criticisms of the spectroscopic parallax method that ultimately resulted in the dismissal of Mt. Wilson results for subgiant class stars. By comparing the Mt. Wilson parallaxes with trigonometric values from Hipparcos, we show that the concerns, while theoretically well-posed, were ultimately overstated and that the spectroscopic parallaxes over all spectral types are remarkably robust. The existence of the subgiant branch in the 1935 publication provided a fundamental clue to stellar evolution, but one that was largely ignored (and remains largely uncredited). The stellar evolutionary path through subgiants was only verified with their striking rediscovery via accurate photometry of star clusters decades later.

1.4.2 Resolved Stellar Halos: The Transverse Motion of M 31

In Chapter 3, the full SPLASH dataset is presented and used to determine the three dimensional motion of the Andromeda spiral galaxy (M31). This motion is of key interest to understanding the past, current, and future dynamical state of the Local

Group. Several approaches exist to measure its tangential component, each probing distinct dynamical components within M 31. One of the techniques uses the projection of the three dimensional center-of-mass motion of M 31 on the line-of-sight motions of its member objects at large angular separation. This technique is most ideal for application to halo tracers, either to the satellite and outer globular cluster sample or to a large number of individual M 31 halo stars. For the former, we combine recent line-of-sight catalogs for dwarf satellites and globular clusters to revise the estimate of van der Marel et al. (2012). For the latter, we use the full kinematic dataset of the Spectroscopic and Photometric Landscape of the Andromeda Stellar Halo (SPLASH) project (Gilbert et al. 2012, and references therein) and supplement it with an observational campaign to increase the number of member stars at large radii (R_{proj} >120 kpc). Potential sources of bias within each of the samples are explored. These two independent estimates using halo populations are combined with other techniques resulting in a final error weighted mean result of (v_W, v_N) = (-96.4 ± 22.4 km s^{-1}, -44.7 ± 25.4 km s^{-1}). With the removal of the tangential motion component, we discuss the potential to explore the internal kinematics of the M 31 stellar halo.

1.4.3 Unresolved Stellar Halos: The Minor Merger in NGC 5387

In Chapter 4, we present a probe into a stellar halo using unresolved low surface brightness features. We have identified a low surface brightness stellar stream from visual inspection of Sloan Digital Sky Survey (SDSS) imaging for the edge-on, spiral galaxy NGC 5387. An optically blue overdensity coincident with the stream intersection with the NGC 5387 disk was also identified in SDSS and in the Galaxy Evolution Explorer Deep Imaging Survey (GALEX-DIS). In the latter, the region contributes

38% of the total far-UV integrated flux from NGC 5387. Deeper optical imaging was acquired with the Vatican Advanced Technology Telescope that confirmed the presence of both features. The stellar stream is red in color, (B-V) = 0.7, has a stellar mass of $6\times\ 10^8 M_\odot$, which implies a 1:50 merger ratio, has a circular radius, R_{circ} ∼11.7 kpc and formed in ∼240 Myr, from a progenitor with a total mass of $\sim 4\times 10^{10} M_\odot$. Spectroscopy from LBT+MODS1 was used to determine that the blue overdensity is at the same redshift as NGC 5387, consists of young stellar populations (∼10 Myr), is metal-poor ($12+log(O/H) = 8.03$), and is forming stars at an enhanced rate (∼1-3 $M_\odot$ yr^{-1}). The most likely interpretations are that the blue overdensity is (1) a region of enhanced star formation in the outer disk of NGC 5387 induced by the minor accretion event or (2) the progenitor of the stellar stream experiencing enhanced star formation.

In Chapter 5, the two interpretations of NGC 5387 are explored in more depth. Neither of the two most likely scenarios have been directly observed in a merger of this mass ratio. Detailed N-body simulations are conducted to conclude that the region is most likely the remnant of the stream progenitor, implying we have caught this event at a unique phase of its evolution. We obtain a better understanding of this conclusion via comparison to nearby star-forming galaxies in the Local Volume Legacy Survey (LVLS) and to Milky Way-LMC analogues in the SDSS footprint. Lastly, we apply galaxy morphology metrics to the images of NGC 5387 to understand how this galaxy would be classified in a "blind" morphology survey, finding the FUV morphology is classified as a major merger (1:4 mass ratio).

1.4.4 Visualizing Phase Space: Next Generation Probes of Stellar Halos

In Chapter 6 the chapters of the thesis are summarized and the next stage of the SPLASH project is described. Recent detailed hydrodynamical and N-body simulations, carried out within the framework of a Λ-CDM cosmogony, can track the formation of single Milky Way sized galaxies. It is clear from these simulations that stars in the halo can have three distinct origins: accretion of satellites, in situ formation, and kicked up disk, and each of these origins imprints a distinct age and chemical pattern in the halo. The M 31 Asymptotic Giants Extended Survey (M 31AGES) aims to constrain these three populations using a new near-infrared survey of the SPLASH footprint that permits the construction of age distribution functions for 72 pencil-beam probes across its stellar halo. These age distribution functions permit the detangling of the origin mechanisms within halo stellar samples and thereby offer observational discriminants for competing numerical models of galaxy formation in the *Lambda*-CDM paradigm.

Chapter 2

Comparison of Hipparcos Trigonometric and Mount Wilson Spectroscopic Parallaxes for 90 Subgiants that Defined the Class in 1935

2.1 Chapter Overview

A history is given of the discovery between 1914 and 1935 of stars of intermediate luminosity between giants and dwarfs with spectral types between G0 to K3. The Mount Wilson spectroscopists identified about 90 such stars in their 1935 summary paper of spectroscopic absolute magnitudes for 4179 stars. Called "subgiants" by Strömberg, these 90 stars defined the group at the time. The position of the Mount Wilson subgiants in the HR diagram caused difficulties in comparisons of high weight trigonometric parallaxes being measured in the 1930s and with Russell's prevailing evolution proposal, and critics questioned the reality of the Mount Wilson subgiants. To show that the 1935 Mount Wilson subgiants are real, we compare, star-by-star, the Mount Wilson spectroscopic absolute magnitudes of the 90 stars defining their sample against those absolute magnitudes derived from Hipparcos trigonometric parallaxes. We address concerns over biases in the Mount Wilson calibration sample and biases created by the adopted methodology for calibration. Historically, these concerns were sufficient to discredit the discovery of subgiants in the Mount Wilson sample. The result is that the majority of the Mount Wilson stars identified as subgiants that also have reliable Hipparcos trigonometric parallaxes do lie among the subgiant sequence in the Hipparcos HR diagram. Moreover, no significant offset is seen between the M_V brightnesses derived from the Mount Wilson spectroscopic parallaxes and the M_V values derived from Hipparcos trigonometric parallaxes with $\sigma_\pi/\pi < 0.10$, which confirms in an impressive manner the efficacy of the original Mount Wilson assessments. The existence of subgiants proved that Russell's contraction proposal for stellar evolution from giants to the main sequence was incorrect. Instead, Gamow's 1944 unpublished conjecture that subgiants are post main sequence stars just having left the main sequence was very nearly correct but was a decade before its time.

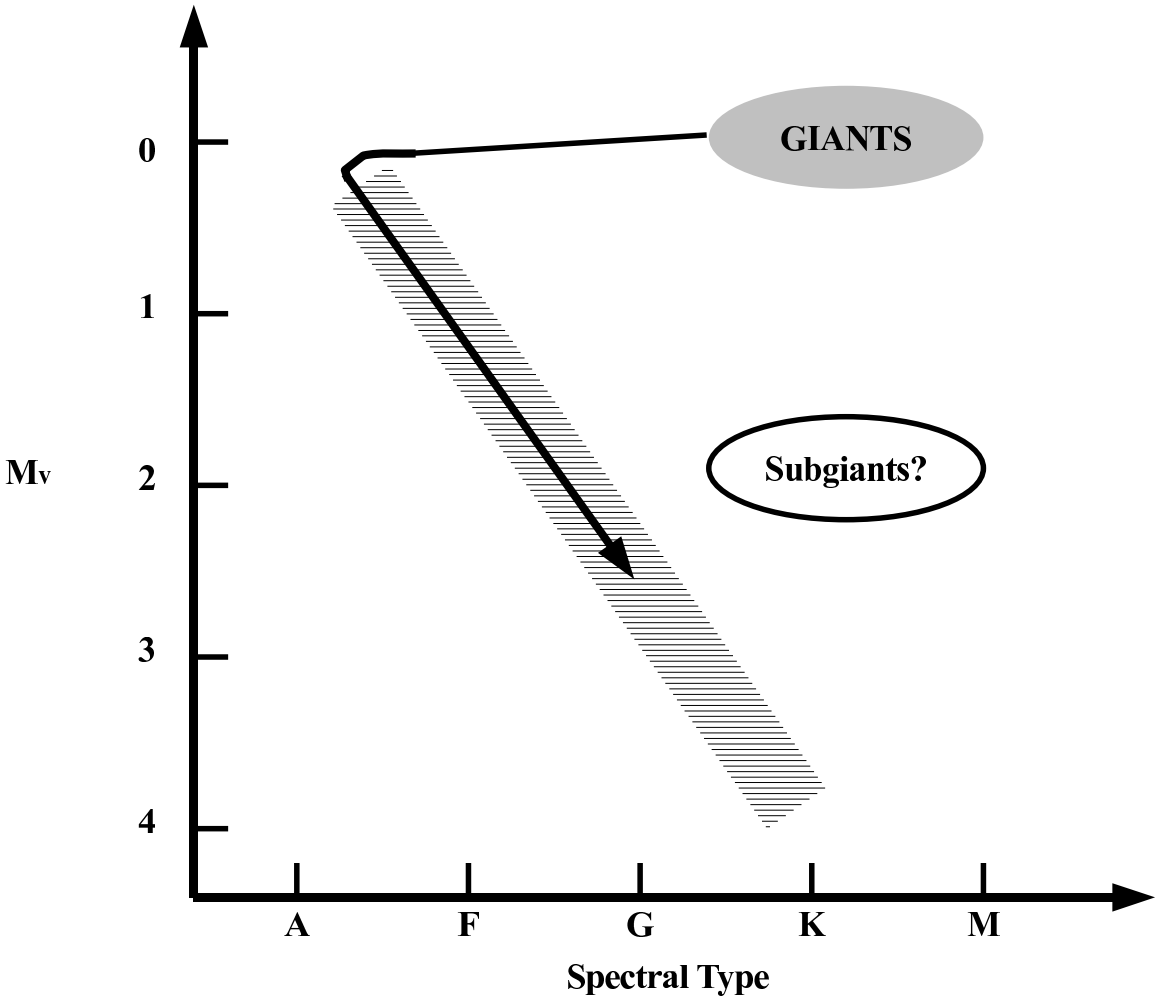

Fig. 2.1.— A schematic representation of Russell's evolutionary proposal for populating the main sequence by contraction of the giants and subsequent evolution down the main sequence at nearly constant radius after the main sequence stars become "rigid." The subgiants could not be accommodated by this contraction scenario. The position of the subgiants is adapted from the position of the subgiants in A35 (their Figure 1).

2.2 Introduction:

Often, in events leading to the beginning of a new field within science, there appears an observation or experiment, not understood at the time, that in the clarity of hindsight opened the field. There are many such episodes. A famous one in physics is the observation of at least 400 years ago that two bodies of different weights, when released from a height, reach the ground at the same time. This eventually lead to the general theory of relativity.

In astronomy, the initial discovery of subgiant stars is such an episode. Subgiant stars are intermediate in luminosity in the HR diagram between the main sequence dwarfs and the giants near $M_V = +0.5$. The subgiants occur at absolute magnitudes between M_V of +2 to +4 and spectral types between G0 and K3. Had they been fully understood from hints of their existence in the 1920s and their definitive discovery by Strömberg (1930) in his absolute magnitude calibration, the path to an understanding of stellar evolution might have been hastened.

The purpose of this paper is to recount the discovery of subgiants and to point out the difficulty that their existence posed for Russell's early theory of stellar evolution. We then address the concern of early doubters of their existence, but show that Strömberg's 1930 subgiants were real by comparing the Mount Wilson spectroscopic parallaxes of Adams et al. (1935) with modern Hipparcos trigonometric parallaxes for the ∼90 stars that defined the stellar class in 1935.

The plan of the paper is this. A history of the discovery of subgiants from 1917 to 1955 is given in the next subsection (Section 2.2.1). This is an extension of the very brief account given in Sandage et al. (2003, hereafter SLV03) The dilemma of the existence of subgiants for Russell's proposal (Russell 1914, 1925b,a) about the direction of stellar evolution and Gamow's conjecture for a solution is discussed in

Section 2.3.

Section 2.4 is an account of the 1957 Vatican conference where the HR diagram of 25 subgiants with trigonometric parallaxes greater than 0″.052 was discussed. The dilemma posed at that conference that field subgiants exist fainter than those in M67 is solved in Section 2.4.2 with an account of the discovery of the true ages of the old open clusters NGC 188 and NGC 6197.

In Section 2.5, Hipparcos trigonometric absolute magnitudes are compared with the 1935 Mount Wilson spectroscopic magnitudes of the ∼90 proposed Mount Wilson subgiants. In Section 2.6, the biases in the Adams et al. (1935) dataset are isolated and properly removed from the data, to address and quantify the historical criticisms that challenged and colored perceptions of the veracity of the Mount Wilson spectroscopic dataset. Section 2.7 is a summary of the work presented here.

2.2.1 The Discovery

Following the invention of the method of measuring absolute magnitudes from stellar spectra by Adams & Kohlschutter (1914), Adams & Joy (1917) published their first long list of absolute magnitudes for 500 stars of spectral classes from F0 to M. The distribution of absolute magnitudes for various intervals of spectral type clearly showed the separation of giants and dwarfs, discovered by Hertzsprung (1905, 1907) and Russell (1914), but also showed a very few stars near $M_V = +2$ in the spectral interval from G0 to K3. The result is well shown in the distribution of Adams & Kohlschutter (1914). A matrix representation of their 500 star sample was set out by Adams & Joy (1922) three years later, reproduced for easier access in Sandage (2004, hereafter S04, Figure 15.6). This representation clearly illustrated how very few of these intermediate luminosity stars were included in the magnitude-limited sample of

Adams & Joy (1917) — so few that one could question the reliability of their existence. However, Curtis (1922) had summarized all spectroscopic absolute magnitudes known at the time, and again, with imagination, one could make out a continuum distribution of absolute magnitudes between $M_V = +0.5$ and $+5$ for spectral types G5 and K0 (S04, Figure 15.5), yet the case for existence of subgiants remained far from definitive.

Subgiants were also consistently appearing in studies of a different kind where absolute magnitudes were estimated by independent methods. The method of "proper motion statistical parallaxes" had been invented by Jacobus C. Kapteyn and Arnold Kohlschütter in application to K stars, but remained unpublished until its application to spectroscopic parallaxes was realized by Adams & Kohlschutter (1914). It relied on the size of the proper motion for "normal" stars, assuming that, statistically, in a large group of such stars, those with smaller proper motions were at larger distances. Luyten (1922) used the method with 4446 stars of known proper motion and showed in a matrix, much like that used by Adams & Joy (1922), that a continuum exists for stars of this type in the HR diagram between giants and dwarfs for spectral types G0 to K3. But again, no such continuum exists later than K3. Still, the number of such stars was minuscule and was generally ignored. The work with the so called "reduced proper motions" was repeated by Lundmark (1932), again using more than 4000 stars.

The final list of the Mount Wilson spectroscopic parallaxes and the resulting HR diagram derived was published in the famous summary paper by Adams, Joy, Humason and Brayton in 1935. In Adams et al. (1935, A35 hereafter), the subgiant sequence was unmistakable between G2 and K3 and at $\langle M_V \rangle = +2.5$, based on the statistical parallax calibrations of Strömberg (1930, 1932, 1936, see S04, Figs. 20.2,

20.3). Adams et al. wrote, "The existence of a group of stars of types G and K somewhat fainter than normal giants has been indicated by the statistical studies of Strömberg (1930, 1932). Although these stars may not be entirely separated from the giants in absolute magnitude, there is some spectroscopic evidence to support the suggestion."

During the later part of this Mount Wilson activity (1920-1935), such stars began appearing in lists of high weight trigonometric parallaxes and their existence could not be denied. By 1936, six extreme subgiants with large trigonometric parallaxes could be said to define a subgiant sequence independently of spectroscopic parallaxes. These were μ Her (type G5, trigonometric parallax = $0''.119$, $M_V = +3.75$); δ Eri (K0, $0''.111$, +3.68); 31 Aql (G8, $0''.059$, + 3.97); β Aql (G8, $0''.073$, +2.83); γ Cep (K1, $0''.072$, +2.223); and η Cep ($0''.070$, K0, +2.68).[1] The first three are fainter than the others by more than a magnitude, which shows the rather large intrinsic dispersion for the class. In the modern development of the Hipparcos HR diagram, this intrinsic spread is seen to be about 3 magnitudes (Perryman et al. 1995; Kovalevsky 1998).

In a historical and singular paper, Morgan (1937) acknowledges the existence of subgiants, calculating the surface gravity of β Aql, η Cep, and γ Cep — the stars defining the subgiant class at that time — to be intermediate between the surface gravities of giants and dwarfs. It is also in this paper that W. W. Morgan sets out the case for abandoning the assignment of absolute magnitudes to the Mount Wilson spectroscopic two dimensional classifications, and replacing them by a continuum of numbers ranging from -9 to $+21$. The numerical continuum was related to the absolute magnitudes but was uncalibrated, representing the raw line ratios measured from the spectra, with the intent to calibrate these values to absolute magnitudes

[1] Values for the trigonometric parallax and M_V are those from that era, but these values are remarkably close to those found by the Hipparcos satellite.

at a later time. This continuum of numbers was, eventually, replaced in the Atlas of Morgan et al. (1943, hereafter MKK) by discrete boxes called luminosity classes, defining the MKK two dimensional system that discards the original Mount Wilson continuum system and replaces it by a digitized system with large classification boxes. In the 1943 MKK Atlas, the subgiant class was defined by the three stars used by Morgan (1937) to which μ Her and δ Eri were added. These five stars are among the "about 90 [stars] of types G and K somewhat fainter than normal giants" referenced to in A35. The Yerkes subgiant class was designated as luminosity class IV and called subgiants following the name first given by Gustaf Strömberg.

By 1955, Eggen could discuss a group of 20 bright subgiants, some of which have companions permitting calculation of their masses. The result was that the mean mass is near 1.2 $M_{\odot}$, consistent with the expectation that the stars in Eggen's 1955 list are "evolving either from or toward the main sequence, near $M_V = +3.0$." Eggen (1955) showed that most of his 20 stars are within the borders of the subgiant sequence in the old open cluster M67 defined by Johnson (1954), although five are fainter (λ Aur, β Hyi, μ Her, 31 Aql, and δ Eri). Johnson had set up a photoelectric sequence in M67 in preparation for a complete photographic durchmusterung (Johnson & Sandage 1955), but had published his sequence before the photographic work was complete. In 1955, it was not clear how the subgiants tied onto the main sequence, a vital aspect that was sought but not clarified from previous work. Eggen's list of 20 subgiants are among those of A35 given in Table 2.1 here.

By 1957, Eggen produced a color-magnitude diagram Eggen (1957, Figure 1) that clearly tied the few subgiants in a sample of 275 field stars brighter than $M_V = 5.0$ to the M67 main sequence and to the base of the first ascent giants. Eggen's Figure 1 was mentioned by Walter Baade at the 1957 Vatican Conference (Baade 1958).

At that conference one of us could produce a list of 25 subgiants with high weight trigonometric parallaxes that defined the subgiant sequence discussed there (Sandage 1958b, reproduced here as Figure 2.3).

After the conference, two massive papers on motions, masses, and luminosities of bright local field subgiants by Eggen (1960, 1964) completed the discovery phase for the subgiant luminosity class.

2.3 The Dilemma for Russell's Evolution Proposal; Gamow's Supposition

2.3.1 Russell's Dilemma

As stated in the Introduction, in his discovery paper and thereafter, Russell (1914, 1925b,a) proposed that stars evolve by contraction from an initial giant phase, whereupon reaching the main sequence dwarfs they become "rigid," stopping the contraction. Although in the 1920s, Sir Arthur Eddington had proved that main sequence stars do not become "rigid" (main sequence stars have a perfect gas equation of state throughout), nevertheless Henry Norris Russell's several modified proposals remained highly influential throughout the late 1920s and early 1930s. The Russell proposal was widely discussed. An example is the Russell-evolution shown in the HR diagram by ten Burggencate (1927, his Figure 30) or in the more accessible place in S04 (Chapter 17; Figure 17.1)

If the position of the subgiants in the HR diagram of A35 was correct as a sequence independent from that of the giants and dwarfs, the Russell proposal could not be correct. Figure 2.1 demonstrates the dilemma caused by the positioning of the Adams et al. subgiants relative to the giants. The mean magnitudes and spectral types of the

giants and subgiants in Figure 2.1 are taken from the A35 summary diagram (their Figure 2.1). Clearly, either Russell's evolution proposal was wrong, or subgiants did not exist.

Concerning attempts to show that subgiants did not exist, consider a most curious paragraph in Adrian Blaauw's scientific autobiography written in 2004, long after the existence of subgiants had been established (Blaauw 2004). As a beginning astronomer at Leiden in the late 1930s, Adrian Blaauw had studied Gustaf Strömberg's papers and had concluded that "[the observational data on proper motions] could equally be represented without the subgiant branch."[2] This is an astounding conclusion in view of the increasing evidence from high weight trigonometric parallaxes and the accumulating evidence from spectroscopic parallaxes even at the time of Blaauw's graduate work (the 1930's). Perhaps, Adrian Blaauw had not realized that the Mount Wilson subgiants of 1935 were linked with those of M67 in 1955, or with the Hipparcos trigonometric parallaxes of 1994, given that the A35 subgiants were two magnitudes brighter than and not connected to the main sequence. It is the purpose of this paper to show that the two groups of stars are identical by identifying the 90 Mount Wilson stars in a distinct sequence near $M_V = +2$ with the Hipparcos subgiants.

2.3.2 Gamow's Conjecture

In a prescient letter from George Gamow to Walter Adams written in March 1944 and discovered by Devorkin (2006) in the Adams papers of the Huntington Library archives, Gamow proposed a radically different scenario of evolution off the main sequence caused by hydrogen shell burning, shown in Figure 2.2 as track II. The

[2]See also very similar comments to this effect — but instead explicitly critiquing R.E. Wilson's work rather than Strömberg's — in the 1979 interview of Blaauw by David DeVorkin, available in the collection of oral histories on line by the American Institute of Physics (http://www.aip.org/history/ohilist/5002.html).

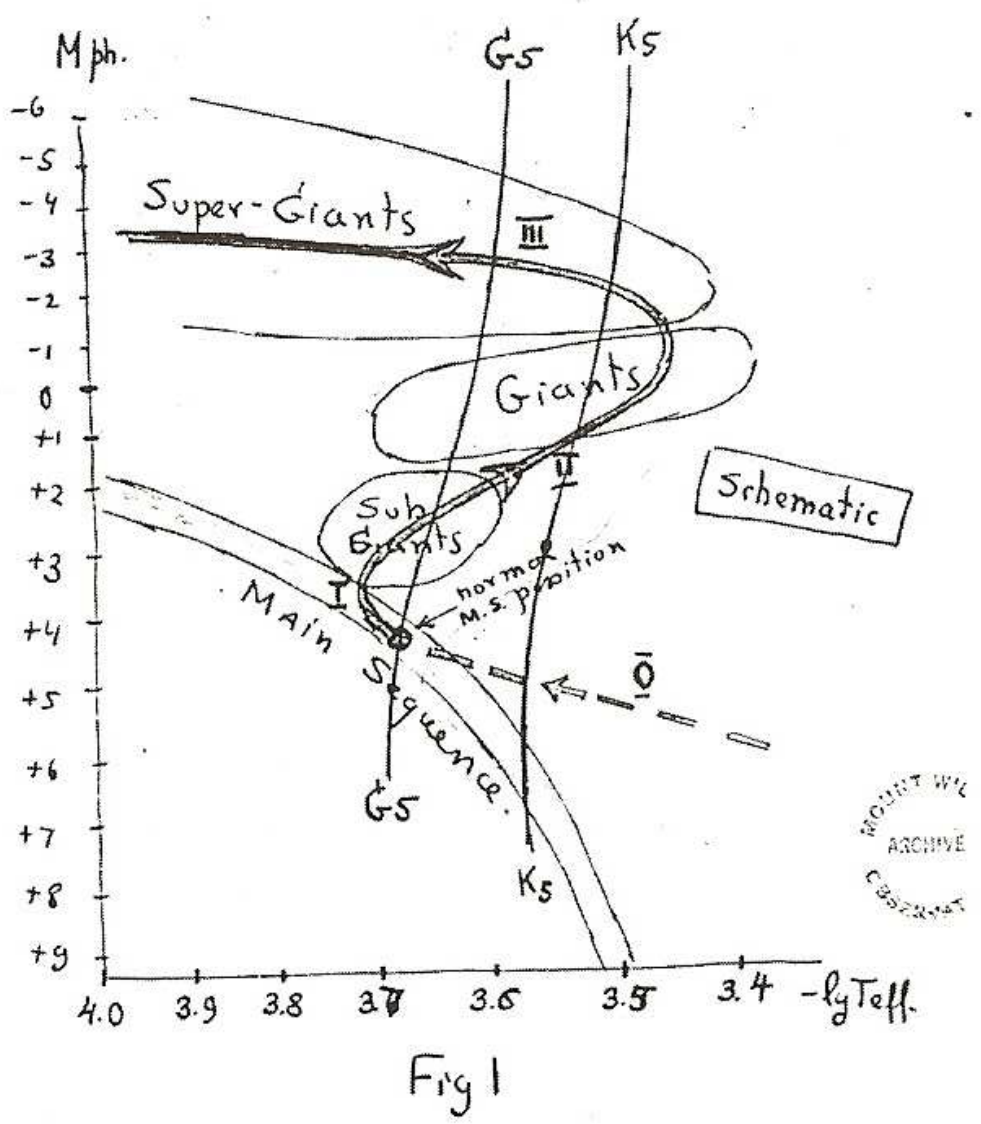

Fig. 2.2.— Gamow's unpublished conjecture from a letter to Adams on March 8, 1944 of evolution off the main sequence, through the subgiants, and then to the giants. This figure is reproduced from the Adams papers archive at the Huntington Library, Sam Marino, CA. A more accessible secondary source is Devorkin (2006).

subsequent expansion of the radius accommodates the subgiants and giants, and then a contraction (track III) gives the Wolf-Rayet stars, and thence to the white dwarfs. Gamow's diagram is remarkably close to the current evolutionary scenario. His conjecture was driven by the results of the model builders, of which he was the most tenacious. Devorkin (2006) tells the story primarily from the many attempts at developing the theory in the early 1940s, all of which failed in important ways.

The breakthrough supporting Gamow's conjecture did come in the early 1950s, largely resulting from improved observational precision that clearly showed a subgiant sequence attached to the main sequence. Moreover, early evolution away from the main sequence was demonstrated in the Population I old Galactic clusters, M67 being the first in 1955. In these new data, the subgiants fit naturally into the observational picture. Gamow's conjecture had been essentially correct, but the breakthrough was most simply displayed before the eyes of the observers with their accurate, faint color magnitude diagrams that began to be produced en masse after 1952.

2.4 The 1957 Vatican Conference and Beyond

2.4.1 The Vatican Conference

Walter Baade's population concepts were discussed from many directions in an important conference in one of the first Semaine d'Etude sponsored and held at the Vatican in 1957 (O'Connell 1958). Among the many topics discussed were comparisons of the HR diagrams of Populations I and II relative to the color-magnitude diagram of M67.

To understand the discussion following a report by one of us on the color-magnitude diagram of stars within 20 parsecs of the Sun based on high weight trigonometric parallaxes, reproduced here in Figure 2.3 (Sandage 1958b, Figure 3, p. 295), we must

understand the mindset at the conference concerning the age dating of the globular clusters, in particular the identification of the oldest Galactic clusters. A supposition, incorrect as it turned out, had been set by a report by one of us during the first days of the conference where a composite HR diagram of clusters of different ages, including M67, was compared with that of the old globular cluster M3 (Sandage 1958a, Figure 3, on p. 42), Here the main sequence turnoff point for M3 is placed at nearly the same magnitude as that for M67.

Because globular clusters were acknowledged to be the oldest objects in the Galaxy, and because, by the aforementioned agreement of the M67 turnoff point with the M3 termination magnitude by incorrect alignments in the HR diagram, it was believed at the conference that the M67 subgiants would define the locus of the faintest field subgiants. But with the clear observational violation of that supposition by the faintest subgiants in Figure 2.3, especially seen by 31 Aql, μ Her, and δ Eri, something did not fit, hence the extended and lively discussion recorded in the conference report (O'Connell 1958, pp. 299-302).

The culprit was, of course, the detail of the placing of the turnoffs of M67 and M3 at the same magnitude in the aforesaid diagram. But it must be remembered that in 1957 the dependence of the main sequence on metallicity had not yet been discovered (Sandage & Eggen 1959), nor had the older galactic clusters NGC 188 and NGC 6791 been analyzed for their ages. The positioning of the main sequence according to metallicity has its own long history and is not especially germane to the subgiant story, but the discovery of clusters older than M67 is relevant.

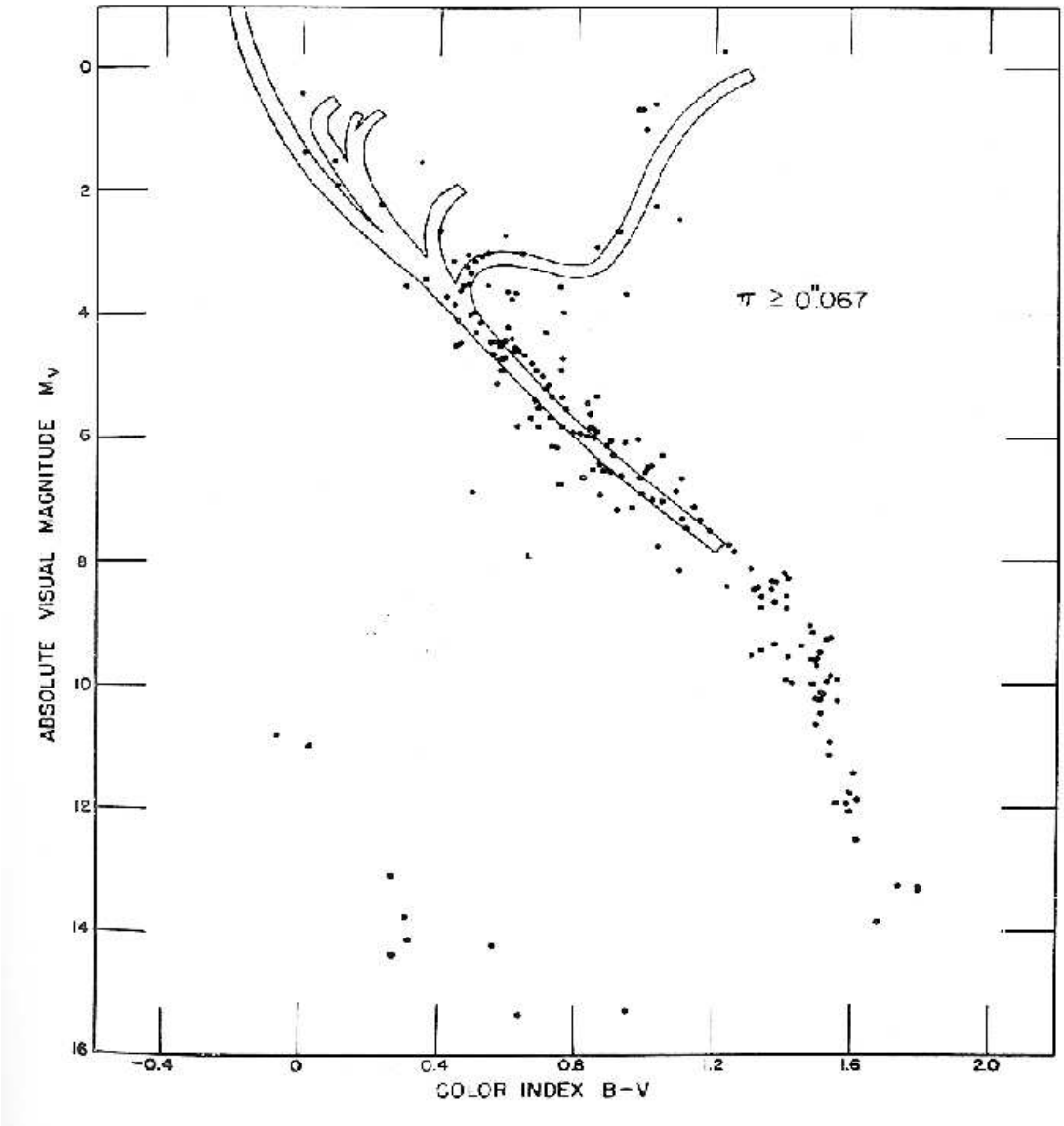

Fig. 2.3.— The HR diagram for stars within 20 parsecs of the Sun with relatively high weight trigonometric parallaxes known in 1957. Nine subgiants are fainter than the M67 subgiants, contrary to the expectation of the Vatican Conference, which raised questions of their reliability. Diagram from Sandage (1958b, his Fig. 3, p. 295).

2.4.2 Many Field Subgiants Exist Fainter than those in M 67, NGC 188, and NGC 6791

Following the suggestions of Ivan King and Sidney van den Berg, photometry of NGC 188 showed the cluster to have a turn off luminosity fainter than M 67 (Sandage 1962). The placement of the M 67 and NGC 188 color magnitude diagrams as it was proposed in 1962 is given in Figure 2.4. This shows that the NGC 188 main sequence turnoff is considerably fainter than that of M67.[3]

Kinman (1965) showed that the galactic cluster NGC 6791 was even older than NGC 188. Many color magnitude diagrams have since been produced, perhaps the most accurate being that of Kaluzny & Rucinski (1995). Chaboyer et al. (1999) give a comprehensive review, which is brought up to date by SLV03. The importance of NGC 6791 is that it does define the lower envelope of the field subgiant distribution. There are many subgiant stars fainter than those M67, but none statistically fainter than the subgiant sequence in NGC 6197, as demonstrated in Figure 2.5 (adapted from Figure 12 of SLV03).

2.5 Comparing the Spectroscopic and Trigonometric Parallaxes

The purpose of the paper is to show that the ∼90 subgiants discovered by the Mount Wilson spectroscopists in the late 1920s and early 1930s, as calibrated from statistical parallaxes by Strömberg (1930), are truly subgiants according to Hipparcos

[3] In Figure 2.4 note that the turnoffs of the three globular clusters are again placed at the NGC 188 turnoff magnitude. This is as incorrect as the placement of M67 at the Vatican Conference. Hence, even as late as 1961 the position of the main sequence as a function of metallicity was not taken into account. A more correct diagram is in Sandage (1986, Figs. 5 and 6).

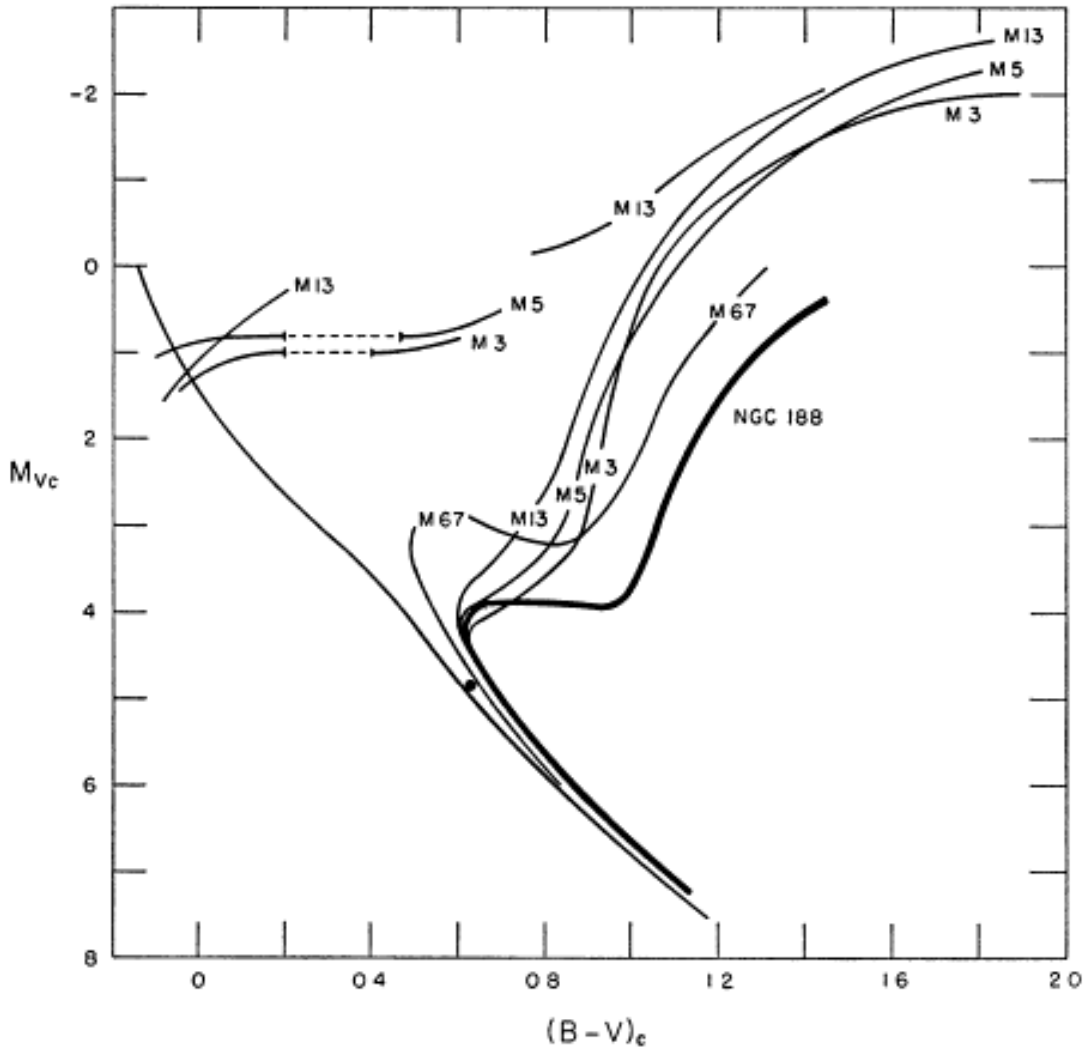

Fig. 2.4.— Solution to the problem of the Vatican Conference with the discovery of the older cluster NGC 188, whose subgiant sequence encompasses all known trigonometric field subgiants known at the time. Diagram from Sandage (1962, his Figure 10)).

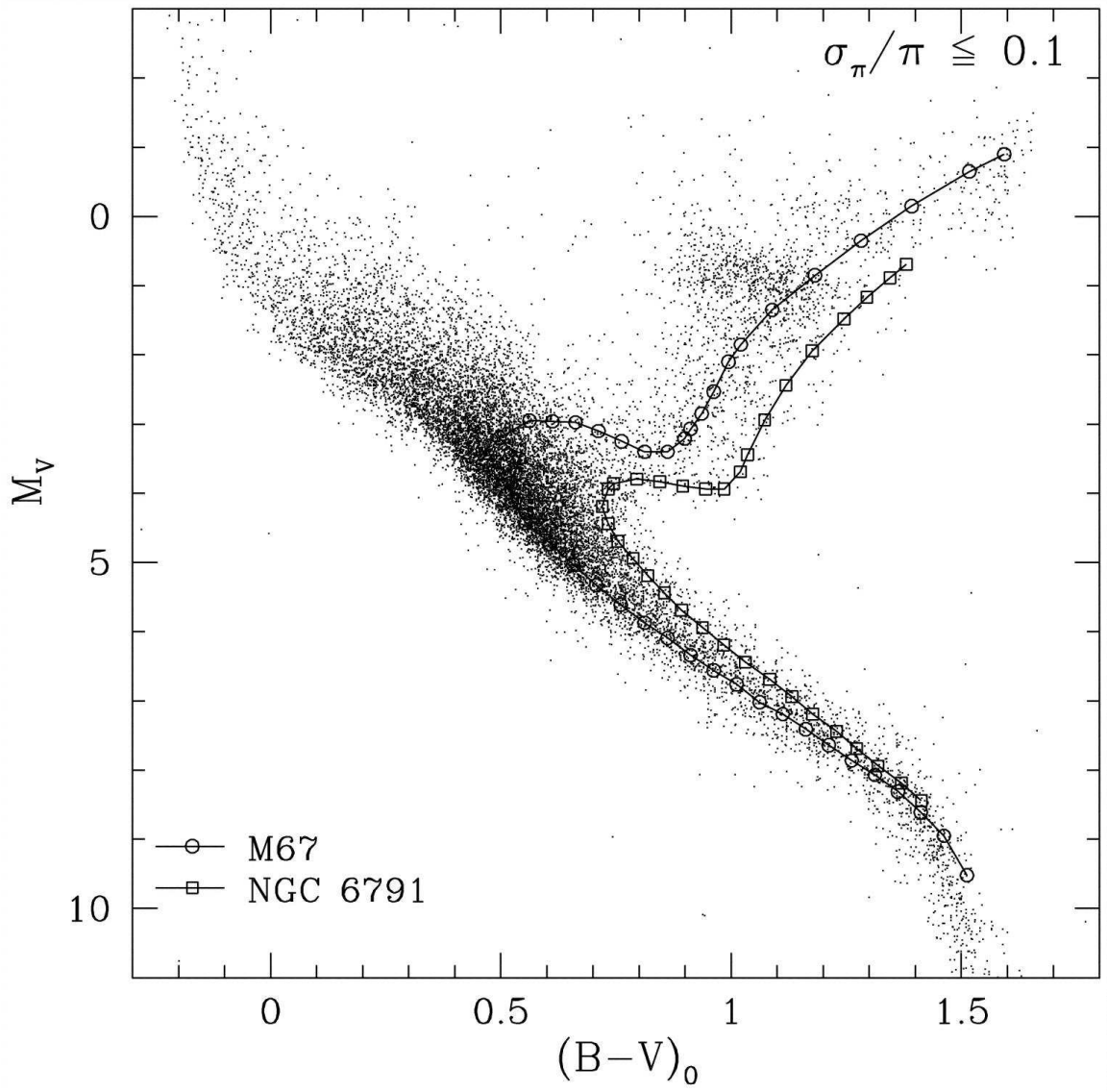

Fig. 2.5.— The HR diagram for Hipparcos field subgiants compared with those for the old galactic clusters M67 and NGC 6791. Many subgiants exist fainter than in M67 and NGC 188. NGC 6791 provides a good lower envelope. Diagram from SLV03 (their Figure 12).

trigonometric parallaxes. As an initial demonstration, we first compare the full A35 spectroscopic sample to the corresponding Hipparcos trigonometric database to highlight the general correlation between the two methodologies. Then, we will explore the key differences between the A35 and Hipparcos parallaxes and potential reasons for these differences.

2.5.1 The A35 Subgiants in the Context of the H-R Diagram

To test whether the Mount Wilson-identified subgiants are real, we employ the trigonometric parallax and photometric magnitude data contained in the revised Hipparcos catalog (Perryman et al. 1995; van Leeuwen 2007a,b, 2008). Matches between the entire Mount Wilson list of 4179 stars as compiled by A35 to the Hipparcos catalog were made solely through the star names — predominantly the Henry Draper number, available for 90% of the stars — as identified in the A35 catalog.[4] We present the full matched catalog in the HR diagrams of Figure 2.6. We note that the A35 catalog contains spectral types, apparent magnitudes, absolute magnitudes and the derived spectroscopic parallax, whereas the Hipparcos catalog contains apparent magnitudes and trigonometric parallaxes. It is also important to bear in mind that the colors and apparent magnitudes in the Hipparcos catalog come from a diverse set of ground-based sources, but we find the data to be reliable and homogeneous enough to make our point (i.e., even with whatever systematic and random uncertainties may lie within the catalog, the correlations we find are strong). In Figure 2.6a we reproduce

[4] Because an electronic version of the extensive Mount Wilson data table, spanning some 93 pages of the Astrophysical Journal, does not exist, these pages were scanned into digital form and then passed through optical character recognition software (OCR) to compile output tables. The OCR software required considerable training because the fontface and typesetting styles used in the 1935 print journal are not included in standard OCR templates. The output digital tables were then reformatted and checked manually for errors. Detailed data for only the subgiants are presented in this paper, but a digital version of the A35 database is available upon request.

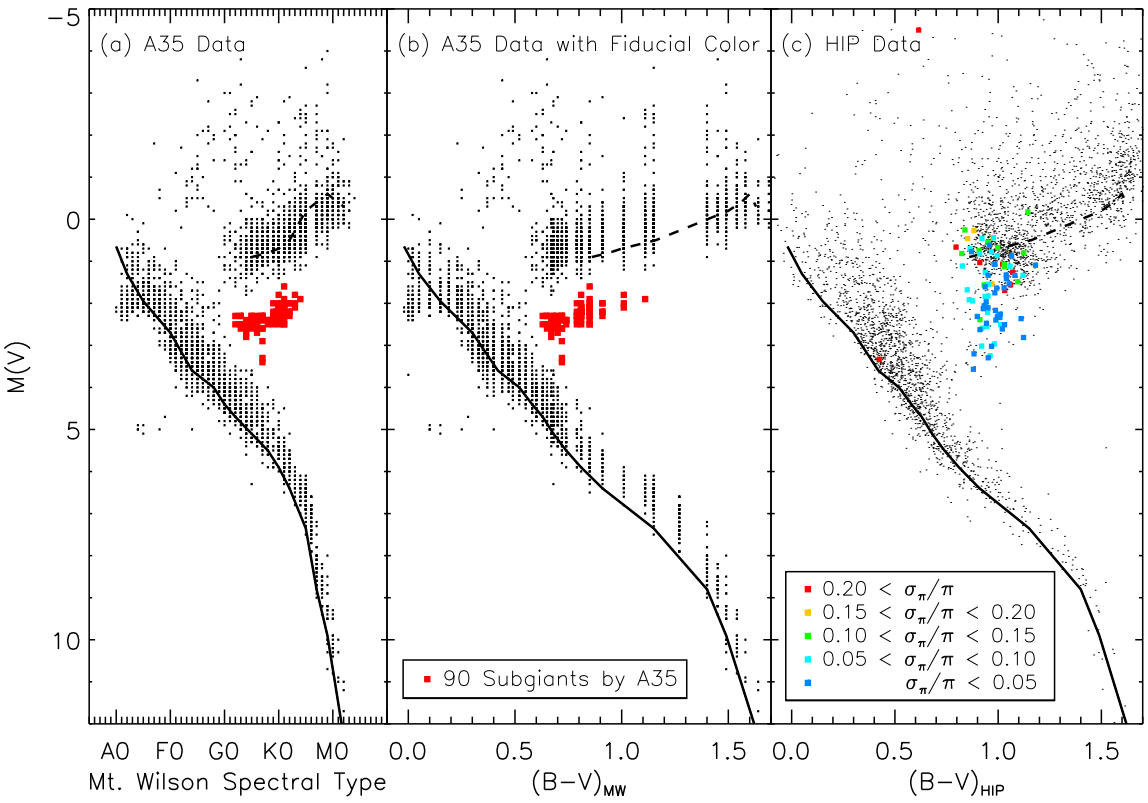

Fig. 2.6.— The HR diagram for the 90 Mount Wilson subgiants from A35 in panel (a) plotted by spectral type and in panel (b) by conversion to a fiducial color, compared to (c) the van Leeuwen (2007a,b, 2008) Hipparcos data for the same stars from the listings in our Table 2.1. The solid line is an example main sequence and the dashed line is an example red giant sequence, with absolute magnitudes taken from Johnson (1966) and colors from Schmidt-Kaler (1982). Red filled squares in panels (a) and (b) indicate those stars we take as those identified as subgiants by A35. In panel (c) these same stars are color coded by their fractional parallax error (σ_π/π). This figure demonstrates that the bulk of the 90 stars identified in A35 are in fact subgiants.

the HR diagram from the original A35 paper and in Figure 2.6b we convert the A35 spectral type to a fiducial $B-V$ color using the standard observed values defining each spectral class as presented in Schmidt-Kaler (1982). In Figure 2.6c, we convert the Hipparcos trigonometric parallaxes to absolute magnitudes using the apparent magnitude information provided in that catalog.

Figure 2.6a is a reproduction of Figure 1 from A35 based on our digitalization of their original catalogue. The stars considered to be subgiants are not explicitly identified in A35. Instead, the authors refer to "stars of type G and K somewhat fainter than normal giants" and a mean magnitude of $M_V \sim 2$. We used the A35 description to identify their subgiants as those stars having $1.6 < M_V < 3.4$ and spectral types from G2 to K4 in the A35 tables; these stars are highlighted as red filled boxes in Figures 2.6a and 2.6b. Fortunately, the majority of the stars we take to be the A35 subgiants are clearly separated from the red giant and main sequences in Figure 2.6a, consistent with the A35 description, and there are few ambiguous examples. We identify 90 such stars as likely to be the A35 "subgiants", and this matches well their statement that they see "about 90 some stars" meeting their criteria.

In Figure 2.6c these same stars are highlighted and color-coded by their Hipparcos fractional parallax error, $\sigma(\pi)/\pi$, which is a standard measure of the reliability of trigonometric parallaxes. The majority of the stars highlighted in Figures 2.6a and 2.6b remain "subgiant-like" in the Hipparcos HR diagram of Figure 2.6c, but the clean separation between the subgiants, giants and main sequence in the A35 data is no longer present; instead they form the more familiar continuous evolutionary sequence from the main sequence to the red giant branch. We emphasize that no Lutz & Kelker (1973) corrections have been applied to the Hipparcos data, but that such corrections are on a scale that will not affect the overall impression given in

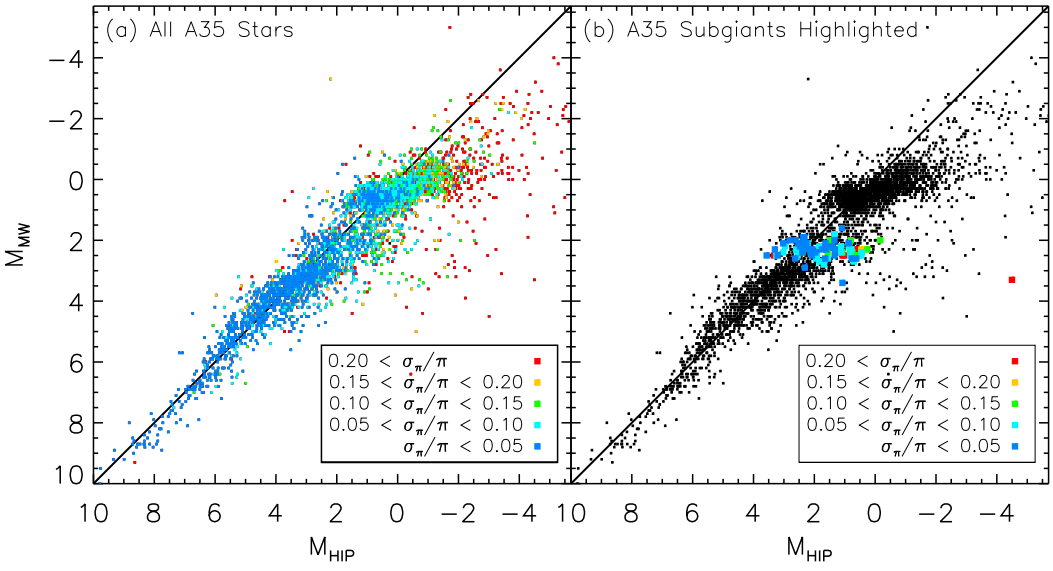

Fig. 2.7.— Comparison of Mount Wilson spectroscopic absolute magnitudes — in panel (a) for the full A35 sample and in panel (b) highlighting the 90 subgiants — with Hipparcos absolute magnitudes for the same stars. The color coding in both panels is by the fractional trigonometric parallax error, or σ_π/π. The A35 and Hipparcos absolute magnitudes for the 90 subgiants are given in Table 2.1.

Figure 2.6c. We discuss the potential effects of the Lutz-Kelker bias in more detail in Section 2.5.3.

Table 2.1 presents the relevant A35 and Hipparcos data for the 90 stars identified as subgiants in Figure 2.6 (the red boxes). Most of the columns of Table 2.1 are self explanatory. Column 9 supplies the value of $\sigma(\pi)/\pi$ from Hipparcos, a useful parameter guiding the interpretation of results. The crucial columns are 10 and 11 where the Mount Wilson absolute magnitudes determined from the spectra are compared with the Hipparcos trigonometric values. Absolute magnitudes from the Hipparcos data are derived by combining the trigonometric parallaxes and apparent magnitudes, while the values adopted by the Mount Wilson astronomers are given directly in the catalogue of A35.[5]

Despite the remarkable correspondence between the spectroscopic and trigonometric absolute magnitudes in Table 2.1, there are two pronounced differences. First, unlike what is seen in the modern Hipparcos panel (Figure 2.6c), the subgiant sequence as positioned by Adams et al. (Figures 2.6a and 2.6b) was neither attached to the main sequence on the left or onto what in later HR diagrams was the base of the first ascent giant branch on the right. Second, the overall scatter along each sequence in the A35 diagram (Figures 2.6a and 2.6b) is smaller than — or at least on par with — that of the more accurate, modern magnitudes in the corresponding Hipparcos diagram (Figure 2.6c). This second effect is most dramatic for the subgiant sequence in A35 (colored points in Figure 2.6), which is nearly horizontal and spans only ~ 1 magnitude of $M(V)$.

Given these morphological differences in the subgiant branch, the significance of the subgiants for stellar evolution were not realized at that time. If it had been, how-

[5] A35 states that their subgiant stars were "selected based on the strength of the lines 4077, 4215, 4324 and 4454. Special reduction curves based on trigonometric parallax were used to determine the absolute magnitudes of these stars."

ever, the placement of these stars could not be explained by the prevailing Russell giant-to-dwarf stellar contraction scenario (Figure 2.1). In contrast, subgiants are a natural phenomenon for the evolutionary model proposed with Gamow's conjecture (Figure 2.2). More specifically, the position of the subgiants in Figure 2.6 is easily explained as stars transitioning from the main sequence to the first-ascent giant branch after hydrogen core exhaustion. As summarized above, this understanding of the role of subgiants in stellar evolution was not to be fully conceptualized until the early 1950s.

Nonetheless, even if it were unrealized at the time, the Mount Wilson spectroscopists had discovered the subgiant sequence from their spectral line classification method. Furthermore, Gamow had, in fact, proposed the correct evolution scenario, but it was a decade before his unpublished conjecture was substantiated based on observations of the main sequence turnoffs in a number of galactic and globular clusters in the 1950s and 1960s.

2.5.2 Magnitude Comparisons

Although the visual comparison of the Mount Wilson HR diagram and CMD (Figures 2.6a and 2.6b, respectively) with the corresponding Hipparcos CMD (Figure 2.6) is quite illustrative, we directly compare the two sets of absolute magnitudes for all stars in the Mount Wilson tables in Figure 2.7. Remarkably, a strong correlation is found among all luminosity classes and spectral types. These results convey the striking efficacy of the Mount Wilson spectroscopists to get the true absolute magnitudes from spectra, and, in particular, for the previously unidentified subgiant class (those stars with $1.6 < M_V < 3.4$ and spectral type from G2 to K4).

There are, however, some differences visible in Figure 2.7 and these differences

vary with the luminosity class. The main sequence stars by far exhibit the cleanest correlation, $\langle M_{V,\mathrm{MtW}} - M_{V,\mathrm{Hipparcos}} \rangle = 0.18 \pm 0.02$; this is largely because the A35 absolute magnitudes of these stars were calibrated using the trigonometric parallaxes available to the Mount Wilson astronomers at that time.

The subgiant and giant branches, however, exhibit a correlation that is visibly shallower than that for the main sequence. Additionally, the giant and subgiant mean offsets are substantially larger: for the giants $\langle M_{V,\mathrm{MtW}} - M_{V,\mathrm{Hipparcos}} \rangle = 0.46 \pm 0.02$ and for the subgiants $\langle M_{V,\mathrm{MtW}} - M_{V,\mathrm{Hipparcos}} \rangle = -0.24 \pm 0.07$. From visual inspection of Figure 2.7, however, it is clear that those stars with the lowest σ_π/π agree better with the A35 results (cyan and blue in Figure 2.7). If we restrict to $\sigma_\pi/\pi \leq 0.05$, then we have, for the main sequence, $\langle M_{V,\mathrm{MtW}} - M_{V,\mathrm{Hipparcos}} \rangle = 0.06 \pm 0.02$, the giants, $\langle M_{V,\mathrm{MtW}} - M_{V,\mathrm{Hipparcos}} \rangle = 0.15 \pm 0.04$, and the subgiants, $\langle M_{V,\mathrm{MtW}} - M_{V,\mathrm{Hipparcos}} \rangle = -0.12 \pm 0.02$. These comparisons are summarized in Table 2.2. Unlike those of the main sequence stars, the absolute magnitudes of the evolved stars were calibrated against a sample of *statistical* parallaxes, which may explain the differences in the behavior of the two classes in Figure 2.7.

Although the overall similarities between the A35 and Hipparcos absolute magnitudes are strong, the magnitude differences are not insubstantial. Furthermore, that the severity of the magnitude differences are correlated with luminosity class may help to explain why the A35 subgiant sequence was not appreciated in the literature of the time. To explore these differences, we first consider the potential effects of the Lutz-Kelker Effect in the Hipparcos absolute magnitudes in Section 2.5.3 as a potential source of the observed mean magnitude offsets in Figure 2.7. In Section 5, we consider the historical discussion regarding the A35 absolute magnitudes to identify and address concerns relating to the efficacy of the A35 calibration technique.

2.5.3 The Lutz-Kelker Effect

The Lutz-Kelker Effect (LKE, hereafter) is an insidious and complex bias afflicting trigonometric parallax samples that was first formalized by Lutz & Kelker (1973). The effect is defined as an offset between the mean absolute magnitudes for classes of stars as determined from trigonometric parallax samples and the true mean absolute magnitude for that stellar class. Because the effect is only identified in the mean values derived for a stellar class its effect on individual stars is difficult to intuit. Here we first review the origin of the bias, and use a brief schematic analysis to assess the severity of the LKE in the matched A35-Hipparcos sample. A more rigorous derivation of the relevant LKE parameters is given in Appendix 1 (Section 2.10).

At the parallax limit of a sample, the volume element just outside of the limit is larger than the one just inside. A symmetric error distribution applied to both volume elements will systematically scatter more stars into a sample than out — because the outer (and larger) volume element is likely to have more stars (though the magnitude of the effect clearly depends on the underlying stellar distribution!). This asymmetrical scattering has the consequence that, statistically, more stars of a given stellar class will be scattered into a parallax-limited sample than out. The parallax for a star scattered into the sample is obviously observed to be larger than the true value, and by consequence, both the inferred distance and intrinsic flux are underestimated. Thus, the mean absolute magnitude of a particular stellar class within the sample will be offset compared to the true intrinsic mean magnitude for that class; this offset is defined as the Lutz-Kelker correction. Early numerical explorations of the bias parameterized it by $\sigma(\pi)/\pi$, the ratio of the error in the parallax to the parallax itself (Lutz & Kelker 1973). The bias is found to be significantly pronounced when $\sigma(\pi)/\pi \gtrsim 0.2$. Because the parallax error is nominally set by the systematics of the

trigonometric parallax program (e.g., temporal baseline, detector pixel scale, overall flux sensitivity), the LKE grows in its relevance towards the volume limit of the survey. Though the LKE is defined as a statistical offset with a *sample* of stars of a given class, Lutz & Kelker (1973) argue that their defined correction could be to be used to correct the derived absolute magnitudes for *individual* stars, and, to some extent, it traditionally has. More recently, the logic behind this practice and Lutz & Kelker's original assertion that the correction could be applied to individual stars has been challenged (van Leeuwen 2007a; Smith 2003; Francis 2014). Irregardless of this "Lutz-Kelker Paradox", it is nonetheless naturally the case that stars with a larger parallax error will show a larger error in derived absolute magnitudes, and, as a class, would be expected to exhibit a larger systematic offset; it is our goal to assess whether this phenomenon has any significant effect in our comparison of A35 absolute magnitudes to those derived from Hipparcos parallaxes. In Figure 2.7a, individual stars are color coded by σ_π/σ. As anticipated, those stars with higher fractional trigonometric parallax errors, show, on average, the largest deviations from the A35 magnitudes — though the degree of this scatter is highly dependent on the luminosity class.

Is the LKE primarily responsible for the magnitude offsets between A35 and Hipparcos (Section 2.4.2; Table 2.2)? The LKE as applied to the Hipparcos catalog, has been explored by numerous authors, including, but not limited to, Oudmaijer et al. (1998), Brown et al. (1998), and van Leeuwen (2007a). Generally, it is advised to reject all stars with fractional errors greater than 10% or $\sigma(\pi)/\pi > 0.10$, but a full treatment of the LKE, and any other relevant biases, requires detailed modeling of the specific sample in question (e.g., Sandage & Saha 2002; van Leeuwen 2007a; Smith 2003; Francis 2014). While the very form and magnitude of the LKE has also been

reassessed and debated (see previous references) we adopt the formalism of Sandage & Saha (2002) for our calculations, which are primarily illustrative; because the latter treatments tend to find bias corrections of an overall smaller magnitude, our examples can then be seen as an upper limit to the influence on the Hipparcos data.

To place the magnitude offsets between the Mount Wilson and Hipparcos data in context, we consider the magnitude and distance distribution for the A35 stars, for which the faintest is $V = 10.5$, the majority are brighter than $V = 8$, and the most distant is only $d = 500$ pc. Hipparcos, however, is complete for $m_V = 7.3$ to 9.0, a limiting magnitude of $m_V = 12.4$, and a median parallax precision of 0.97 mas (i.e., that of a 1000 pc star). As given in Table 2.2, the magnitude differences between A35 and Hipparcos data are generally small compared to the precison feasible for the A35 magnitude measurements, especially so when restricted to $\sigma(\pi)/\pi < 0.05$. Using the restriction $\sigma(\pi)/\pi < 0.05$, a star with the median parallax error would have a corresponding distance ($d = 50$ pc) well within the Hipparcos sampling volume, and at a magnitude for which the Hipparcos sample is complete. Using this fiducial, we conclude that any trigonometric parallax bias offsets in our sample are going to be quite small, and unlikely to strongly influence the impression of the magnitude comparisons given in Section 4.2.

This rough assessment of the role of the LKE in our comparison suggests that it does not significantly influence the general impression given in Figures 2.6 and 2.7. In Appendix 1 (Section 2.10) a detailed numerical exploration of the LKE in the spirit of Sandage & Saha (2002) affecting the Hipparcos data for the A35 sample supports this conclusion.

2.6 Reconciling Criticisms of the A35 Subgiant Sequence

In the previous section we showed that the subgiants discovered in the A35 dataset are bona fide subgiants in the Hipparcos catalog. In our historical account of the discovery of subgiants, we have discussed in detail why the prevailing stellar evolution theory in 1935, the Russell contraction scenario, biased the immediate interpretation of the A35 results at the time of publication. We have not, however, discussed the reasons why the A35 data, which show a clear subgiant sequence, were insufficient to challenge Russell's notions.

Numerous works investigated the reliability of the A35 database, as it remained one of the largest catalogs of absolute magnitudes well into the middle of the 20th-century. A full discussion of this body of work, as well as rigorous comparisons to pre-Hipparcos databases, is given by Blaauw (1963). Our goal, to show conclusively that the Mount Wilson spectroscopists discovered subgiants in their seminal 1935 work, requires addressing the concerns expressed for the A35 calibration methodology by revisiting the doubts on its reliability. More specifically, we must determine whether specific, cited problems artificially created the subgiant sequence in Figure 2.6.

First, we describe the methods employed by A35. Adams & Kohlschutter (1914) first detected a correlation between specific sets of line intensities and the proper motion of the star — more specifically, that for a given spectral type the line intensities for small and large proper motion stars were systematically different. From this initial discovery, a series of line ratios were established as a means of identifying both the spectral type and the absolute magnitude (luminosity) of a star from spectroscopy. This work became the basis for the two decade observing campaign that culminated

in the 4179 member catalog by A35.[6]

This method of "spectroscopic parallax" itself was never a point of contention in the literature; rather, it was the calibration of the technique against existing parallaxes that raised concerns. The calibration required two key decisions: (i) a choice of a suitable external calibration sample, and (ii) the grouping of the existing spectral line data into appropriate classes. For the former, Gustaf Strömberg's parallax program was selected by A35 as an ideal calibration sample, even though his statistical parallax sample for giant stars suffered effects from Malmquist bias. Clearly, this bias would propagate into the A35 catalog, but in manner difficult to intuit; concerns over this problem led to a general distrust of the reliability of the absolute magnitudes for giant stars, and a dismissal of the A35 subgiant sequence as likely attributable to the effect. For decision (ii), the Mount Wilson spectroscopists chose to group the line ratios based on the peaks in their distribution — a process that can suppress outliers (see Appendix 2; Section 2.11) — instead of using an independent criterion to classify the stars by spectral type and luminosity class. The effect of this choice on the A35 catalog is less immediately obvious, but, as will be explained in Section 2.6.2, it resulted in an overall suppression of the true observational errors in the A35 sample. This suppression is visible in Figures 2.6a and 2.6b as the narrow vertical dispersion across all sequences (main, subgiant, and giant) the but most conspicuous for evolved star sequences in Figure 2.6 and the overall "disconnected" nature of all three luminosity sequences in the HR diagram.

Both of the above choices in the calibration process by the Mount Wilson spectroscopists were heavily discussed in the literature, and became a source of contention regarding the legitimacy of spectroscopic parallaxes for any stars not on the main

[6]The full and fascinating history of the Mount Wilson spectroscopic parallax program and work related to the project, including biographical sketches of the contributing scientists, is detailed in S04.

sequence, i.e., any stars not calibrated directly to trigonometric parallaxes. We first address the cited concerns over the effects of Malmquist bias in the selected calibration sample on the A35 survey in Section 2.6.1. Then we qualitatively describe the problems with the A35-adopted calibration methods in Section 2.6.2 and correct the A35 magnitudes for these effects in Section 2.6.2. A detailed quantitative derivation parallel to the more qualitative discussion in Section 2.6.2 is given in Appendix 2 (Section 2.11).

2.6.1 A Test for an Incompleteness (Malmquist) Bias in the 1930 Calibration by Strömberg

The A35 sample featured three luminosity classes cleanly distinguished by their position in the HR diagram: dwarfs, subgiants and giants. The absolute magnitudes were determined from spectral line ratios using independent calibrations for each luminosity class and spectral type. More specifically, the main sequences stars were calibrated with absolute magnitudes from trigonometric parallaxes, whereas the, on average, more distant subgiants and giants were calibrated to statistical parallaxes. In Figure 2.7, the difference in calibration techniques is obvious, with the Mount Wilson absolute magnitudes calibrated to the statistical parallaxes showing a stronger deviation from the Hipparcos values than those calibrated to trigonometric parallaxes.

The statistical parallaxes used to calibrate the giant and subgiant sequences were derived using a sample complete to an apparent magnitude of $V = 5.9$ (Strömberg 1930), whereas the full A35 sample contains significantly fainter stars ($V = 10.5$). In a sample that is not volume limited, intrinsically luminous objects are systematically over represented because they can be surveyed over a larger volume of space than intrinsically fainter objects at the same apparent magnitude limit. The Strömberg

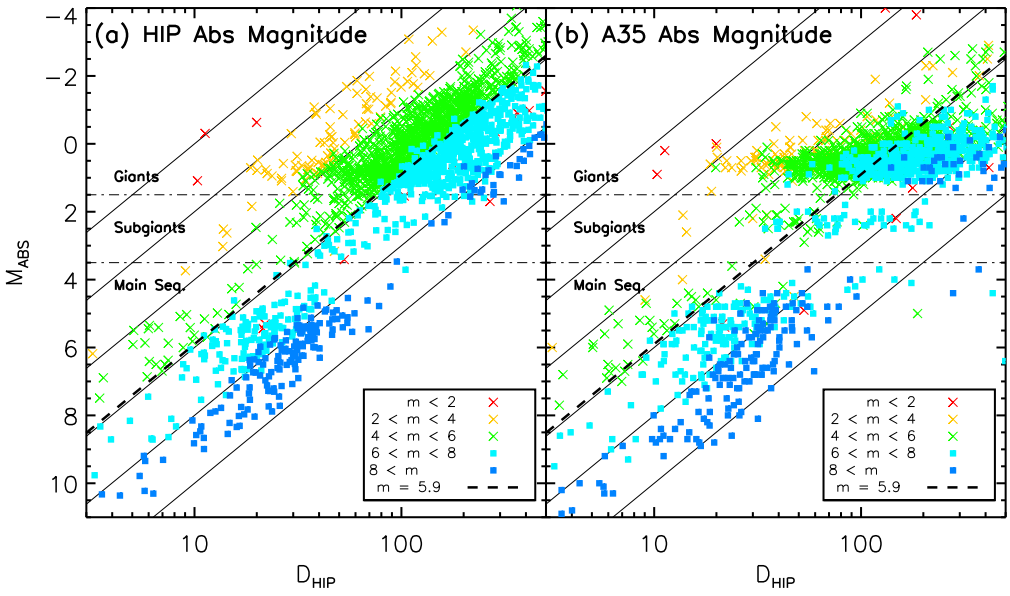

Fig. 2.8.— Spaenhauer diagrams for the matched (a) Hipparcos and (b) A35 magnitude samples, both of which plotted using the Hipparcos distances (D_{HIP}). The thin black lines are the apparent magnitude limits of 0, 2, 4, 6, 8 and 10 magnitudes. The horizontal dot-dash lines mark the separation between luminosity classes of dwarf, subgiant, and giant, while the dashed line separates stars brighter (crosses) and fainter (squares) than $V = 5.9$. The Malmquist bias has the effect of creating intrinsic luminosity trends with distance appear at the faint limit of a sample. As apparently fainter stars are added any trends imposed by the Malmquist bias will disappear, whereas real trends will persist with the fainter samples. Panel (b) shows that the subgiants persist as a distinct group beyond $V = 5.9$.

(1930, 1932) calibration sample was subject to this "Malmquist bias", which skews the mean absolute magnitude of a sample systematically brighter than the true mean absolute magnitude. Thus, with their samples calibrated with the Strömberg data, the A35 absolute magnitudes calculated for the subgiants and giants sample would be systematically brighter than those that would be calibrated against an unbiased sample.

The bias would also apply to any dwarf stars misidentified as giants and for which the giant star calibration were utilized. Under one interpretation, the A35 subgiants were stars misplaced in the HR diagram and made systematically even brighter due to the Malmquist bias. Meanwhile, with the Malmquist bias in the giant star calibration skewing the magnitudes of real giant stars systematically brighter, the separation between luminosity classes would be exaggerated as well, and presumably contribute to the disjoint appearance of the subgiants in the A35 HR diagram.

To judge the viability of these concerns, we can diagnose the role of the Malmquist bias, and even treat its effects, on the A35 magnitudes. The Spaenhauer diagram (Sandage 2001), an effective tool for detecting and correcting the effects of the Malmquist bias, plots the absolute magnitude (M) versus the distance to the object (D). In the Spaenhauer diagram, the presence of the Malmquist bias produces fictitious behavior in the magnitudes with respect to distance. A key requirement for diagnosing the Malmquist bias in a sample is having distance estimates that are independent of the luminosity estimates being explored. One means to diagnose and assess the strength of the Malmquist bias is to assess how the implied behavior of data in the Spaenhauer diagram changes as fainter samples are added incrementally (Sandage 2001).

We demonstrate this technique in Figure 2.8, where we plot (panel a) the Hippar-

cos absolute magnitudes versus the trigonometric distance, which at the maximum radius in this sample, $D < 400$ pc, should not show any significant effects due to this bias. The thick black dashed line represents the flux limit of the Strömberg statistical parallax sample ($V = 5.9$). For the stars with $m_V < 5.9$ ("x" symbols) in Figure 2.8a, those at the greatest distance (the giants) tend to have an intrinsically brighter absolute magnitude. Were one limited to only a $V < 5.9$ sample, one would *incorrectly* infer that there are no intrinsically faint stars beyond 40 pc. But when stars having fainter apparent magnitudes are added (the filled boxes), the previously apparent behavior — i.e., that there are no intrinsically faint stars beyond 40 pc — disappears at those distances at which the sample is now complete. While this particular demonstration is quite simple, in other, more complex datasets the Malmquist bias has historically induced many false impressions (see historical review by Sandage 2001).

Figure 2.8b is similar to Figure 2.8a except the Spaenhauer analysis is applied to A35 absolute magnitudes, which are also plotted against the Hipparcos distance (M_{HIP}). In Figure 2.8b we see the same behavior as in Figure 2.8a for the main sequence stars ($M > 3.5$); again, the magnitude trend with distance disappears as fainter apparent magnitude samples are considered. If we restrict ourselves to those stars with $V > 5.9$, the giants and subgiants are nearly horizontal in magnitude with respect to distance and the two branches are offset from one another. While both trends — the horizontal shape and the separation between branches — are shown to be specious by comparison to the pure Hipparcos data in Figure 2.8a, we can also see by Figure 2.8b that the specious character is not introduced by the Malmquist bias but that, in fact, these features are intrinsic to the A35 absolute magnitudes: As we view increasingly fainter samples in Figure 2.8b, the shape of the giant and subgiant

branches and their separation do not change. This demonstration effectively dispels the notion that the A35 sample for giants and subgiants was significantly compromised by the Malmquist bias in the calibration of Strömberg (1930), and that this bias does not readily account for a false introduction of the subgiant sequence nor does it fully account for the shape of the giant branch. For a full exploration of these criticisms and their implications in the literature of that time, we refer the reader to Blaauw (1963).

2.6.2 Correcting the A35 Calibration Method

Having determined that the Malmquist bias is not the source of the morphological differences between the A35 and Hipparcos CMD, we now explore the A35 calibration as the culprit. For the A35 data, visual estimates of relative spectral line intensities were calibrated empirically to absolute magnitudes derived from trigonometric parallaxes for the dwarfs and to statistical parallaxes for the evolved stars (Strömberg 1930). In this section, we qualitatively describe the luminosity calibration used by A35 and explore how their process induced systematic errors in their derived absolute magnitudes. A complementary quantitative derivation of these errors is given in Appendix 2 (Section 2.11).

Combinations of line intensities had already been shown to classify the stars by their spectral type and in Adams & Kohlschutter (1914), the Mount Wilson spectroscopists discovered a set of line intensities that were sensitive to luminosity. Once the Strömberg (1930) sample of 1647 stars became available, the Mt. Wilson spectroscopists began to explore how to exploit it for calibrating their data. The (Strömberg 1930) stars were first grouped into their spectral classes based on the Mount Wilson criteria. Within each of these classes, the line intensities were observed to cluster

around certain mean values (I_o), and these were correlated with the proper motion of the star (a proxy for the distance to the star). Each of these distinct line intensity groups represented one of the classes from the modern luminosity classification system, though at the time this was primarily limited to the dwarf and giant classes. However, from his calibration sample of 1930, Strömberg had already noted the existence of stars intermediate in luminosity between the giants and dwarfs and he termed these stars "subgiants" for their location relative to the giant branch. Thus, for each of the *three* groups of line intensity, a calibration curve was determined as a linear regression of the form $M = \alpha I + \beta$. These calibrations, derived from the Strömberg sample of 1647 stars, were then applied to the full Mount Wilson sample of 4179 stars in the seminal 1935 catalog.

Though at a cursory glance this calibration procedure seems valid, there is a key flaw in the method: the line intensities were used *both* to determine calibration groupings *and* to derive the calibration curves. Because these two separate steps rely on the same underlying data, they are not independent (impartial). The calibration is, therefore, "partial" to those line intensities tightly clustered around the visually identified mean value, and this bias will have an effect on the derived absolute magnitude distribution. In the case of A35, the Mount Wilson spectroscopists proceeded as if both steps, grouping and calibration within the group, were uncorrelated. This assumption produced both of the morphological differences between Figure 2.6b and Figure 2.6c: (i) the exaggerated separation between the luminosity classes, and (ii) the suppressed dispersion along each of the three sequences.

To illustrate the nature of the bias generated by this procedure, Figure 2.9 uses a pair of fictitious data sets to compare "impartial" and "partial" methods for which the grouping and calibration steps are uncorrelated and correlated, respectively. Figures

2.9a and 2.9b demonstrate the ideal or "impartial" calibration scenario, applied to an "error-free" dataset. In Figure 2.9a, we see the ideal calibration curve between absolute magnitude and line intensity derived from the distribution given in Figure 2.9b. In this case, intensity values (I) are selected by an "impartial" or independent means and the distribution of values, $D(I)$, and its intrinsic, cosmical spread, σ, are well sampled. Here the calibration utilizes the linear fit $M = \alpha I + \beta$ and the scale of the uncertainty in magnitudes, σ_M, follows the usual propagation, $\sigma_M = \alpha\sigma$. Our description here is analogous to the Blaauw (1963) discussion of "impartial" calibration of a dataset having no observational errors, but where the spread in line intensities is only given by a true intrinsic variation among a stellar type.

In Figure 2.9c the linear calibration fit resulting from a "partial" calibration is "torqued" or rotated from that derived in an "impartial" manner. The origin of this torque is the "partial" nature of the adopted line intensity groupings. The observed spread of line intensities in a sample where random observational errors are known to be convolving with the intrinsic line intensity spread, $D(I_{obs})$, there is a natural tendency to reject extreme outliers as being produced by the wings of the uncertainty distribution — presumed itself to be normally distributed with a dispersion μ — as a means to winnow the sample to one resembling the error-free distribution, $D(I)$. However, the resulting fitted calibration, $M_{obs} = \alpha I_{obs} + \beta$ (based on those points shown in light grey, which fall in the distribution $D(I)$) not only has a steeper slope, but also a much smaller dispersion in M than would obtain in the error-free case (Figure 2.9). As shown in Appendix 2 (Section 2.11), for the same line intensity spread, σ_i, the σ_M dispersion is reduced by a factor of $\sim 1/\sqrt{(}1 + \mu^2/\sigma^2)$ from the partial to the impartial analysis.

Thus, the effect of pursuing a "partial" calibration is not only an improper calibra-

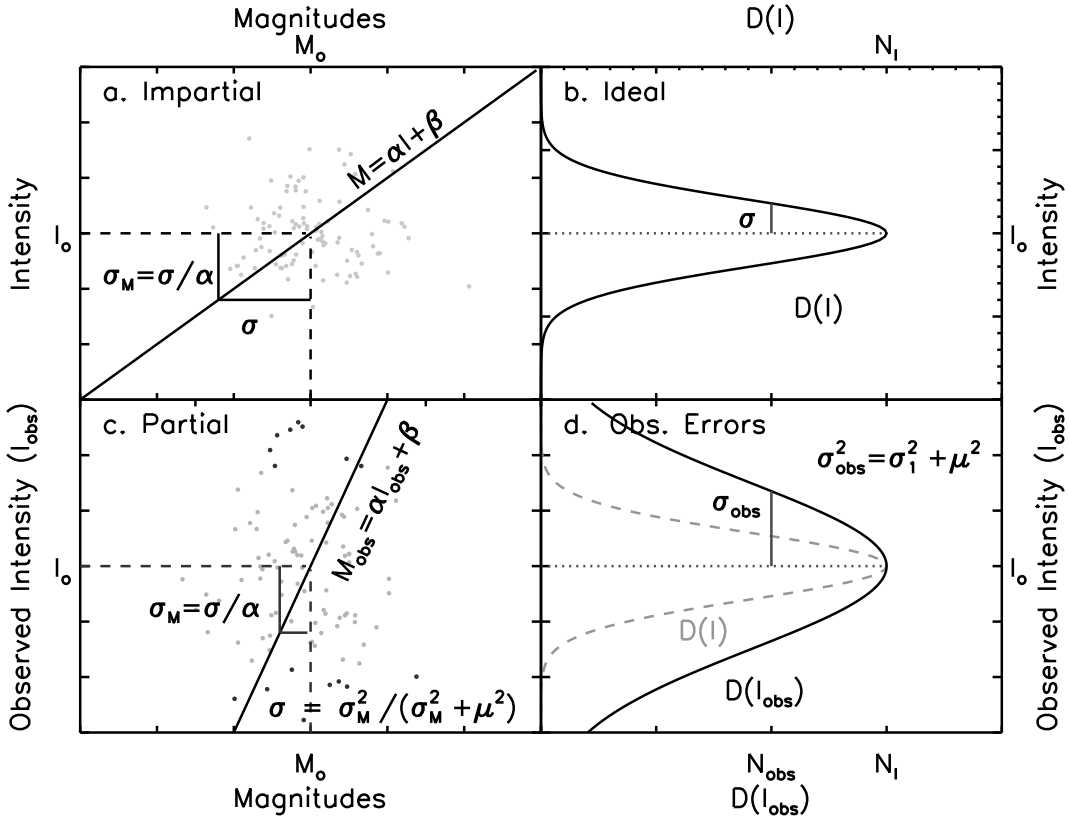

Fig. 2.9.— Demonstration of the impartial (*panels a and b*) and partial (*panels c and d*) calibration techniques for fictitious datasets without (i.e., "ideal") and with observational uncertainties, respectively. In the left panels, a fake dataset is drawn from the Gaussian distributions (filled circles) shown in the right panels; in both cases the black solid line represents the intrinsic spread, $D(I)$, of the data unconvolved with observational errors. For the case of the impartial calibration (*panels a and b*), all of the data drawn from the Gaussian distribution is used to derive the calibration line $M = \alpha I + \beta$ in *panel a*. For the case of the partial calibration, observational errors (presumed to be normally distributed with an RMS spread μ) inflate the observed spread of line intensities, $D(I_{obs})$ (*dashed curve*), but some measurements — the *black filled circles* in *panel c* — are rejected from the calibration sample as "extreme observational outliers". The spread of the remaining sample (it grey circles) mimics that of the intrinsic, error-free sample, $D(I)$ (*panel d*). However, the resulting calibration (*panel c*), $M_{obs} = \alpha I_{obs} + \beta$, is "torqued" with respect to that one would obtain from the error-free dataset (*panel a*). The actual quantitative differences are derived rigorously in Appendix 2 (Section 2.11), following the discussion by Trumpler & Weaver (1953).

tion relation for each relevant luminosity class, but the resulting range of magnitudes is also artificially compressed through the suppression of outliers. The former effect is evident in the comparison of M_{A35} to M_{HIP} in Figures 2.7a and 2.7b, in which the subgiant and giant branches appear "torqued" with respect to a one-to-one correlation, as well as in the compression of the subgiant and giant sequences in Figures 2.6b and 2.6c. A rigorous mathematical discussion of reduced errors in the A35 magnitudes is given in Appendix 2 (Section 2.11). Thus, the origin of the key differences in the A35 and Hipparcos CMDs lies in a subtle bias in the calibration technique used in A35.

Now, we can ask a different question: Though we have already shown that the subgiants in A35 are real, was their discovery a fortunate accident of this calibration error?

The Systematic Error

The "partial" nature of the A35 magnitude calibration curves was discussed at length in the literature of the time, most notably by Stromberg (1939), Strömberg (1940), Strömberg (1941), Russell & Moore (1938), Russell & Moore (1940), and van Rhijn (1939). These authors not only described the nature of the calibration bias, but also proceeded to correct the absolute magnitudes. The correction procedure relied on the existence of distances derived independent of A35, which are used to correct the "torque" shown in Figures 2.7a and 2.7b. A more detailed history of these papers and their efforts to correct the A35 catalog is given by Blaauw (1963), including more modern use of the A35 catalog by Oke (1957, 1959) and Wilson & Vainu Bappu (1957).

While the "torque" correction method worked well for the dwarfs of all spectral

types, application to the more distant subgiants and giants remained difficult owing to the smaller number of such stars having independently measured distances. As ground-based trigonometric samples grew, however, the correction method was applied to more giant type stars. For the A35 giants, however, the intensity line calibration method so torqued the axis (see the "squished" giant branch in Figure 2.6a), that the resulting corrections to A35 had large uncertainties. For the subgiants in Figure 2.6a, so compressed as to be completely detached from the main sequence and giant branches, correction of the A35 magnitudes was deemed impossible. An example calibration to spectral type K is given in Figure 5 of Blaauw (1963), to which Blaauw states, "With the accidental errors so strongly dominating the cosmic dispersion, it is obviously meaningless to try to introduce corrections to the Adams values for the giants. For the subgiants the situation is similar." Thus, the A35 data for the giants and subgiant classes were largely ignored owing to the inability to reconcile the bias introduced by the "partial" calibration.

It is important to note, that even at the time of Adrian Blaauw's 1963 summary article, only 41 K-giants and 12 K-subgiants had well measured trigonometric parallaxes — representing less than 10% of the total number of such stars in A35 (Blaauw 1963, S04). With the substantially larger Hipparcos database, 90% of the A35 stars now have independently measured parallaxes. In the next section, we endeavor to use these data to correct the full A35 HR diagram for the calibration bias to determine if the subgiants were created artificially by these biases.

Correcting for Systematic Errors in the Luminosity Calibration

In this subsection, we use the Hipparcos trigonometric parallaxes (Perryman et al. 1995; van Leeuwen 2007a,b, 2008) as a comparison sample to remove the torque

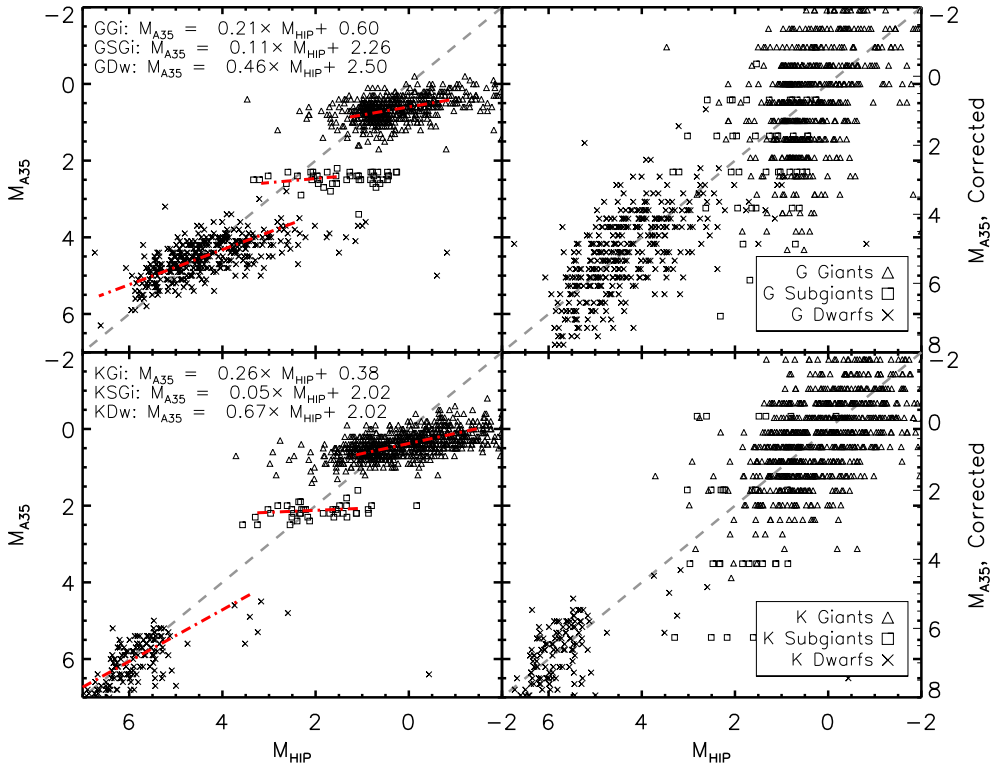

Fig. 2.10.— Procedure followed to calibrate the A35 magnitudes to the Hipparcos magnitudes following the detailed discussion in Blaauw (1963), and separated by G (*top*) and K (*bottom*) spectral types. The left panels display the original data with fits to the dwarfs (GDw, KDw), subgiants (GSGi, KSGi) and giants (GGi, KGi). We used the luminosity classifications in the Hipparcos catalog. In the right panels these calibration fits are applied to the A35 magnitudes and refit to demonstrate the removal of the torque.

in the A35 calibration curves (e.g., Figure 2.9c to 2.9a). First, we will describe the calibration method utilized by previous authors. Then, we will demonstrate its effectiveness for the G and K type stellar classes (i.e., those containing the majority of the subgiants in A35). Lastly, we apply the correction for all stars in A35 to revisit Figure 2.6 and create a corrected version of Figure 1 from A35. With this we aim to answer the question: if we remove the calibration torque in the A35 sample, do the 90 stars in A35 remain subgiants or do they largely join the main sequence or giant branches? Effectively, we ask whether the "partial" calibration method — the separation of stars into tightly concentrated fiducial values — artificially create the distinct, separated subgiant class?

To correct the A35 magnitudes using the Hipparcos sample, we transform our previous discussion into our set of variables specific to A35 and Hipparcos. Where possible, we follow the conventions used in the literature. We separate the sample by the A35 spectral type: A, F, G, K, and M, and then by luminosity class: dwarf, subgiant, and giant, using the A35 absolute magnitude. We first compute the mean magnitude for the spectral type and luminosity class in both the A35 sample, $\langle M_{A35} \rangle$, and the Hipparcos sample, $\langle M_{HIP} \rangle$, and define the difference between the two as,

$$\Delta\langle M \rangle = \langle M_{HIP} \rangle - \langle M_{A35} \rangle. \tag{2.1}$$

Then, we fit a linear regression for each luminosity class. The slope (m) of the fitted line represents the torque on the feature due to the improper calibrations (e.g, the relationship of Figure 2.9c). The quantity A, defined by Russell & Moore (1938) as the ratio of the dispersion of the measurement and the true dispersion is empirically derived by:

$$A = (1/m) - 1. \tag{2.2}$$

We then can compute the corrected magnitude for each star within a spectral and luminosity class using the following equation (Blaauw 1963, ; Equation 14):

$$M_{Corr} = M_{A35} + \Delta\langle M\rangle + A(M_{A35} + \Delta\langle M\rangle - \langle M_{HIP}\rangle) \tag{2.3}$$

where M_{Corr} is our final corrected A35 absolute magnitude, M_{A35} is the A35 absolute magnitude and, A is a quantity calculated from the results of the linear regression for a spectral and luminosity class and defined in Equation 2.

The process for correcting the magnitudes is demonstrated in Figure 2.10 for the A35 subgiant spectral classes G (top panels) and K (bottom panels). In the left panels of Figure 2.10, the original A35 magnitudes are plotted against the corresponding Hipparcos magnitudes (M_{HIP}, as in Figure 2.7) — and illustrate the severe torque on the subgiant and giant luminosity calibrations in these classes. For each luminosity class, a linear regression is fit against those Hipparcos stars with σ_π/π less than 0.10 for the giants and less than 0.05 for the subgiants and dwarfs. The results of the linear regression are given in the left panels. In the right panels, the results of the fits are used in Equation 2.3 and applied to M_{A35}. In the right panels we accomplish both of the goals of this proceedure: not only has the torque been corrected, but the observational scatter is increased to appropriate levels.

Having demonstrated that the larger Hipparcos database can correct the A35 magnitudes for the subgiants and giants, we proceed to use the Hipparcos data to correct the entire A35 sample and create the true HR diagram for the A35 sample. In Figure 2.11a the original A35 HR diagram is reproduced with the A35 spectral types color-coded in greyscale. In Figure 2.11b the corrected A35 magnitudes are plotted and the scatter within each of the luminosity and spectral type bins is greatly increased. In Figure 2.11c the Hipparcos HR diagram is shown with the same color

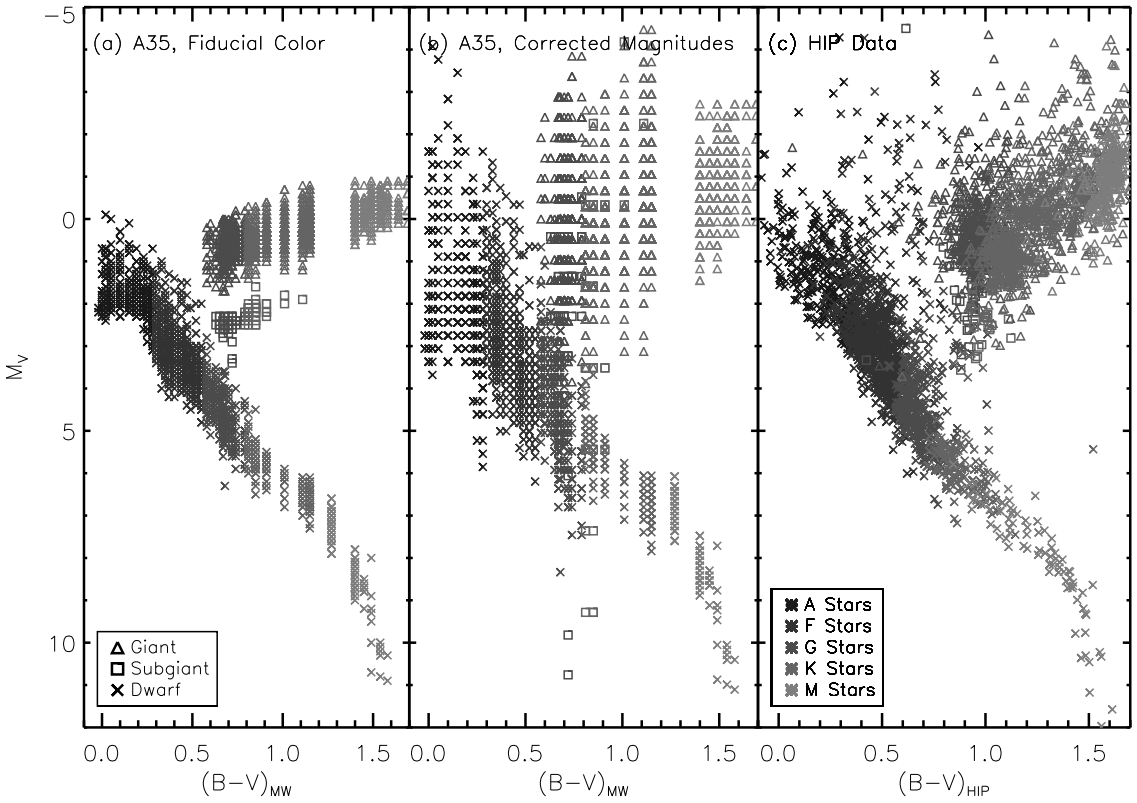

Fig. 2.11.— Application of the magnitude corrections to the A35 HR Diagram. In panel (a) we reproduce the A35 HR diagram with color axis translated from spectral types to a fiducial color. In panel (b) we apply the magnitude calibration proceedure described in Section 2.6.2, and in panel (c) we reproduce the Hipparcos HR diagram for the A35 sample. Panel (b) demonstrates how correcting for the bias in the A35 methods brings visual impression of the A35 subgiants into better agreement with that of Hipparcos, most notably the subgiants now connect the main sequence and giant branch and the magnitude scatter along the sequences is now greater than that of Hipparcos.

scaling. Comparing Figures 2.11a, 2.11b, and 2.11c, it is clear that the correction procedure has recovered the true scatter appropriate to the A35 magnitudes, and this scatter is now larger than that of the modern, and more precise, magnitudes. Additionally, the subgiant sequence, shown in open boxes, is no longer detached from the main sequence or giant branch, instead a continuum of magnitudes is produced between these two phases of stellar evolution. In this modified version of the A35 diagram, the true transitionary nature of the subgiant sequences is revealed. Had it been realized at the time, it is possible that Gamow's conjecture might have been voiced more vociferously in scholarly circles, and potentially the ultimate understanding of stellar evolution would have been hastened.

2.7 Summary

1. The discovery of subgiants culminated with the summary paper by the Mount Wilson spectroscopists in 1935 that gave the absolute magnitudes of 4179 stars determined from line ratios in their spectra that are sensitive to gravity.

2. The 90 Mount Wilson subgiant candidates formed a distinct sequence in the HR diagram between giant and dwarf stars and that was not attached either to the main sequence or to the giant sequence (Figure 2.6).

3. The problem posed at the 1957 Vatican Conference that high weight trigonometric parallaxes for a few field subgiants put them fainter than the subgiants in M67, believed then to be the oldest stars in the Galaxy (along with the globular clusters), was solved with the later discovery of the older Galactic clusters of NGC 188 and NGC 6791.

4. A test is made of the reality of the ∼90 stars that the Mount Wilson spectroscopists identified as part of the subgiant sequence via a star-by-star comparison of the

Mount Wilson and the Hipparcos absolute magnitudes. A majority of the 90 Mount Wilson candidates that we have identified as the Adams et al. "subgiants" are clearly in the domain of subgiants when viewed in the modern Hipparcos color-magnitude diagram.

5. A strong correlation is found between the A35 spectroscopically derived absolute magnitudes for their subgiants and the corresponding absolute magnitudes for these stars derived using Hipparcos data. This statement holds even more broadly across all luminosity classes in the A35 database. We find for the subgiants that $\langle M_{V,\mathrm{MountWilson}} - M_{V,\mathrm{Hipparcos}} \rangle = -0.12 \pm 0.02$ and with a dispersion of 1.02 magnitudes, when restricted to stars having Hipparcos $\sigma_\pi/\pi < 0.05$.

6. Tests for an observational selection incompleteness bias (e.g., the Malmquist bias) in the Strömberg (1930) calibration of the Mount Wilson subgiant sequence indicates that this bias did not artificially create the subgiant sequence in the A35 database as had been posited in the literature.

7. The reason for the narrow, disconnected A35 subgiant sequence is instead explained by a subtle bias in the A35 calibration curves that, while well known, could not be corrected for in the case of evolved stars due to the limited number of these stars in pre-Hipparcos trigonometric parallax samples. However, even after use of the Hipparcos parallaxes to correct for this historically well-discussed calibration bias we find that the A35 luminosity classes are robust and that the detection — and therefore discovery — of subgiants by the Mt. Wilson spectroscopists is upheld.

2.8 A Note on the Preparation of this Chapter

This work began as a collaboration between the authors in 2005 and progressed primarily by exchange of letters between AS and SRM until the death of AS in

2010. AS conceived the original concept and framework of the paper, and authored the original drafts of the manuscript. The historical insights described herein would not have been possible without AS's encyclopedic knowledge of, and indeed direct involvement in, many of the events described. Quantitative analyses and later stages in the crafting of the manuscript were carried on by RLB and SRM (in large part well after the passing of AS), and were only possible after intense study of pertinent writings of the numerous historical characters that played a role in the story described here. Special consideration was given to the handwritten letters, annotated drafts of the manuscript, and relevant published papers by AS himself so that we might attempt the closest fidelity of the final work to his original intent. Much as described by Sandage after the death of Edwin Hubble (albeit with far less significance of the product offered in the present paper!), RLB and SRM found themselves "lost in the shadow of a giant" in attempting to bring this work to the conclusion originally envisioned by the lead author. Much of his original outline and text has been preserved in this edition of the manuscript, but unfortunately we had to resort to our own less elegant prose in most of the later sections. AS is rightfully maintained as the primary author in that he was the originator and true leader of the project, but most especially to recognize his enthusiasm to rectify the historical judgement of the A35 work and to uphold the reputation of the Mount Wilson spectroscopists. This enthusiasm remained vibrant even as AS's health began to fail in 2008, and steadfast into his final months during which his production efficiency still well-outpaced that of his coauthors (who, at the time, were well behind in completing their contributions). An edited draft of the manuscript, with his sections already long completed, was sent directly by AS via postal delivery and received by SRM two days after "Uncle Allan's" passing.

2.9 Acknowledgements

We wish to recognize helpful conversations with Richard Patterson and John Grula. RLB acknowledges assistance with OCR software from the Alderman Library Scholars Lab at the University of Virginia. Additionally, we acknowledge the encouragement from the family, friends and colleagues of AS, who also wished to see this work completed, including Mary Sandage, wife of the late Allan Sandage.

Table 2.1. Data For the 90 Mount Wilson Subgiants That From Their Spectra Defined the Class in 1935

Star Name Mt. W.	Star Name Hip.	Hiparcos V	Hiparcos $B-V$	Sp.Type Mt. W.	Sp.Type Hip.	π (mas) Mt. W.	π (mas) Hip.	$\sigma(\pi)/\pi$ Hip.	$M_V(\pi)$ Mt. W.	$M_V(\pi)$ Hip.
HD 28	HIP 443	4.61	1.03	K0	K1 III	20	25.38	0.04	2.1	1.63
HD 1037	HIP 1176	6.63	1.03	G8	G8 III/IV	13	7.76	0.10	2.4	1.08
HD 2589	HIP 2242	6.18	0.88	G9	K0 IV	17	25.37	0.02	2.5	3.20
HD 3546	HIP 3031	4.34	0.87	G3	G5 III	42	19.34	0.04	2.6	0.77
HD 4398	HIP 3607	5.49	0.98	G6	G8/K0 III	23	9.78	0.07	2.4	0.44
HD 5268	HIP 4257	6.15	0.91	G3	G5 IV	17	8.60	0.09	2.5	0.82
HD 5286	HIP 4288	5.46	1.01	K1	K1 IV	17	25.69	0.05	2.3	2.51
HD 5395	HIP 4422	4.62	0.96	G4	G8 III/IV	36	15.84	0.04	2.6	0.62
HD 6473	HIP 5412	6.24	0.92	G6	K0	17	6.97	0.08	2.5	0.46
HD 8512	HIP 6537	3.60	1.07	K0	KO III	46	28.48	0.03	2.1	0.87
HD 10486	HIP 8044	6.33	1.02	K2	K2 IV	13	18.04	0.04	2.0	2.61
HD 16042	HIP 12053	8.24	1.07	G4	K0 V	6	4.02	0.28	2.4	1.26
HD 20618	HIP 15514	5.91	0.86	G5	G8 IV	21	15.88	0.07	2.5	1.91
HD 21467	HIP 16181	6.03	0.95	G6	KO IV	21	14.44	0.06	2.7	1.83
HD 29613	HIP 21685	5.46	1.05	K1	K0 III	21	16.42	0.04	2.2	1.54
HD 34538	HIP 24679	5.48	0.93	G9	G8 IV	21	20.69	0.04	2.3	2.06
HD 34642	HIP 24659	4.81	0.99	K0	K0/K1 III/IV	30	29.63	0.02	2.3	2.17
HD 37160	HIP 26466	4.09	0.95	G6	G8 III/IV	42	28.10	0.03	2.5	1.33
HD 37601	HIP 26941	6.05	0.95	G9	K0 III	17	16.26	0.04	2.3	2.11
HD 37981	HIP 26930	6.72	1.10	K1	K1 IV	10	8.98	0.11	2.0	1.49
HD 39169	HIP 27600	7.85	1.06	K0	G5	7	5.52	0.43	2.1	1.56
HD 39364	HIP 27654	3.76	0.98	G7	G8 III/IV	79	29.05	0.02	3.4	1.08
HD 40959	...	...	...	G5	...	5	...	...	2.4	...
HD 45410	HIP 31039	5.86	0.93	G8	K0 IV	20	17.56	0.04	2.5	2.08
HD 46480	HIP 31676	5.94	0.90	G7	G8 IV/V	24	18.82	0.04	2.9	2.31
HD 55280	HIP 35146	5.20	1.08	K2	K2 III	22	16.88	0.05	2.0	1.34
HD 71952	HIP 41894	6.23	1.01	K0	K0 IV	14	16.65	0.04	2.2	2.34
HD 73593	HIP 42604	5.35	0.99	G6	G0 IV	26	18.11	0.04	2.6	1.64
HD 75558	HIP 43463	7.38	0.91	G3	G5	11	5.37	0.20	2.5	1.03
HD 77818	HIP 44766	7.62	1.00	K0	K1 IV	8	8.72	0.10	2.2	2.32
HD 78249	HIP 44990	7.07	0.98	K2	K1 IV	10	15.11	0.05	2.2	2.97
HD 79452	HIP 45412	5.98	0.84	G3	G6 III	18	7.17	0.13	2.3	0.26
HD 84406	HIP 48034	6.94	0.95	K0	G5	13	13.24	0.05	2.5	2.55
HD 84453	HIP 47973	6.81	0.95	K0	K0 IV	11	12.06	0.07	2.1	2.22
HD 86359	HIP 48881	7.45	0.92	G7	G5	9	10.69	0.10	2.3	2.59
HD 90752	HIP 51204	7.23	0.97	G9	K0	9	7.27	0.20	2.2	1.54
HD 91011	HIP 51451	6.98	1.03	K0	K0	10	6.76	0.15	2.2	1.13
HD 92588	HIP 52316	6.25	0.88	K1	K1 IV	17	29.08	0.03	2.5	3.57
HD 93636	HIP 52882	6.15	1.14	K1	K0	14	5.45	0.14	2.0	-0.17
HD 94178	HIP 53179	7.52	0.91	G7	G5	9	9.41	0.11	2.4	2.39
HD 94264	HIP 53229	3.79	1.04	K2	K0 III/IV	46	33.40	0.02	2.2	1.41
HD 96074	HIP 54275	7.65	0.93	G8	G5	9	6.06	0.13	2.4	1.56
HD 96436	HIP 54336	5.52	0.96	G7	G9 IIICN	24	16.05	0.06	2.6	1.55

Table 2.1 (cont'd)

Star Name Mt. W.	Star Name Hip.	Hiparcos V	Hiparcos $B-V$	Sp.Type Mt. W.	Sp.Type Hip.	π (mas) Mt. W.	π (mas) Hip.	$\sigma(\pi)/\pi$ Hip.	$M_V(\pi)$ Mt. W.	$M_V(\pi)$ Hip.
HD 97100	...	...	...	G5	...	5	...	...	2.5	...
HD 102928	HIP 57791	5.62	1.06	K0	K0 IV	17	12.59	0.08	2.2	1.12
HD 105639	HIP 59285	5.95	1.12	K3	K3 III	14	11.94	0.07	1.8	1.34
HD 110646	HIP 62103	5.91	0.85	G4	G8 IIIp	22	14.26	0.05	2.8	1.68
HD 111028	HIP 62325	5.65	0.99	K1	K1 III/IV	20	22.36	0.04	2.4	2.40
HD 113817	HIP 63960	7.09	0.98	G8	K0 III	11	4.67	0.20	2.4	0.44
HD 115202	HIP 64725	5.21	1.01	K1	K1 III	23	25.68	0.03	2.1	2.26
HD 116713	HIP 65535	5.11	1.18	K1	Kp	19	15.73	0.05	1.6	1.09
HD 123409	HIP 68955	6.89	1.00	G6	K0	13	5.71	0.14	2.5	0.67
HD 126400	HIP 70538	6.48	0.94	G7	K0 III	14	12.99	0.08	2.4	2.05
HD 127243	HIP 70791	5.58	0.86	G4	G3 IV	26	10.59	0.06	2.7	0.70
HD 138716	HIP 76219	4.61	1.00	K1	K1 IV	29	34.54	0.02	2.1	2.30
HD 140301	HIP 77007	6.30	1.12	K0	K0 III	13	7.94	0.11	2.0	0.80
HD 140687	...	...	...	K1	...	9	...	...	2.3	...
HD 142091	HIP 77655	4.79	1.00	K1	K0 III/IV	26	32.13	0.02	1.9	2.32
HD 143586	...	...	...	G9	...	5	...	...	2.3	...
HD 150275	HIP 80850	6.35	1.00	K0	K1 III	14	8.00	0.07	2.2	0.87
HD 151216	HIP 81977	9.17	1.03	K1	K2	4	3.20	0.36	2.2	1.70
HD 152781	HIP 82861	6.33	0.95	K2	K0/K1 III/IV	14	24.72	0.03	2.3	3.30
ADS 10394B	...	...	...	K0	...	5	...	...	1.8	...
HD 156461	HIP 84647	7.23	1.02	G3	G8 III	11	5.86	0.20	2.5	1.07
HD 159466	HIP 85979	6.52	0.95	G4	G8 III	14	6.40	0.15	2.5	0.55
HD 160042	HIP 86352	6.19	0.83	G7	G6 III/IV	14	9.66	0.09	2.4	1.11
HD 162076	HIP 87158	5.69	0.94	G5	G5 IV	20	13.04	0.05	2.3	1.27
HD 165438	HIP 88684	5.74	0.97	K1	K1 IV	17	28.61	0.03	2.1	3.02
HD 167042	HIP 89047	5.97	0.94	K0	K1 III	18	20.00	0.03	2.2	2.48
HD 173399	HIP 91782	8.99	0.42	G2	F2 V	12	7.39	0.89	2.5	3.33
HD 173949	HIP 91915	6.02	0.97	G7	G7 IV	16	8.95	0.06	2.3	0.78
HD 181391	HIP 95066	4.98	0.94	K0	G8 III/IV	24	21.17	0.04	2.3	1.61
HD 185351	HIP 96459	5.17	0.93	K0	K0 III	27	24.64	0.02	2.4	2.13
HD 194433	HIP 100852	6.24	0.96	K1	K1 IV	17	25.21	0.05	2.5	3.25
HD 196925	HIP 101082	5.96	0.94	G8	K0 III+	18	15.88	0.03	2.4	1.96
HD 198149	HIP 102422	3.41	0.91	G7	K0 IV	63	69.73	0.01	2.6	2.63
HD 198732	HIP 103071	6.32	0.88	G5	K0 III	19	13.33	0.09	2.6	1.94
HD 198896	HIP 102990	7.91	0.62	G7	Am	9	0.33	6.55	3.3	-4.50
HD 199223	HIP 103301	6.04	0.82	G6	G6 III/IV	17	9.02	0.13	2.3	0.82
HD 200004	HIP 103728	6.55	0.85	G3	G6/G8 III	14	6.05	0.16	2.3	0.46
HD 202403	HIP 104844	7.08	0.80	G5	G5	8	5.21	0.23	2.3	0.66
BD +15 466	...	...	...	K3	...	4	...	...	2.1	...
HD 212943	HIP 110680	4.78	1.04	K0	K0 III	30	20.39	0.04	2.3	1.33
HD 216640	HIP 113148	5.53	1.11	K4	K1 III	17	23.27	0.03	1.9	2.36
HD 218527	HIP 114273	5.42	0.91	G4	G8 IV	23	11.64	0.11	2.4	0.75
HD 221148	HIP 115953	6.26	1.12	K3	K3 IIIvar	13	20.44	0.04	2.0	2.81

2.10 APPENDIX 1:

Estimation of Lutz-Kelker Corrections

As briefly described in the main text, the Lutz-Kelker Effect (LKE, hereafter) is a bias that occurs due to the finite magnitude and sensitivity limits of trigonometric surveys. The scattering of stars in and out of the sample due to observational errors is asymmetric, more stars are scattered into the survey limits due to the larger volume element just outside of the survey than are scattered out from the volume element just inside. In this appendix, we supplement the brief discussion of the LKE in the main text by providing additional background on the LKE and a rigorous estimation of the appropriate offsets for the A35 catalog. As stated in the main text from a qualitative assessment, we find the LKE to be a very small effect for the A35 sample, especially when appropriately restricted by σ_π/π.

2.10.1 Background

Lutz & Kelker (1973) provided the first mathematical derivation of the Lutz-Kelker Effect (LKE), which had been alluded to in earlier work (i.e., Trumpler and Weaver (1953), but see Sandage & Saha (2002) for a detailed history of the bias). In this landmark paper, Lutz and Kelker found that the LKE was present for parallaxes independent of apparent magnitude and that it was best characterized by the dimensionless parameter, σ_π/π. The authors estimated the magnitude of the LKE as a

Table 2.1 (cont'd)

Star Name Mt. W.	Star Name Hip.	Hiparcos V	Hiparcos $B-V$	Sp.Type Mt. W.	Sp.Type Hip.	π (mas) Mt. W.	π (mas) Hip.	$\sigma(\pi)/\pi$ Hip.	$M_V(\pi)$ Mt. W.	$M_V(\pi)$ Hip.
HD 221639	HIP 116251	7.20	0.92	G9	K1 V	10	14.58	0.05	2.4	3.02
HD 222107	HIP 116584	3.81	0.98	G7	G8 III/IV	40	38.74	0.02	2.3	1.75
HD 222404	HIP 116727	3.21	1.03	K1	K1 IV	55	72.50	0.01	2.1	2.51

function of $\sigma(\pi)/\pi$ for the case of a uniform stellar distribution ($P(\pi) \sim \pi^4$) for observations of stars with known intrinsic luminosity. Hanson (1979) derived a generalized form of the Lutz & Kelker derivation to other stellar distributions ($P(\pi) \sim \pi^n$), but still did not account for targeting bias in the trigonometric survey. Lutz (1979) expanded the results of Lutz & Kelker (1973) further and found two, as yet, unexplored complications for generalizing the LKE to other datasets. First, the intrinsic luminosity function of the sample must be known and *explicitly* included in the derivation of the Lutz Kelker correction. Second, the behavior of the LKE with σ_π/π is more complex when an apparent magnitude (m_{app}) limit is imposed on the observational sample. Lutz (1979) highlights the most insidious aspect of the LKE; namely, that it has no general form. Instead, the appropriate Lutz-Kelker corrections must be derived independently for the specifications of a sample or even a subsample within a larger sample already characterized for LKE.

2.10.2 Estimation of LKE for a General Sample

Sandage & Saha (2002) formalized these complications into an easily adapted set of Monte-Carlo simulations that permits the calculation of Lutz-Kelker corrections for any trigonometric sample. This work vividly illustrated the interplay of an m_{app} limit and the underlying stellar distribution in determining both the magnitude *and sign* of the Lutz-Kelker corrections. More specifically, their simulations revealed that the sign of the LKE can change across σ_π/π bins in a sample. In total, the complications explored by Sandage & Saha (2002) emphasized the complexity of the bias and how its behavior is intrinsically unintuitive. To assess the role of the LKE on the Hipparcos absolute magnitudes matched to the A35 sample, we adapt the methodology of Sandage & Saha (2002) to estimate the appropriate LKE corrections for the A35.

The work of Sandage & Saha was specifically focused on understanding the effect of the LKE on RR Lyrae stars, a class of stars typified by a narrow range of intrinsic luminosities. Our goal of understanding the effect of the LKE on the Hipparcos absolute magnitudes for the full A35 sample is more complicated due to the large range of intrinsic luminosities in the A35 sample. For the purposes of our calculation, we take the A35 absolute magnitudes to be the "true" intrinsic magnitude of the star. Then, we generate simulated datasets that we use to explore the LKE for A35.

To generate our simulated datasets, we populate a spherical volume of radius, $R = 400$ pc, assuming a model stellar distribution. This radius includes the majority of the A35 sample as was demonstrated in Figure 2.8. Stars are drawn from the A35 uniformly and, for full exploration of the bias, we repeatedly select stars until we have $N = 100,000$ stars. Each star is randomly assigned a distance within our volume drawn from the model distributions. This process is completed independently for each of the three model stellar distributions of Sandage & Saha (2002), more specifically $N \sim R^n$ for $n = 1, 2, 3$. After placing the star in our volume, we compute apparent magnitude and the true parallax for each star, given its simulated distance. The true parallax is then given a random error drawn from a Gaussian distribution with width, $\sigma_\pi(m_{app})$. In a true parallax sample, this error will depend on the apparent magnitude of the star (m_{app}). To simulate the errors from the Hipparcos sample, we fit a linear relationship to the rms errors in the A35 sample, resulting in:

$$\sigma_\pi(m_{app}) = 0.07 * m_{app} + 0.431. \tag{2.4}$$

This final parallax, the true parallax with an added error based on the apparent magnitude, is our simulated observed parallax for each star in our simulated sample.

Having calculated an observed parallax, we can compute the implied absolute

magnitude for our simulated sample and compare it to the true magnitude used at the onset of the simulation. We calculate $\Delta M_{LKE} = M_{obs} - M_{true}$ for each star and compute the average value for the full sample as a function of σ_π/π.

The resulting Lutz-Kelker corrections are shown in Figure 2.12 as a function of σ_π/π for each of the stellar distributions, $N \sim R^n$ with $n = 0, 1, 2$. On the whole, these corrections are negligible for $\sigma_\pi/\pi < 0.05$. and, in general, are of the order of the errors typical of the A35 apparent magnitudes. For a more specific comparison, we give the corrections for the σ_π/π bins used for the paper in Table 2.3 for each of the stellar distributions. Thus, after proper consideration of the LKE, we conclude that it does not strongly influence our comparison of the A35 identified subgiants

2.11 APPENDIX 2: How Random Errors Reduced Scatter in the A35 Magnitude Calibrations

In the main text, we presented a qualitative description of the bias introduced by the A35 spectroscopists by the due to choices in their calibration techniques. We applied a correction proceedure to correct for the bias and produce the true A35 HR diagram. In supplement to the qualitative discussion given in the main text, we present a mathematical description of the bias in the A35 diagram due to the "impartial" calibration technique. This mathematical approach is based on the summary given by Blaauw (1963) of the various critiques given in the literature (e.g. Strömberg 1939, Russell and Moore 1938, 1940) and is translated into the modern lexicon for the benefit of the reader.

In general, luminosity calibration occurs in two stages. First, a luminosity sensitive

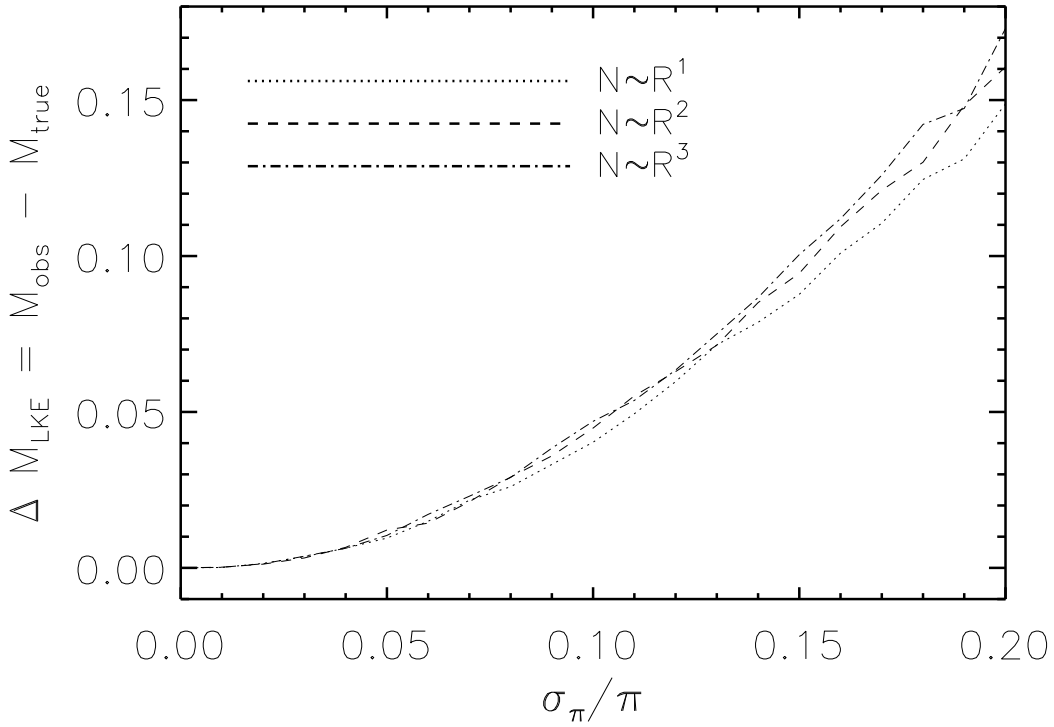

Fig. 2.12.— The Lutz-Kelker mean magnitude offset as a function of σ_π/σ. These values were derived by adapting the methodology of Sandage & Saha (2002) to properites of the A35 sample. The offset is given for three assumed stellar distributions, $N \sim R^1, R^2, R^3$ in dotted, dashed and dot-dashed lines respectively. Over all the corrections for each stellar distribution track each other well in the A35 volume.

Table 2.2. Lutz-Kelker Corrections for A35 Sample

σ_π/π	$N \sim R^1$ ΔM_{LKE}	$N \sim R^2$ ΔM_{LKE}	$N \sim R^3$ ΔM_{LKE}
0.01	0.000	0.000	0.000
0.05	0.095	0.012	0.010
0.10	0.040	0.045	0.047
0.15	0.088	0.094	0.100
0.20	0.149	0.161	0.173
0.25	0.205	0.222	0.241

criteria is identified, in this case a set of spectral line intensities (I). Second, an empirical relationship is created to map between the luminosity sensitive parameter and the absolute magnitude (M). To understand the origin of the systematic errors, we must consider how the magnitudes were calibrated.

2.11.1 The Ideal Case

First, we start with the ideal situation in which our target distribution is well sampled by our observational data, meaning that the mean value (I_o) and dispersion (σ_{I_o}) calculated from the observational data are representative of their true, physical values. We start with a distribution of line intensities, $D(I)$, akin to the demonstration of Figure 2.9b in the main text. For simplicity in our derivation, we assume that $D(I)$ is a Gaussian distribution, though the distribution could be any general function. With this assumption, we can write that the mean value is,

$$\langle D(I) \rangle = I_o \tag{2.5}$$

with a dispersion of σ_I. We require that $D(I)$ is uniquely connected to a distribution of intrinsic magnitudes, $D(M)$.

Again, we assume that the target magnitude distribution, $D(M)$, will be Gaussian, such that the mean is given $\langle D(M) \rangle = M_o$ with a dispersion of σ_M. We further assume that the relation to connect $D(M)$ to $D(I)$ is unique, and, in imitation of the A35 calibration technique, that this relation is linear of the form:

$$M = \alpha I + \beta. \tag{2.6}$$

By propagation of errors through this calibration formula (Equation 2.6), errors

in I (δI) translate to errors in M (δM) by

$$\delta M = \alpha \delta I. \tag{2.7}$$

Likewise, the dispersion in M due to uncertainty in I is estimated by

$$\sigma_M = \alpha \sigma_I, \tag{2.8}$$

and the mean magnitude of the resulting magnitude distribution $D(M)$ is determined by

$$M_o = \alpha I_o + \beta. \tag{2.9}$$

We choose from our line intensity sample, $D(I)$, a subset with luminosity classifications from another technique, ideally trigonometric parallaxes. The line intensity measurements (I) for this subsample will be observed to cluster narrowly around some central value, $I_1 \pm \Delta I$, and, ideally, this central value is I_o and the spread is given by σ_I. For these stars we fit for α and β as described in Equation 2.5, and derive our set of absolute magnitudes ($D(M)$) with which we proceed to perform our science experiment. The mean values and dispersions of our absolute magnitude sample are computed directly from our line intensities following the relations given in Equations 2.7, 2.8, and 2.9.

This calibration case is deemed "impartial," because our line intensity data were grouped into calibration subsamples using a system "impartial" to the particulars of our observational systematics and errors embedded within the line intensity distribution. Figure 2.13a is a visualization of this "ideal" scenario. A priori, we divide our distribution into luminosity classes (dwarf, subgiant, and giant) from the overall distribution and these classes, determined by an independent means, can be used to

calibrate our full sample.

2.11.2 The Case of A35

In reality, however, our measurements are always imperfect due to (i) observational errors and (ii) "cosmic errors," (i.e. intrinsic star to star variation) both of which behave as "random" errors in our dataset. For sufficiently large sample sizes, these errors can be minimized or, at least well characterized by the observational data itself. *If* the the random errors are well understood and appropriately characterized, then the case of calibration reduces to that of the "ideal".

In practice, these two independent types of error – observational (random) and cosmic — are indistinguishable without the acquisition additional data, and for our purpose here, we group them as a single, random error, μ_I. Now, we consider the effect of these, unrealized, random errors on the ideal case presented previously. This treatment is akin to that followed by the Mount Wilson spectroscopists for the absolute magnitudes presented in A35, and will demonstrate how incomplete consideration of random errors in the observational data, here $D(I)$, can produce reduced systematic errors in the resulting absolute magnitude distribution, $D(M)$.

For clarity, we redefine the line intensity distribution described previously, $D(I)$, to reflect observational error, $D(I_{obs})$. We assume it is Gaussian that can be described by $\langle D(I_{obs})\rangle = I_{o,obs}$ with scatter σ_{obs}, analogous to that case previously discussed. The mean value is not affected by random errors, so

$$\langle D(I)\rangle = \langle D(I_{obs})\rangle = I_o, \tag{2.10}$$

as was given in Equation 2.5 for the ideal case. The scatter in our line intensity distribution ($D(I)$), however, increases such that the uncertainties add in quadrature,

i.e.,

$$\sigma^2_{I,obs} = \sigma^2_I + \mu^2_I, \tag{2.11}$$

where σ_I the scatter for the ideal case. This discussion is visualized in Figure 2.13b, in which the ideal distributions of Figure 2.13a are given a random error, μ.

As before, we proceed to determine a relationship between $D(I)$ and $D(M)$ for physically motivated subsets of $D(I)$, the spectral and (ultimately) luminosity classes of the target stars. Effectively, this is accomplished by selecting appropriate stars within a narrow range of some value $I_{1,obs} \pm \Delta I/2$ for each of our subsets. Instead of grouping from an independent source as was done in the ideal case (Figure 2.13a), we instead plot a marginal distribution of all of our line intensities and identify peaks in the resulting distribution. This distribution is represented in Figure 2.13c by the dot-dash grey histogram, and we are able to identify the appropriate peaks, and their mean values, from this this distribution. Having identified each independent distribution, we proceed to reject individual data points to isolate each distribution. The result of this process is shown in the grey thick line of Figure 2.13c.

Thus, we have now restricted our observational data to a narrow range around a mean and these values no longer properly sample the observed scatter (Figure 2.13b) *or* the true scatter (Figure 2.13a). Stars with large errors are removed under the assumption that they are not related to the true distribution of $D(I)$, and, as demonstrated in Figure 2.13c, the resulting distributions are less broad.. In this instance, our intuitive proceedure for propagating error, $\delta M = \alpha \delta I$, is no longer valid within these restricted sub-samples (Trumpler & Weaver 1953).

Instead, the true values I do not scatter symmetrically around the observed value $I_{1,obs}$. Following Trumpler & Weaver (1953; §1.51), for the case of "accidental" errors

over a small range in a univariate distribution, the true mean value, $\langle I \rangle$, is described by:[7]

$$\langle I \rangle = I_{1,obs} + \frac{\mu_I^2}{D(I_{1,obs})} \frac{\delta D_{obs}}{\delta I_{obs}} (I_{1,obs}) + O(\mu_I^2) \tag{2.12}$$

Where $O(\mu_I^2)$ represent terms of higher order in μ_I^2 that are sufficiently small to ignore for our purposes.

Since $D(I_{obs})$ is a Gaussian distribution, it and its derivative can be substituted into Equation A8, such that, with rearrangement, we obtain[8]:

$$\langle I \rangle = I_{1,obs} - (I_{1,obs} - I_o) \times \frac{\mu_I^2}{\sigma_{I,obs}^2}. \tag{2.13}$$

With additional rearrangement, we obtain a form that better elucidates the systematic error between the true and the observed mean values:

$$\frac{\sigma_I^2 + \mu_I^2}{\sigma_I^2} = \frac{(I_{1,obs} - I_o)}{(\langle I \rangle - I_o)} \tag{2.14}$$

First, we note that the previous equation is the ratio of the relations, $(\langle I \rangle - I_o)$ and $(I_{1,obs} - I_o)$ are, effectively, divisions on the true and observed intensity axes scale, respectively. Second, the ratio of the true and observed axes is independent of the observed values (I_{obs}). Third, Equation 2.14 is always less than unity, as the observational error is always larger than zero ($\mu_I > 0$).

Now, we again fit a relationship to calibrate our subset, deriving: $\langle M \rangle = \alpha \langle I \rangle + \beta$. Though similar in form, this is *not* equivalent to the relationship derived earlier for our

[7]The equation A8 comes from §1.51 *Correction of a univariate distribution for observational errors* for the case of *Average errors for small intervals of the measured values* of Trumpler and Weaver (1953).

[8]This relation deviates slightly from the precursor to Equation 7 of Blaauw (1963) due to what we suspect to be a typographical error in that text.

idealized case, $M_o = \alpha I_o + \beta$. Here, when we derive our calibration curve, we compare $\langle M \rangle$ against the measured value, $\langle I_{obs} \rangle$ and not the true value, I_o. Effectively, as was demonstrated for $D(I_{obs})$ in Equation A10, we measure our relation on an axis that is compressed by the observational errors, and this compression is propagated into the resulting distribution of absolute magnitudes $D(M_{obs})$

And so, our derived values, $D(M_{obs})$, are compressed compared to the true distribution $D(M)$. There are two factors to consider in estimating the degree of compression in $D(M_{obs})$. First, we know that the observed dispersion is greater than the true dispersion by a factor of $\sigma_{I,obs}/\sigma_I$, e.g. going from Figure 2.13a and Figure 2.13b. Second, the effective range of intensities is compressed by our outlier rejection by $\sigma_I^2/(\sigma_I^2 + \mu_I^2)$, e.g., the transition from Figure 2.13b and Figure 2.13c. Combining the two factors, we arrive at the ratio of the true dispersion (σ) to the final dispersion of absolute magnitudes (σ_{A35}):

$$\frac{\sigma_{A35}}{\sigma} = \frac{\sigma_{I,obs}}{\sigma_I} \times \frac{\sigma_I^2}{(\sigma_I^2 + \mu_I^2)} \tag{2.15}$$

Substituting for $\sigma_{I,obs}$ from Equation 2.11, we obtain a final expression relating the A35 dispersion to the true dispersion and random errors:

$$\sigma_{A35} = \frac{\alpha\sigma}{\sqrt{1 + \mu_I^2/\sigma_I^2}} \tag{2.16}$$

The denominator, $\sqrt{1 + \mu_I^2/\sigma_I^2}$, is always greater than unity, and σ_{A35} will, therefore, be smaller than the true dispersion of the luminosity class. Perhaps against our intuition, the resulting random errors in $D(M)$ are not increased proportional to the errors in the line intensities, but are reduced by this observational error.

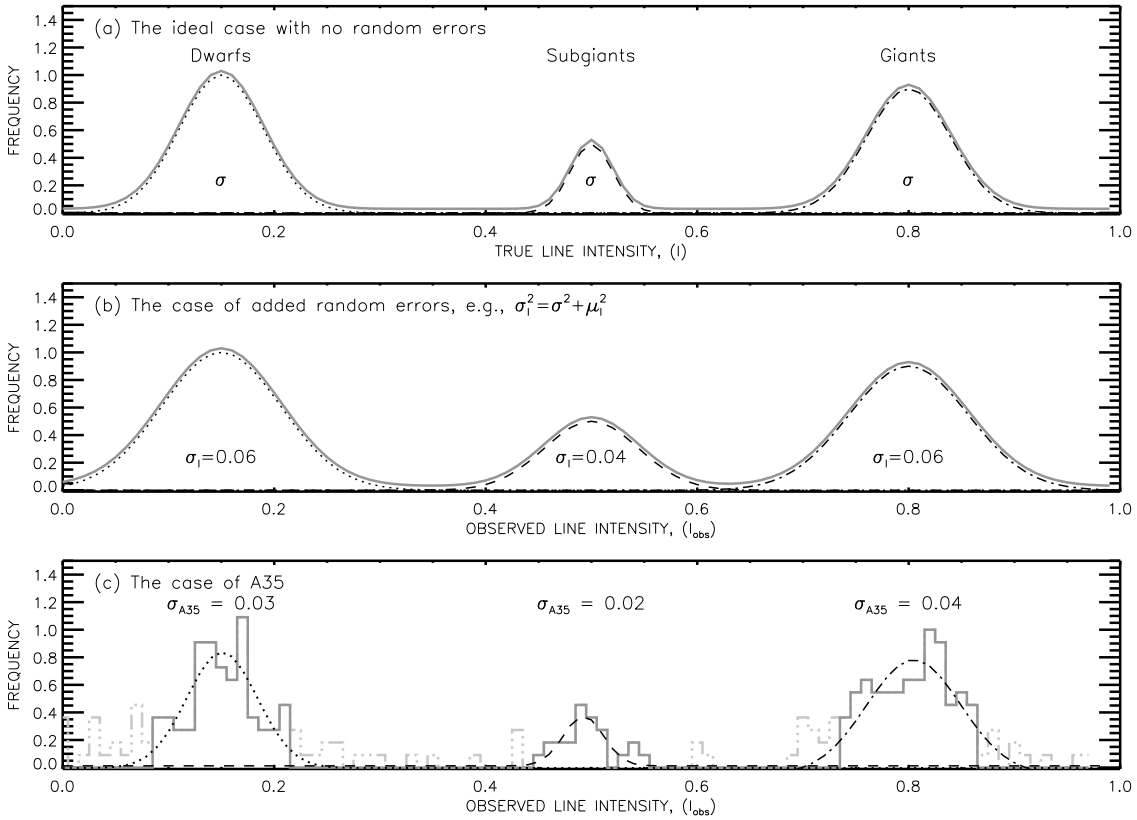

Fig. 2.13.— Schematic demonstration of the line intensity calibration scenarios described in the text. Each panel presents both a "total" distribution in thick grey, and the distribution for each of the three component luminosity classes in A35: dwarfs (dotted), subgiants (dashed), and giants (dot-dashed). In panel a, an "ideal" case is displayed with large samples of each class and no observational errors. Here each distribution is easily identified and distinguished for calibration. In panel b, a random error, μ, broadens each distribution, but the three distributions are still easily discriminated and their mean value is preserved. In panel c, we simulate the actual line intensity data of A35 by discretely sampling each of the luminosity class distributions (proportional to their representation in A35), and adding noise from a uniform distribution. In panel c, the light grey dot-dash distribution is the original sample, and the thick grey is the resulting sample after rejecting outliers and isolating the peaks. As in panel b, the mean value of each peak is preserved, but the resulting dispersion is suppressed from the outlier rejection. Though, we note that if all points are used in to fit each of the three distributions, then the true intrinsic dispersion is recovered.

Chapter 3

The Tangential Motion of M 31 Using Line-of-Sight Tracers in the Stellar Halo

3.1 Chapter Summary

Knowing the three dimensional motion of the Andromeda spiral galaxy (M31) is central to understanding the past, current, and future dynamical state of the Local Group. Measuring the true proper motion of such a distant object is extremely challenging. An alternative technique to measuring the transverse velocity relies on the projection of the three dimensional center-of-mass motion of M 31 on the line-of-sight motions of M 31-bound objects over a large angular span. This technique is most powerful when applied to tracer populations in the M 31 halo, either the satellite and outer globular cluster sample, a large number of individual M 31 halo stars, or both. To exploit the former, we combine recent line-of-sight velocity catalogs for dwarf satellites and globular clusters to improve upon the previous measurement of van der Marel et al. (2012). For the latter, we use the full kinematical dataset on M 31 red giant stars provided by the Spectroscopic and Photometric Landscape of the Andromeda Stellar Halo (SPLASH) project (Gilbert et al. 2012) and supplement it with an observational campaign to increase the number of M 31 member stars at large projected radii (R_{proj} >120 kpc). After we explore potential sources of bias within each of the samples, we derive two independent estimates of the M 31 motion using halo populations, and then combine these with other techniques to obtain a final error-weighted mean result of (v_W, v_N) = (-96.4 ± 22.4 km s^{-1}, -44.7 ± 25.4), where v_W and v_N are the plane of sky motions to the West and North, respectively. We also discuss the potential to explore the internal kinematics of the M 31 stellar halo with this dataset after compensating for the bulk transverse motion.

3.2 Introduction

3.2.1 History of Measurements of the M 31 Transverse Motion

The Local Group is a unique laboratory for understanding the evolution of galaxy groups because (1) the proximity of objects within it makes it possible to gather detailed information on its constituent objects, and (2) it is a rather dynamically simple system dominated by its two most massive constituents, our Milky Way (MW) and the Andromeda galaxy (M 31). The next largest members of the Local Group — M 33 and the Large Magellanic Cloud — are smaller in mass by at least a factor of 10. General consideration of this distribution of mass within the Local Group form the basis of the Timing Argument (Kahn & Woltjer 1959). More specifically, galaxies observed to be in a binary system at $z = 0$ are likely to have been bound at early times in the Universe and thereby are sufficiently massive to overpower the local Hubble expansion. Thus, the evolution of binary galaxy systems from early times until the present can be well described with simple Newtonian dynamics (Kroeker & Carlberg 1991). Accordingly, the Timing Argument is able to predict the total mass of the Local Group, as well as the relative masses of the the MW, and M 31, with only three observable quantities and the assumption that the MW and M 31 are on a radial orbit (or nearly so): (i) the present separation of the MW and M 31, (ii) the age of the Universe, and, (iii) the line-of-sight velocity of M 31. Thus, the Timing Argument provides one of the simplest means by which to estimate the total mass of the Local Group (Kroeker & Carlberg 1991). Moreover, its applicability and cosmological reliability have been validated through detailed Λ-CDM simulations (Li & White 2008). Our understanding of the dynamical evolution of Local Group as deduced from the

Timing Argument relies critically on the assumption of a radial orbit for the MW-M 31 system. However, that M 31 has no significant tangential motion, is a notion for which observational support has only come recently and remains unconfirmed.

While the line-of-sight motion of M 31 has long been measured to great precision (Slipher 1914, as early as), the measurement of the proper motion has proven to be quite difficult using traditional techniques. The measured proper motion (μ), is both proportional to the tangential velocity of the object (v_t) and inversely proportional to its distance (d), as:

$$\mu_{tot}(''\ year^{-1}) = \frac{v_t\ (km\ s^{-1})}{4.74\ \times\ d\ (pc)}. \tag{3.1}$$

Peebles (1994) placed constraints on the tangential velocity for M 31 using cosmological arguments, finding that $v_{t,M\,31} < 160$ km s^{-1}. The distance to M 31 (770 kpc; Freedman & Madore 1990) combined with this estimate, imply that its proper motion must be $\mu_{M\,31} < 0.04$ mas year^{-1} from Equation 3.1. Few modern astrometric instruments have both measurement accuracy and flux sensitivity to achieve this (see summary Table 1 of Majewski 2010), and ground based optical imaging efforts have largely produced null results, despite a history of such efforts stretching as far back as Barnard (1917) using Mt. Wilson photographic plates (a full history, including erroneous measurements by van Maanen, is given in Hodge 1992).

The diffraction limited imaging capabilities of the Hubble Space Telescope (HST) offer a significant advantage over astrometry derived from ground based imaging. Initial HST proper motions relied on establishing an astrometric reference frame from a set of known background quasars in the targeted field (Piatek et al. 2002; Kallivayalil et al. 2006a,b). However, the need to have a significant number of quasars in the background of the HST imaging for an object places strong constraints on the

quasar density of the field and significant supplementary efforts are required for the identification of these critical quasar sources. Thus, the initial HST proper motion efforts focused only on objects with existing large ground based spectroscopic studies coincident with HST observations of those objects — primarily the Large and Small Magellanic Clouds (Piatek et al. 2002; Kallivayalil et al. 2006a,b). Sohn et al. (2012) devised an alternative profile fitting technique to establish the astrometric reference frame using galaxies of any morphology (i.e., not just the compact, star-like quasar morphology), which greatly increases the number of potential reference objects in a given HST pointing. As discussed in van der Marel (2014), this technique permits HST derived proper motions for nearly any object in the Local Group with the acquisition of only a *single new epoch*, provided there is an appropriate archived observation.

A relatively recent alternative to measuring stellar proper motions is the use of radio interferometry with extremely long baselines, which can reach precisions of $\sim$10μas year^{-1} for an individual source (typically Galactic) and $\sim$1 μas year^{-1} for ensembles of sources at a common distance (typically extra-galactic; Reid & Honma 2014, and references therein). Of particular interest for M 31 is the use of H_2O masers, which, in the MW, are commonly found within compact H II regions in the Milky Way disk (Genzel & Downes 1977, among others). The proper motion technique has also been applied to H_2O maser sources in the M 31 companion galaxies M 33 and IC 10 (730 kpc and 660 kpc distant, respectively; Brunthaler et al. 2005, 2007). The more powerful analogues to the H_2O masers, which are refereed to as megamasers as they are $\sim10^6$ times more powerful than those found in the Galaxy, can be found within accretion disks around super-massive black holes. The megamasers are also used to determine geometric distances to distant galaxies in the Hubble flow by tracking their

Keplerian motion within the accretion disk using similar techniques (e.g., Reid et al. 2013; Kuo et al. 2013; Herrnstein et al. 1999, and others). Galactic water masers in H II complexes, however, have both a large scatter in luminosity and short overall lifetimes (estimated as $\sim 10^5$ years; Imai et al. 2001). Despite great effort, searches for such masers in the H II complexes of M 31 has yet to identify appropriate proper motion sources (Imai et al. 2001, and references therein) until recent efforts (Darling 2011).

Given the observational limitations on traditional proper motion techniques, statistical methods have historically provided the most powerful constraints on the transverse motion of M 31. The statistical methods fall into two categories: (i) those that use inferences from cosmological parameters and the current bound state of the Local Group to constrain the transverse motion of M 31 and, (ii) those that use the projection of the center-of-mass motion of M 31 onto the line-of-sight or three-dimensional velocities of its satellites at relatively large projected radii to measure the transverse motion indirectly.

For the former class of statistical techniques, constraints on the transverse motion of M 31 are similar in spirit to the Timing Argument previously discussed. More specifically, these techniques include using the Timing Argument to back out a range of permitted tangential motions (e.g., Peebles et al. 2001; Peebles 1995, 1994) or using the three dimensional motion of M 33 and its lack of significant tidal distortion to model its orbit and back out the permitted relative transverse motion of M 31 (Loeb et al. 2005). In the latter class, van der Marel & Guhathakurta (2008, vdMG08 hereafter) used a combination of statistical techniques, the most novel being the use of the projection of the bulk transverse motion onto the line-of-sight velocity of its dwarf galaxy companions.

Before discussion of the vdmG08 work for the transverse motion of M 31, it is worth mentioning that the idea of using the line-of-sight motions across an angularly extended object to infer its bulk transverse motion has enjoyed a long history in application to the Large Magellanic Cloud. Wilson (1918) first noted that the average radial velocities of emission-line nebulae in the Large Magellanic Cloud varied systematically with their average declination. Wilson, however, incorrectly attributed this to internal motions in the Cloud. Hertzsprung (1920), on the other hand, proved that the observed velocity gradient could be reproduced assuming a single bulk motion for the Cloud but accounting for the projection effects of the broad ($\sim$15.2°) angular extent of the Cloud onto the motions of the individual nebulae[1]. The realization that this projection effect could be used in turn to estimate the bulk motion of the Large Magellanic Cloud came from Luyten (1928), the cause being a pessimistic discussion of the viability of direct proper motion techniques for the Cloud at that time. The technique was developed further by Wilson (1944a,b) and first applied en masse by Feitzinger et al. (1977) to estimate a bulk transverse motion for the Cloud. Dubbed "ingenious" by later authors (Lin & Lynden-Bell 1982), the complexity of the Cloud internal dynamics complicated its applicability with high precision. Nevertheless, the inferred large transverse motion was supported by modelling of the Magellanic stream (Mathewson et al. 1977; Lin & Lynden-Bell 1982), and the predicted motion of v_t $\sim$275 km s^{-1} (Feitzinger et al. 1977) is actually in reasonable agreement with that from current state-of-the-art techniques (Kallivayalil et al. 2013, and references therein).

With precise line-of-sight velocities for the growing sample of M 31 dwarf galaxy satellites (a summary of these discoveries and their implications is presented in Bul-

[1]The quoted angular extent is computed from the observations of the Cloud included in Table 1 of Hertzsprung (1920) and is not based on more modern studies on the extent of the Cloud.

lock 2010), vdMG08 presented the first application of the line-of-sight technique to M 31. More specifically, vdMG08 combined a series of techniques utilizing (i) the three dimensional motions of its star forming satellites, (ii) the line-of-sight motions for 18 dwarf galaxies bound to M31, (iii) the line-of-sight motions for dwarf Spheroidal satellites at large projected radii to produce the first measurements (in contrast to constraints) of the M 31 transverse motion. Although the errors for an individual technique were large, the error weighted mean measurement in vdMG08 provided the first direct observational evidence of a radial orbit for the M 31 and MW system.

Two technical advances since vdMG08 have permitted a revival of the use of direct proper motion measures for determined the three dimensional motion of M 31. First, the use of resolved background galaxies to set a frame of reference in HST images by Sohn et al. (2012) enabled a direct proper motion measurement, on several epochs of HST+ACS archival fields. Second, Darling (2011) used the unparalleled collecting area of the Green Bank Telescope to detect a sample of OH masers distributed amongst five star forming complexes in the disk of M 31. In an ongoing follow-up program with the Very Long Baseline Interferometer (VLBI) described by Darling an independent direct M 31 proper motion measurement using OH water masers should soon be possible.

The Complications of Internal Motions in M 31

In addition to the requisite sensitivity of the observations and the technical difficulty of the analyses, each of the techniques for measuring v_t described probes a distinct structural component of M 31 — (i) the satellite populations (vdM08), (ii) stellar populations in the inner halo (Sohn et al. 2012), and (iii) water masers in the disk (Darling 2011) — that has its own set of complications related to the internal motions

of the sampled M 31 kinematical subcomponent. For the satellite galaxies, it must be assumed that the ensemble of individual objects represent a "bound", virally relaxed system, an assumption that can only actually be truly validated by having full three-dimensional motions of the satellites to begin with.

For the use of the inner halo stars, the internal stellar kinematics of the inner halo stellar populations cannot be assumed to be relaxed/mixed and must each be carefully modelled, which is especially challenging given the contamination of the Great Southern Stream (GSS) along the HST sight-lines (Brown et al. 2006a, 2007, 2008, 2009). vdm12 approaches this problem using state-of-the art simulations of the GSS, a necessity given that the GSS system is actually quite expansive and has created several kinematically distinct stellar debris features that often superimpose on a single sky position.

Within the M31 disk, not only must the overall bulk disk motions of the H_2O maser system be understood, a daunting but tractable task, but the individual peculiar motions of the star forming regions must be either individually estimated from other objects in the region or be averaged out from a sufficiently large statistical sample. Typical peculiar motions for Galactic masers are on the level of 10-50 km s^{-1} (Reid & Honma 2014, and references therein).

To overcome the above limitations, or at least to minimize their effects, one can combine each of the individual estimates to reduce random errors. Since tracer population is effectively independent of the others, even systematic errors can be reduced. In this work, we proposed to supplement the proper motion measurements previously discussed with a probe of a fourth structural component, that of the "smooth" stellar halo of M 31. The tangential motion is measured using the identical approach presented by vdMG08 for satellites, but has the benefit of being applied to hundreds

of individual tracers on prescribed sight lines, rather than the dozens permitted by the available number of satellites. Like the other tracer populations, the halo stars as a tracer population has both strengths and weaknesses. A particular strength of this technique is that, once a suitable sample of M 31 member stars is identified, the three-dimensional motion can be measured from the line-of-sight velocities without additional numerical modeling; moreover, that measurement is independent of the distance to M 31 unlike direct proper motion measurements (see Equation 3.1. A weakness of this technique is the complexity of identifying "secure" M 31 member stars, against foreground contamination from the MW. Moreover, the existence of coherent substructures within the M 31 stellar halo could bias the resulting motion.

3.2.2 This Work

In this work, we revisit the measurement of the tangential motion of M 31 using its variable projection as a function of position onto the line-of-sight velocities of halo tracers first attempted by vdMG08. In Section 3.3, we develop the general methods and tools necessary for using line-of-sight velocities for this purpose. The techniques are then applied to the current sample of M 31 dwarf satellites and globular clusters with well measured heliocentric velocities, which has been expanded considerably since the last application of this technique in vdM12. We also motivate and describe an empirical technique to test how non-virialized substructure contamination in the satellite and globular cluster sample could influence our measurements.

Considering that the satellites or globular clusters could have been accreted recently and thereby may not represent a virialized population, vdMG08 suggested the use of individual red giant halo stars as an alternative. In Section 3.4, the dataset of the Spectroscopic and Photometric Landscape of the Andromeda Stel-

lar Halo (SPLASH), which contains precision heliocentric velocities for hundreds of M 31 halo member stars, is described. In particular, we detail a multi-observatory campaign aimed at both increasing the number of high-likelihood member stars at large projected radii (>120 kpc) and expanding the azimuthal extent over which M 31 halo member stars are identified at these projected radii. The SPLASH techniques for discriminating between foreground MW dwarf stars and target M 31 RGB stars are described in Section 3.5, as well as the adaptation of these techniques for spectroscopy at lower resolution. Consideration is given to the removal of known halo substructures from the sample, which can include both streams of stars as well as intact dwarf satellites. We also investigate the complexity of using the variable of interest — heliocentric radial velocity — as one of the discriminating criteria for M 31 membership, a standard practice for the discrimination of foreground MW stars from target M 31 populations in this work and others, without imposing a bias on the final three-dimensional motion.

In Section 3.6, we present the M 31 tangential motion derived from individual halo stars and explore, in depth, potential biases within our sample, including those of our adopted M 31 halo membership selection and unidentified residual substructure. The results of these explorations are used to estimate an appropriate systematic uncertainty for our estimate. In Section 3.7, a final error-weighted mean tangential motion is reported that includes both the two new estimates obtained from the present as well as previous estimates, as summarized in vdM12. In Section 3.8, the finding of the paper are summarized and the implications for further study of the halo discussed.

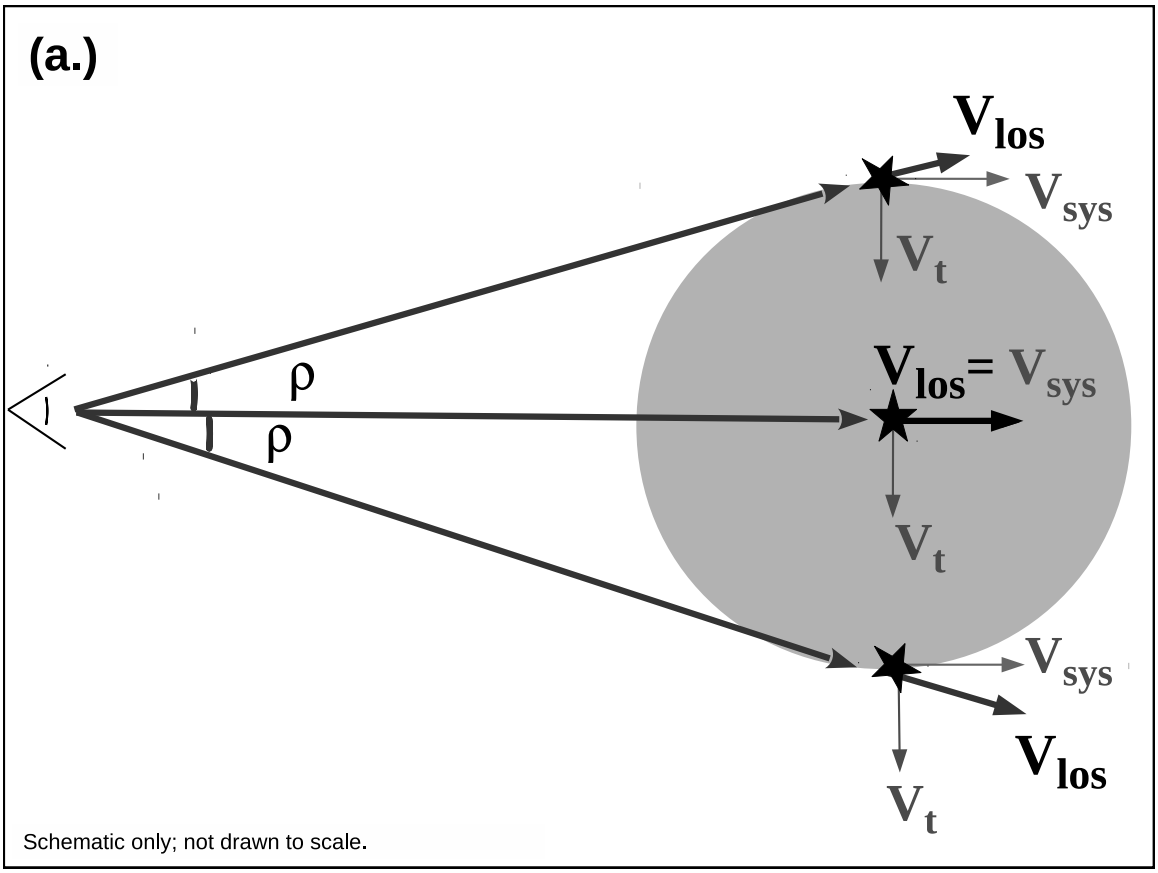

Fig. 3.1.— Demonstration of how the the center-of-mass motion of M 31 projects onto the heliocentric line-of-sight velocity for widely separated tracers. **(a)** Schematic illustration of center-of-mass motion of an object in the sky plane along two dimensions — v_{sys} along the line-of-sight to the center of mass and v_N perpendicular to v_{sys} — and the effect of observing tracers at lines-of-sight at widely separated angles, ρ. Vectors are not drawn to scale and the tracer (black star) has no internal motion with respect to the center-of-mass ($v_{int,los}$=0). For a tracer at $\rho \sim 0$, the line-of-sight of the center of mass and of the tracer are aligned, such that $v_{los} \sim v_{sys}$. For a tracer at ρ>0, the line-of-sight for the tracer is no longer aligned with that for the center of mass $v_{los} \neq v_{sys}$, where the magnitude of the difference depends on both the radial (ρ) and azimuthal (ϕ) location of the tracer. **(b)** The predicted magnitude for the projection of the M 31 center-of-mass motion as measured by vdm12 computed along appropriate lines-of-sight for $R_{proj} \sim 2/3\ R_{virial}$ ($\sim 14°$ or 200 kpc). The values are computed using Equation 3.6 and assuming no internal motion ($v_{int,los} = 0$) and are plotted for each (ρ,ϕ) using the color bar at the top of the panel. The ρ and ϕ dependence of v_{los} mimics a rotation approximately aligned with the plane of the sky, as was first noted by Hertzsprung (1920) for observations of the Large Magellanic Cloud.

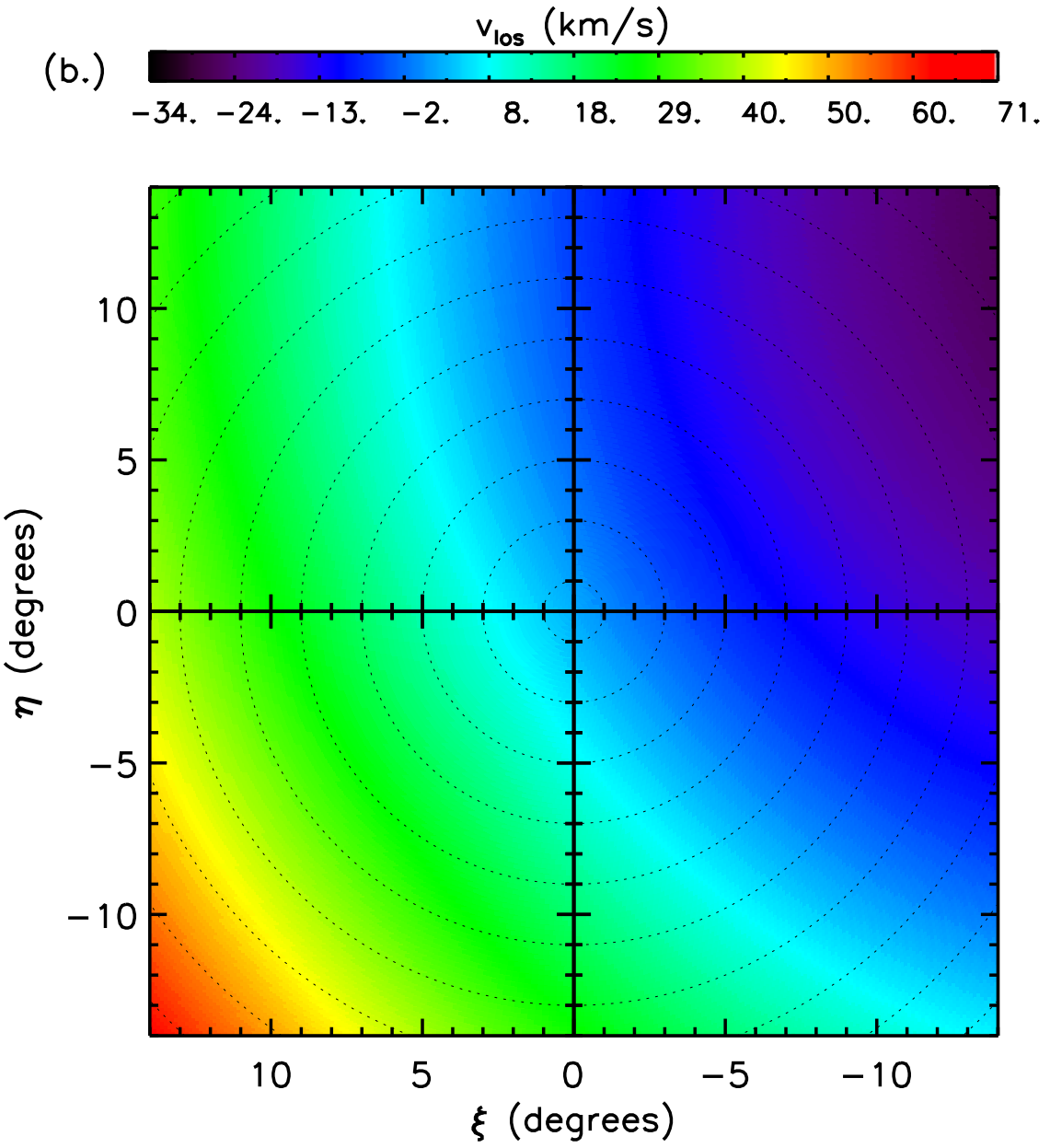

Fig. 3.1.— cont. **(b)** The predicted magnitude for the projection of the M 31 center-of-mass motion as measured by vdm12 computed along appropriate lines-of-sight for $R_{proj} \sim 2/3\ R_{virial}$ ($\sim 14°$ or 200 kpc). The values are computed using Equation 3.6 and assuming no internal motion ($v_{int,los} = 0$) and are plotted for each (ρ,ϕ) using the color bar at the top of the panel. The ρ and ϕ dependence of v_{los} mimics a rotation approximately aligned with the plane of the sky, as was first noted by Hertzsprung (1920) for observations of the Large Magellanic Cloud.

3.3 The Tangential Motion from Satellite Tracers

We first demonstrate the use of line-of-sight tracers to measure the tangential motion of M 31 by resisting the line-of-sight analysis of vdMG08 and vdM12 applied to satellite tracers, primarily dwarf galaxies in vdMG08 and outer halo globular clusters in vdM12. Throughout the following sections the general theory and techniques for estimating the three-dimensional motion from line-of-sight tracers are described in application to these tracers. First, we develop the procedure in Section 3.3.1. Second, a sample of satellite systems, both dwarf galaxies and globular clusters, is defined in Section 3.3.2. Third, the tangential motion and its errors are estimated in Section 3.3.3. Fourth, a test for the role of substructure is described and applied to this sample in Section 3.3.4. Lastly, the final result is discussed in Section 3.3.5

3.3.1 Theory

The total three dimensional space velocity of an M 31 tracer object ($\mathbf{v_i}$) can be written as the sum of its internal motion with respect to the center of mass ($\mathbf{v_{int}}$) and the bulk motion of the center of mass ($\mathbf{v_{M31}}$):

$$\mathbf{v_i} = \mathbf{v_{M31}} + \mathbf{v_{int}}. \tag{3.2}$$

The quantity $\mathbf{v_{M31}}$ — the three dimensional motion of M31 — can be decomposed into three observable quantities: (i) the systemic line-of-sight motion of M 31, v_{sys}, (ii) the magnitude of the motion in the plane of the sky, v_t, and (iii) the direction of the motion in the sky, Θ_t, where Θ_t is defined as a position angle (i.e., the angle east of north in sky right orientation). Here, the combination of v_t and Θ_t define the tangential motion of M 31. We can define a coordinate system with its origin at

the M 31 center-of-mass, which is defined to be its central coordinates: $(\alpha,\delta)_{J2000}$ = (00:42:44.3, +41:15:09). In a Cartesian coordinate system, we can define **z** as the line-of-sight from the center-of-mass of M 31 to the Sun, **x** as the Right Ascension (R.A.) passing through the center of M 31 (e.g., West-to-East), **y** as the Declination (Dec) passing through the center of M 31 (e.g., South-to-North). Using these definitions, the motion in the plane of the sky can be decomposed into the motions along the directions of west and north in the sky, by:

$$v_W \equiv v_t \cos(\Theta_t + 90^\circ) \tag{3.3}$$

$$v_N \equiv v_t \sin(\Theta_t + 90^\circ) \tag{3.4}$$

Thus, the three dimensional motion of M31 can be expressed as a vector:

$$\mathbf{v_{M31}} = [v_{sys}, v_N, v_W] \tag{3.5}$$

The quantity, $\mathbf{v_{int}}$, is the motion of the tracer itself with respect to the center-of-mass of M 31. Following the example of vdMG08, the only assumption made on this parameter is that each dimension of the motion for an individual tracer, $v_{i,los}$, $v_{i,N}$, $v_{i,W}$, is drawn from a Gaussian with dispersion σ_{int}. This assumption is true if the halo is both isothermal and isotropic. As discussed in vdMG08, there is evidence to support both assumptions, but neither plays a particularly large role in our analysis *if* tracers with potential membership in kinematically coherent substructures or "unvirialized" objects can be removed.

The position of an M 31 halo tracer in the plane of the sky relative to the center of mass can be described by two angles: ρ and ϕ, where ρ is the projected angular distance from the center-of-mass of M31 (defined previously) and ϕ is the position

angle of the tracer measured from north through east. These definitions of ρ and ϕ are identical to those used in similar studies using line-of-sight velocities (van der Marel & Cioni 2001; van der Marel 2001, vdMG08, vdM12).

The three dimensional motion of M31 can be projected onto the line-of-sight at generic coordinates (ρ, ϕ) as:

$$v_{i,los} = v_{sys}\cos(\rho) + v_t \sin(\rho)\cos(\phi - \Theta_t) + v_{int,los} \tag{3.6}$$

The radial effect is demonstrated schematically in Figure 3.1a, albeit with no internal motion for the tracer (i.e., $\mathbf{v_{int}} = \mathbf{0}$). As demonstrated in the figure, at the limit of small angular separation, e.g., for $\rho \approx 0$, Equation 3.6 reduces to,

$$v_{i,los} = v_{sys} + v_{int,los}, \tag{3.7}$$

i.e., the transverse velocity has no effect on the line-of-sight motion. For large angles, however, the tangential velocity component takes on increasing significance, as demonstrated schematically for a two dimensional case by Figure 3.1a. The virial radius of M31 is $R_{virial} \sim 300$ kpc, which at the distance to M31 (780 kpc; Sarajedini et al. 2009), implies a total theoretical radial extent on the sky of $\sim$20°. Observationally the M31 stellar halo has been traced confidently to 165 kpc (11°) along its minor axis (Gilbert et al. 2007, 2012) and to $\sim$100 kpc in panoramic photometric studies for all ϕ ($\sim$8°; Ibata et al. 2014).

In Figure 3.1b, the error weighted mean result of vdM12 is used to predict the line-of-sight component for all ϕ and to the extent of the Gilbert et al. (2007) kinematically confirmed detection of M 31 member stars. As shown in Figure 3.1b, the large scale effect of the tangential motion is an apparent, albeit slightly asymmetric, rotation

in the plane of sky of magnitude $v \sim 30$ km s^{-1} about the systemic motion of M31 ($v_{sys} = 300$ km s^{-1}, Cappellari et al. 2011). As demonstrated in the panels of Figure 3.1, the magnitude of the motion (v_t) is best constrained by using tracers at large projected separations (ρ). The direction of the motion, Θ_t, can only be constrained reliably with tracers covering a wide range of azimuthal angles (ϕ). Thus, to estimate the tangential motion of M31 using halo tracers, a kinematical sample extending both to large projected radii and spanning a range of azimuth is required.

3.3.2 Sample of Satellite Tracers

The most recent use of v_{LOS} as applied to M 31 halo tracers was that of vdM12, which used a sample of twenty-three dwarf satellite galaxies and eight globular clusters beyond 40 kpc ($\sim$3°) that were available in the literature at that time. Since that analysis, line-of-sight velocities have been published for twenty-four more halo globular clusters beyond 75 kpc ($\sim$5°) and ten more dwarf satellite galaxies. These new data are first described in Sections 3.3.2 and 3.3.2 and and then merged with those objects used in vdM12 into a single catalog in Section 3.3.2.

Recent Measurements for Globular Clusters

The Pan-Andromeda Archaeological Survey (PAndAS, hereafter; Ibata et al. 2014, and references therein) has added 80 new globular clusters to the previous sample of 450 in the Revised Bologna Catalog (Galleti et al. 2004). The line-of-sight velocities for 78 outer halo globular clusters, of which 63 had no previous measurements, were released in Veljanoski et al. (2014). A reasonable fraction of their clusters clearly overlap the Great Southern Stream (GSS), a large and dominant accretion debris structure in the inner halo of M 31 with kinematical properties consistent with the

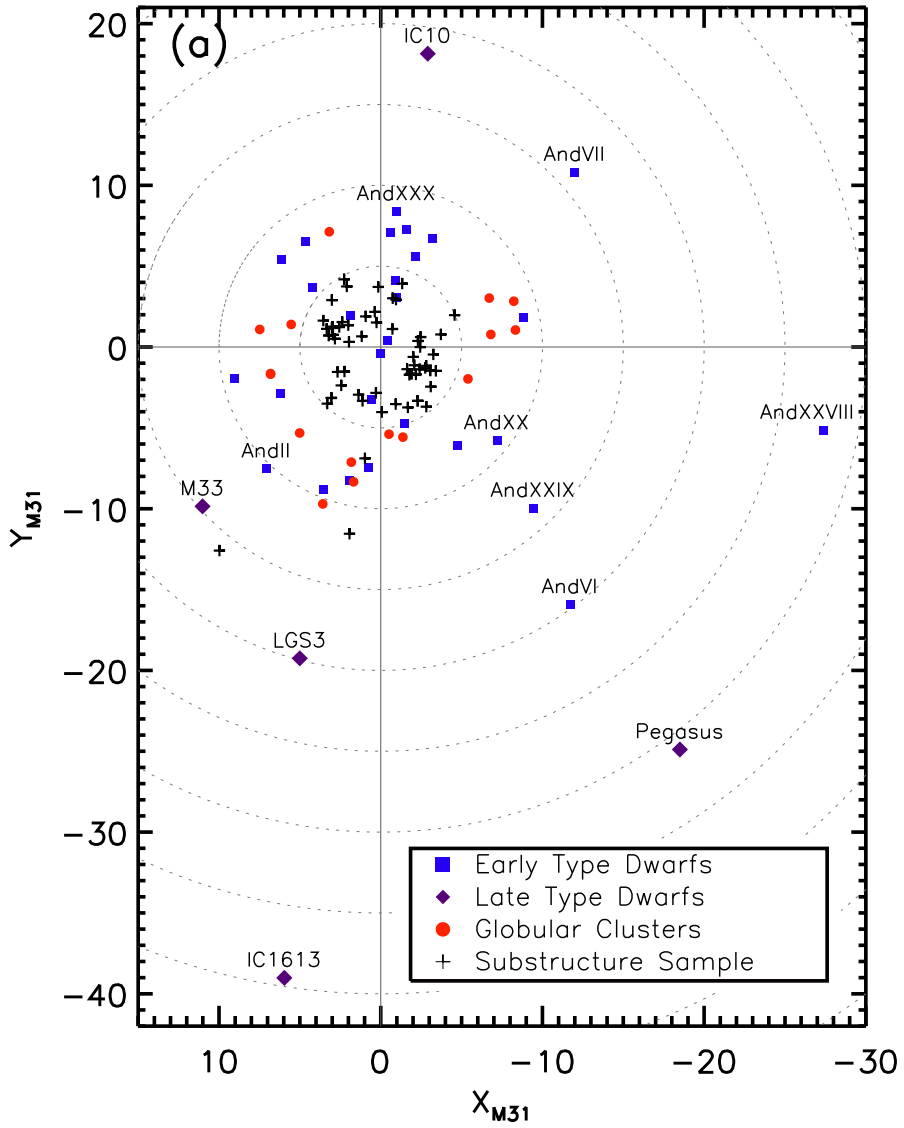

Fig. 3.2.— Spatial distribution of dwarf satellite galaxies and globular clusters used to estimate the transverse motion of M 31 as described in Section 3.3. The angular coordinates (ρ,ϕ) of the objects (see Table 3.1) are projected onto a Cartesian coordinate system (X_{M31}, Y_{M31}). Globular cluster are plotted as red circles, whereas satellite galaxies are divided into early type as blue squares and late type or purple diamonds. Objects classified as potential members of halo substructure (as described in Section 3.3.2), are shown as black pluses. Due to the large angular separations of some satellite galaxies (p >15°), two visualizations are required. **(a)** The wide field distribution of M 31 satellites and globular clusters scaled to show the relatively distant satellite galaxies: IC 10, Andromeda XXVIII, Pegasus, and IC 1613. **(b)** The more familiar visualization of the M 31 halo spanning the approximate area imaged by PAndAS (Ibata et al. 2014). Here the ρ <5° exclusion due to potential associations with substructure is particularly visible. Satellite galaxies in this range are all included, since none have any clear associations with the substructure from kinematical and imaging studies.

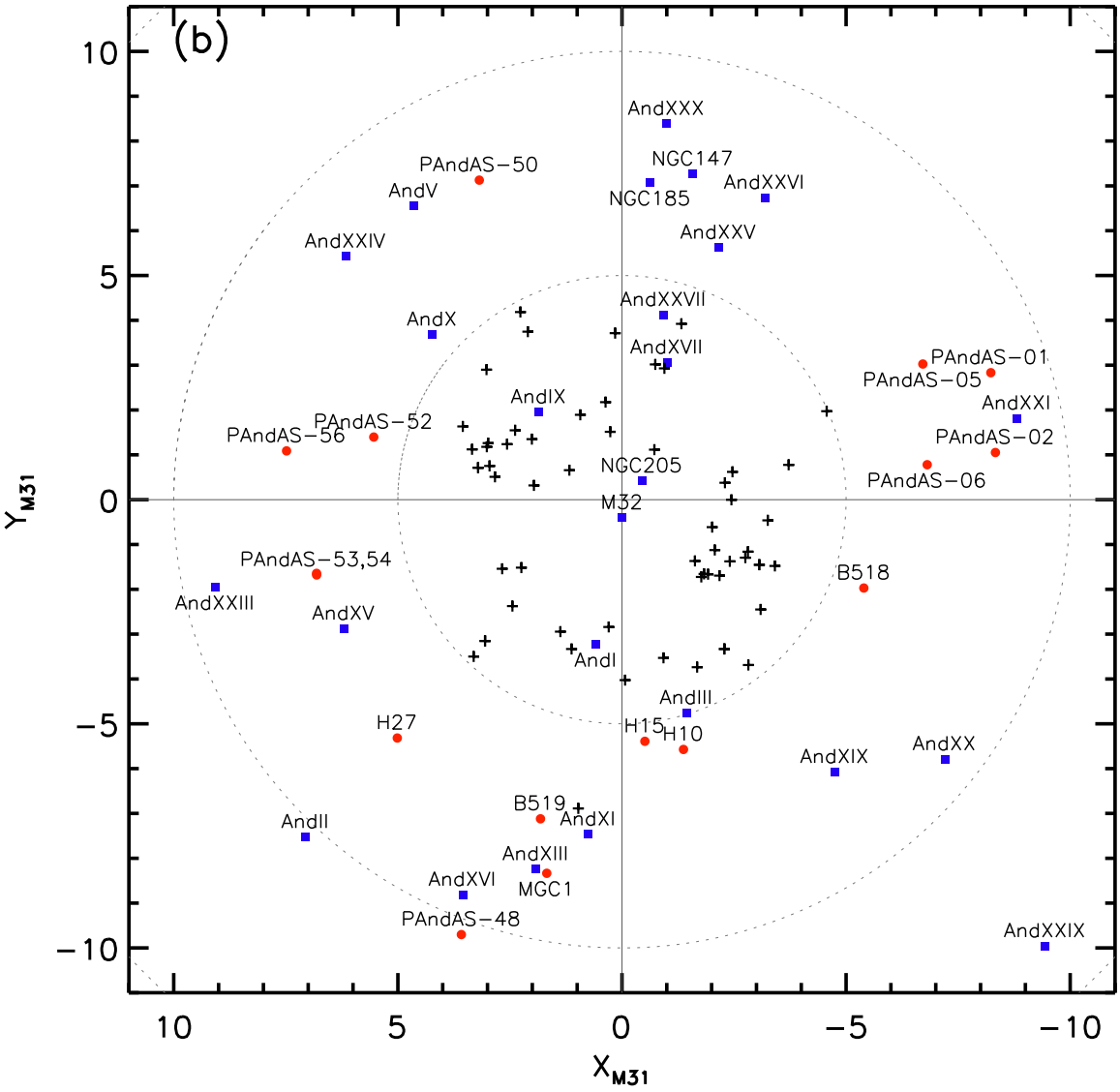

Fig. 3.2.— cont. **(b)** The more familiar visualization of the M 31 halo spanning the approximate area imaged by PAndAS (Ibata et al. 2014). Here the ρ <5° exclusion due to potential associations with substructure is particularly visible. Satellite galaxies in this range are all included, since none have any clear associations with the substructure from kinematical and imaging studies.

tidal disruption a relatively large disk galaxy progenitor (Fardal et al. 2008). If a cluster were associated with the GSS debris then it would violate the only assumption of our fitting technique — that all objects be pulled from the same underlying virialized distribution. To avoid any potential clusters associated with the GSS debris, only those clusters with projected radii greater than 5° will be included in our sample. This is larger than the restriction applied by vdM12 (3°), but is broadly consistent with the GSS dominance within this radius in stellar kinematical samples described (Gilbert et al. 2009b, 2012). All of the heliocentric velocities for globular clusters beyond 5° in Veljanoski et al. (2014, their Table 4) are adopted. Even though new measurements were obtained for several clusters, the previous measurements were adopted by Veljanoski et al. (2014), if the previous measurement was of greater signal-to-noise. Consistent with Veljanoski et al. (2014), we too adopted the velocity measurement from spectroscopic data of higher signal-to-noise. An additional eleven globular clusters in Veljanoski et al. (2014) spatially overlap, in projection, halo substructures identified in the panoramic PAndAS imaging (Ibata et al. 2014) and will not be used for our halo sample. Eleven of the twenty-eight globular clusters from $\rho = 5°$ to $\rho = 10°$ are excluded as likely members of substructure due to spatial projection on tidal debris (see Ibata et al. 2014). With these restrictions on the Veljanoski et al. (2014) catalog and we are left with a total of seventeen globular clusters for our transverse motion analysis.

Recent Measurements for Dwarf Satellites

Tollerud et al. (2013) measured the line-of-sight kinematics of Andromeda XXVIII and Andromeda XXIX, and both are adopted for our sample. Collins et al. (2014) measured the line-of-sight kinematics of eighteen satellites including a revision of

some values of Tollerud et al. (2012) by increasing the sample of stars for those satellites. The line-of-sight velocities for nine objects in Collins et al. (2014), more specifically those of Andromeda XVII, XIX, XX, XXIII, XXIV, XXV, XXVI, XXVII and XXX, are adopted for our satellite sample, as there are no prior measurements in the literature. The observational efforts of Collins et al. (2014) significantly increased the number of member stars for Andromedas XI, XII, and XXII from that of Tollerud et al. (2012). The heliocentric velocity for Andromeda XII and XXII in Collins et al. (2014) agrees within 2σ with that of Tollerud et al. (2012) and is adopted in our sample, given the substantially better sampling of Collins et al. (29 member stars; 2014). The Collins et al. (2014) result for And XI disagrees by more than 5σ with that of Tollerud et al. (2012). As discussed in detail by Collins et al. (2014, in their Appendix B), the disagreement originates from significant differences in the measured velocities of individual stars common to both datasets. We adopt the value from Collins et al. (2014) for And XI, given their larger number of member stars. The systemic velocities for a number of the satellites of Tollerud et al. (2012) were remeasured by Collins et al. (2014) using the same spectroscopy but with application of their membership algorithm and resulted systemic velocities consistent with those initially measured by Tollerud et al. (2012). For consistency with vdM12, we maintain the values by Tollerud et al. (2012) for those objects.

Summary

The final compilation of data on satellite and globular cluster tracers is given in Table 3.1, with object morphological types indicated in column 2. The objects used in the analyses of vdMG08 and vdM12 are also indicated in column 8 of Table 3.1, albeit their heliocentric velocities may have been updated in more recent studies, as

indicated in column 7. We exclude those globular clusters from vdM12 that are within our 5° inner radius. Those objects having suspected associations with substructure, having large relative velocities to M 31 indicative of not being bound to M 31 (i.e., an "in-falling dwarf"), or suspected satellites of satellites (i.e., Andromeda XXII as discussed in Tollerud et al. 2012), are also indicated in column 6. The projected distribution of these objects is given in Figures 3.2a and 3.2b, which are wide field and zooms of the M 31 stellar halo, respectively. The final sample includes thirty dwarf satellites and seventeen globular clusters from ρ=0.40° to ρ=39.5°, but with three dwarfs and eleven globular clusters suspected of having association with substructure or being "in-falling dwarfs".

3.3.3 Tangential Motion from Satellites

To fit for the tangential motion of M 31, Equation 3.6 is revised by the substitution of the values of v_W and v_N in Equation 3.3 and 3.4, respectively, with the final result of:

$$v_{pec} = v_{LOS} - \cos(\rho)v_{sys} + \sin(\rho)\sin(\phi)v_W - \sin(\rho)\cos(\phi)v_N, \tag{3.8}$$

where v_{pec} is the internal motion of the tracer along the line-of-sight (previously referred to as $v_{int,los}$). Equation 3.8 is now linear in the three quantities we wish to measure, v_{sys}, v_W, and v_N, which constitute the three dimensional motion of M 31. Equation 3.8 can be written independently for each of the halo tracers with the true internal motion along the line-of-sight absorbed into the quantity v_{pec} for each tracer. Thus, a system of equations is built with three common unknowns, v_{sys}, v_W, and v_N, and one unknown unique to each tracer, v_{pec}. The resulting system of equations can then be solved for the three dimensional motion of M 31 (v_{LOS}, v_W, and v_N) by minimizing the scatter in the residual motion, v_{pec}, of the set of tracers. The

dispersion of the resulting distribution of v_{pec} is fit and called σ_{pec}.

The minimization of the distribution of v_{pec} from Equation 3.8 is implemented using the amoeba algorithm of Press et al. (1986), which is especially efficient at solving systems of equations in this form. The uncertainty for the set of values resulting from the minimization is determined using a set of Monte Carlo simulations. By appropriate rearrangement of Equation 3.8, the three-dimensional motion of the M 31 center-of-mass from the initial minimization is used to model the anticipated projection onto the line-of-sight for the position (ρ, ϕ) of each data point in the input sample. A value for v_{pec} is drawn randomly for each data point from a Gaussian deviate with dispersion σ_{pec} and is added to the modeled value for the coordinates of each object (ρ, ϕ). This creates a unique visualization of the best fit model to which our transverse motion fitting algorithm is then applied. The process is repeated for N_{trials} =5000 to build a sample of simulated measurements. The dispersion of the resulting distribution for each of the three-dimensional components is adopted as its measurement uncertainty.

The result obtained from the combined satellite and globular cluster sample is as follows: $(v_{sys}, v_W, v_N)_{sats}$ = (-310.2 $\pm$ 130.5 km s^{-1}, -122.6 $\pm$ 101.3 km s^{-1}, -1.0 $\pm$ 83.8 km s^{-1}) with σ_{pec} = 87.8 km s^{-1}. This value agrees within the errors of the values determined previously by vdM12 of $(v_{sys}, v_W, v_N)_{vdm12}$ = (-279.3 $\pm$ 16.4 km s^{-1}, -176.1 $\pm$ 144.1 km s^{-1}, 8.4 $\pm$ 85.4 km s^{-1}) and σ_{pec} = 84.8 $\pm$ 10.6 km s^{-1}, with a slight decrease in the measurement errors for v_W and v_N, albeit with significantly larger error for v_{sys}.

We rerun our measurement in a bootstrap resampling fashion, by removing a single object and obtaining a new estimate. The resulting distributions of parameters aid in determining whether the result depends critically on any single object. This process

results in a mean result of (v_{sys}, v_W, and v_N) = (-304.3 ± 12.2 km s^{-1}, -122.0 ± 14.0 km s^{-1}, -2.5 ± 11.9 km s^{-1}) with σ_{pec} = 87.9 ± 1.1 km s^{-1}, where the quoted errors represent the 1-σ ranges of the resulting distribution for each parameter. Thus, the majority of the bootstrap simulations produce results well in agreement with those from the initial run and our sample is unlikely to be significantly biased by the inclusion or exclusion a single object.

3.3.4 An Empirical Test for Bias Due to Unidentified Substructure

A pressing concern in our analysis relates to the nature of stellar halos. More specifically, if the halo itself is formed *entirely* or only *fractionally* from accreted substructure. In either case, the relaxation timescales for halo constituents are long and, given that individual satellite galaxies or globular clusters each will have fallen into the halo at unique moment (t_{acr}) spanning a Hubble time, it is difficult to apply a single virialization timescale (as estimated from its current R_{proj} likely to be at or near its apocentric radius) to an individual member of the population. Moreover, numerical simulations undertaken both in a cosmological and single-galaxy sense seem to yield a two-component halo, an inner (∼30 kpc), kinematically hotter, and younger region, which is populated primarily by recent and/or wet mergers, and an extended, lower surface brightness structure that extends to large radii (e.g., to ∼R$_{virial}$; Cooper et al. 2013; Johnston et al. 2008; Bullock & Johnston 2005). Deep, detailed probes of both the MW and M 31 support these portraits (most recently Deason et al. 2014; Gilbert et al. 2012, among others).

An assumption of our method is that the velocities are drawn from a parent population with equal chances that motion along our **x**, **y** or **z** coordinate system, as would

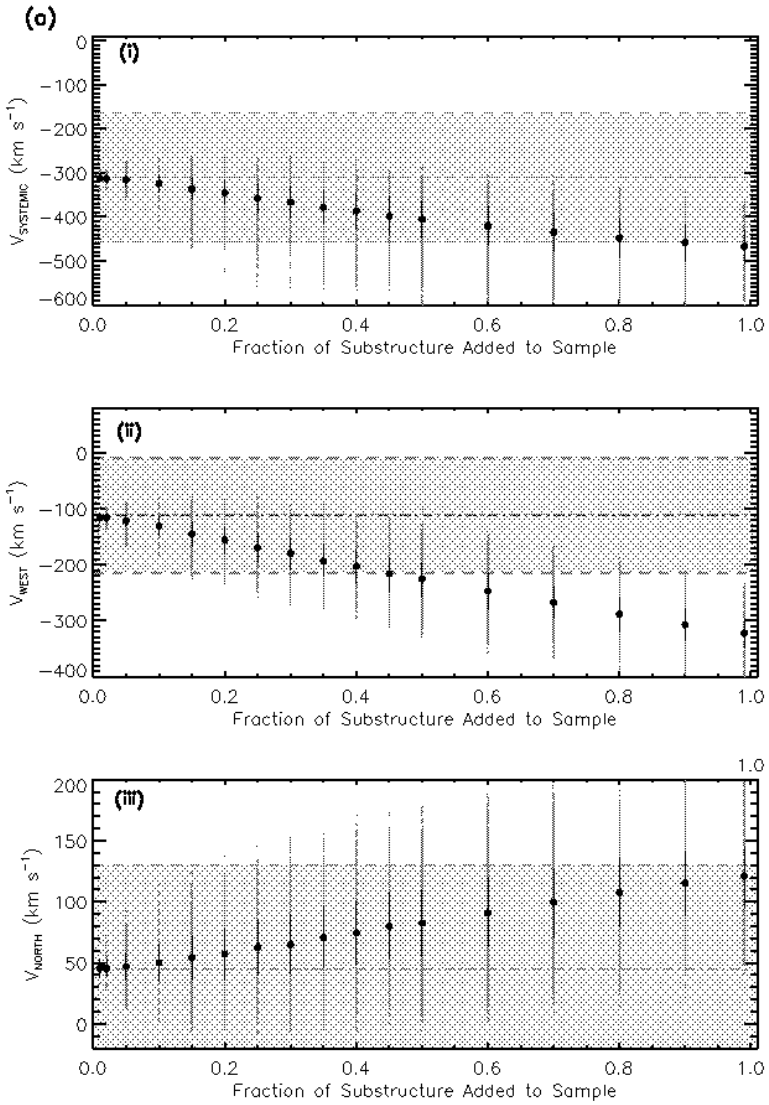

Fig. 3.3.— Behavior of the M 31 three-dimensional motion components, (panel i) v_{sys}, (panel ii) v_{west}, (panel iii) v_{north}, as they are fractionally contaminated by known substructure using the additive (sub-fig a) and replacement (sub-fig b) techniques. Individual results from the Monte Carlo procedure are shown for each substructure fraction as light grey points. The mean and one standard deviation (1σ) range for each substructure fraction is over plotted in black. The value determined by our fit (e.g., that of Section 3.3.3) is the horizontal dot-dash line and the 1σ range is shaded between the dashed horizontal lines. **(a)** Results of the additive substructure technique by which the normal sample is supplemented with objects from the known substructure sample. For all three parameters, the a contamination fraction >50% significantly bias the result. **(b)** Results of the replacement substructure technique by which the objects in the normal sample are replaced randomly by objects from the substructure sample. Contamination fractions >35% result in a 1σ disagreement from the initial result.

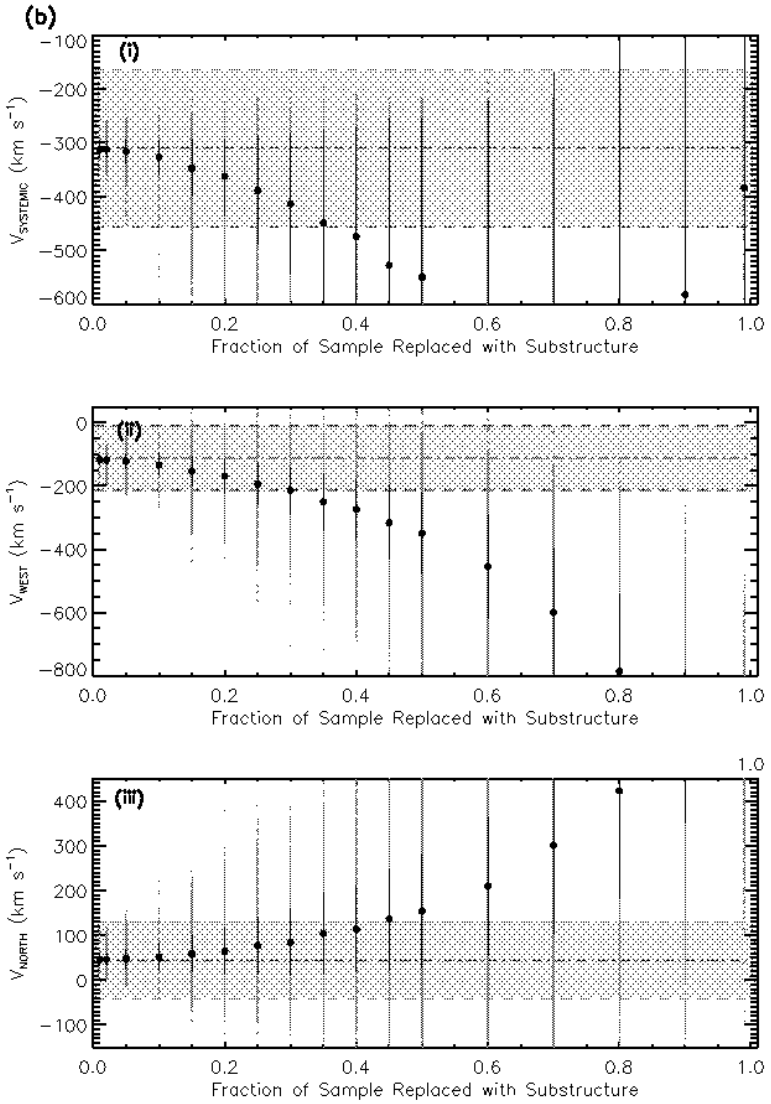

Fig. 3.3.— cont. **(b)** Results of the replacement substructure technique by which the objects in the normal sample are replaced randomly by objects from the substructure sample. Contamination fractions >35% result in a 1σ disagreement from the initial result.

be expected for an axis-symmetric (or nearly so) dispersion supported structure. If, however, there are coherent velocity structures within our sample, as would occur if we selected members of a substructure, then our resulting line-of-sight velocity field will not represent our assumed virialized structure. The ultimate concern for the transverse motion is understanding how unidentified substructure within our sample could bias any of the three components of the M 31 bulk motion..

There are two obvious approaches for exploring the potential effect of substructure in our transverse motion measurement. First, one could mimic our dataset by appropriately sampling high resolution galaxy simulations undertaken in a cosmological sense and with simulated stellar content; second, one could use the data on hand for those objects associated with known substructure to fractionally "contaminate" our halo sample. In the former, assumptions relating to the particular Λ-CDM model may induce systematic biases in the measurement too subtle to be readily distinguished; more specifically, the properties of the dwarf satellite galaxies contributing to the accretion history of the MW-sized galaxy followed. Further, Λ-CDM models require abundance matching prescriptions to translate between a dark-matter only simulation to those objects observed in the current haloes of nearby galaxies in order to simulated realistic present-day dwarf satellites and these prescriptions have come into question (Boylan-Kolchin et al. 2011, 2012). Moreover, the low mass dwarf galaxies that form the haloes of MW sized galaxies are particularly sensitive to the star formation, feedback, and IMF prescriptions. Albeit there are numerous other scientific questions that can be probed from sampling Λ-CDM models, this approach likely does not provide a data set well-suited for our ultimate goal — that of estimating bias from unidentified substructure in the tangential motion estimate.

The latter approach, however, does provide a means to address our concern. This

empirical technique is both independent of the halo formation model (e.g., the fraction of substructure) and of prescriptions to predict the properties of individual dwarf satellite stars. We adopt the latter approach as an appropriate means of empirically studying the role of substructure in the tangential motion measurement.

In our discussion of the satellite sample, care was given to produce a relatively substructure-clean halo sample, whose complement is a relatively clean sample of known substructures. The halo sample can be fractionally contaminated by stars from the substructure sample to build a unique visualization of the dataset. Then, by measuring the tangential motion — identically to that of the original dataset — we gain insight into how contamination by substructure biases the resulting measurement and its uncertainty. Unfortunately, as discussed in the general discussion of the tangential motion, where a tracer is located within the halo gives it less or more weight in the fit. Thus, we undertake this procedure in a Monte-Carlo sense to average over these effects.

First, a fraction of tracers is chosen uniformly from within the substructure-clean halo sample. A corresponding set of stars is chosen at uniformly from the substructure sample and replaces those in the primary halo sample. The tangential motion is estimated for this realization as described in the previous subsection. The procedure is repeated N_{trials} =1000 times for each substructure fraction. As with the estimation of uncertainties, statistics on the resulting distribution, its mean and dispersion, provide insight into how substructure could bias the tangential motion estimate.

For our satellite tracers, there are thirty dSphs and seventeen globular clusters for 47 total objects the halo sample. There are three satellites and eleven globular clusters beyond 5° for fourteen objects in the substructure sample. In permit study of the substructure fraction to large contaminations, we supplement the substructure sample

with the fifty objects in Veljanoski et al. (2014) within 5° for a total substructure sample of sixty-four objects.

The test is performed in two contamination schemes. The first is undertaken in an 'additive' sense, such that the halo sample is fractionally supplemented with objects from the substructure sample; The second is undertaken in an 'replacement' sense, such that the halo sample is fractionally replaced with objects from the substructure sample. In either case, the objects to be inserted, and when required the objects to be replaced, are chosen at random but, given the relatively small size of the halo and substructures samples (e.g., each is <100 objects), we do not permit an object to be chosen from the substructure sample more than once. The substructure estimate is completed for substructure contamination fractions of 5% to 95% in steps of 5%, as well as at 1%, 2% and 99% with 1000 trials computed for each fraction.

The results of this the empirical substructure measurement are given in Figure 3.3a and 3.3b. The distributions for each of the measured parameters, v_{sys}, v_W, and v_N are given in sub-panels i, ii, and iii, in which results from individual Monte Carlo realizations are shown in light grey with the mean and dispersion over plotted in in black. The results from the fit in Section 3.3.3 are given by the dash-dot grey line in each panel and the 1σ range shaded in grey (and bounded by the dashed lines). For our purposes we consider a mean value that falls outside of the 1σ parameter space to be a significantly biased result.

For the 'additive' procedure (Figure 3.3a), a significant deviation occurs at 50% substructure contamination for v_W, but for v_{sys} and v_N the mean values are confined to the 1σ range of our initial fit. Thus, our result in Section 3.3.3 is relatively robust to the 'additive' substructure procedure. For the 'replacement' procedure (Figure 3.3b), however, all three parameters begin to show significant deviations

from the initial result at the ∼40% contamination fraction limit. Moreover, as the sample becomes dominated by substructure the range of values over the Monte Carlo simulation become very large and the fits are, in a sense, highly sensitive to the 'choice' of objects in the sample.

From these tests, we find that our exclusion of objects with $\rho < 5°$, while conservative compared to vdm12, is an important factor in our final results. Thus, consideration must be given to the selection of objects for samples attempting to measure or study global motions in the M 31 halo (and by proxy for all haloes). For example, the rotation measured in the globular cluster sample by Veljanoski et al. (2014), using a similar procedure as applied here, did not make a distinction between substructure and halo populations, and, given the significant scatter seen when including the full globular cluster sample in Figure 3.3, may not represent intrinsic rotation in the halo globular clusters, but rather coherent motions for the globular clusters associated with the well-documented and extensive substructure in the inner M 31 halo (Ibata et al. 2014, and references therein).

3.3.5 Summary

In this section, the theory of and techniques related to the measurement of tangential motions using line-of-sight motions is demonstrated using the line-of-sight velocities of dwarf satellites and globular clusters. The sample of satellites and globular clusters of vdMG08 and vdM12 is expanded using recent observations to include 49 tracer objects, 43 of which are beyond $R_{proj} = 75$ kpc (5°) The resulting tangential motion and uncertainties is found to be broadly consistent with previous measures, with a decrease in the errors for the v_W and v_N components of the M 31 three-dimensional motion, which is most likely due to the improved, albeit slight, sampling for both ρ

and ϕ. An empirical test for bias due to substructure is developed and applied to the satellite and globular cluster sample. We find our initial fit (Section 3.3.3) is largely robust to substructure contamination in an 'additive' sense and to 40% contamination in a 'replacement' sense. More specifically, if we were contaminated by substructure to 40% we would obtain results consistent to 1σ with our chosen sample in either case. We further note that the inclusion of satellites or globular clusters associated with substructure does substantially increase the scatter in the Monte Carlo simulation and the overall errors in the result.

3.4 The SPLASH Dataset

The Spectroscopic and Photometric Landscape of the Andromeda Stellar Halo (SPLASH) is a multi-facility project aimed at studying the global properties of the stellar halo and its constituent dwarf satellite galaxy population. The SPLASH project consists of two phases, both of which are ground-based: (i) wide-field imaging of the M 31 stellar halo on 4-meter class telescopes, and (ii) follow-up spectroscopy on 8-meter class telescopes. The goal of measuring the tangential motion of M 31 will utilize the entire SPLASH kinematic dataset, whose extent is visualized in Figure 3.4. First, we describe the 72 pointing imaging campaign in Section 3.4.1, which is specially designed for photometric identification of likely M 31 giant stars from the dominate MW foreground populations. Of the 72 fields in the imaging campaign, a total of 53 fields have corresponding observations with Keck+DEIMOS (Section 3.4.2), of which 39 were presented in Gilbert et al. (2012), and six were used in application to their dSph content in Tollerud et al. (2012, 2013).

While the combination of the published SPLASH catalogs span an impressive range of radial and azimuthal coverage, we present a supplementary observing cam-

paign to improve spectroscopic sampling in the outer halo at or beyond $R_{proj} \sim 100$ kpc. Eight fields are acquired from Keck+DEIMOS in our 'R08' ring at $R_{proj} = 120$ kpc ($\sim 8°$), providing full azimuthal coverage at this radius. At the average surface brightness of the outer M 31 halo at this R_{proj} is ~ 31 mag arcsec^{-2} and typically results in only 1-2 M 31 member stars per Keck+DEIMOS mask (Gilbert et al. 2012). To improve statistics along some lines of sight, additional spectroscopy was obtained with MMT+Hectospec for two fields in the 'R08' ring (Section 3.4.3), which requires adaptation of the standard SPLASH spectroscopic analyses and consideration to maintaining a homogeneous a sample in the final catalog. Although both the photometric and spectroscopy data come from a variety of sources (as discussed in Sections 3.4.2 and 3.4.3), effort is placed on making the most homogeneous selection of M 31 halo members (described in Section 3.5).

3.4.1 Washington + DDO51 Photometric Catalogs

Observations

Imaging data for 72 fields in the halo of M 31 were obtained in the Washington+$DDO51$ filter system from the Mayall 4-m telescope at the Kitt Peak National Observatory using the Mosaic 1 and Mosaic 1.1 imagers. These data were obtained over six observing seasons from 2005 to 2010 and combined with the pilot study by Ostheimer (2003) to form the imaging component of the SPLASH survey. For all of these observations, we make use of the Washington+$DDO51$ photometry system, consisting of the M, $T2$ and $DDO51$ filters. Figure 3.4 presents the locations of the imaging fields to $R_{proj} \sim 15°$ as boxes properly scaled to their actual footprint. In Figure 3.4, the familiar M 31 disk is entirely within the first concentric ring of $R = 2°$, which demonstrates the full angular extent of the M 31 halo on the sky. We will now summarize the

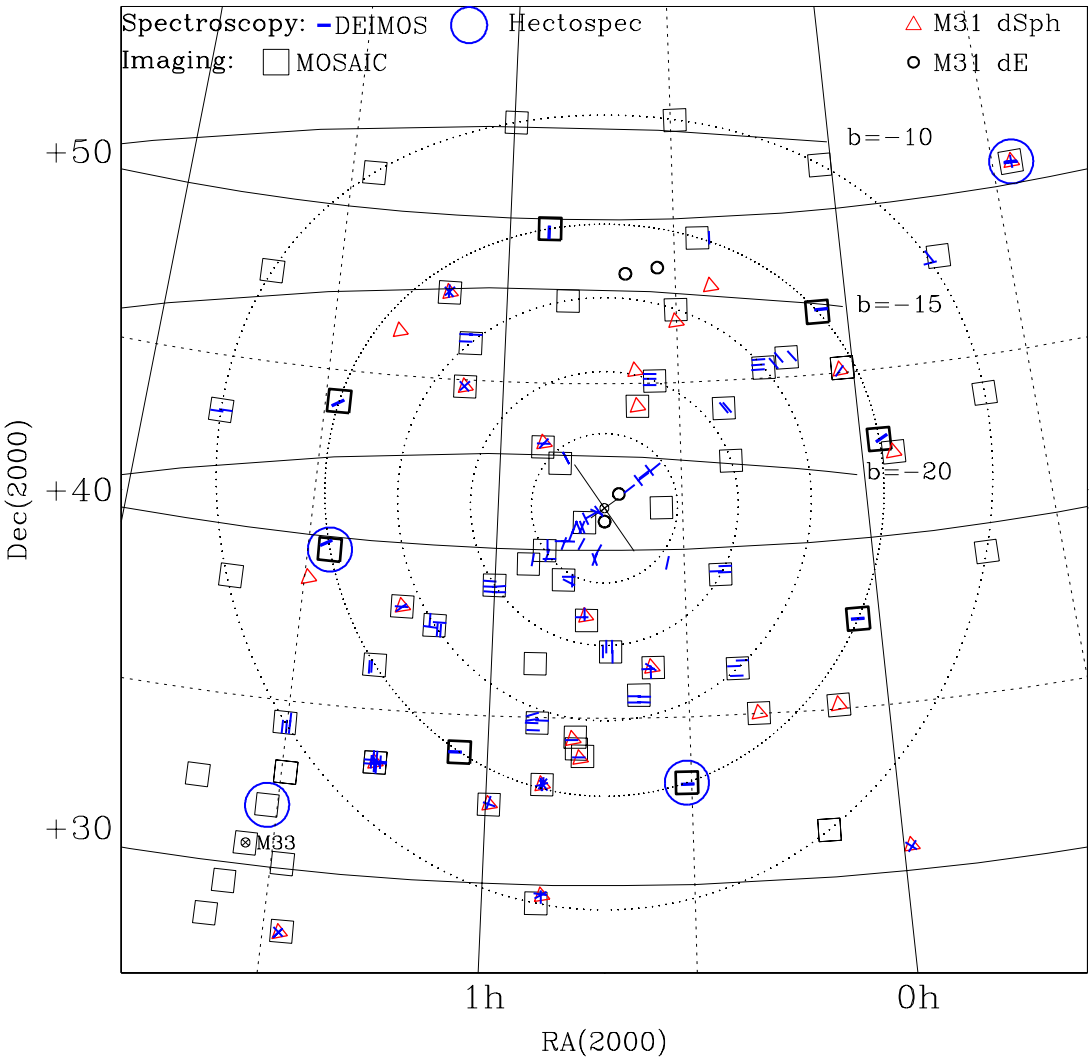

Fig. 3.4.— Map of the M 31 stellar halo as probed by the SPLASH survey. The satellites Andromeda VI and Andromeda XXVIII are not shown due to their large angular separations (ρ=19.8° and ρ=27.9°, respectively; see Figure 3.2a). The full extent of the SPLASH survey, including the KPNO4m+MOSAIC imaging (open boxes), Keck+DEIMOS spectroscopy (blue filled rectangles), and MMT+Hectospec spectroscopy (blue open circles) are given. The footprint of the different telescopes and instruments are to scale, but the symbol size for the globular clusters and dwarf satellites are not. Dashed rings indicate the radii of 2°, 4°, 6°, 8°, and 11°, corresponding to projected distances of 22.5 kpc, 45 kpc, 90 kpc, 120 kpc, and 165 kpc, respectively. Those KPNO4m+MOSAIC imaging fields for the spectroscopic outer halo campaign (see discussion in Section 3.4.1) are highlighted as thick boxes.

general procedures for the observations, image processing, and photometric catalogs required for the photometric arm of SPLASH.

The standard SPLASH imaging survey consists of a set of exposures at each pointing of length 900s, 2×900s and 3×1800s for the M,$T2$ and $DDO51$ filters, respectively. All but the 2010 observing run used the Mosaic 1 instrument, which consisted of eight 2048×4096 CCD chips each with its own amplifier covering an area of 0.36×0.36 degrees. The 2010 observing run used the Mosaic 1.1 instrument, which consists of eight 2048×4096 CCD chips each with two amplifiers covering the same total area. Both Mosaic 1 and Mosaic 1.1 have spatial resolution of $\sim 0.26''$ pixel^{-1}, which was well matched to our best seeing, $0.7''$. Our typical seeing, however, was $\sim 1.0''$. The observations were obtained in overall "good" conditions, but these were not always photometric. When appropriate, we obtained exposures in the Washington+$DDO51$ photometric calibration fields SA98, SA110 and SA114 from Geisler (1990).

Image Processing

Image processing was completed using the standard procedures developed and customized for the Mosaic cameras in the `MSCRED` package of `IRAF`. We generally follow the those techniques developed for the NOAO Deep Wide-Field Survey, which describe in detail each of the steps required to properly reduce these data.[2] Each observation run was reduced independently following the same prescription. Calibration frames, namely biases and dome flats, were acquired nightly but applied to the data as master calibration for each observing run. The readout time for the Mosaic 1 imager was >120 s and thus the nightly calibrations were combined in order to reach appropriate final statistics for the calibrations. After primary flat fielding from the

[2] `h`ttp://www.noao.edu/noao/noaodeep/ReductionOpt/frames.html

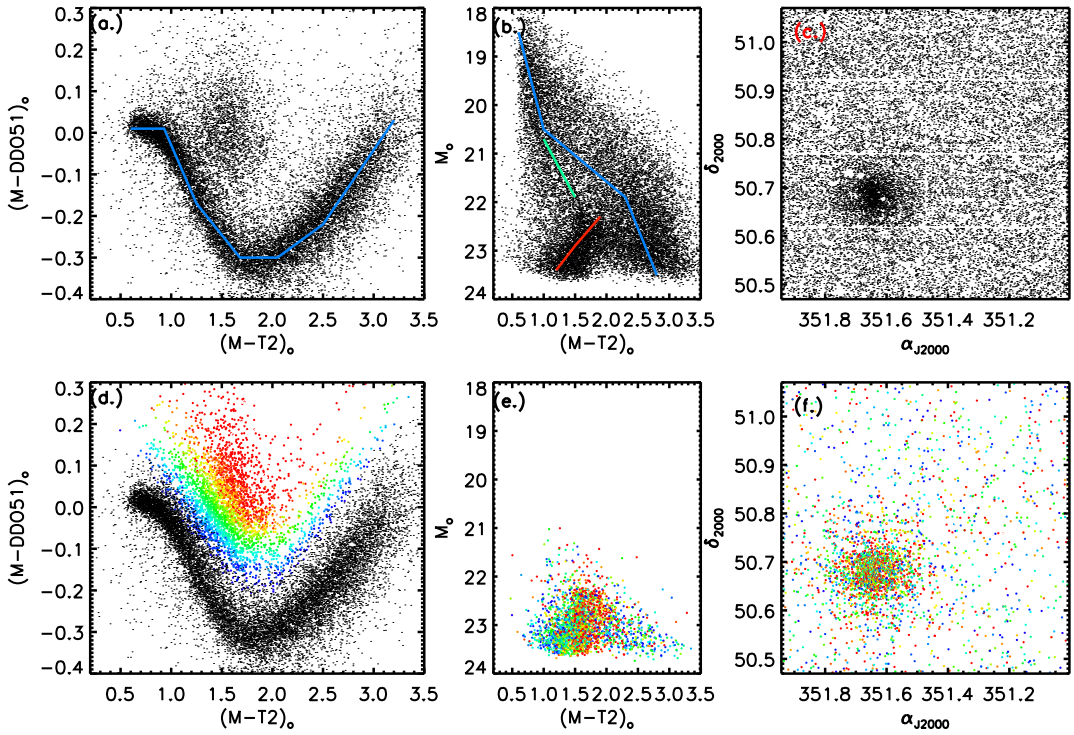

Fig. 3.5.— Demonstration of the dwarf-giant separation technique permitted by our Washington+$DDO51$ imaging for the dwarf satellite galaxy Andromeda VII (R. Beaton, in preparation). **(a)** de-reddened color-color diagram, $(M-T2)_\circ$-$(M-DDO51)_\circ$, emphasizing the two dominant stellar populations in our deep imaging: (i) the foreground MW dwarf "swoosh" (blue schematic) and (ii) the "cloud" of M 31 giant candidates. **(b)** The corresponding color-magnitude diagram, $(M-T2)_\circ$-$M_\circ$, in which the faint end of the MW main sequence (blue schematic) overlaps the magnitudes and colors for the Andromeda VII (and by proxy the M 31) red giant population (red schematic). The green schematic is a main sequence for a MW substructure, Triangulum Andromeda (Majewski et al. 2004). **(c)** The sky distribution of the two populations. **(d)** The color-color diagram as in panel (a), but with the points color coded by their giant probability (*gprob*; Section 3.4.1). Objects on the dwarf "swoosh" have *gprob*=0 (black), where as those in the giant "cloud" have *gprob* increasing proportional to their separation from the "swoosh" (where *gprob*=1 is red). **(e)** The color-magnitude diagram as in panel (b), but those source with *gprob* ∼0 are excluded and the remaining points are color coded as in panel (d). **(f)** The sky distribution as in panel (c), but with the same coding and exclusions as in panel (e). The contrast between the galaxy population and the foreground populations is greatly enhanced and permits photometric pre-selection of likely M 31 red giants at the extremely low surface densities required in the outer halo.

domeflats, inspection of our $DDO51$ frames contained a pupil-ghost image and the $T2$ frames contained significant fringing. Both of these image artifacts were removed in the secondary flat fielding process before the application of 'super sky flats.'

A master pupil image was created by stacking all of the $DDO51$ images obtained over an observing run and using object masks to flag the sources in each image. This master image was then converted into a pupil template using `MSCPUPIL`, which is scaled to and subtracted from each individual $DDO51$ image in the task `RMPUPIL`. The procedure for removing the fringing in the $T2$ frames is similar, except the where the pupil image is concentrated in the center of the field, the fringing covers the full field-of-view. A high signal to noise fringe template was constructed by stacking the object-masked images and a scaled version was subtracted from each individual image using `RMFRINGE`.

The pupil free $DDO51$, fringing free $T2$, and the M images are then stacked by filter, again using custom source masking for each image. The stacks are then smoothed using a 120×120 pixel median filter to remove any small scale spatial gradients. The procedure just described is performed iteratively, as it is often necessary to remove some images used to create the master frames due their specific characteristics, e.g., image artifacts like bright foreground stars or trails from plane crossings. The final smoothed stack is adopted as the 'super sky flat' and applied to the entire image dataset. Astrometric corrections were derived for the M image using the `MSCCMATCH` task, which contains a well measured distortion pattern for the Mosaic instrument. The `MSCCMATCH` routines derive the astrometry relative to stellar sources in the USNOB1 catalog with both reliable photometry and well measured proper motions (Monet et al. 2003, 2002).

Photometry

Our photometry catalogs are created through a series of procedures initially developed by Ostheimer (2003) in the pilot program and subsequently refined for the full SPLASH project. First, point spread functions (PSF) are fit in the software DAOPHOT for each individual chip of Mosaic instrument for each image frame. Generally, we follow the PSF fitting prescription described in the DAOPHOT manual (Stetson 1987). While it is possible to script this process, we found scripting failed frequently for these long exposures with relatively high sky background and the majority of the PSFs were fit to bright, isolated stars by hand. Second, for each pointing we co-add the M, $T2$, and $DDO51$ images after scaling by S/N. Third, we use a custom iterative procedure that detects and subtracts sources in multiple rounds. More specifically, Source Extractor (Bertin & Arnouts 1996) is used detect objects in our stacked image, which are then removed from the image using the source subtraction procedure within ALLSTAR using a PSF fit to the multi-band image stack. Then, the procedure is repeated on the source-subtracted image until no additional sources are detected at a 3.5σ detection threshold. This iterative source finding process ensures that we are able to identify all potential stars in the image and builds a "master" detection list for each pointing. We use ALLFRAME (Stetson 1994) to simultaneously perform PSF fit photometry on each of our individual images for the majority of the objects in our master source list.

The ALLFRAME software was specifically designed to use a master detection list to produce PSF photometry on a series of images of the same pointing. The software will, thus, force fit detections that may not meet the S/N criteria for detection in a single frame, *if* that detection has meets the S/N criteria for the majority of the other frames. This helps to mitigate potential problems due to differences in weather con-

ditions over the $\sim$ 3 hours required to complete a single pointing. Like DAOPHOT, ALLFRAME will also derive the image quality parameters *chi* and *sharp*, that measure the 'fluffiness' and 'contrast' of a source compared to the sky background and detector statistics. Both of these parameters are powerful metrics for either identifying spurious sources like cosmic rays or separating compact, star-like sources from those consistent with extended galaxies. Lastly, the final ALLFRAME photometry is combined with the stellaricity parameters determined by Source Extractor on our deep, all filter stack using a neural net algorithm (Bertin & Arnouts 1996), $flag$ and *prob*, to construct a final catalog of detections.

A major contaminate to our deep photometric catalogs is the population of background galaxies that become a fractionally large population at the magnitudes relevant for M 31 red giant stars (i.e., V, I <20). We intentionally retain the image quality information from both DAOPHOT and Source Extractor because of the complementary morphology measurement goals of either program. The DAOPHOT parameters are explicitly optimized to identify clean samples of stars and the SExtractor parameters optimized to identify galaxies. Thus, by combining the parameters, we hope to mitigate any systematic biases that might influence photometric star-galaxy separation from the use of a single set of image quality metrics.

Individual magnitudes are combined and calibrated for each frame of each pointing using the procedure developed by Siegel (2002) known as `MAGMA`. `MAGMA` uses a set of photometric transformation equations for a set of observations to iteratively solve for color and magnitude across multiple passbands. The transformation equations are given specific to an individual frame, which allows for combining frames taken over multiple nights, multiple observing conditions, and even multiple telescope-instrument combinations. When permitted by the observing conditions, photometric

transformation are derived from standard star fields using the colors and magnitudes for the Washington+$DDO51$ system from Geisler (1990). These fields were selected to span typical color ranges in $M-T2$ and $M-DDO51$ appropriate for study of cool, evolved stars and their separation from foreground main sequence populations of the same spectral type. The transformations are generated using aperture photometry on each standard star and a interactive procedure to fit zeropoints, airmass terms, and color terms for each photometric night. The resulting transformation errors are typically negligible in comparison to the random uncertainties for a given object in our source catalog.

Many fields originally taken in non-photometric conditions were reobserved on photometric nights[3] and then 'bootstrap' calibrated using common stars. `MAGMA` 'bootstraps' non-photometric data to photometric data by averaging magnitudes and colors common to multiple observations and deriving appropriate transformations to tie these fields together. In these cases, the photometric transformation errors are proportional to the number and properties of stars used for the bootstrapping. For those fields without 'bootstrap' reobservation, zeropoints are derived to USNOB1 photometry and combined with fiducial magnitudes for foreground MW features in the color-magnitude and color-color spaces. In both of these cases, the corresponding calibration errors are larger than those of the full calibration procedure and once folded into the final magnitude uncertainty accurately represent the precision of the final reported magnitude.

Once calibrated, magnitudes from individual frames of the same filter are averaged and the resulting errors are the appropriate quadrature sums of the individual magnitude errors. Errors associated with the photometric calibration in each magnitude

[3]Efforts to bootstrap calibrate the SPLASH imaging formed the bulk of the 2010 imaging observations.

are also added in quadrature to errors from the PSF photometry to compute the final reported magnitude error. We use (Schlegel et al. 1998) dust maps to estimate the reddening at the position of each star using transformations to the Washington+$DDO51$ system derived by Majewski et al. (2000).

Figure 3.5a, Figure 3.5b, and Figure 3.5c present an example photometric catalog for the satellite galaxy Andromeda VII (R. Beaton, in preparation). The Andromeda VII field was selected to demonstrate the SPLASH photometry due to its location closest to the Galactic plane ($b \sim -9.96°$), thereby representing the 'worst case' for foreground populations. Moreover, because its stellar constituents are located at a common distance — unlike a generic pointing in the M 31 halo that, for a spherical halo, could sample large line-of-sight depths — its signature in color-color (Figure 3.5a), color-magnitude (Figure 3.5b), and sky distribution (Figure 3.5c) spaces is apparent from visual inspection, while its own extended two-dimensional structure reaches equivalent surface brightnesses to our halo fields at large R_{proj}. Figure 3.5a is the Washington+$DDO51$ color-color diagram, which uses the $(M - T2)_\circ$ color as a proxy for stellar temperature or stellar type and $(M - DDO51)_\circ$ as a proxy for surface gravity or stellar luminosity class. There are two features of note in Figure 3.5a: (i) the foreground MW "swoosh" (highlighted by the blue schematic), and (ii) a "cloud" of red giant stars.

Figure 3.5b is the corresponding color-magnitude diagram for this field, in which the foreground populations (the MW disk is schematically highlighted in blue and a MW halo substructure in green) swamp the target Andromeda VII red giant branch (highlighted in red). While Andromeda VII is of high enough contrast to isolate in color-magnitude space, the contamination from foreground main sequence populations, as is evident in the color-color diagram, cannot constrained. Figure 3.5c

presents the spatial distribution of sources in the Andromeda VII pointing. Andromeda VII can be readily identified due to its relatively high surface density at these magnitudes as an over dense region of stars in the lower left of the panel, but its extended structure at overall lower surface brightness is impossible to constrain given the overall high background. From this discussion, however, the situation can be improved by isolating those stars in the color-color giant "cloud."

Color-Color Selection of RGB Stars

The power of the Washington+$DDO51$ photometry system is in its ability to separate foreground main sequence stars from target evolved stars of the same spectral type (Majewski et al. 2000), which has been crucial for the study of numerous MW halo substructures (including Majewski et al. 2012; Sohn et al. 2007; Muñoz et al. 2006b,a; Westfall et al. 2006; Majewski et al. 2005; Muñoz et al. 2005; Palma et al. 2003; Kundu et al. 2002, among others). The dwarf-giant separation is permitted by the $(M - DDO51)$ color, which is dependent on both the metallicity and temperature of that star. The Washington M and $T2$ filters are used to identify cool stars and the addition of the intermediate-band $DDO51$ filter, which is contained within the broad-band M filter and centered on the surface gravity sensitive MgB spectral feature, permits separation of cool stars by their luminosity class. Thus, the $M - DDO51$ color serves as a efficient tool to clean our photometry samples of foreground MW dwarf contamination on a star by star basis. Unlike many of the previously listed applications of the Washington+$DDO51$ system to MW halo substructure — objects whose stellar sequences are at nearly identical distances and are thereby relatively easy to isolate as demonstrated for Andromeda VII in the previous section — our purpose is to probe the large and primarily diffuse M 31 stellar halo, which in any

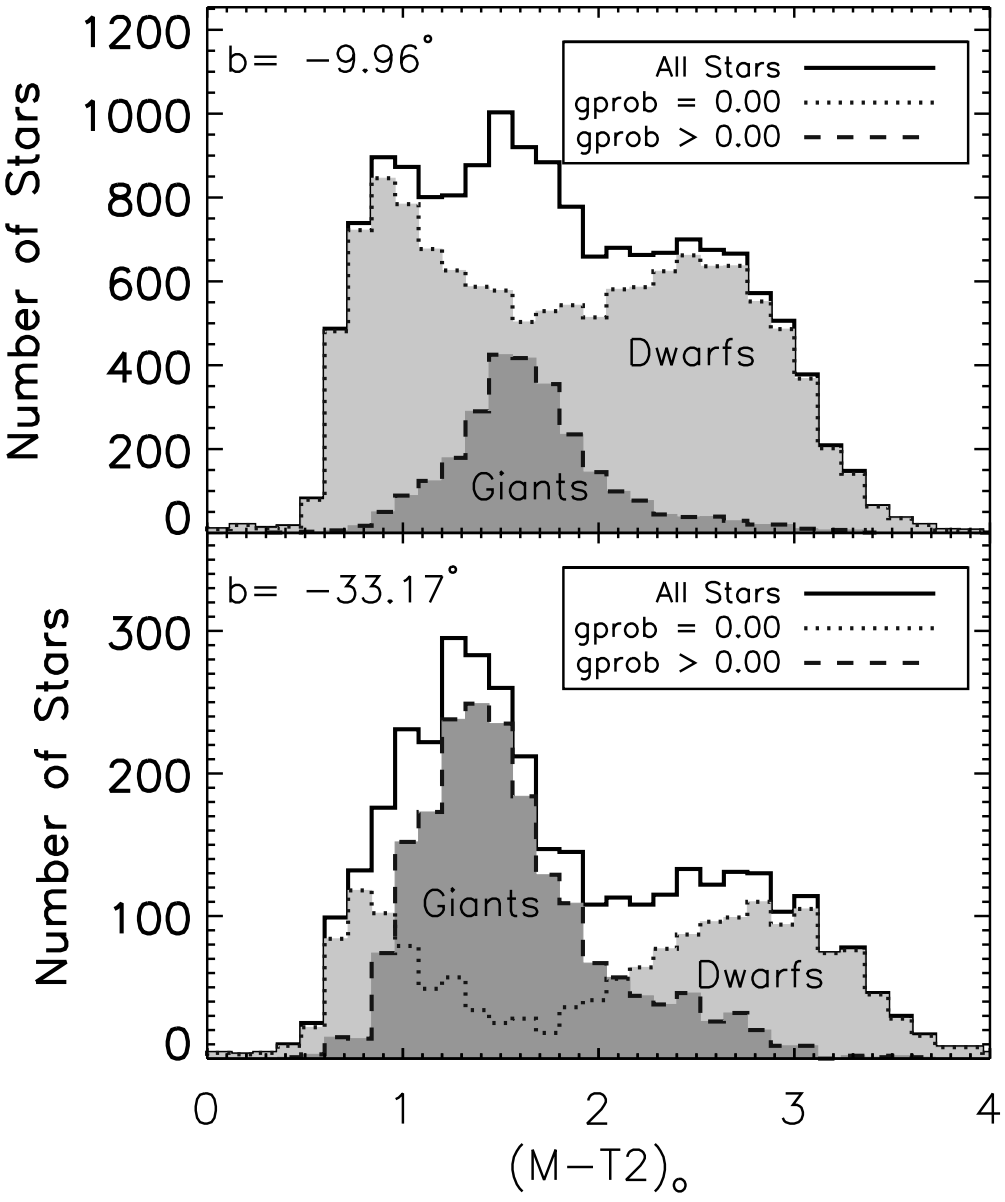

Fig. 3.6.— Demonstration of dwarf giant separation as a function of $M-T2$ color for two dwarf Spheroidal fields, Andromeda VII (top) and Andromeda XIV (bottom), in the SPLASH footprint (R. Beaton, in preparation). These two satellites were chosen because they have overall similar numbers of red giant stars and are located near the Galactic latitude extremes of the SPLASH survey coverage (b=-9.96° and b=-33.17°, respectively) and thereby demonstrate the level of foreground contamination present across the survey fields.

given field spans a large line-of-sight depth. Thus, we require a generalized dwarf-giant separation criteria for application to halo fields and we derive a photometric giant probability, *gprob*, for each detection based on its location in the color-color diagram. This parameter, described below, is the primary means by which we separate giants and dwarfs in our photometry catalogs.

The *gprob* parameter is derived using the $(M-T2)_\circ$, $(M-DDO51)_\circ$ color of a source and a fiducial MW dwarf sequence in color-color space. For each star, we first estimate the distance between a specific star and the point on a fiducial dwarf sequence at the same $(M-T2)_\circ$ color. We then derive color errors, $\sigma_{(M-T2)}$, $\sigma_{(M-DDO51)}$, as the quadrature sum of the errors in each individual magnitude (e.g., $\sigma_{(X-Y)} = \sqrt{\sigma_X^2 + \sigma_Y^2}$). Then, we convert the ($M-T2$, $M-DDO51$) point into a probability distribution defined as a two-dimensional Gaussian centered on the point with standard deviations equal to the color errors ($\sigma_{(M-T2)}$, $\sigma_{(M-DDO51)}$) The final value is calculated for each star by convolving the probability distribution for the star centered on its $(M-T2)_\circ$, $(M-DDO51)_\circ$ position (with the same probability distribution) shifted to the fiducial location of the MW dwarf sequence. An uncertainty, σ_{gprob}, is estimated for each detection based on the uncertainties associated with the individual numerical integrations and calculations. The *gprob* values range from 0 to 1.0, where $gprob = 0$ is a star that falls on the dwarf locus and $gprob \geq 0.0$ has some chance of being a giant. Stars with $gprob = 1.0$ are the most "secure" giants and are located far from the dwarf locus in color-color space.

In Figure 3.5d, we demonstrate the derivation of *gprob* by color-coding the star-like sources in Andromeda VII in the $((M-T2)_\circ, (M-DDO51)_\circ)$ color-color diagram. We note that the MW dwarf locus forms an easily identifiable "swoosh" that shows only minor deviations across the wide range of Galactic latitudes covered in the

SPLASH M 31 halo survey (see Figure 3.4). As shown in Figure 3.5d, *gprob* is a smooth distribution moving away from the dwarf "swoosh." The most secure giants, *gprob* $\sim$ 1.0 are located near the center of the giant "cloud." Unfortunately, objects with very red $(M - DDO51)_\circ$ colors ($(M - DDO51)_\circ \geq 0.25$) and likely to be background galaxies, are automatically classified as "secure giants" by our system, but are easily removed by applying an upper limit to the permitted $(M - DDO51)$ color. We note that, for emphasis, we have manipulated the order of points plotted such that *gprob* =0.0 are overplotted on the *gprob* > 0.0 points to demonstrate the highest contrast between the two features.

Figures 3.5e and 3.5f present a visualization of our giant probability, *gprob*, parameter, color-coded identically to Figure 3.5d, both in color-magnitude space (Figure 3.5e) and distribution on the sky (Figure 3.5f), but with all dwarf-like objects (*gprob*<0.1) removed. Figure 3.5f demonstrates the distribution of targets identified as probable giants in color-magnitude space. As expected, the majority of the red giants are fainter than $M \sim 21.5$ consistent with red giants at M 31 distance ($m - M = 24.4$), and over a large range in $(M - T2)_\circ$. The distribution of probable giants in 3.5e do not show the same smooth *gprob* distribution as noted in Figure 3.5d. This indicates the potential for missed giants from choosing around the over dense portion color-magnitude space alone, i.e., explicitly selecting the red giant sequence in 3.5b. Figure 3.5f demonstrates the spatial distribution of targets identified as probable red giants. The *gprob* parameter is not sensitive to spatial distribution and thereby represents a robust means of tracing M 31 giant populations to low stellar density.

The Andromeda VII field is located relatively near the MW disk (b=-9.96°) and one could argue that the foreground populations drop off dramatically as the angular

distance from the disk increases. To explore this concern, we compare the foreground dwarf and target giant populations, as classified by *gprob*, for the Andromeda VII field previously discussed and Andromeda XIV located at the opposite extreme in the SPLASH Galactic latitude coverage (b=-33.17°; Majewski et al. 2007). Figure 3.6 presents a marginal distribution of the $(M-T2)_\circ$ color for star-like sources in the Andromeda VII and Andromeda XIV Mosaic pointings as compared to those for likely dwarfs and likely giants as classified by *gprob*. Even at our most extreme Galactic latitude, the foreground dwarf population has a not insignificant contribution to the total number of source for all $M-T2$ colors.

The M 31 Outer Halo Campaign

The goal of the present work is to constrain the transverse motion of the M 31 center-of-mass using its variable projection along widely separated lines-of-sight. As shown in Figure 3.1a, the projection effect for v_t is strongest for those sight lines at large angular separations (ρ), but the direction of the motion (Θ_t) is best constrained by sampling the azimuthal (ϕ) variations of the effect as shown in Figure 3.1b. To gain the best constraints on the transverse motion, any new spectroscopic data obtained for this purpose should be at large angular separation, which requires identification of M 31 red giants at extremely low surface brightnesses (Gilbert et al. 2012). Fortunately, this situation is precisely where the Washington+$DDO51$ dwarf-giant selection is most powerful. The SPLASH survey — with a demonstrated record of high efficiency spectroscopic follow up to 32 mag arcsec^2 — is uniquely poised to measure the transverse motion of M 31. Unfortunately, the Gilbert et al. (2012) spectroscopic coverage for R_{proj}>6° (90 kpc) is sparse in total number of both the confirmed M 31 members and in azimuths sampled. Thus, we undertake a campaign to improve the

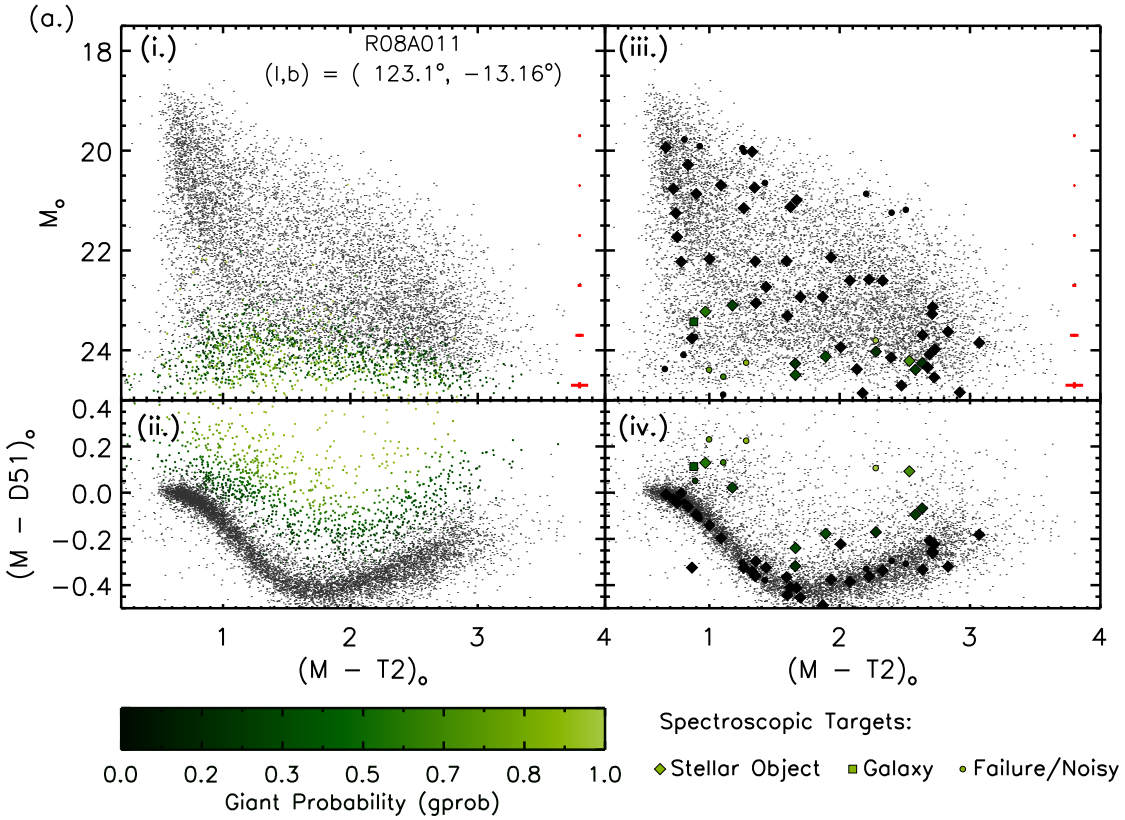

Fig. 3.7.— Washington+$DDO51$ photometry (panels i and ii) and spectroscopic target selection (panels iii and iv) for the eight new Keck+DEIMOS masks at 120 kpc (the R08 ring): **(a)** R08A011, **(b)** R08A071, **(c)** R08A101, **(d)** R08A149, **(e)** R08A197, **(f)** R08A250, **(g)** R08A281, **(h)** R08A311. In each of the sub-figures a-h the panels are as follows: **(i)** Color magnitude diagram color coded by the giant probability, or *gprob*, as indicated by the color bar at the lower left. The mean color and magnitude errors are indicated by the thick red pluses on the left for the range of magnitudes spanned by the diagram. **(ii)** Color color diagram color coded by *gprob*. **(iii)** Color magnitude diagram with all star-like sources as black points and the spectroscopic targets indicated by larger symbols. Those objects spectroscopically classified as failures or too noisy for measurement are filled circles, those objects classified as galaxies are filled squares, and stellar objects are filled diamonds. Each target symbol is color coded by its *gprob* value. **(iv)** Color-color diagram with symbols as in panel (iii). The need to "fill" masks with sources often leads to inefficient targeting at these low stellar densities (as compared to the stellar density of Andromeda VII in Figure 3.5).

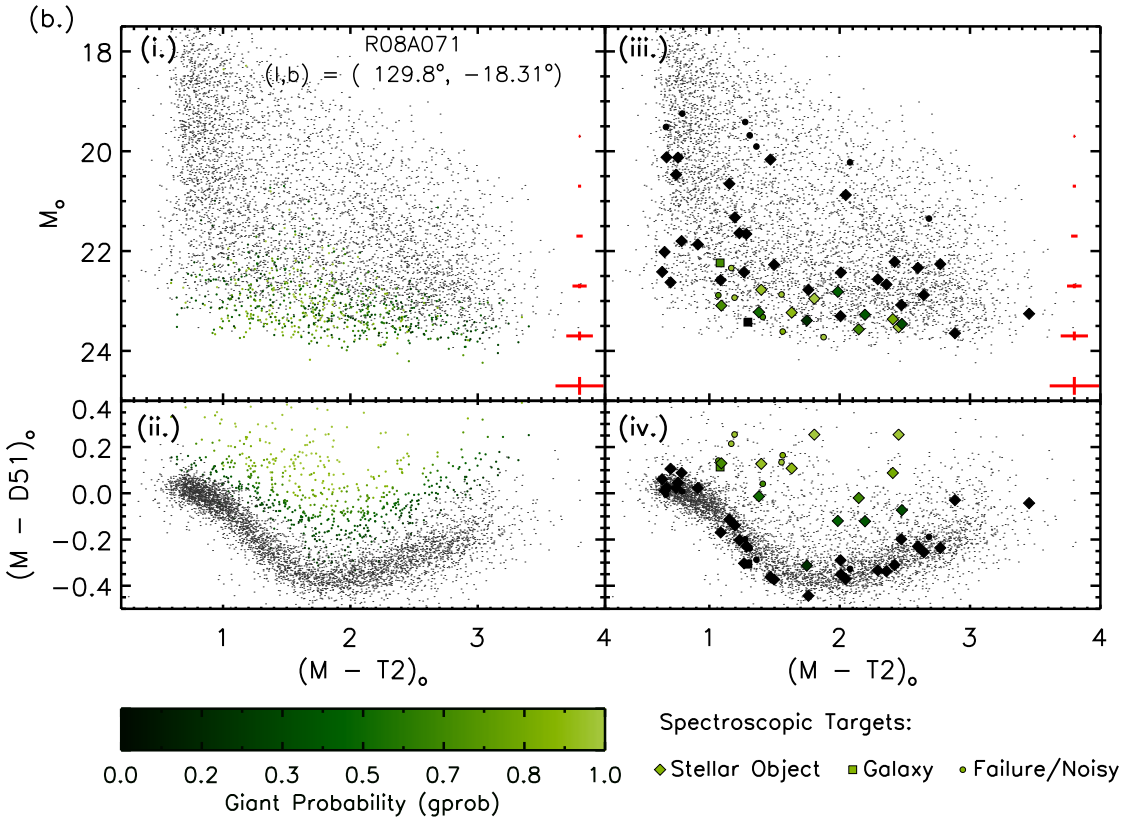

Fig. 3.7.— cont. — Washington+$DDO51$ photometry and spectroscopic target selection for R08A071.

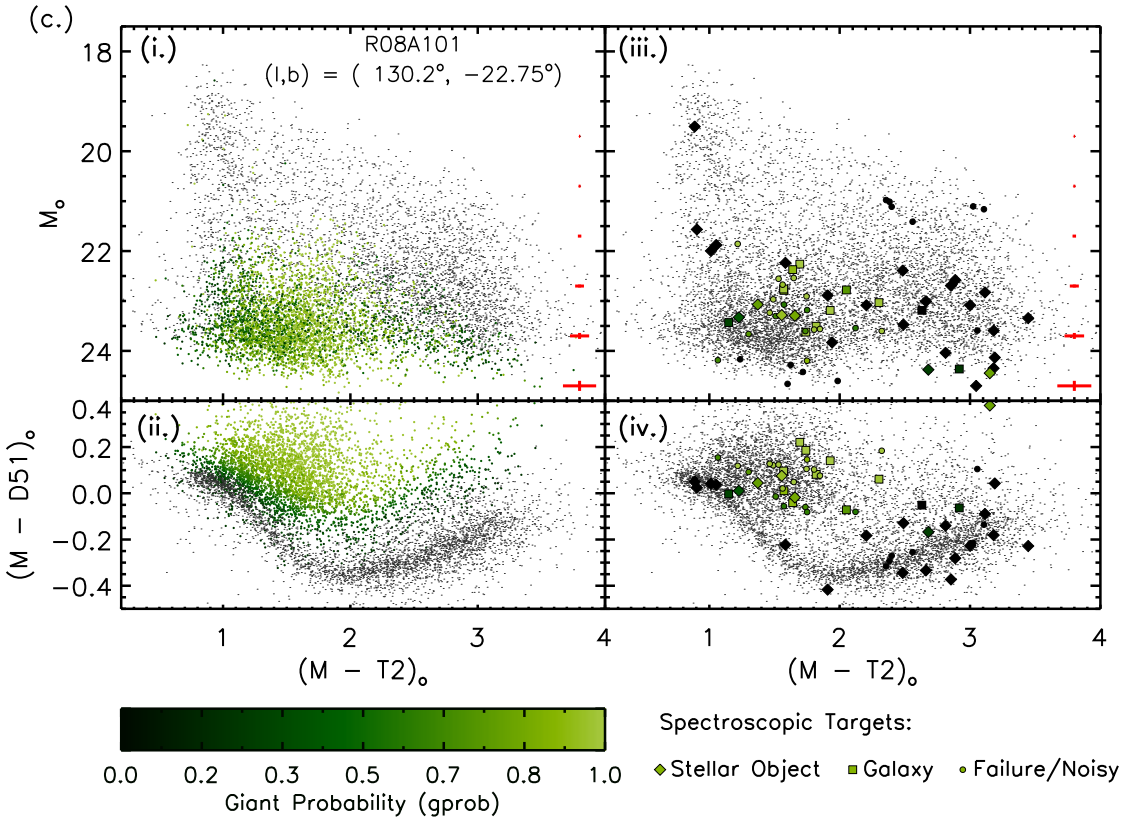

Fig. 3.7.— cont. — Washington+$DDO51$ photometry and spectroscopic target selection for R08A101.

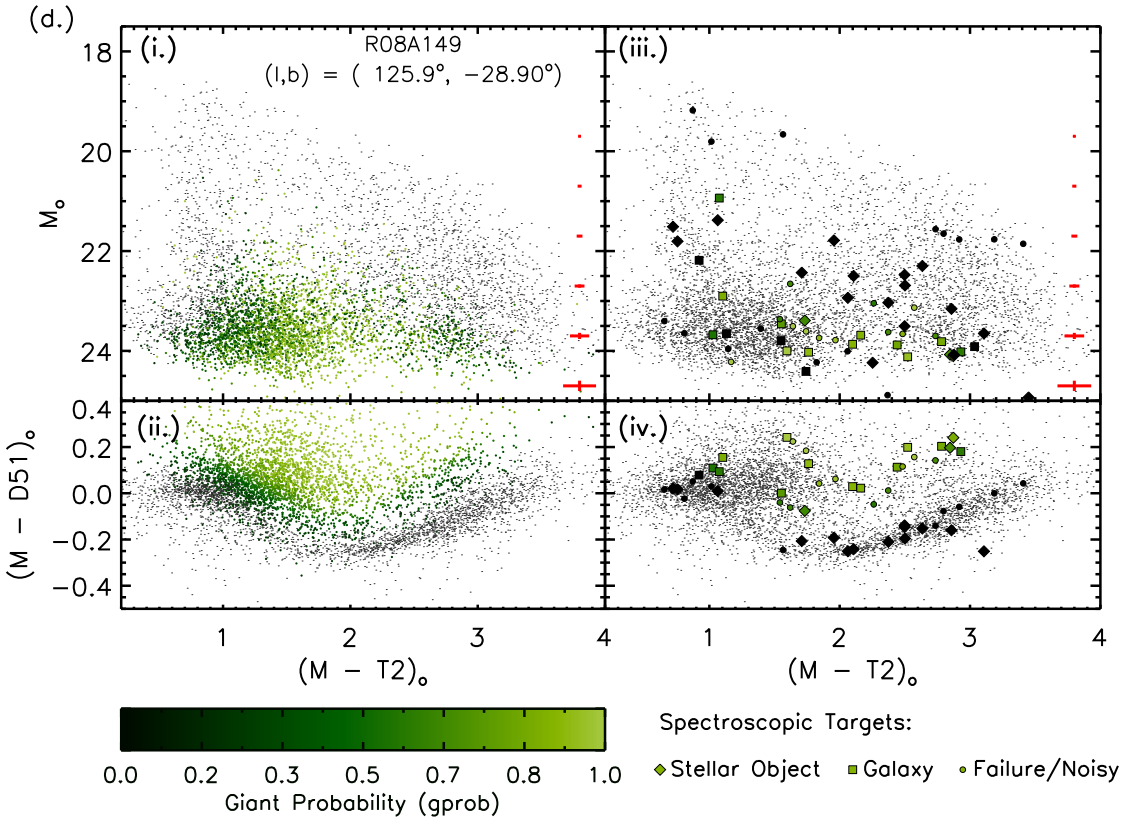

Fig. 3.7.— cont. — Washington+$DDO51$ photometry and spectroscopic target selection for R08A149

number of confirmed M 31 red giants beyond R_{proj}>6° (90 kpc), choosing to focus our resources on an 8° ring, hereafter referred to as 'R08', which samples a physical radius $R_{proj} \sim 120$ kpc or 40% of R_{virial}.

From inspection of Figure 3.4, there are a number Mosaic fields in the 'R08' ring in the SPLASH survey with an average azimuthal spacing of $\Delta\phi \approx 30°$. A total of ten halo fields, e.g., those fields without a known dwarf satellite, have been completed and those are, in order of azimuthal angle measured as the position angle from the M 31 major axis: R08A011, R08A071, R08A101, R08A149, m8 R08A197, R08A250, R08A281, R08A311, and R08A341. The coordinates and observation conditions for the imaging observations of these fields is given in Table 3.2. Pursuant to the goals of this work, we present the photometry only for those fields with new spectroscopic observations and the data products required to discuss those observations. Exploration of the M 31 'R08' ring using only photometric giant selection is beyond the scope of the work presented here.

The panels of Figure 3.7 and Figure 3.8 present the photometry catalogs for the eight 'R08' fields that were targeted with new spectroscopic observations. In each of the sub-figures, a-h for Figure 3.7 and a-b for Figure 3.8, panel (i) is the $(M-T2)_\circ$-$M_\circ$ color magnitude diagram with the average color and magnitude errors shown by the red crosses for a range of magnitudes, and panel (ii) is the $(M-T2)_\circ - (M-DDO51)_\circ$ color color diagram[4]. In both panels, the star-like sources are color coded by their giant probability (*gprob*) as indicated in the color bar. The majority of the visible differences in the color-magnitude (and by proxy color-color) diagrams are due to the variable observing conditions (and by proxy the resulting image fidelity and photometric depth) and not necessarily due to variations in the MW foreground or the M 31 red giant stars.

[4]Panels (iii) and (iv) will be discussed in later sections.

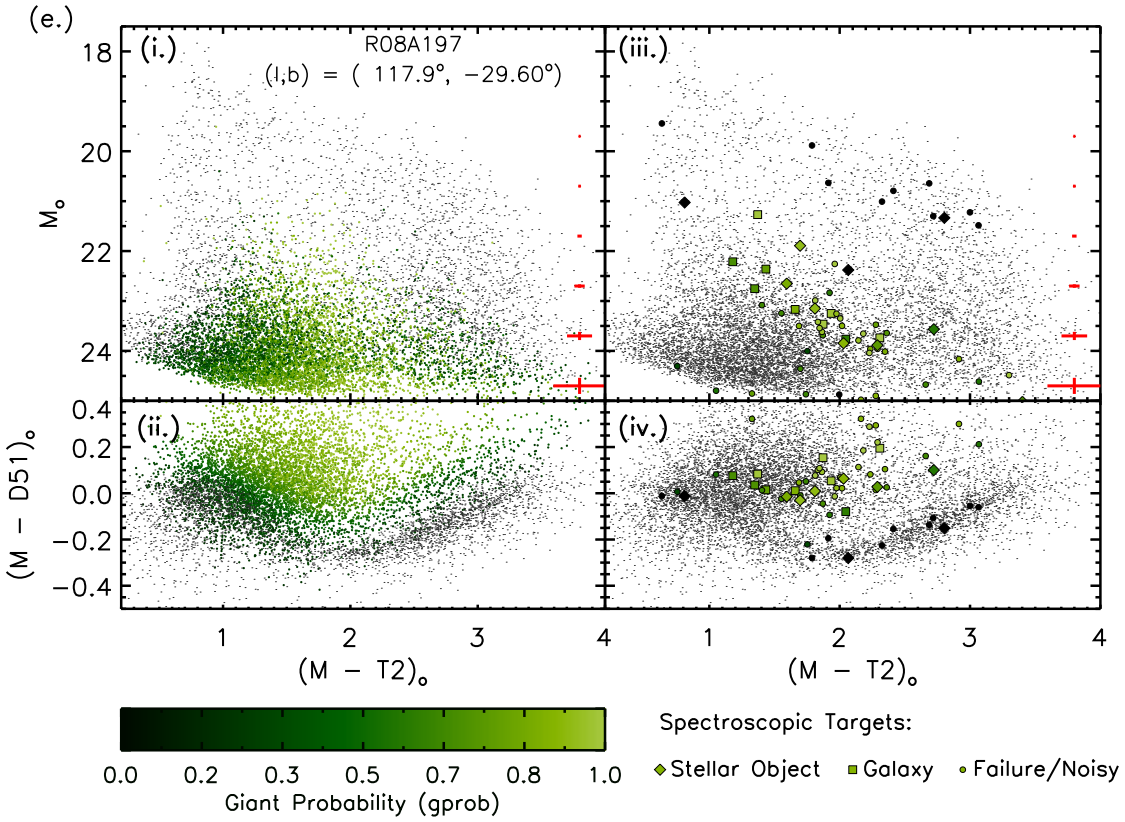

Fig. 3.7.— cont. — Washington+$DDO51$ photometry and spectroscopic target selection for R08A197.

3.4.2 Keck+DEIMOS Observations

The selection of targets, observations, image processing, and, finally, the spectroscopic analyses are now described.

Targeting

Photometric data for Keck+DEIMOS observations come from a variety of sources. The bulk of the observations were obtained with the Mosaic Camera on the Kitt Peak National Observatory (KPNO) 4 m Mayall telescope. The photometric catalogs are in the Washington+$DDO51$ photometric system, which combines the sensitivity to cool, late type stars of the Washington M and T_2 filters with the intermediate band $DDO51$ filter (Majewski et al. 2000). The $DDO51$ filter spans the Mg b Triplet, a spectral feature sensitive to stellar surface gravity and, when paired with the broadband M filter, is able to separate stars in the dwarf and giant luminosity classes for the same spectral type. The native M and T_2 magnitudes were transformed into V and I following the conversion relations derived in Majewski et al. (2000).

The thirty-nine fields adopted from Gilbert et al. (2012) contains several masks that did not use the SPLASH Washington+$DDO51$ catalogs previously described. The photometry in several of the inner fields (R_{proj} <30 kpc; f109, H11, f116, F115, f206, f135, f125, f130, mask4, and H13s) were derived from observations with the MegaCam instrument on the 3.6 m CFHT[5]. The imaging was acquired in g' and i' filters and the photometric catalogs were transformed to the Johnson-Cousins V and I system using observations of Landolt photometric standards stars as described by Kalirai et al. (2006). The photometry in the Andromeda X field was derived from V

[5]Based on observations obtained with MegaPrime/MegaCam, a joint project of CFHT and CEA/DAPNIA, at the Canada-France-Hawaii Telescope (CFHT) which is operated by the National Research Council (NRC) of Canada, the Institute National des Sciences de l'Univers of the Centre National de la Recherche Scientifique of France, and the University of Hawaii.

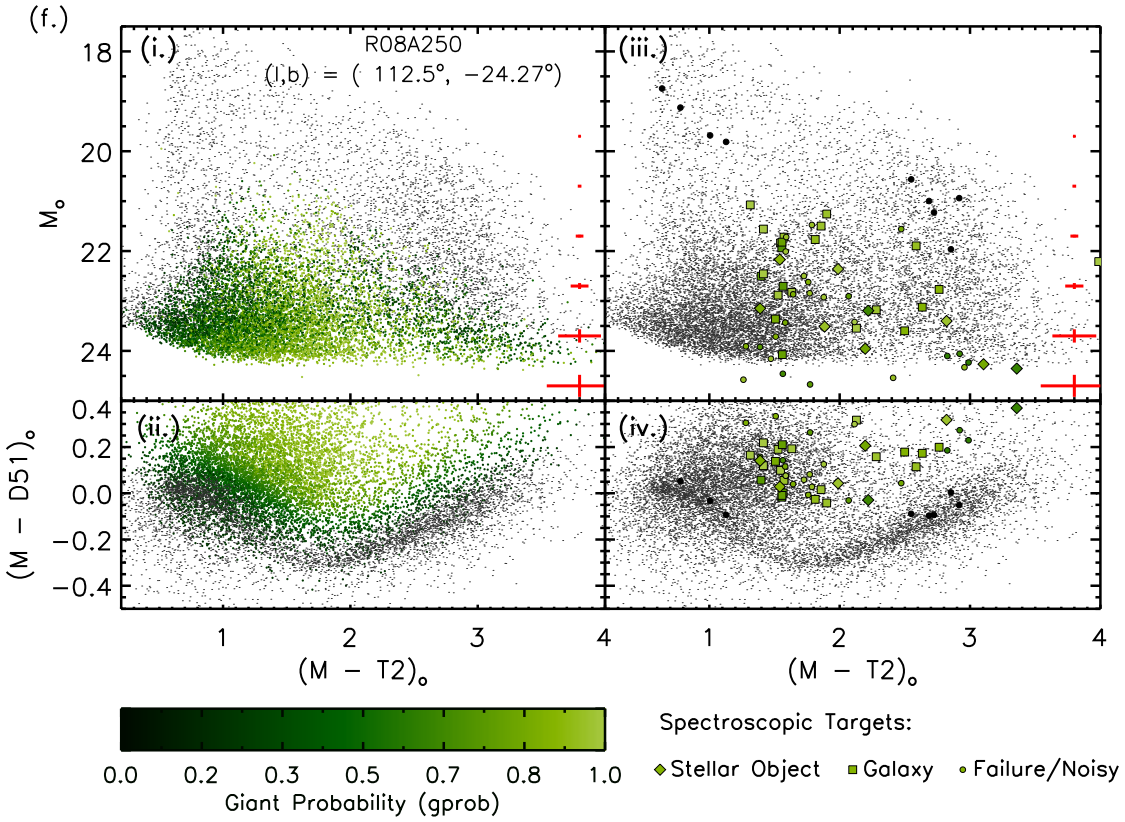

Fig. 3.7.— cont. — Washington+$DDO51$ photometry and spectroscopic target selection for R08A250.

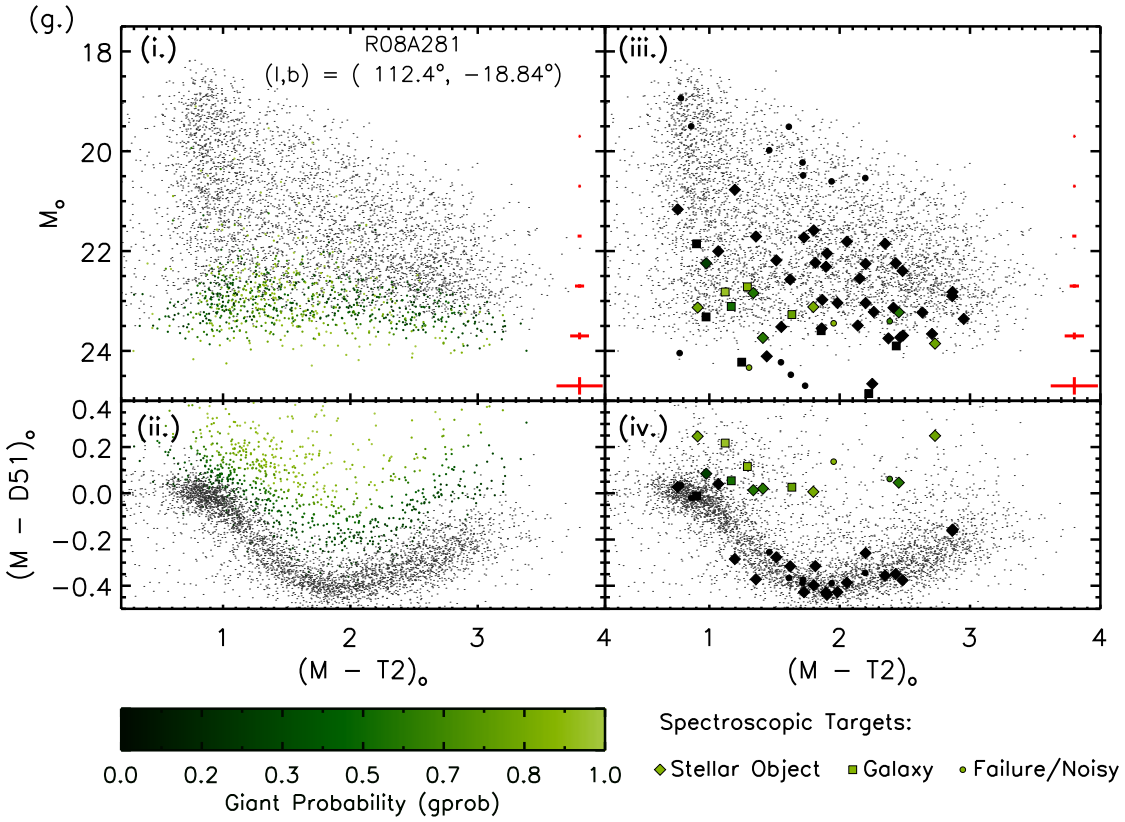

Fig. 3.7.— cont. — Washington+$DDO51$ photometry and spectroscopic target selection for R08A281.

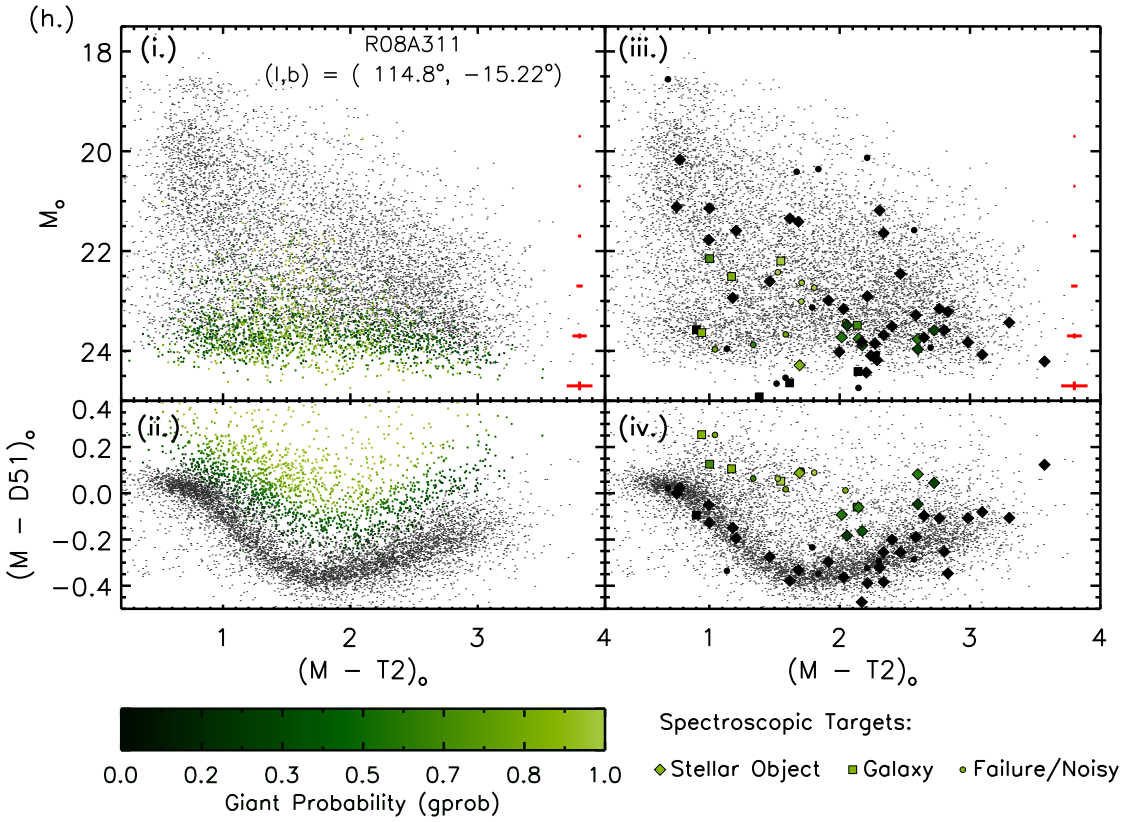

Fig. 3.7.— cont. — Washington+$DDO51$ photometry and spectroscopic target selection for R08A311.

and I images on the William Hershel Telescope (Zucker et al. 2007; Kalirai et al. 2010). Photometry for the fields "streamE" and "streamF" was obtained from V and I imaging obtained with the SuprimeCam instrument on the Subaru Telescope (Tanaka et al. 2010). Washington+$DDO51$ photometry was acquired after the spectroscopic observations for the Andromeda X, streamE and streamF fields and are used for the analyses presented here.

Seventeen fields were used in Tollerud et al. (2012), thirteen of which were included or partially included in Gilbert et al. (2012). Targeting photometry for Andromeda XI, XII, XV, and XVI was obtained via archival MegaCam images from the CFHT in the g' and i' filters. Targeting photometry for Andromeda XVIII and Andromeda XXII were obtained from B and V imaging obtained from the LBC cameras on the Large Binocular Telescope[6]. Washington+$DDO51$ imaging were obtained for all seventeen fields in Tollerud et al. (2012) and used to derive V and I magnitudes for all of the spectroscopic targets. The photometry for the two fields of Tollerud et al. (2013), Andromeda XXVIII and XIX, were obtained from the Sloan Digital Sky Survey in the g' and i' photometric bands (Aihara et al. 2011). The g' and i' magnitudes were converted to V and I following the transformation equations of Lupton (2005)[7].

The above photometric catalogs were used to design spectroscopic slitmasks for use in the DEIMOS spectrograph on the Keck II 10 m telescope (Faber et al. 2003). The full mask design process is detailed in Guhathakurta et al. (2006). The field of view for a DEIMOS mask is $16.7' \times 5'$, an area which is significantly smaller than our wide-

[6]The LBT is an international collaboration among institutions in the United States, Italy and Germany. LBT Corporation partners are: The University of Arizona on behalf of the Arizona university system; Istituto Nazionale di Astrofisica, Italy; LBT Beteiligungsgesellschaft, Germany, representing the Max-Planck Society, the Astrophysical Institute Potsdam, and Heidelberg University; The Ohio State University, and The Research Corporation, on behalf of The University of Notre Dame, University of Minnesota and University of Virginia.

[7]`https://www.sdss3.org/dr8/algorithms/sdssUBVRITransform.php`

field imaging catalogs (~ 0.5 deg^2). Spatial placement and orientation of each mask was driven by considerations required to maximize the success of the observations, e.g. a location with and overall high density of star-like detections within the magnitude and color range and with appropriate bright alignment stars ($I \sim 18$). For satellite and stream fields, however, masks were placed on the over dense portion of the spatial distribution. Generally, the photometric catalogs were of sufficient dynamic range to include appropriate alignment stars on the same astrometric system, typically that of the USNOB1 (Monet et al. 2003, 2002).

Each star in the photometric catalog is given a spectroscopic priority based on the I magnitude, $V - I$ color, and *gprob* (described in previous section). For masks in the inner regions (R_{proj}<30 kpc) and for many satellite targets, the stellar density of high probability targets was sufficient to fill the ∼100 slits on each mask — even without *gprob*. In the outer regions (R_{proj}>30 kpc), however, higher numbers of low priority targets or intentionally selected filler targets were selected. Often these filler targets were potential members of the Triangulum Andromeda overdensity (Majewski et al. 2004; Rocha-Pinto et al. 2004; Sheffield et al. 2014; Deason et al. 2014, among others), which is depicted by the green schematic line in Figure 3.5.

Observations

Spectroscopic observations with Keck+DEIMOS were acquired over eleven observing seasons from 2002 to 2012 using the 1200 line mm^{-1} grating with a dispersion of 0.33 $\AA$ pixel^{-1}. The slit width of 1″ yields a resolution of 1.6 $\AA$ FWHM. The typical spectral range is 6450-9150 $\AA$. This wavelength range includes the Ca II triplet absorption feature at 8500 Åand the Na I absorption feature at 8190 $\AA$. The normal exposure time is 1 hour each, with modifications made appropriate to the specific observing

conditions. The deviations from the normal procedure described here are detailed in the original publications for individual fields and masks (Tollerud et al. 2012; Gilbert et al. 2012; Tollerud et al. 2013, and references therein).

Eight fields at 120 kpc ('R08' ring) were acquired with Keck+DEIMOS specifically for the tangential motion measurement. These were obtained under good conditions over two half nights on UT 08/02/2011 and UT 08/03/2011 under good to exceptional conditions. A log for the eight fields newly acquired for this work is given in Table 3.3. The target selection, described in the previous subsection, is demonstrated for each field by large symbols color coded by *gprob* in Figures 3.7a-h in sub-panels (iii) and (iv) for color-magnitude and color-color space respectively.

Data Processing

The spectra were reduced using custom modified versions of the `spec2d`[8] and `spec1d` software packages developed at the University California, Berkeley for application to DEIMOS data in the DEEP2 Survey (Davis et al. 2003; Newman et al. 2013; Cooper et al. 2012). The `spec2d` software handles all of the image level pre-processing, including flat-fielding, night-sky emission line subtraction, a two-dimensional wavelength solution, and extraction of one-dimensional spectra from the two-dimensional spectral data. The `spec1d` software handles all of the spectral processing, more specifically the cross-correlation to measure redshifts for individual spectra. The cross-correlation library includes stellar spectra for a wide range of luminosity and spectral types obtained with DEIMOS and galaxy spectra from the Sloan Digital Sky Survey (see discussion in Simon & Geha 2007).

Each spectrum and its `spec1d` redshift is visually inspected for its quality and given a rating based on the reliability of the measurement (this procedure is described

[8] `http://deep.ps.uci.edu/spec2d`

in detail by Gilbert et al. 2007). The rating, known as *zquality*, is an integer flag which is assigned as follows:

1. $zquality = -2$ for those stars used for mask alignment (in $4'' \times 4''$ boxes),
2. $zquality = -1$ for failures in the spectral extraction or image processing,
3. $zquality = 0$ for a galaxy spectrum,
4. $zquality = 1$ for redshifts that are manually refit,
5. $zquality = 2$ for spectra that are too noisy for a reliable redshift,
6. $zquality = 3$ for spectra with a redshift based on two stellar absorption features, and
7. $zquality = 4$ for spectra with a redshift based on three or more stellar absorption features.

Once classified, the correction of the Earth's orbital motion into the heliocentric frame is calculated based on the mean MJD of the observations. A correction for slit-centering errors is determined for each one-dimensional spectrum by comparing the observed position of the atmospheric A-band relative to the night sky emission lines (Simon & Geha 2007; Sohn et al. 2007).

Repeat measurements of individual objects were used to estimate a systematic velocity uncertainty of 2.2 km s^{-1} (Simon & Geha 2007; Kalirai et al. 2010; Tollerud et al. 2012). Random uncertainties for those data from Gilbert et al. (2012) are taken directly from the `spec1d`, whereas those from Tollerud et al. (2012), Tollerud et al. (2013) and the new data acquired here in the R08 ring were derived from a Monte Carlo spectral re-visualization technique described in Tollerud et al. (2012). The total uncertainty is the quadrature sum of the systematic and random uncertainty.

For the new observations presented in this work, a total of 578 objects were observed over the 8 masks, of which 328 redshifts were successfully measured and 285 of these were of stellar type. These statistics, broken down for individual masks, are given in Table 3.3. In the targeting sub-panels of Figures 3.7a-h, the large symbols denoting the spectroscopic targets are coded by *zquality*, where circles are those objects with no reliable redshift (*zquality*= -2,-1,1, or 2), squares are galaxies (*zquality*=0), and diamonds are stellar objects (*zquality*=3 or 4). With the new observations folded into those in previous works, the final Keck+DEIMOS spectroscopic dataset includes 53 unique fields, 128 individual DEIMOS masks, and is comprised of 6451 individual stellar spectra from $R_{proj} = 0.5°$ to $R_{proj} = 27.9°$.

3.4.3 MMT+Hectospec Observations

In supplement to the Keck+DEIMOS observations, spectroscopic data were acquired using the MMT+Hectospec for fields beyond R_{proj} =100 kpc. Hectospec is a fiber-fed optical spectrograph made for the f/5 system of the MMT 6.5 m telescope with a 1° diameter field-of-view and 300 optical fibers arranged in a "fisherman on the pond" geometry (Fabricant et al. 2005). The large field-of-view and 300-object multiplexing is well matched to the Washington+*DDO*51 $36' \times 36'$ and the anticipated density of M 31 halo members at large projected radii ($>\approx 30$ deg^{-2} Gilbert et al. 2006, 2012). The MMT primary aperture is 6.5 m in diameter resulting in a collecting area that is a factor of 2.4 times smaller than that of Keck II. In addition, the optical fibers travel a distance of 26 m from the telescope to the optical bench with an average throughput of 77% (Fabricant et al. 2005). For observations at equivalent spectral resolution, equivalent signal-to-noise as the Keck+DEIMOS observations would be obtained in at total integration ∼3.1 hours with MMT+Hectospec. Thus, the trade-

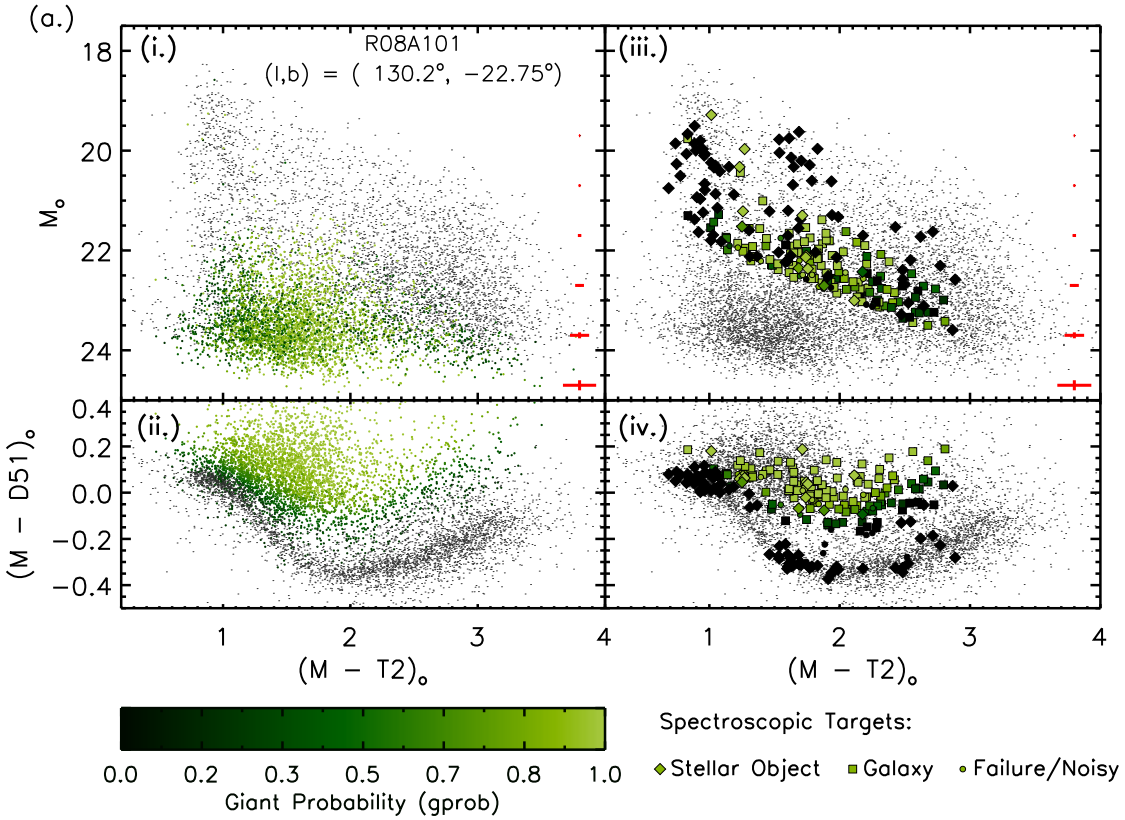

Fig. 3.8.— Washington+$DDO51$ photometry (panels i and ii) and spectroscopic target selection (panels iii and iv) for the new MMT+Hectospec observations at R_{proj}=120 kpc (the R08 ring): **(a)** R08A101 and **(b)** R08A197. In each of the sub-figures the panels are as follows: **(i)** Color magnitude diagram color coded by the giant probability, or *gprob*, as indicated by the color bar at the lower left. The mean color and magnitude errors are indicated by the thick red pluses on the left for the range of magnitudes spanned by the diagram. **(ii)** Color color diagram color coded by *gprob*. **(iii)** Color magnitude diagram with all star-like sources as black points and the spectroscopic targets indicated by larger symbols. Those objects spectroscopically classified as failures or too noisy for measurement are filled circles, those objects classified as galaxies are filled squares, and stellar objects are filled diamonds. Each target symbol is color coded by its *gprob* value. **(iv)** Color-color diagram with symbols as in panel (iii). The combination of a larger field-of-view (∼1°) and larger number of targets per configuration, result in broader color and magnitude coverage, albeit at a shallower magnitude limit ($T2 \sim 21.0$) then those of Keck+DEIMOS (Figure 3.7).

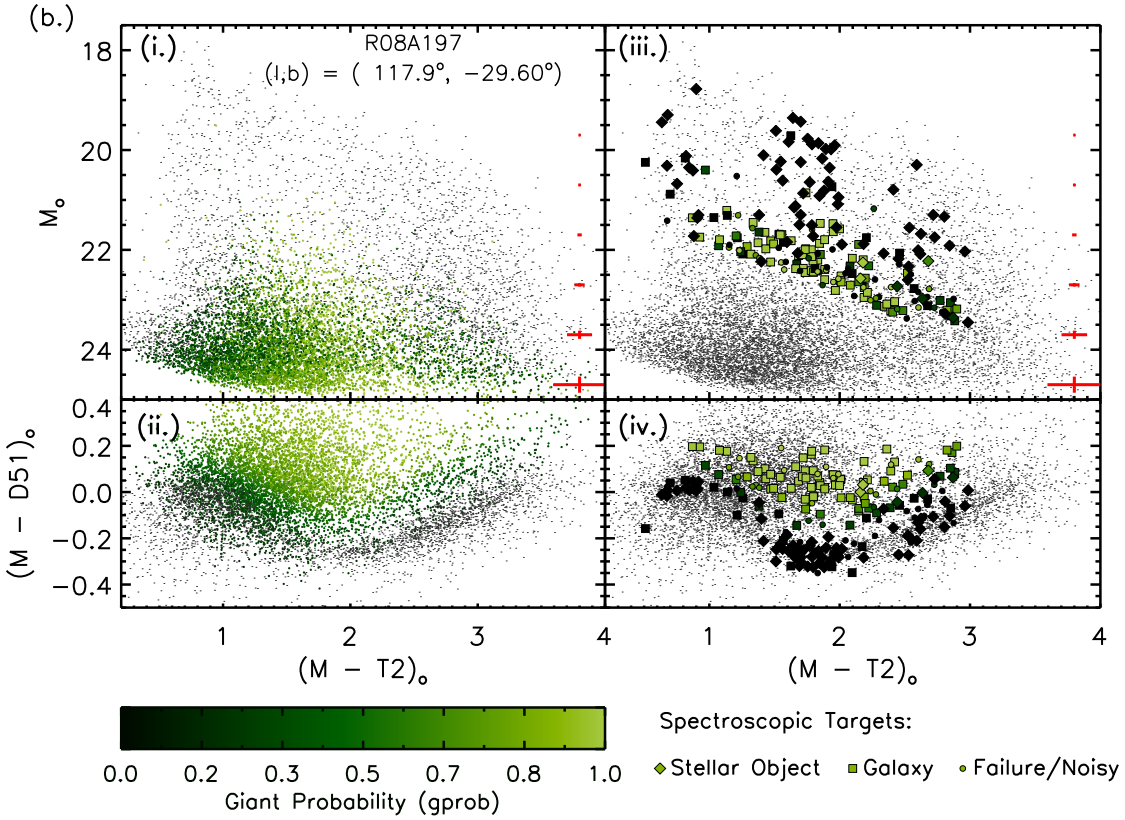

Fig. 3.8.— cont. Washington+*DDO*51 photometry for new MMT+Hectospec spectroscopy in R08197.

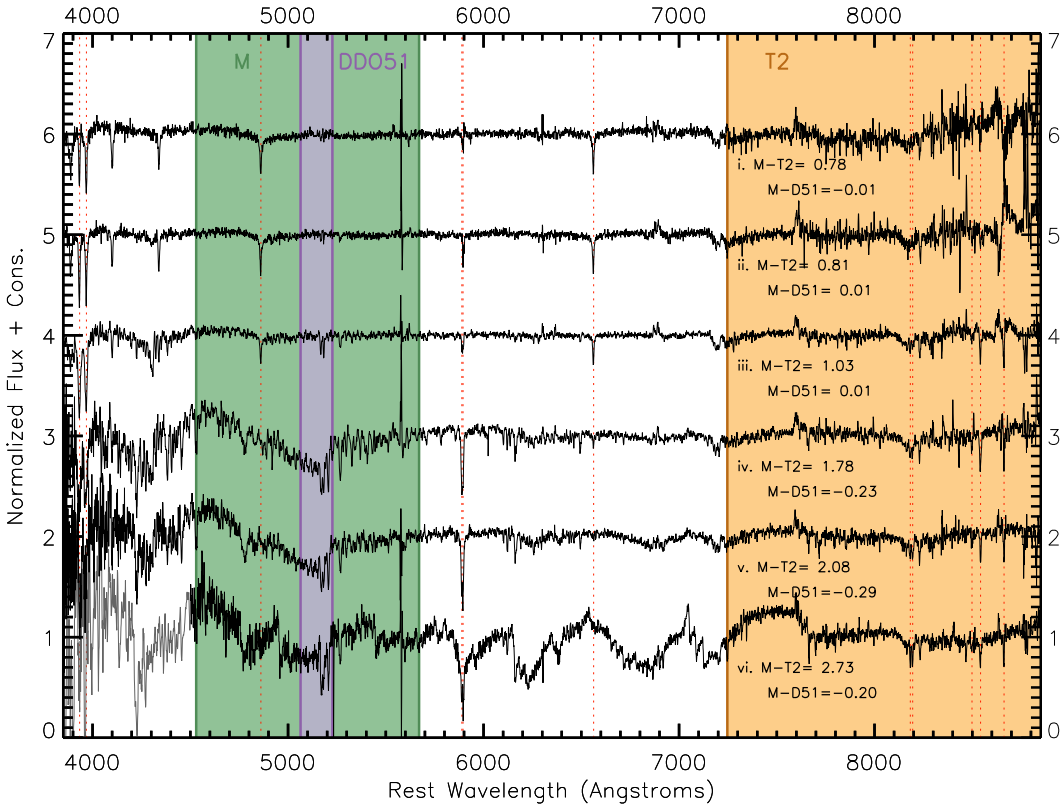

Fig. 3.9.— Example stellar spectra obtained with MMT+Hectospec over the rest wavelength range from λ3850 Åto λ 8850 Å. Red dotted lines indicate the wavelengths for the stellar absorption features used for the radial velocity measurement and evaluation (Section 3.4.3 and Table 3.6). Spectral regions shown in black are at native resolution ($\sim$1.22Åpixel^{-1}), whereas those regions in grey have been smoothed with a median filter. The approximate passbands of the M (λ_{cent} = 5100 Å; green), $DDO51$ (λ_{cent} = 5415 Å; purple), and $T2$ (λ_{cent} = 8204 Å; orange) filter are indicated as filled boxes. The six objects span the full $(M-T2)_\circ$ and $(M-DDO51)_\circ$ range of the spectroscopic targets.

off in observing efficiency is more than compensated by the nearly 30× gain in area for spectroscopic observations at these low surface brightnesses.

Washington+$DDO51$ catalogs served as the basis for the MMT+Hectospec observations in the fields R08A101 and R08A197. The design of the fiber positioning system of Hectospec (Fabricant et al. 2005) constrains the fiber positioning and, thereby, restricts the target selection. An interactive GUI called `XFITFIBS`[9] is used to convert prioritized target lists into appropriate fiber configurations that take into account fiber placement concerns. Similar to the targeting for the Keck+DEIMOS catalogs, our photometry catalogs were ranked using their $M - T2$ color, $T2$ magnitude, and the giant probability parameter from the color-color diagram. Secondary targets were selected from the Triangulum Andromeda main sequence turn off (Majewski et al. 2004). Of the 300 fibers, approximately 70 were reserved for night sky measurements and the `XFITFIBS` software distributes these appropriately amongst the science targets to maximize the success of sky removal. `XFITFIBS` also selects appropriate guide stars (R >16) from the user catalog that must be placed in an 86° arc around the exterior of the instrument field-of-view. Our Washington+$DDO51$ catalogs are astrometrically calibrated to the USNOB1 catalog and, if necessary, we supplement our catalog with appropriate bright guide stars from the USNOB1 catalog (Monet et al. 2003, 2002). The targets for the MMT+Hectospec observations are shown as the large symbols (color coded by *gprob*) in panels (iii) and (iv) of Figures 3.8a and Figures 3.8b.

Observations were acquired using the 270 groove mm^{-1} grating producing a dispersion of 1.2 $\mathring{A}$ pixel^{-1} for continuous spectral coverage from 3770-9200$\mathring{A}$ and a line full width at half maximum of 6.2 $\mathring{A}$ (Fabricant et al. 2005). Hectospec is operated in queue service mode in order to average time losses across all observing programs

[9] `https://www.cfa.harvard.edu/~john/xfitfibs/`

and the observations presented here were spread across dark time during the Fall 2011 trimester. As such, the individual observing conditions vary greatly in both atmospheric seeing and transparency. We boosted our target integration times to compensate for these variable conditions. The log of observations is presented in Table 3.4 for those fields targeted with MMT+Hectospec.

In theory observations split over multiple nights should pose few concerns, if the fiber configuration was performed identically night-to-night. Owing to the need to compensate for field-rotation over the course of the night, the instrument requires a change in its position angle to observe the same field before and after transits due to the 86° maximum reach of the guide probes (Fabricant et al. 2005). This restriction has the effect of requiring unique fiber configurations for pre- and post- transit observations, which has the effect of "shuffling" the target-to-fiber assignments. In theory, this shuffling assists our effort by averaging over detector and fiber specifics, but in practice fiber positioning restrictions cause objects to be added and dropped between observing nights. After data processing challenges relating to the varying configurations were realized from data acquired in 2007[10], the 2011 data was scheduled specifically to avoid these problems — although care was still taken to check the configurations for each night for any variations in the fiber positioning.

The processing of the Hectospec data is complex and a custom end-to-end pipeline was written for semi-automatic image processing, spectral extraction, and redshift measurements (Fabricant et al. 2005; Mink et al. 2007). Flat-fielding and overscan corrections are applied in the `MSCRED` environment in `IRAF` before spectra are extracted with attention given to modeling distortions on the chip. Wavelength solutions are derived for the two-dimensional image, applied to each extracted spectrum, and then tweaked as required using OH sky emission lines. Sky subtraction is performed on

[10]These data targeted known substructure are not used for the transverse motion measurement.

a per-exposure basis for each individual object using the average sky spectrum for the nearest six sky fibers. The resulting sky template is then normalized to the OH λ 8399 $\mathring{A}$ feature in each object. This procedure has been tested reliably for galaxy spectra to a magnitude of R$\sim$23 (Fabricant et al. 2005). Once the sky is removed, objects from individual exposures are combined. The λ 6800$\mathring{A}$ and λ 7600$\mathring{A}$ features are divided out and a known red leak from a fiber LED is modeled and removed (Mink et al. 2007). The final product is a wavelength calibrated variance-weighted co-addition of individual exposures rebinned to a common wavelength solution for each of the unique science objects.

The observations used here were processed using the recently completed IDL implementation of the pipeline at the Smithsonian Astrophysical Observatory Telescope Data Center. Due to the night-to-night configuration and data quality concerns, the data was custom processed on a night to night basis. The one-dimensional spectra were matched between configurations and nights using their sky positions before visual inspection and comparison to its matches. Those spectra with low signal-to-noise, exceptionally large residuals from sky subtraction, or spectral features inconsistent with the other matches were removed. The remaining co-added exposures in each field were then co-added to produce the final spectrum for each object. Given that the observations span a range of ΔM $\sim$4 magnitudes and $\Delta(M - T2) \sim 2.5$ in color (see Figures 3.8a and 3.8b) as well as condition variations for those stars observed on different nights, the signal-to-noise varies amongst the ensemble of spectra.

A set of stellar spectra from the MMT+Hectospec dataset are given in Figure 3.9 for the rest wavelength range λ3850Å to λ8850Å. Each spectrum is shown its native resolution with no smoothing, except for the bluest portion of star (vi), which is exceptionally red and likely of late-M stellar type. The sharp spikes, for example at

λ5700Å, are largely residuals due to sky subtraction and only begin to strongly distort the spectra at the reddest wavelengths (e.g., $>\lambda$7500Å). The spectra are ordered from top to bottom by their observed $M-T2$ color (i.e., intentionally without correction for foreground extinction), which span a total range of 2 magnitudes ($0.7 > M-T2 < 2.8$) and vary in spectral type from late G to mid-M based on visual comparison to those templates provided in Turnshek et al. (1985). For visualization purposes the approximate M, $DDO51$, and $T2$ passbands are given, which permits a comparison of the $M-DDO51$ color to the MgB and MgH features to demonstrate its utility as previously described in Section 3.4.1.

Measurement of Line of Sight Velocities

Given the queue scheduled nature of the observations, adequate spectral templates for our desired K-type and M-type stars were limited within the standard MMT+Hectospec spectral template suite and, thus, the cross-correlation results using the available templates were largely unsatisfactory. Therefore, we developed a procedure making use of a series of spectral lines common to the K- and M- spectral types for both the giant (III) and dwarf (V) luminosity classes by comparison spectral data for such stars available by Turnshek et al. (1985). The initial line list was comprised of the absorption lines: Ca H (λ 3933.6614 $\AA$), Ca K (λ 3968.4673 $\AA$), Hβ (λ 4861.34 $\AA$), Na Doublet (λ 5889.860, 5895.924 $\AA$), Hα (λ 6562.81 $\AA$), the infra-red calcium triplet (CaT, hereafter; λ 8498.43, 8542.32, 8662.44$\AA$), and a handful of TiO absorption features. The wavelengths for the initial line list are shown Figure 3.9 for six spectra in the MMT+Hectospec, with the TiO lines excluded due to their multitude over the shown spectral range.

A fully-automated python code, which was originally developed to fit equivalent

widths with appropriate analytical functions, was adapted for the direct measurement of individual line centers (G. Damke, in preparation). The code uses a Gaussian function with both the central wavelength and the full-width at half maximum (FWHM) as free parameters, though these values can be constrained to appropriate ranges. The code is able to fit individual lines within individual spectral windows, or to determine a joint solution for multiple spectral lines over a single spectral window or within individual sub-windows for each of the spectral lines. The range of velocities permissible to the code is thereby set by the spectral windows specified for individual lines and as a result the code can be specified for galaxies or for stars, but not both simultaneously. Thus, we opt to remove obvious emission line galaxies by visual inspection and focus only on stellar spectra, which is conducted as *zquality* classification before the measurement of the radial velocity. The code produces the best results when applied to continuum normalized spectra (G. Damke, in preparation) and the continuum normalization was performed for each final co-added spectrum using a low-order polynomial in the `IRAF` procedure `CONTINUUM`.

The R08A101 field had, on average, the highest quality data (see Tables 3.4 and 3.5). A training set of the objects in the R08A101 data was selected visually to span a range of signal-to-noise, spectral type, and luminosity type. This training set was used to explore combinations of joint-line fits and individual line fits to determine a combination with the greatest applicability to our science targets. Those lines that were found by visual examination to be either consistently not detected, poorly fit, or contaminated by nearby night sky lines for the objects in the training set were removed from consideration. At the conclusion of this evaluation procedure, the initial line list was reduced to: Ca H, Ca K, Hβ, the two lines of Na D, Hα, and the three lines of the CaT.

The full set of R08A101 science targets, pre-culled of background galaxy contaminants with bright emission lines, was then fit using these "best" lines. The spectral windows applied for each line were customized to avoid wavelength regions consistently dominated by sky subtraction residuals and provide appropriate bandwidth to measure the stellar continuum. The Ca H and Ca K absorption lines were best fit jointly over a contiguous spectral window from $\lambda 3880\mathring{A}$ to $\lambda 4058\mathring{A}$, in part due to the low S/N at these wavelengths for red targets (see Figure 3.9). The Hβ line was not uniformly detected due to its characteristic weak expression stars of the M spectral type (Turnshek et al. 1985) and as is evident the $M-T2$ color progression of Figure 3.9. The Na D, while being identifiable for all stellar objects in the sample, consistently had large residuals from sky-subtraction that caused significant distortion of the line shape and, thereby, consistently resulted in a poor quality fit to the line center. The first and third lines of the CaT were also commonly contaminated by sky subtraction residuals (these are visible in the example spectra of Figure 3.9) and only the second line (CaT_2, hereafter; λ 8542.32$\mathring{A}$) was consistently well fit for those objects in the R08A101 field. From the inspection of the line fitting across the full R08A101 object list, the final line list included: Ca H + Ca K, Hα, and CaT_2. The absorption lines and spectral windows used for the radial velocity measurements are specified in Table 3.6.

The procedure was applied to the entire set of MMT+Hectospec observations. Measurement uncertainties for each of the fit parameters, more specifically the redshift and line-width, were measured independently by the python procedure (G. Damke, in preparation). The Gaussian was constrained by a minimum FWHM of approximately two resolution elements (2.6$\mathring{A}$) motivated to avoid fitting sky-subtraction residuals (typically very sharp), and by a maximum FWHM of 15$\mathring{A}$, or 30% of the

smallest spectral window, to avoid fitting any residual low order noise. The final redshift was computed as the error weighted mean of the four line fits, with those fits with that did not converge rejected entirely. The resulting velocities were inspected manually over the full spectral coverage and given a *zquality* rating using criteria identical to that implemented for the Keck+DEIMOS spectra previously described. We note that this entire procedure was completed "blind" to the knowledge of the Keck+DEIMOS computed velocities for any stars common to both samples. Some comparisons, however, were made to the cross correlation results from the Hectospec pipeline and found to agree for those spectra with reliable measurements in both procedures, which were typically those stars with high S/N.

The final MMT+Hectospec sample consists of 442 individual spectra, 158 (36%) of which are stellar, 216 (49%) of which are galaxies, and 68 (15%) of which were unusable. The classifications for individual targets are visually depicted in panels (iii) and (iv) of Figures 3.8a and 3.8b by the coding of the large symbols, identical to those previously presented for the new Keck+DEIMOS observations. The final number of science objects in each field is given in Table 3.5 for each of the fields.

3.5 Selection of M31 Members

Our sample of spectroscopic objects in the joint Keck+DEIMOS and MMT+Hectospec datasets contain several distinct populations that must be disentangled before proceeding to measure the tangential motion of M 31. Of the 53 fields with spectroscopic observations used in this work, 17 (32%) are designed around dwarf satellite galaxies and the easiest population to remove are the high likelihood dwarf satellite members (Section 3.5.1). After removing the potential dwarf galaxy members, the remaining stars consist of our target M 31 giants and the foreground MW dwarfs, for which the

latter dominate by number in all fields but those at the highest M 31 stellar density. Since the two populations of stars, on average, span the same spectral type, separation of the two populations requires use of parameter spaces that distinguish the populations by both luminosity class, spectral type, and kinematical properties (Section 3.5.2). Once high likelihood M 31 halo members are identified, those stars belonging to coherent velocity substructures from recent satellite accretions need to be isolated (Section 3.5.3). Lastly, the M 31 selection criterion must be evaluated for potential velocity bias (Section 3.5.4).

3.5.1 Removal of dwarf Spheroidal Members

Since the identical datasets used in the Tollerud et al. (2012) and Ho et al. (2012) are also used for this work, all high probability dwarf satellite member stars from those analyses are excluded from the tangential motion sample. This still leaves a number of "likely" dSph members that were rejected for the purposes of Tollerud et al. (2012) and Ho et al. (2012), i.e., to produce a pristine sample of dwarf satellite member stars for study of internal kinematics. In the efforts of Gilbert et al. (2012) to make the most clean sample of M31 halo members, these "likely" stars were also excluded if they were within $3\sigma_{disp}$ of the systemic velocity for the galaxy, where σ_{disp} is the velocity dispersion of the satellite. For our purposes, we use the kinematical parameters from Tollerud et al. (2012) directly instead of adopting those of Collins et al. (2014) as was done in Section 3.3. We adopt the Gilbert et al. (2012) criteria for the satellites common to Tollerud et al. (2012) or Ho et al. (2012).

DEIMOS masks for the satellites Andromeda XXVIII and Andromeda XXIX were obtained by Tollerud et al. (2013). Stars were targeted in these objects using SDSS g' and r photometry and no Washington+$DDO51$ data exist for these fields that would

permit adoption of the Tollerud et al. (2012) membership algorithm. Following the example of Gilbert et al. (2012), we consider any stars within $3\sigma_{disp}$ of the satellite's systemic velocity as members of that dwarf satellite.

3.5.2 M31 Likelihood

Gilbert et al. (2006) developed a multi-dimensional maximum-likelihood technique optimized to identify M 31 red giants from foreground MW dwarfs. Gilbert et al. (2006) explored numerous measurements permissible from the combined spectroscopic and photometric data in the SPLASH survey, including equivalent widths from stellar absorption features, optical colors and magnitudes, and radial velocities, to isolate a set of five parameter spaces, for which the resulting contrast between an the giant (P_{giant}) and dwarf (P_{dwarf}) probabilities was sufficient to isolate the two populations. The technique is quite powerful and has enabled numerous insights into the M31 stellar halo to unprecedented surface brightnesses for resolved stellar spectroscopy including those studies presented in Gilbert et al. (2006); Kalirai et al. (2006); Gilbert et al. (2007, 2009b, 2012) among others. First, we summarize this technique and apply it to the full SPLASH sample of stars from Keck+DEIMOS; Second, we discuss alterations to the technique for the MMT+Hectospec sample, the spectra for which are at lower spectral resolution than that of Keck+DEIMOS.

The Gilbert et al. (2006) probability distributions determined using the pilot M 31 imaging program of Ostheimer (2003) are shown in the panels of Figure 3.10, in which contours for the dwarf distribution are given in blue and the giant distribution in red. The five metrics are:

1. Position in the color magnitude diagram relative to a fiducial isochrone for M 31 (ΔX_{CMD}, ΔY_{CMD}; Figure 3.10a),

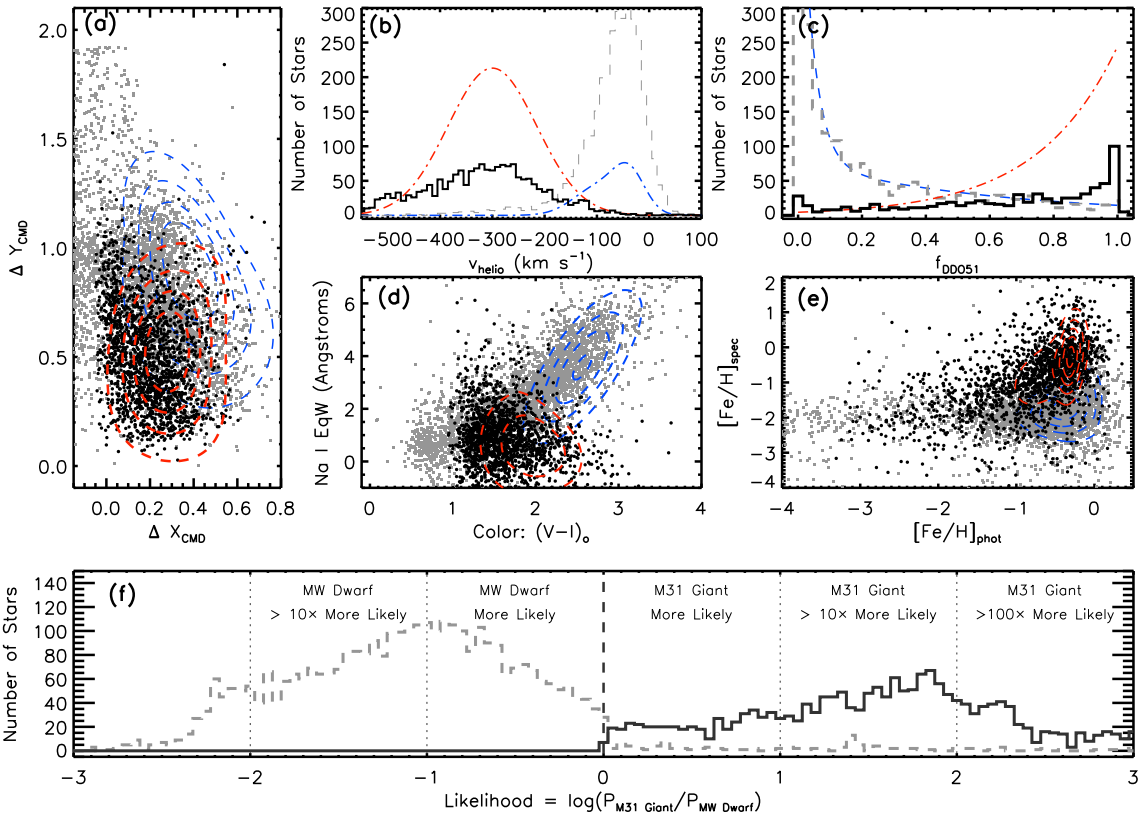

Fig. 3.10.— Demonstration of the likelihood diagnostics of Gilbert et al. (2006) for the SPLASH dataset used in this work (Section 3.4. **(a)** A color-magnitude space defined relative to fiducial M 31 isochrones. **(b)** The heliocentric radial velocity (v_{helio}). **(c)** A parameter derived from the $DDO51$ magnitude, f_{DDO51}. **(d)** A space defined from the $(V-I)_\circ$, a proxy for stellar temperature (spectral type), against the equivalent width of the Na I doublet at λ8200 Å, a quantity sensitive to surface gravity (luminosity class). **(e)** A two dimensional space comparing the photometric and spectroscopic estimates of metallicity ([Fe/H]). In each of the panels, the hashed contours define the probability distributions from Gilbert et al. (2006) for the giants (red) and dwarfs (blue). **(f)** Marginal distribution of final likelihood values, which are computed from the individual likelihoods as described by Equation 3.10. The dashed grey histogram indicates those objects more likely to be dwarfs and the solid black histogram those objects more likely to be giants. Stars more likely to be dwarfs are plotted as grey points in panels (a) - (e), and those stare more likely to be giants are shown as black points.

2. Heliocentric radial velocity compared to distributions for M 31 and the MW (v_{helio}; Figure 3.10b),

3. The M-$DDO51$ color as compare to distributions for dwarf and giant stars (f_{DDO51}; Figure 3.10c),

4. The lack of correlation between Na I EqW and color (Na I EqW, $(V\text{-}I)_\circ$; Figure 3.10d),

5. An overall correlation between the metallicity ([Fe/H]) determined from photometric (comparison to isochrones) and spectroscopic (the IR CaT) techniques ($[Fe/H]_{phot}$, $[Fe/H]_{spec}$; Figure 3.10e).

The ΔX_{CMD}, ΔY_{CMD}, and $[Fe/H]_{phot}$ measurements are computed in comparison to a grid of theoretical stellar isochrones shifted to M 31 distance ($(m-M) = 24.4$) in the Victoria-Regina system (VandenBerg et al. 2006) with an age of t=12.6 Gyr, no alpha enhancement (i.e., $[\alpha/Fe]$=0.0), and spanning a metallicity range of $-2.3 \leq$[Fe/H]$\leq$ 0.5. More details on these measurements can be found in Sections 3.2.5 and 3.2.6 of Gilbert et al. (2006).

The probability distributions shown in Figure 3.10 are then used to compute a giant probability (P_{giant}) and a dwarf probability (P_{dwarf}) for each individual star, i, in each of the parameter spaces, j. For each diagnostic j, the likelihood that a star i is a red giant is determined using the formula:

$$L_{ij} = \log(\frac{P_{giant}}{P_{dwarf}}). \tag{3.9}$$

The final overall likelihood of being an M 31 red giant is the weighted average of

the individual likelihoods for each star:

$$\langle L_i \rangle = \frac{\Sigma_j w_j L_{ij}}{\Sigma_j w_j}. \tag{3.10}$$

Generally, all likelihoods receive identical weight (i.e., $w_j = 1$), and only those stars that are outliers in the three two dimensional parameter spaces (i.e., those shown in Figures 3.10a, 3.10d and 3.10e) receive down weighting. In these cases, the objects are down weighted as described in Gilbert et al. (2006). The effect of the down weighting is to restrict the resulting sample to the regions of parameter space well sampled by the training set (See Section 3.3 of Gilbert et al. 2006). We note that in the event that one parameter space cannot be used — as occurs for the f_{DDO51} parameter for those fields without Washington+$DDO51$ data — the individual likelihood is set to zero ($L_{ij} = 0$), as it effectively has equal chance of being a giant or dwarf if no data is available for given diagnostic space.

Using Equations 3.9 and 3.10, $L = 0$ represents a star that has equal probability of being a MW dwarf or a M 31 halo star. Negative values of L represent stars more likely to be MW dwarfs than M 31 halo stars. Positive values of L represent stars more likely to be M 31 halo stars than MW dwarfs. For practical reasons, L is given a floor at L=-5 and a ceiling of L=5 (see Gilbert et al. 2006, for additional discussion).

The Gilbert et al. (2006) likelihood diagnostics are applied to the full Keck+DEIMOS sample in Figures 3.10a - 3.10e, in which stars more likely to be MW dwarfs (i.e., L <0) are shown in grey and those more likely to be M 31 giants (i.e., L >0) are shown in black. The implementation of the L code used for this work is identical to that of Gilbert et al. (2012), and is optimized identify M 31 halo stars (as opposed to dwarf satellite stars as was done for Kalirai et al. (2010)). Comparison of the probability distributions (hashed blue and red contours for dwarfs and giants, respectively) and

the classification based on final likelihood, L, indicated by the grey or black points in Figure 3.10 show overall good agreement.

Figure 3.10f is a marginal distribution of the L computed from Equation 3.10, where likely dwarfs are shown in dashed grey and likely giants in solid grey. From inspection of Figure 3.10f, it is clear that the tails of the likely dwarf and likely giant distributions overlap in the range of $L \sim \pm\ 0.5$ and Gilbert et al. (2006) devised an empirical means to alleviate some of the degeneracy, which will be discussed in Section 3.5.2 after a discussion of the adaptation of the L implementation for our MMT+Hectospec sample.

Spectral Measurements for MMT+Hectospec Data

The M 31 likelihood method was tailored to the Keck+DEIMOS dataset, and, thus, some care must be taken to ensure their application to the MMT+Hectospec data is consistent in its selection of M 31 members. The data products measured directly from the spectra in the likelihood calculations are: (i) the heliocentric line-of-sight velocity (v_{helio}), (ii) the equivalent width of the Na Doublet at $\lambda 8200 \AA$ (Na D EW), and (iii) the spectroscopic metallicity derived from the reduced equivalent width of the CaT (CaT EW). Thus, we proceed to evaluate these efficacy of these specific measurements on the MMT+Hectospec spectra, make adjustments as required, and compare the measurements for spectra common to both samples.

There are eighteen spectra common to the Keck+DEIMOS and MMT+Hectospec datasets in the R08A101 and R08A197 fields. Only six of the eighteen are both of stellar type and of sufficient S/N in both datasets for reliable velocity (i.e., of *zquality* 3 or 4) and equivalent width measurements[11]. Visual inspection of the MMT+Hectospec

[11] We note that on occasion the redshifted stellar absorption lines will be inaccessible for measurement of equivalent widths for reasons that include, but are not limited to, being red/blue shifted

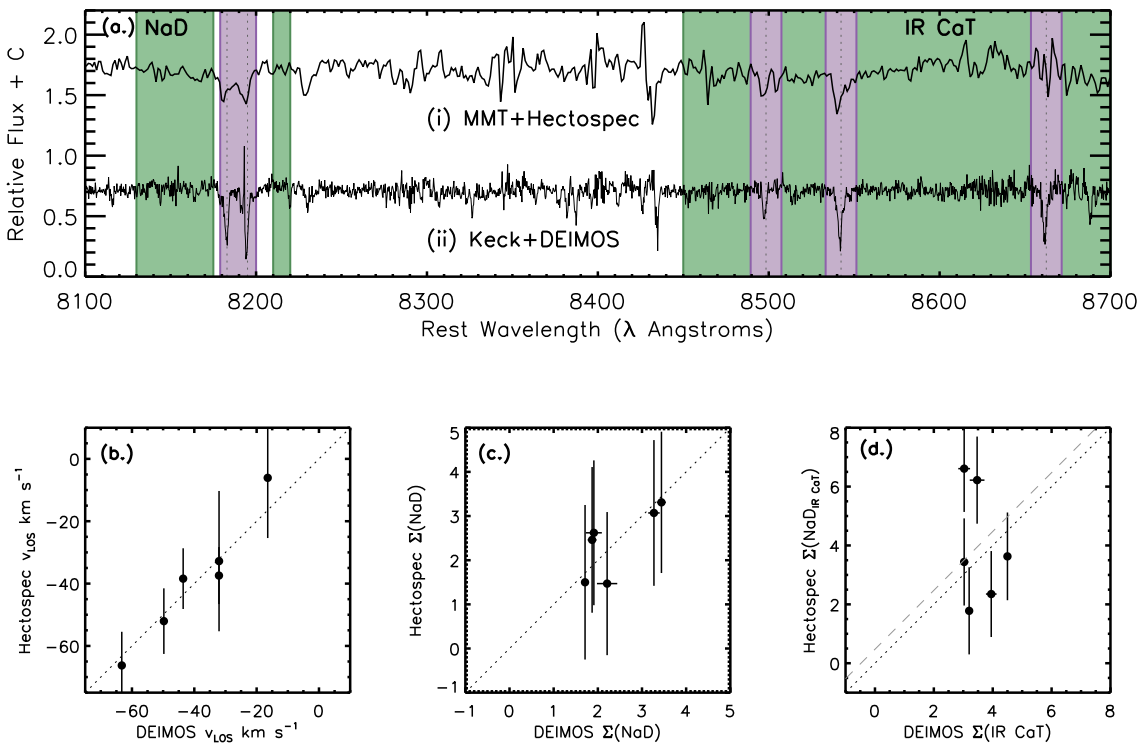

Fig. 3.11.— Comparison of measurements used in the likelihood calculation that are derived from spectroscopy for stars common to the Keck+DEIMOS and MMT+Hectospec samples. **(a)** Comparison of a sample spectrum from MMT+Hectospec (top) to that of Keck+DEIMOS (bottom) for the spectral range relevant for the equivalent width measurements. The rest wavelengths of the spectral lines for the infrared Na Doublet (Na D) and the infrared calcium triplet (Ca T) are indicated as dashed vertical lines. The spectral regions used to estimate the continuum (F_{cont}) and measure the line flux (F_λ) for either set of spectral features is shaded as green for the continuum and purple for the line flux (exact values are given in the text and in Table 3.6). **(b)** Comparison of the heliocentric radial velocities (v_{LOS}). **(c)** Comparison of the NaD equivalent width. **(d)** Comparison of the CaT equivalent width. In each of panels (b), (c), (d) unity trend is shown as a dotted line and the mean difference between the two datasets is shown as a hashed line for panel d only, as the relationships in panels b and c are consistent with unity. The equivalent widths compared in panel (c) and (d) were measured using identical techniques, although masking of sky subtraction residuals was required for the MMT+Hectospec data. Generally, the results from the MMT+Hectospec campaign are consistent with those of the higher resolution Keck+DEIMOS data, albeit with larger measurement uncertainties.

spectra for these source indicate overall spectral features consistent with foreground Milky Way dwarfs. We note that the observations for MMT+Hectospec and Keck+DEIMOS were prepared concurrently and that the overlap stars contain only dwarfs is happenstance. While we cannot compare M 31 halo stars directly, the luminosity dependence for the λ8200Å Na D feature is such that having a dwarf dominated sample permits better comparison of the equivalent width measurement technique; more specifically, the line is not expressed in the spectrum for a star of the giant luminosity class (Schiavon et al. 1997).

Figure 3.11a compares the spectrum a single stellar object over the wavelength range relevant for the equivalent with measurements (e.g., λ8200Å Na D to beyond the infrared CaT). The rest wavelengths of the NaD and CaT spectral features are overplotted in Figure 3.11a and the lines show overall similar shapes at the two resolutions in the MMT+Hectospec (top) and Keck+DEIMOS (bottom) spectra, though we note the decreasing S/N beyond λ8300Å due to night sky emission residuals in the MMT+Hectospec. Figure 3.11b compares the heliocentric velocities derived from the two datasets using the methods described in Section 3.4. The line-of-sight velocities measured in the two datasets agree within the measurement errors and the mean difference between the Keck+DEIMOS and MMT+Hectospec measurements is $\Delta(v)$ =-0.7 km s^{-1}. The MMT+Hectospec line-of-sight velocities have larger measurement errors than Keck+DEIMOS both due to reduced precision because of the spectroscopic resolution and differences in the measurement technique. It may be possible to improve the uncertainty of the MMT+Hectospec velocities with the use of a template based cross-correlation method as is done for the Keck+DEIMOS spectra.

The equivalent width measurements for the Na D and CaT are compared in Figures 3.11c and 3.11d. For consistency with Gilbert et al. (2006), we use identical

onto a chip gap or within the proximity of a series night sky emission lines.

equivalent width measurement techniques that we now describe. For Na D the continuum flux (F_{cont}) is measured using a blue ($\lambda 8130\mathring{A}$ to $\lambda 8175\mathring{A}$) and red window ($\lambda 8210\mathring{A}$ to $\lambda 8220\mathring{A}$) on either side of the doublet and these regions are indicated in Figure 3.11a by green shading. The line flux (F_λ) is measured using direct integration from $\lambda 8175$ Å to $\lambda 8210$ Å (depicted in Figure 3.11a by the purple shading) and the equivalent width derived as follows:

$$W_{line} = \Sigma \frac{F_{cont} - F_\lambda}{F_{cont}} d\lambda, \tag{3.11}$$

where each F_λ is weighted by its corresponding value in the error spectrum. A similar procedure is adopted for the IR CaT that uses the region from $\lambda 8450$Å to $\lambda 8700$Å to measure the continuum (F_{cont}; depicted by the green shading in Figure 3.11a) and the line flux (F_λ) by direct integration over 18Å spectral windows centered on each line (depicted by the purple shading in 3.11a). The specific details of the equivalent width measurements are summarized in Table 3.6. Given the decreased S/N do the high number of night sky lines at these red optical wavelengths, the equivalent width measurement is performed in a Monte Carlo sense; more specifically, the spectral regions are re-realized by randomly adding Gaussian noise, the properties of which are set by the value of the corresponding error spectrum at each wavelength. A total of $N_{trials} = 1000$ are used for the Keck+DEIMOS data. The final reported equivalent width is the resistant mean (i.e., the mean computed with iterative 3σ clipping) and the error is the corresponding standard deviation computed from the distribution of the trials.

The initial attempts to measure the equivalent widths for the MMT+Hectospec data were not successful using the procedure for Keck+DEIMOS. Upon close inspection of the spectral regions for the six stars, spectral regions around individual lines

were noted to be consistently influenced by sky residuals. This not only alters the flux measurements, but the corresponding error spectrum is of a quite large magnitude (even approaching infinity), which result in unphysical variations in the Monte Carlo measurement technique. For these two reasons, these regions with large sky residuals in all six stars were masked in both the MMT+Hectospec science and error spectrum. Moreover, the Monte Carlo realizations were extended to $N_{trials} = 5000$ to improve sampling and obtained stability of the final equivalent width values measured over multiple passes of the software. The equivalent widths were measured as shown in Figures 3.11c and 3.11d, with overall good agreement with those for the higher resolution Keck+DEIMOS spectra. The mean difference between the MMT+Hectospec and Keck+DEIMOS measurements are $\Delta(NaD)$ =0.0 Å for the Na D and $\Delta(CaT)$ =-0.5 Å for the CaT (indicated as the dashed grey line in Figure 3.11d). Again, the measurement uncertainties for the spectroscopic quantities measured from the MMT+Hectospec spectra are larger than those from Keck+DEIMOS, which is due in part to the lower spectral resolution and in part to the larger overall fluctuations in the error spectrum. We note that the Monte Carlo procedure developed in application to Keck+DEIMOS spectroscopy may not be ideal for the MMT+Hectospec data considering to its 4× broader spectral resolution and, thereby, poorer sampling of the spectral lines.

Adaptations of Likelihood to MMT+Hectospec Data

Having confirmed the fidelity of spectral measurements on the MMT+Hectospec data against that of Keck+DEIMOS, we now compute the L values as previously described. Figure 3.12 compares the L_i for the diagnostic spaces that use spectroscopically derived quantities. Figures 3.12a, 3.12b, and 3.12c compare the L_i for v_{los},

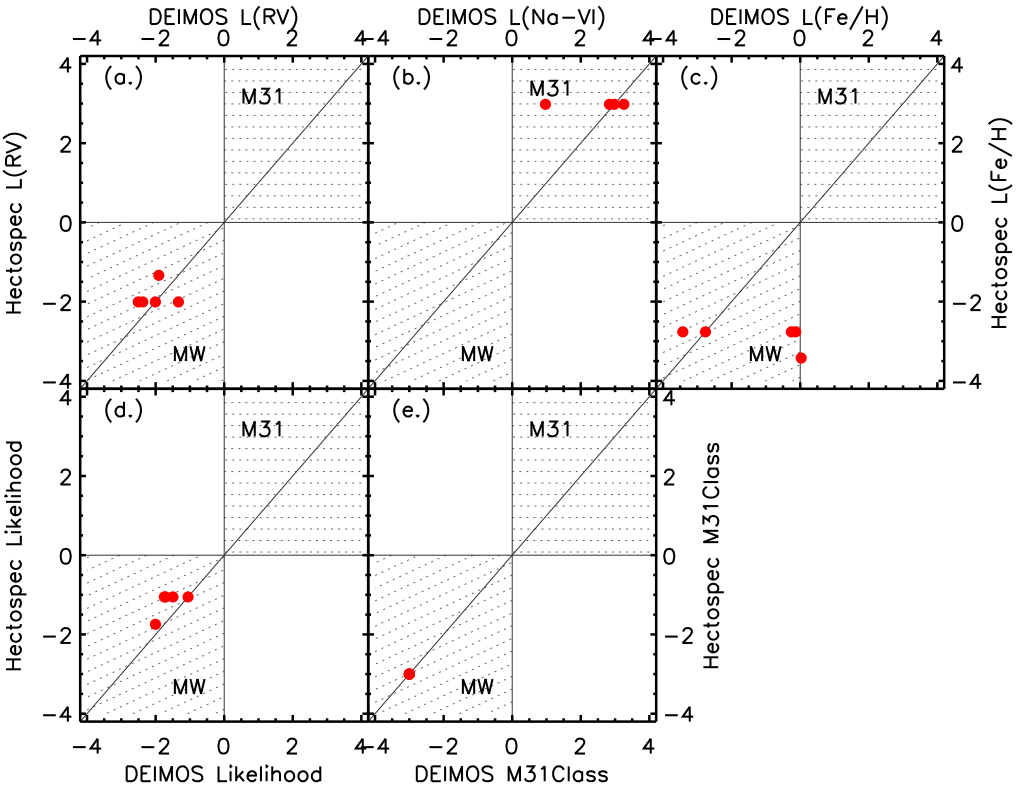

Fig. 3.12.— Comparison of the giant probabilities computed in the diagnostic spaces (i.e., Figure 3.10) for stars common to the Keck+DEIMOS and MMT+Hectospec samples. **(a)** Likelihood being an M 31 giant from the radial velocity ($L(RV)$). **(d)** Likelihood of being an M 31 giant from the $(V-I)_\circ$-Na EqW space ($L(Na-VI)$). **(c)** Likelihood of being an M 31 giant from the spectroscopic-photometric [Fe/H] space ($L(Fe/H)$). **(d)** Mean likelihood (L) from the three spaces depicted here and two relying on photometry. **(e)** M 31 class as described in Section 3.5.2. In all three spaces, a unity trend-line is shown in grey and the space for consistent M 31 or MW classification for both spectral quantities is given by the hashing or angled hashing, respectively (the white spaces demonstrate inconsistent classification). Unfortunately, the stars common to both samples are all relatively high likelihood MW dwarfs, which severely restricts the parameter space probed by these comparisons. The comparisons, however, tend to agree in their overall classification.

Na EqW-$(V-I)_\circ$, and $[\mathrm{Fe/H}]_{spec}$-$[\mathrm{Fe/H}]_{phot}$ derived from the Keck+DEIMOS and MMT+Hectospec datasets, respectively. The six stars are determined to have low P_{giant} in all three spaces in both datasets. Figures 3.12d and 3.12e compare the final L and the $m31class$ parameter for the six stars, which depend on the values shown in Figures 3.12a, 3.12b, and 3.12c. Again, the diagnostics agree well for both spaces for all six stars. Thus, we conclude that the MMT+Hectospec data can be folded successfully into the larger Keck+DEIMOS sample with no immediate concerns.

M31Class

A problem with the L parameter is its treatment of "marginal" stars, those objects with L_i values that vary from negative (dwarf like) to positive (giant like). A sub-classification system, described by the parameter $m31class$ was designed to identify marginal stars in a systematic fashion. The sub-classification uses two criteria: the mean likelihood (L) and the objects $(V-I)_\circ$ color relative to a set of fiducial M 31 isochrones ($\Delta X_{CMD}, \Delta Y_{CMD}$; Section 3.5.2). Gilbert et al. (2006) noted that those stars with $|L| \leq 0.5$ often had L_i for individual diagnostics that were distributed across the giant ($L_i > 0$) and dwarf ($L_i < 0$) division. Thus, those stars with $|L| \geq 0.5$ are considered "secure" dwarfs or giants, as their individual L_i classifications tend to agree for all diagnostics. The "secure" stars are giving an $m31class = \pm 3$, where $+3$ are secure giants and -3 are secure dwarfs. The secure giant class, however, requires an additional constraint using X_{CMD}; more specifically, $X_{CMD} < 0.0$ implies that the $(V-I)_\circ$ color for the star is bluer than the fiducial M 31 isochrones, and is thus is photometically inconsistent with an M 31 stellar population. To be considered a "secure" M 31 giant, $m31class = +3$ stars must have $X_{CMD} < 0.0$.

The average error on X_{CMD} from the sample of Gilbert et al. (2006) is $\sim$0.05, and

a star with $-0.05 \leq X_{CMD} \leq 0$ is *statistically* consistent with $X_{CMD} \sim 0.0$. Thus, $m31class = +2$ are those stars with $|L| \geq 0.5$, but with $-0.05 \leq X_{CMD} \leq 0$. An $m31class = +1$ are those stars with $0.0 < L \leq +0.5$ and $-0.05 \leq X_{CMD}$, or those stars more likely to be giants and with a color consistent with the M 31 red giant branch.

Marginal dwarfs are defined similarly with $m31class = -1$ being those stars with $-0.5 < L \leq 0.0$ and $-0.05 \leq X_{CMD}$, under the reasoning that these are more likely to be giants due to their $(V - I)_\circ$ color. Thus, $m31class = -2$ are those stars with $-0.5 < L \leq 0.0$ and $X_{CMD} < -0.05$.

In summary, securely classified objects have $m31class = \pm 3$ for dwarfs ($m31class < 0$) and giants ($m31class > 0$). Marginally classified objects will have $m31class = \pm 2$ or $m31class = \pm 1$, where the former is more secure than the latter. Thus, $m31class$ permits separation of "marginal" and "secure" classifications within our likelihood diagnostic system. The $m31class$ definitions are summarized in Table 3.7.

3.5.3 Known Halo Substructure

Although application of L and $m31class$ will isolated stars with kinematic and photometric properties consistent with those of the M 31 halo, we must now consider the removal of fields that are dominated by known halo substructure, which violate the primary assumption of our transverse motion fitting technique. There are several categories of known substructure:

The star-counts, dominated primarily by luminous red giant stars, for the "inner" halo of M 31 ($R_{proj} < 40$ kpc) are dominated by the GSS (Ferguson et al. 2002; Brown et al. 2007; Ibata et al. 2014). Thus, our star selection criteria will preferentially sample the GSS within the stellar halo. In addition, the GSS can be kinematically

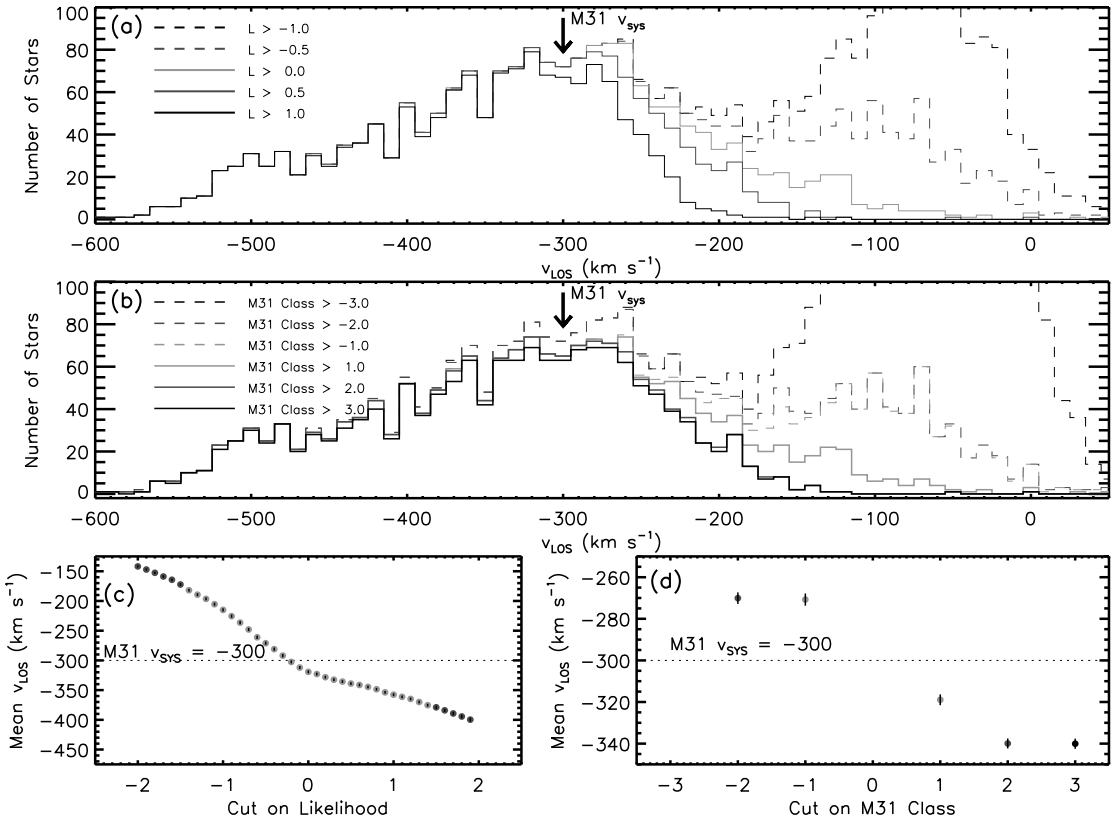

Fig. 3.13.— Exploration of potential bias in the the v_{LOS} distribution induced by the likelihood (L) and m31class parameters of Gilbert et al. (2006). The sample of stars shown here is culled of both dwarf satellite member stars (Section 3.5.1) and kinematically cold components (Section 3.5.3). **(a)** Marginal distributions of heliocentric line-of-sight velocities (v_{LOS}) for a series of cuts on the overall M 31 likelihood (L; Equation 3.10) as indicated by the legend in the upper right of the panel. **(b)** Marginal distributions of v_{LOS} for a series of cuts on $m31class$ as indicated by the legend in the upper right of the panel. **(c)** Mean v_{LOS} calculated for a set of samples with different cuts on L. The standard error on the mean is shown in black and the color coding of the points is such to match the corresponding distribution in (a). **(d)** Mean v_{LOS} calculated for a set of samples with different cuts on $m31class$. As is detailed in the text, those cuts that isolate "cleanest" samples of M 31 stars have the unintended consequence of biasing the overall v_{LOS} distributions to both larger mean blueshifts and to smaller overall dispersions (i.e., a "colder" population).

detected, and kinematically dominate, in numerous fields where it does not dominate in total stellar density, perhaps due to the color and magnitude restrictions of the Keck+DEIMOS targeting, which could preferentially select GSS debris if they are on the near side of the M 31 disk (Gilbert et al. 2009b). As in previous studies global kinematic studies of the M 31 stellar halo (e.g., Gilbert et al. 2012, 2014), those fields with kinematic GSS detections are excluded from our halo sample. Those fields completely removed are: H11, H13d, R06A220, a13, a3, d1, f116, f123, f135, f207, and m4.

In addition to those structures associated with the GSS, Gilbert et al. (2012) further identify coherent velocity peaks embedded within the heliocentric velocity distribution for a number of fields. The stellar halo of a galaxy is thought to be a relatively 'hot' or large dispersion population over its full extent, albeit it has low stellar density. From previous SPLASH work the dispersion of the M 31 halo is $\sigma_{halo} \sim 100 km/s$. Thus, in a random sampling of stars along a line-of-sight in the halo it is reasonable to expect that the velocities of stars be drawn randomly from a Gaussian deviate of width σ_{halo}. In the best case, a single Keck+DEIMOS mask could sample as many as 50 to 100 giant candidates, which implies that at 100% spectroscopic efficiency the resulting distribution of v_{los} for the most luminous stars will poorly sample the parent halo population and most likely resemble a uniform distribution across a large velocity range. Thus, if the marginal distribution for a mask or field contains a clear velocity peak, that peak is an indication of a kinematic substructure.

In the analyses of Gilbert et al. (2012), effort was taken to identify kinematic peaks in all the fields within the SPLASH footprint. With typical widths of less than 10 km s^{-1}, these peaks are kinematically cold, as is typically found for satellite debris streams

(Johnston et al. 2008, and references therein). We note that our ability to identify kinematic substructure is biased toward those substructures that are of small angular width (i.e., to be well sampled in a Keck+DEIMOS FOV), of high surface brightness (i.e., to be well sampled at our limiting magnitude), and of velocity dispersions 10 km s^{-1} (i.e., to be identified as a 'peak'). Physically these kinematic constraints bias detection in the inner halo toward those debris accreted more recently from 'disky' type progenitors on non-circular orbits (Johnston et al. 2008), and in the outer halo we are biased toward old, great circle debris on orbits of large radii. Moreover, we are biased to finding such components in those fields that are better sampled, either due to multiple masks being observed for a field or fields that have permit high spectroscopic efficiency — which could occur for fields at higher stellar density (i.e., small R_{proj}) or for fields with more complete photometric catalogs (i.e., those observed in excellent conditions). The combined effect of these considerations is that the SPLASH survey is systematically more likely to find substructure in the inner halo ($R_{proj} < 90$ kpc or 6°) and was considered in far more detail by Gilbert et al. (2012).

Gilbert et al. (2012) identified several kinematically cold components (*kcc*) and we adopt those identifications for our purposes. Not all of these features, however, have corresponding detections in wide-field photometric studies (e.g., those found in PAndAS summarized in, Ibata et al. 2014) and, without additional observations, no additional properties for these substructures are known. Thus, we adopt an exclusion of all stars within $2\sigma_{kcc}$ of the mean velocity for each *kcc* Those fields with kinematically cold components and the number of stars in each substructure are indicated in Table 3.7. Those Keck+DEIMOS and MMT+Hectospec fields not in Gilbert et al. (2012) were examined and no evidence for *kcc* was found in any field.

Additional masks serendipitously overlap substructures identified as photometric

overdensities in surveys with wider angular coverage, two examples being Stream E and Stream F from Tanaka et al. (2010). The kinematic sample for these fields reveals no corresponding signature of a kinematic cold component. These masks were not explicitly designed to target these features and the lack of a corresponding detection could stem from any number of the considerations previously discussed regarding our ability to detect debris. Without a clear kinematic peak, there is no objective means to disentangle substructure member stars for removal from our sample. Thus, the M 31 halo sample for these masks are used in their entirety. Those fields with photometric substructures and no corresponding kinematic detection are indicated in Table 3.7 with no stars identified in the *kcc* column.

Additional exploration of the criteria used to produce a clean halo sample will be presented in Section 3.6. In Section 3.6.3, the empirical substructure tests developed for the dwarf satellite galaxy and globular cluster sample (presented in Section 3.3.4) will be applied to understand the potential effects of undetected substructure. Those stars culled from the halo sample as discussed in this Section will be used in the substructure sample for the empirical substructure analyses.

3.5.4 Selecting M 31 Halo Members

With dwarf satellite galaxy members and substructure culled from the sample and L and $m31class$ diagnostics computed for each star, we can now select an appropriate sample of halo stars for the transverse motion analysis. Given the discussions of L and $m31class$, we adopt $m31class > 0$ to produce our halo sample. This includes all stars that are likely M 31 giants (i.e., $L > 0$), and ensures that those stars have $(V - I)_\circ$ colors consistent with fiducial M 31 isochrones (i.e., $-0.05 \geq X_{CMD}$).

It is worth noting that this $m31class$ criteria is a less restrictive than that adopted

for study of the global properties of the M 31 halo by Gilbert et al. (2012, 2014). The motivation for a less restrictive cut than Gilbert et al. (2012, 2014) is demonstrated by Figure 3.13. Figures 3.13a and 3.13b are marginal distributions for v_{LOS} after a series of cuts on the diagnostics L and $m31class$, respectively. In Figures 3.13a and 3.13b designations for high probability MW dwarfs are dashed and for high probability M 31 giants are solid. From visual inspection of Figures 3.13a and 3.13b, it is evident that choices of L or $m31class$ that produce the most secure samples of M 31 red giants have the consequence of altering the distribution of v_{los}; more specifically, the distribution shifts systematically to more negative velocities and becomes overall more asymmetric. The shift to more negative velocities in the v_{los} distribution for more secure M 31 giant samples is demonstrated in Figures 3.13c and 3.13d, which compares the mean line-of-sight velocity computed for restrictions on L and $m31class$.

From inspection of the panels of Figure 3.13, it is evident that the most secure sample of stars will bias our study of the transverse motion of M 31. More specifically, the systemic velocity of M 31, v_{sys}, measured in the transverse motion fit is effectively the mean velocity of the input sample. On the other hand, providing too lenient a restriction on the diagnostics will contaminate the halo sample with foreground MW dwarfs, which will also induce bias to our measurement. The compromise of $m31class > 0$ both provides a sample dominated by likely M 31 halo stars and only minimally biases the mean velocity of the sample. Moreover, while the distribution for $m31class > 0$ is not completely symmetric about the systemic line-of-sight velocity of M 31 v_{sys}, the positive velocity tail is reasonably populated.

With these considerations in mind, we define the M 31 halo sample as those stars with $m31class > 0$. The spectra for all stars with exceptionally large velocities relative to M 31 (e.g., $\Delta v_{LOS} > -300 km/s$) are inspected visually and those found to

have an Na D $\lambda 8200\mathring{A}$ feature are removed. The mean velocity of our input sample is -318 m s^1. The final sample contains 697 stars distributed in angular radius of $0.65° < \rho < 28.8°$. The number of M 31 halo stars for each field are given in Table 3.7.

3.6 M 31 Transverse Motion from its Halo Stars

Having selected a sample of M 31 halo member stars from the SPLASH project, we know proceed to measure the transverse motion of M 31 in Section 3.6.1. We then proceed to use Monte Carlo simulations to explore sources of bias that come in the following categories: (i) bias from M 31 star selection (Section 3.6.2, and (ii) bias from unknown substructure (Section 3.6.3). The efforts of this section are discussed and summarized in Section 3.6.4.

3.6.1 Initial Result

We use the identical transverse motion measurement procedure described for the dwarf satellite galaxies and globular clusters in Section 3.3.3. The resulting transverse motion is: (v_{sys},v_W,v_N) = (-323.8 ± 7.4 km s^{-1}, -67.6 ± 8.1 km s^{-1}, +74.8 ± 7.7 km s^{-1}) with σ_{pec} = 103.9 km s^{-1}, where the errors are derived from the Monte Carlo simulations described previously. This number agrees with our earlier measurement from the dwarf satellites and globular clusters within the quoted uncertainties on those measurements. We note that the uncertainties derived from the Monte Carlo technique are small, all being less than 10 km s^{-1}, but do not include any systematic uncertainty.

The resulting v_{sys} is offset from the well measured line-of-sight velocity of the M 31 center by Δv_{sys} = 24 km s^{-1}, but is consistent with the mean v_{los} of the input

halo star sample (see Figure 3.13d). While this is, at first, alarming, the transverse measurement technique should fit $v_{sys} \sim \mathrm{Mean}(v_{LOS})$. Nevertheless, we adapt our fitting procedure to fix v_{sys} to -300 km s^{-1} and then only fit for v_W and v_N, but following the identical fitting and uncertainty procedure. This results in a solution of (v_W,v_N) = (-0.6 $\pm$ 8.0 km s^{-1}, +48.2 $\pm$ 7.6 km s^{-1}) with σ_{pec} = 104 km s^{-1}, which is significantly different from our initial result. An offset of similar magnitude in v_{sys} has been fit for the dwarf satellite galaxy and globular cluster sample both in prior work by vdMG08 and vdM12 and in our measurement in Section 3.3.3, and in all cases the v_{sys} is statistically consistent with the mean velocity of the input sample. In those instances, however, the three dimensional motions were statistically consistent with the results obtained by fixing v_{sys} to the observed value. Given our small measurement uncertainties, our results do not. No consideration, however, has been given to any systematic uncertainty in the measurement for our sample. We proceed to investigate potential sources of systematic uncertainty from our sample selection in the following sections

3.6.2 Bias from M 31 Halo Star Selection

While extreme care has gone into the creation of a M 31 halo star sample using all available data products in the SPLASH project, it is still meaningful to test if these cuts could cause a systematic bias in the resulting measurements. For our purposes, there should be no significant bias from the spectroscopic targeting selection function, as has been demonstrated in the global structure fits of Gilbert et al. (2012, 2014). We therefore focus on that selection that occurs from within our full stellar spectroscopic selection, i.e., the process of identifying M 31 halo member stars. The sources of star selection bias are threefold: (i) bias from known substructure, i.e., the *kcc* criteria,

(Section 3.6.2), (ii) bias from the likelihood selection, $L > 0$ (Section 3.6.2), and (iii) bias from the $m31class$ selection, $m31class > 0$ (Section 3.6.2). Each of these biases will be explored by changing the restrictions on the input sample and rerunning the transverse motion measurement of Section 3.6.1. In each of the tests that follow, only the parameter of interest is varied, the remaining parameters are held fixed to those values of Section 3.6.1. The ensemble of measurements will be compared to the initial result to understand how the M 31 halo star selection could bias the measured transverse motion.

Inclusion of all Substructure

As a first test, we measure the tangential motion of M 31 without the exclusion of fields dominated by substructure and using several variants on our measurement scheme. These will be used as the limiting cases in the discussions to follow.

First, we augment the halo sample with the inclusion of the those stars in dwarf satellite galaxies, fields dominated by the GSS, and the *kcc*, with the result: (v_{sys},v_W,v_N) = (-413.5 ± 6.5 km s^{-1}, -200.4 ± 4.4 km s^{-1}, -74.8 ± 3.5 km s^{-1}) with σ_{pec} = 98.6 km s^{-1}. This augmentation results in significantly larger negative heliocentric velocities for all three motion components, most notably v_{sys} is now offset from the true value by $\Delta v_{sys} = 113.5$ km s^{-1}. In number, the dwarf spheroidal stars dominate this substructure sample, and could be responsible for the larger motions. Thus, we augment the halo sample with just those fields dominated by the GSS and the stars associated with *kcc* with the result of: (v_{sys},v_W,v_N) = (-326.6 ± 6.0 km s^{-1}, -84.8 ± 4.8 km s^{-1}, $+228.15 \pm 5.2$ km s^{-1}) with $\sigma_{pec} = 87.0$ km s^{-1}, which while resolving concerns over v_{sys} still strongly change the transverse motion. We also fix v_{sys} = 300 km s^{-1} to obtain: (v_W,v_N) = (-121.5 ± 3.8 km s^{-1}, -95.9 ± 3.7 km s^{-1}) with σ_{pec}

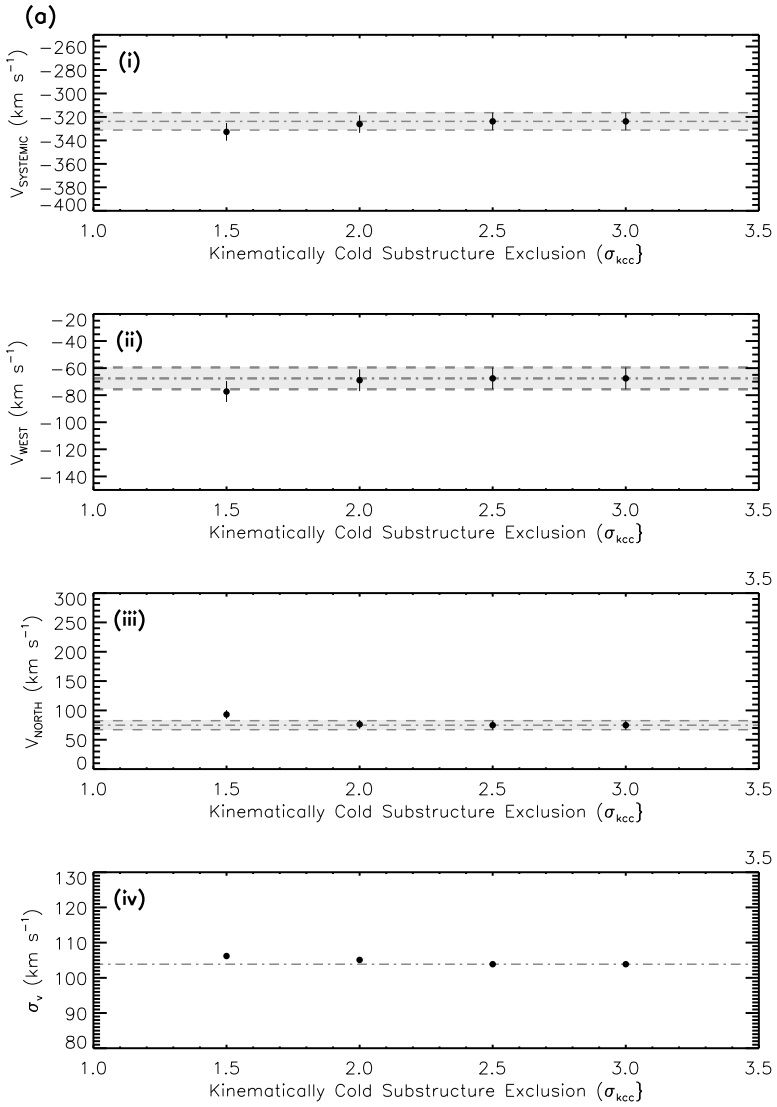

Fig. 3.14.— Exploration of potential bias in the three dimensional M 31 center-of-mass motion induced by the halo giant selection criteria for a range of cuts on those criteria. In each sub-figure a - c, the individual panels show the behavior of (i) v_sys, (ii) v_west, (iii) v_north, and (iv) σ. **(a)** Exclusion of kinematically cold components (kcc) using the proximity to the peak in terms of its dispersion (Section 3.5.3). **(b)** Constriction on overall likelihood (L; Equation 3.10). **(c)** Constriction on $m31class$ (Section 3.5.2). The parameter tested in each of the sub-panels is studied holding all other parameters fixed. Inferences from these tests are discussed in Sections 3.6.2, 3.6.2, and 3.6.2 for each of the sub-panels a, b, c, respectively.

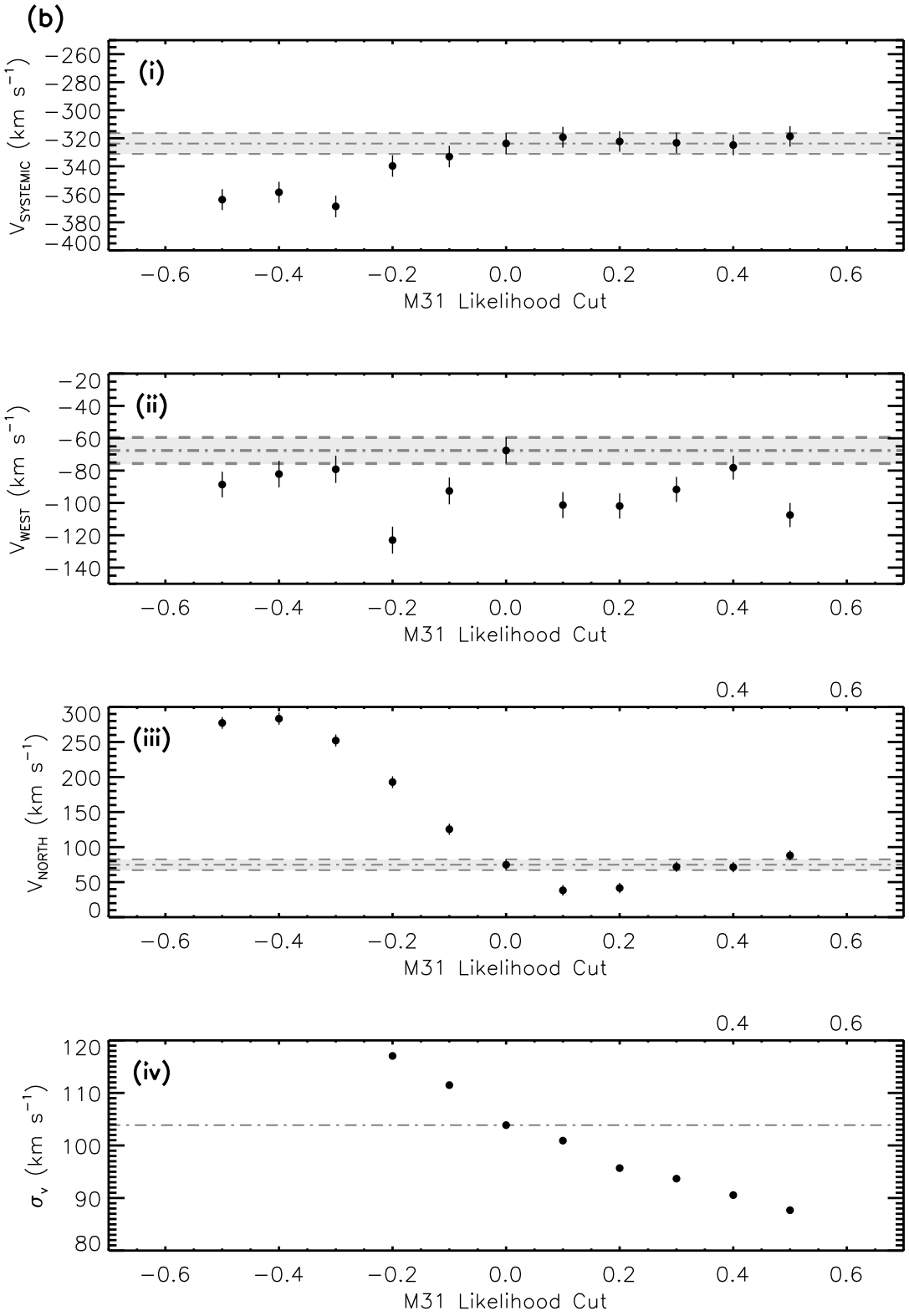

Fig. 3.14.— cont. Exploration of potential bias from the constriction of L selection criterion.

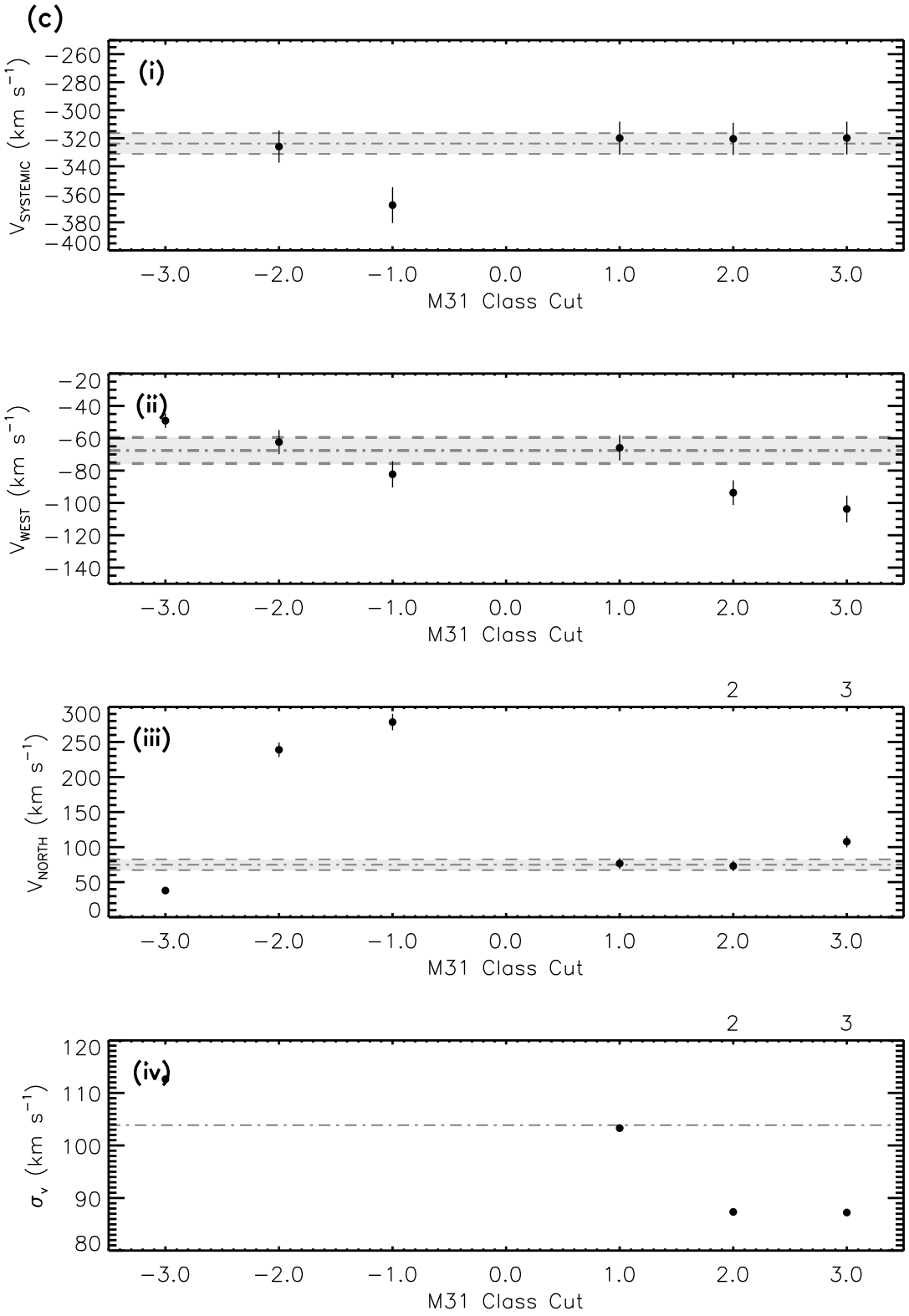

Fig. 3.14.— cont. Exploration of potential bias from the constriction of the $m31class$ selection criterion.

= 99.2 km s^{-1}, and (v_W,v_N) = (−857.3.4 ± 21.9 km s^{-1}, +319.5 ± 16.2 km s^{-1}) with σ_{pec} = 352. km s^{-1}, for the two cases of augmenting the sample with all substructure and just the GSS and *kcc*, respectively. While the former is reasonable, the later is clearly non physical and we can be confident that the exclusion of the GSS dominated fields, which dominate the *kcc* in number, was prudent.

For demonstration, we also measure the transverse motion with just the substructure fields and without the halo fields. The result of fitting to dwarf satellite galaxies, fields dominated by the GSS, and those flagged as *kcc* is: (v_{sys},v_W,v_N) = (−413.5 ± 6.5 km s^{-1}, −200.4 ± 4.4 km s^{-1}, −74.8 ± 3.5 km s^{-1}) with σ_{pec} = 98.6 km s^{-1}. The result of fitting to fields dominated by the GSS and the *kcc* is: (v_{sys},v_W,v_N) = (−355.7 ± 6.6 km s^{-1}, −483. ± 7.6 km s^{-1}, +2515.9 ± 35.9 km s^{-1}) with σ_{pec} = 46.9 km s^{-1}. Given the large v_{sys} in both cases, we also fix v_{sys} = 300 km s^{-1} to obtain: (v_W,v_N) = (−137.2 ± 4.2 km s^{-1}, −114.6 ± 4.2 km s^{-1}) with σ_{pec} = 96.5 km s^{-1}, and (v_W,v_N) = (−1238 ± 31 km s^{-1}, +2209 ± 37 km s^{-1}) with σ_{pec} = 351 km s^{-1}, for the two cases respectively. Again, the results for fitting just the GSS fields produce non-physical results, where as for the combined GSS and dwarf satellite sample, the result not unrealistic. This is not surprising, given that the dwarf satellites, on average, have small velocity dispersions about their systemic motion, and we have already demonstrated the efficacy of measuring the transverse motion to the sample of these same systemic velocities. The sampling of the dwarf satellites, however, is not uniform and some have hundreds of member stars. This over or under sampling, effectively, acts as a weighting function when we fit to individual stars, giving preference to those dwarfs that are better sampled. The inclusion of the satellite stars in theory should not dramatically change our results. It does, in fact, bias our result by having large numbers of stars with the same motion, i.e., the effect we anticipate

from substructure bias.

Thus, we have demonstrated that the inclusion of the GSS fields and the dwarf spheroidal stars in our tangential motion measurement does in fact introduce a strong bias in the result. Moreover, we note that even the non-physical solutions have small uncertainties, which is additional motivation for the remaining probes for systematic uncertainty presented in this Section.

Tests for Bias from Known Substructure

Stars associated with kinematically cold components (*kcc*) were identified using their separation (Δv_{los}) from the estimated systemic velocity of the *kcc* determined by Gilbert et al. (2012). In Figure 3.14a, we vary Δv_{los} from $3\sigma_{kcc}$ to $1.0\sigma_{kcc}$ in steps of $0.5\sigma_{kcc}$ and measure the transverse motion for each resulting sample. The sub-panels of Figure 3.14a show the evolution of (i) v_{sys}, (ii) v_W, (iii) v_N, and (iv) σ_{pec} compared to those values and 1-σ ranges determined in Section 3.6.1. From inspection, only when stars that satisfy $1.0\sigma_{kcc} < v_{los} < 1.5\sigma_{kcc}$ does the transverse motion deviate by more than $1\sigma_{kcc}$ from the initial result. Considering our adopted selection of $3\sigma_{kcc}$, we do not consider our transverse motion measurement to be biased due to known substructure.

Tests for Bias from Likelihood

To estimate the effects of restricting the M 31 halo sample by L on the measured transverse motion, we repeat the measurement of Section 3.6.1 using different values of L. The results of this test are given in Figure 3.14b for (i) v_{sys}, (ii) v_W, (iii) v_N, and (iv) σ_{pec} compared to those values and 1-σ ranges for the tangential motion determined in Section 3.6.1. The L test is only performed over the range for which

the L characteristic is marginally effective, (i.e., $-0.5 \leq L \leq 0.5$). From Figure 3.14b sub-panel (i), we note that v_{sys} remains constant for $L > 0$ and becomes steadily more negative with $L < 0$. Similar monotonic behavior is observed v_N (Figure 3.14b, sub-panel iii); more specifically, v_N systematically and sharply decreases (to first order) as the L cut becomes more restrictive, but the behavior is relatively steady beyond and within 2σ of our adopted value $L > 0$. The behavior of v_W (Figure 3.14b, sub-panel ii), however, is erratic even for more "secure" M 31 halo selections (i.e., increasing cuts on $L > 0$). Thus, the net effect of more restrictive cuts on L than those adopted is change the value of v_W, which also would affect the net transverse motion (v_t) and its direction (Θ_t). We do not, however, find evidence in this exploration for either adopting a different membership criterion or clear means of estimating a systematic error for our selection on L.

Tests for Bias from $m31class$

To estimate the effects of restricting the M 31 halo sample by $m31class$ on the measured transverse motion, we repeat the measurement of Section 3.6.1 using different values of $m31class$. The results of this test are given in Figure 3.14c for (i) v_{sys}, (ii) v_W, (iii) v_N, and (iv) σ_{pec} compared to those values and 1-σ ranges determined in Section 3.6.1. The behavior of the fitted parameters with $m31class$ is to first order similar to that noted for L. In all sub-panels the transverse motions are relatively stable for more restrictive cuts, albeit with some strong deviations for the most restrictive case of $m31class = +3$. On the whole, however, changing the $m31class$ to be more restrictive does not have a strong effect on the measured parameters, while being less restrictive has some effect.

3.6.3 Empirical Test for Substructure

We use the empirical substructure estimates developed in Section 3.3.4. As in 3.3.4 we run the test in two modes: "replacement" for which a fraction of objects in our halo sample are randomly replaced with those classified as substructure, and "augmentation" for which objects in the substructure sample are added to our halo sample. There are 693 objects in our clean sample and 2303 objects in the substructure sample, which come from dwarf satellite member stars, fields dominated by the GSS, and kinematically cold components identified in individual fields. The detailed breakdown of these sub-classifications are given in a field by field manner in Table 3.8.

The results of this the empirical substructure measurement are given in Figure 3.15a and 3.15b, for the 'additive' and 'replacement' tests, respectively. The distributions for each of the measured parameters, v_{sys}, v_W and v_N, are given in the sub-panels i, ii, and iii, in which results from individual Monte Carlo realizations are shown in light grey with the mean and dispersion over plotted in in black. The results from the fit in Section 3.6.1 are given by the dash-dot grey line in each panel and the 1σ range shaded in grey (and bounded by the dashed lines). For our purposes we consider a mean value that falls outside of the 1σ parameter space to be a significantly biased result. We note that the additive and replacement procedures are statistically identical in terms of total substructure contamination at 100% contamination additively and 50% contamination in replacement and we confirm that the results consistent at these two points.

For the additive case (Figure 3.15a), the transverse motion deviates from 1σ at a relatively low substructure contamination fraction. For the individual sub-panels the deviations occur: (i) at 20% added substructure, (ii) at 10% added substructure, and (iii) at 5% added substructure for v_{sys}, v_W, v_N, respectively. Thus, for the

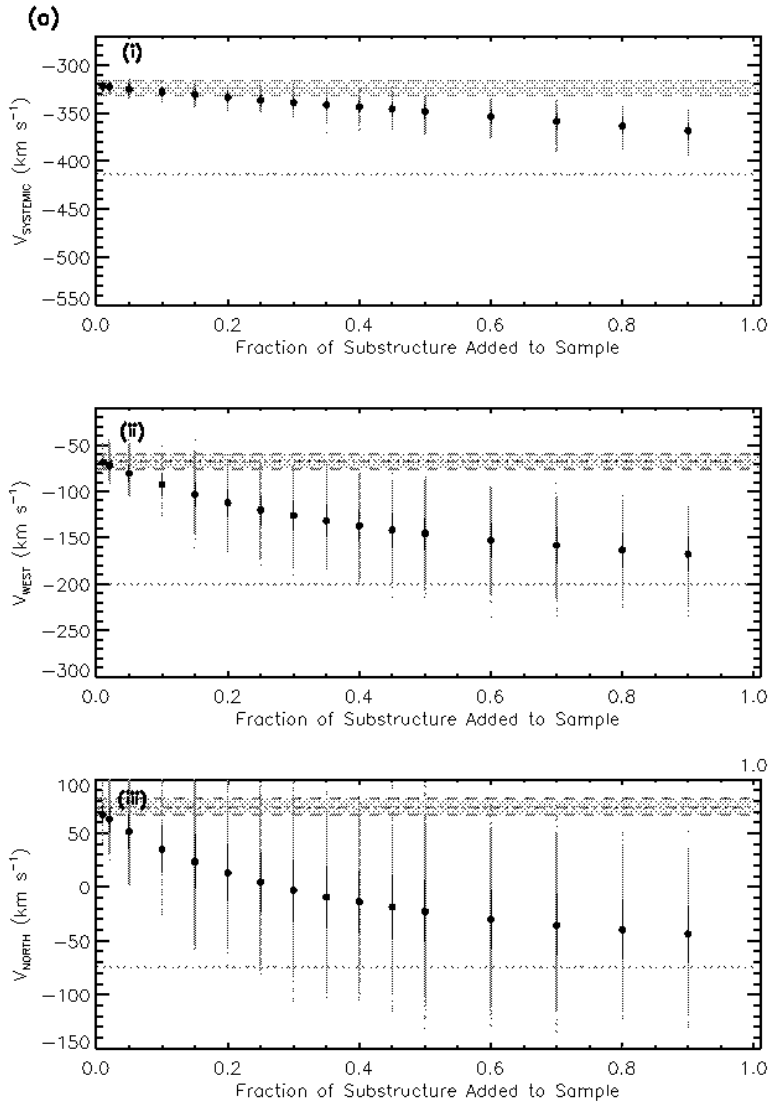

Fig. 3.15.— Exploration of potential bias in the three dimensional bulk center-of-mass motion of M 31 induced by unidentified substructure, for the three components: (panel i) v_{sys}, (panel ii) v_{west}, (panel iii) v_{north}, as they are fractionally contaminated by known substructure using the additive (sub-fig a) and replacement (sub-fig b) techniques. Individual results from the Monte Carlo procedure described in Section **??** are shown for each substructure fraction as light grey points. The mean and one standard deviation (1σ) range for each substructure fraction is overplotted in black. The value determined by our fit (e.g., that of Section **??**) is the horizontal dot-dash line and the 1σ range is shaded between the dashed horizontal lines. The grey dashed line in each panel represents the result of a fit that includes both the substructure and halo samples. **(a)** Results of the additive substructure technique by which the normal sample is supplemented with objects from the known substructure sample. For all three parameters, the a contamination fraction $>\sim$10% significantly bias the result. **(b)** Results of the replacement substructure technique by which the objects in the normal sample are replaced randomly by objects from the substructure sample. Contamination fractions $>\sim$5% result in a 1σ disagreement from the initial result.

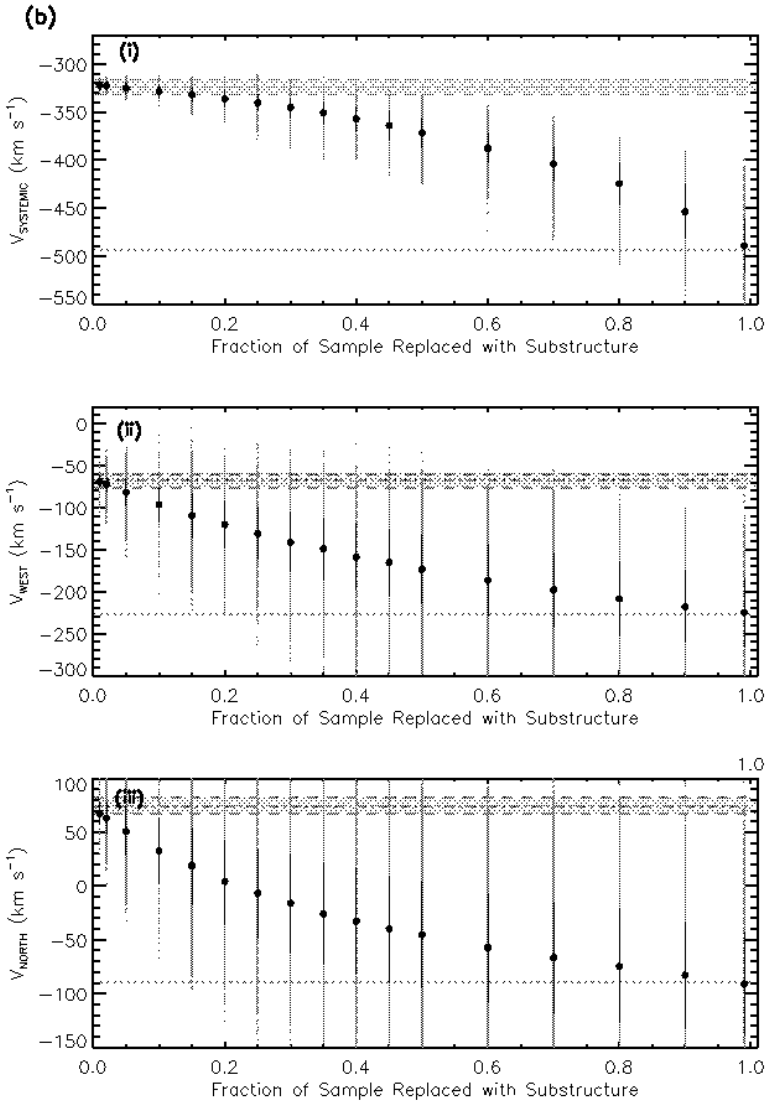

Fig. 3.15.— cont. **(b)** Results of the replacement substructure technique by which the objects in the normal sample are replaced randomly by objects from the substructure sample. Contamination fractions $>\sim$5% result in a 1σ disagreement from the initial result.

addition of substructure to our halo sample even at relatively small levels will 'pull' the transverse motion measurement out of its 1σ range. While the v_{sys} continues to grow more negative as the substructure fraction increases, both v_W and v_N seem to approach an asymptotic value of ~ -160 km s^{-1} and ~ -30 km s^{-1}, respectively at $\approx$50% added contamination. These asymptotic values are consistent with our transverse motion measurements using the full substructure sample.

For the replacement case, Figure 3.15b, similar behavior is observed as for the additive case (Figure 3.15a). More specifically, deviations beyond 1σ occur: (i) at 25% replacement, (ii) at 10% replacement, and (iii) 10% replacement for v_{sys}, v_W, v_N, respectively. Again, the transverse motion is 'pulled' out of the 1σ range at relatively low contamination levels. While the v_{sys} continues to grow more negative as the substructure fraction increases, both v_W and v_N seem to approach an asymptotic value of ~ -200 km s^{-1} and ~ -70 km s^{-1}, respectively at $\approx$50% contamination. These asymptotic values are consistent with our transverse motion measurements using the full substructure sample.

3.6.4 Discussion & Summary

In the preceding sections we first estimated the transverse motion of M 31 and explored sources of bias in this number in both the M 31 halo star selection criteria and the potential role of substructure contamination. In tests of the former, no compelling evidence emerged that our selection criteria induced any biases in the resulting transverse measurements and suggested that the chosen criteria could be restricted further without significant changes to the final transverse motion measurement. In tests of the latter, the transverse motions from the halo stars were found to be sensitive to substructure at relatively low levels, $\sim$10%. A relevant question to pose is if there

is evidence that the SPLASH halo sample, as currently defined, contains potential substructure sample at a level greater than 10%?

An Estimate of Substructure Contamination in the Halo Sample

As previously discussed, Gilbert et al. (2012) put careful consideration into substructure contamination for the fitting of a surface brightness profile to the kinematically confirmed M 31 halo populations. As such, Gilbert et al. (2012) identified a number of *kcc* features within 90 kpc, as well as removing several fields that were kinematically dominated by GSS debris — all of which we remove from the sample considered here. We demonstrated that our removal of the known *kcc* was sufficient to not bias our result. Thus, we are confident that the identified substructure within 90 kpc have been culled from our sample. Likewise, the sampling of individual lines-of-sight within 90 kpc is sufficient to identify *kcc*, but, as previously discussed, is biased *against* warmer kinematical populations. In the surface brightness profile of Gilbert et al. (2012), there is relatively little variation in field-to-field surface brightness estimates within 90 kpc, suggestive that any large substructures have been systematically removed. Thus, we adopt a conservative upper limit for 'missed' substructure at 10% for those objects within 90 kpc.

Beyond 90 kpc, Gilbert et al. (2012) sees large field-by-field variations in the surface brightness estimates, which would be expected if the field placement was serendipitously sampling substructure. Approximately 6 of the 23 fields beyond 90 kpc deviated from the smooth halo profile by more than $\Delta\mu$=0.5 mag arcsec^{-2}. While the overall number of stars is higher in these fields, there is no identifiable kinematical coherence without a more complete sample of stars at these locations. Using the star counts in individual fields, approximately 25% of the total sample beyond 90 kpc in

Gilbert et al. (2012) are 'excess' over the best fit surface brightness profile. While we have not yet folded our new M 31 members from the outer halo campaign into the Gilbert et al. (2012) analysis, we conservatively adopt a substructure contamination rate of 25% for those fields beyond 90 kpc.

In summary, we used structure from surface brightness profile of Gilbert et al. (2012) to the SPLASH dataset (sans the outer halo campaign of this work) to place conservative upper limits on the fractional substructure contamination of our halo sample. A deeper investigation of this issue is beyond the scope of this work. The substructure fraction upper limits are 10% within 90 kpc and 25% beyond 90 kpc. Our halo sample contains a total of 697 stars, 483 of which have $R_{proj} \leq 90$ kpc and 214 of which have $R_{proj} > 90$ kpc ($\rho > 6°$). Using our estimates for the inner and outer populations, this results in a contamination of ∼48 stars within 90 kpc and a contamination of ∼53 stars beyond 90 kpc. Our total estimation of substructure contamination is approximately 101 stars, or 15% of our total sample of 697 halo stars.

From Section 3.6.3, our current 1σ measurement uncertainties are only consistent with a contamination fraction from ∼10%, though the exact fractions depend on the substructure test and the motion component studied. Thus, our conservative substructure contamination fraction of 15% exceeds that permitted from the measurement errors, which provides sufficient motivation to estimate a systematic uncertainty using our empirical substructure simulations.

A Systematic Uncertainty

To estimate the systematic uncertainty for the transverse motion measurement, we will compare our transverse motion result to the mean transverse motion estimated at

a 15% contamination level in both empirical substructure simulations (Section 3.6.3). For the 'additive' and 'replacement' substructure simulations the mean transverse motion at 15% contamination are as follows: (v_{sys},v_W,v_N) = (-331 km s^{-1}, -103 km s^{-1}, 23.6 km s^{-1}) and (v_{sys},v_W,v_N) = (-332 km s^{-1}, -109 km s^{-1}, 19 km s^{-1}), respectively. For all three motion components, the 'replacement' technique has the largest deviation from our initial result and we compute the difference to be, (Δv_{sys},Δv_W,Δv_N) = (-9 km s^{-1}, -41 km s^{-1}, -56 km s^{-1}), which we adopt as our conservative systematic uncertainty in each parameter.

For each motion component, the systematic uncertainty is larger than the measurement uncertainties, which are (σv_{sys},σv_W,σv_N) = (7.4 km s^{-1}, 8.1 km s^{-1}, 7.7 km s^{-1}). We add the two uncertainties in quadrature to obtain combined uncertainty of (σv_{sys},σv_W,σv_N) = (12.6 km s^{-1}, 41.8 km s^{-1}, 56.7 km s^{-1})

Final Transverse Motion Estimate

With considerations for the sources of bias explored and quantified, our final transverse motion estimate is: (v_{sys},v_W,v_N) = (-323.8 $\pm$ 12.6 km s^{-1}, -67.6 $\pm$ 41.8 km s^{-1}, +74.8 $\pm$ 56.7 km s^{-1}) with σ = 103.9 km s^{-1}.

3.7 Discussion

We compare our final result for the satellites and globular clusters and the SPLASH halo stars to those measured in vdMG08 and vdM12. All of the individual transverse motions, those measured in this work, those measured from the three-dimensional motions of IC 10 and M 33 and the distant Local Group satellites from vdMG08, and those calculated from the direct proper motions of Sohn et al. (2012) given in vdM12, are given in Table 3.8. These transverse motion measurements, v_N and v_W are also

given in Figure 3.16a, in which the structural component probed is indicated by the symbol — stars in the inner halo as squares, the satellites as circles, and the halo stars as a diamond — and the symbol colors indicate the origin of the measurements — red for vdMG08, yellow for vdM12, and blue for this work, which broadly correspond to the technique employed, statistical inferences from satellites in vdMG08, direct proper motions in vdM12, and line-of-sight tracers used in this work.

It is currently unknown if the stellar populations comprising the 'smooth' halo would have a net rotational motion. Since most satellite debris stripped and follow the orbit of their progenitor, the problem relates to the motions of the infalling satellites. If the 'smooth' halo is dominated by debris that still maintain a memory of its original motion, then it is feasible.

For demonstration, we compute the error weighted means for each tracer population and compare them to the result for halo stars in Figure 3.16b. These error weighted mean values are also given in Table 3.8. We note that the errors on our single halo measurement are comparable to those of the mean values for techniques applied to the satellite and inner halo tracer populations. We then compute the error weighted mean for all measures, resulting in: (v_W,v_N) = (-96.4± 22.4 km s^{-1}, -44.7 ± 25.4 km s^{-1}), which is shown in bold black in Figure 3.16b and given in Table 3.8.

We note that the measurement we obtained by fixing $v_{sys} = -300$ km s^{-1} is very similar in magnitude and direction to that of our final error weighted result. While these similarities are compelling, it would be unwise to alter our methodology ex post facto, but consideration should be given to fixing v_{sys} in future applications of measuring transverse motions from the line-of-sight velocities.

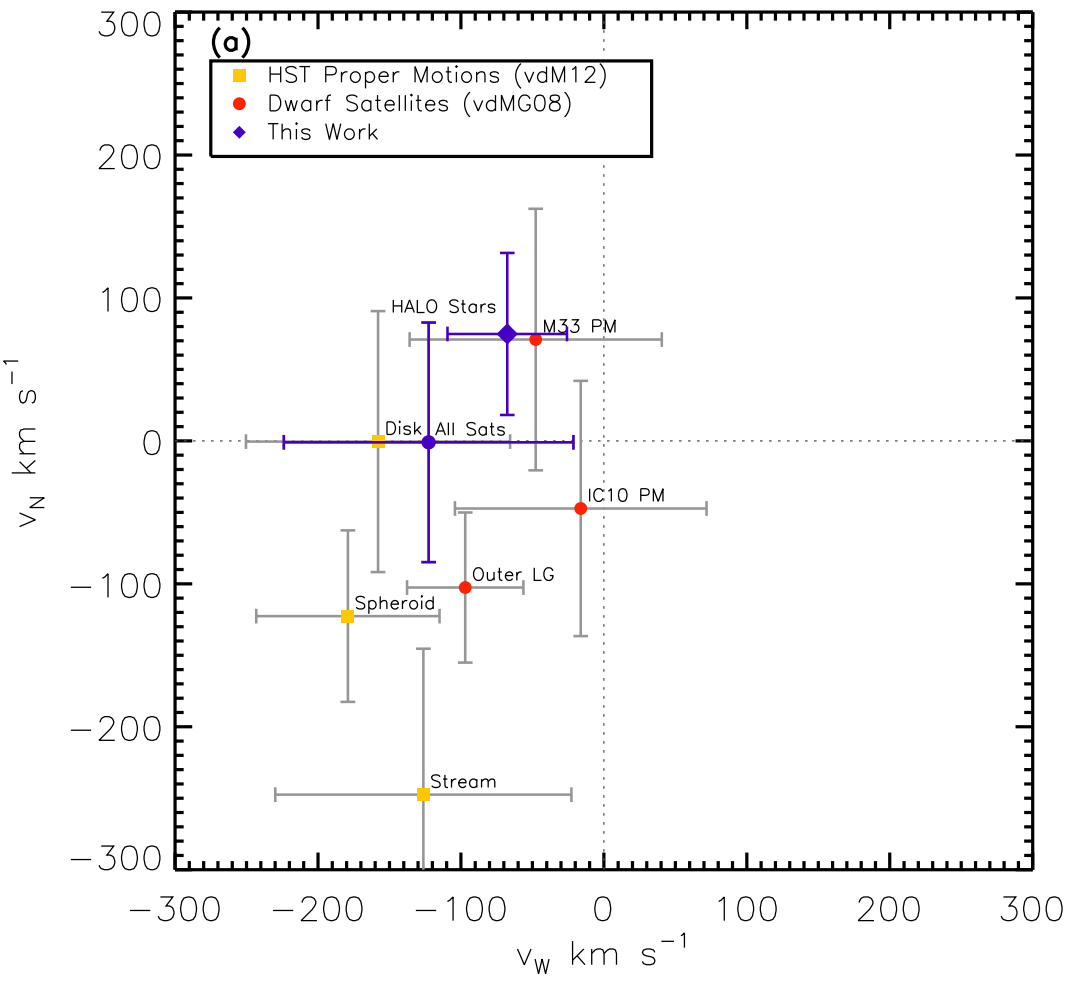

Fig. 3.16.— Transverse motion, v_W, v_N, measurements for M 31. **(a)** Measurements from different techniques using individual tracers: direct HST proper motions (square), statistical tests using the motions of dwarf satellite galaxies (circles), and that of the halo stars (five pointed star). Each point is color-coded based on the source of the measurement, either vdM12 (yellow), vdMG08 (red), this work (blue). **(b)** Error weighted mean measurements for the following: all techniques employing the satellites (circle), all of the direct HST proper motion measurements (square), and the halo stars (star). The final error weighted mean transverse motion is shown in black. Both the individual measurements and the mean values are given in Table 3.7.

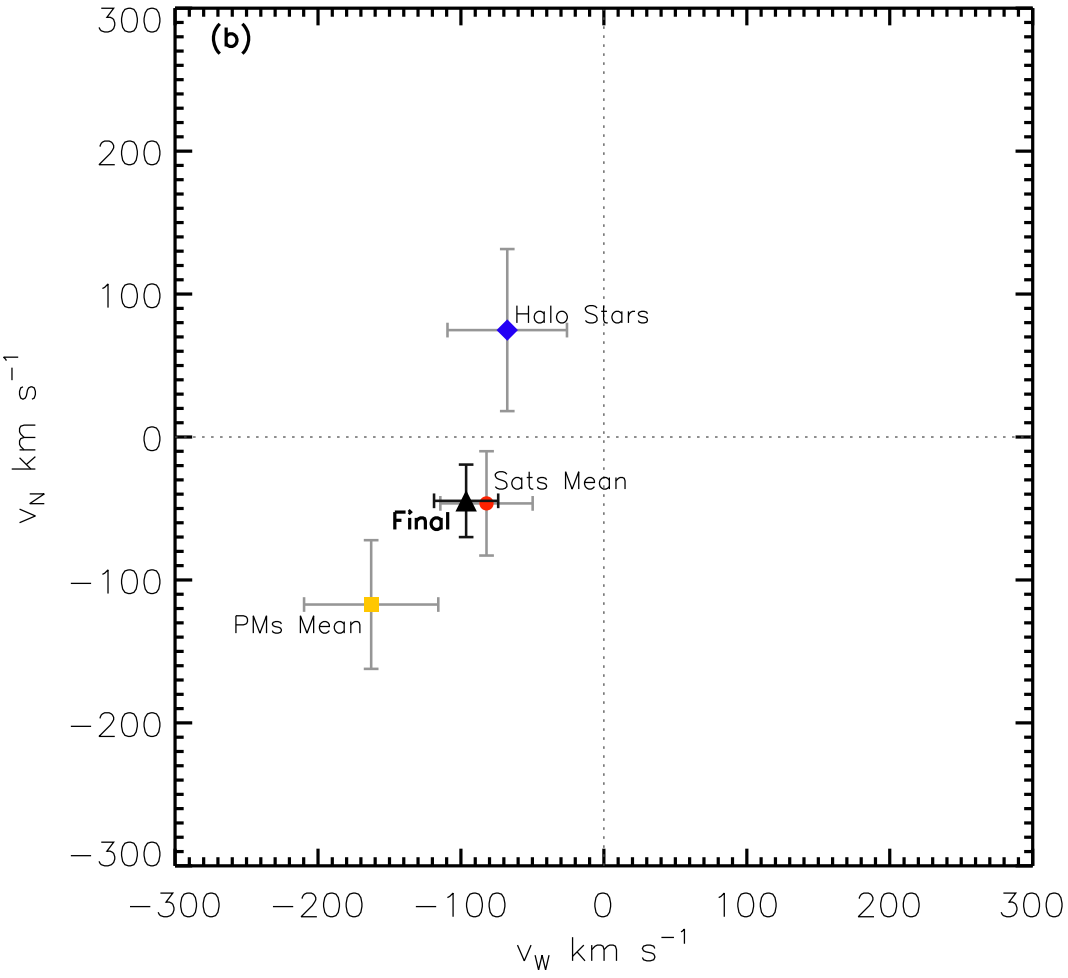

Fig. 3.16.— cont. **(b)** Error weighted mean measurements for the following: all techniques employing the satellites (circle), all of the direct HST proper motion measurements (square), and the halo stars (star). The final error weighted mean transverse motion is shown in black. Both the individual measurements and the mean values are given in Table 3.7.

3.8 Summary

1. The transverse motion of M 31 is measured using the line-of-sight motions of its dwarf satellite galaxies and outer halo Globular Clusters ($\rho > 5°$). The result is consistent with prior measurements in vdMG08 and vdM12, but with slightly reduced measurement uncertainty. As in previous work, the overall agreement between this and other techniques suggests that the internal motions of these objects are not the dominant term in their motion.

2. We develop an empirical technique to test for systematic bias in our transverse motion fitting technique from unidentified substructure, by fractionally contaminating the 'substructure free' sample with those objects in identified substructure. We find that our measurement from satellites and Globular Clusters is not biased by substructure to a contamination fraction of 50%.

3. A targeted observational campaign in the outer halo of M 31 is described that relies upon the Washington+$DDO51$ filter system to identify high probability M 31 member stars from photometry alone. The campaign results in the construction of the largest sample of stars at these projected radii ($R_{proj} > 120$kpc) in any halo.

4. Owing to new observations obtained with MMT+Hectospec, the diagnostic techniques developed for Keck+DEIMOS are successfully adapted for lower resolution spectra. The success suggests that these instruments could support efforts to further constrain the stellar halo at large radii by producing large samples of stars at these surface brightnesses.

5. After the removal of known substructures, the tangential motion of M 31 is measured using the line-of-sight velocities of its halo member stars, and no

systematic bias is found in our M 31 halo star selection criteria.

6. The empirical substructure test is applied to the halo star sample to find it biased beyond the 1σ measurement uncertainty at relatively low contamination fractions. We use the surface brightness profile fluctuations beyond R_{proj} =90 kpc found in Gilbert et al. (2012) to estimate our substructure contamination at these radii, for which sampling is insufficient for the detection of kinematically cold components (*kcc*). This estimate is then used to estimate a systematic uncertainty and appropriately adjust our final uncertainty in the transverse motion measurement.

7. The transverse motions derived in this work are compared to those in previous studies and found to be in agreement. This observation alone argues against the 'smooth' halo having a strong rotation component, although more detailed tests on the M 31 halo stars with the transverse motion removed should be attempted.

Table 3.1. Satellites and Outer Halo Globular Clusters

Name	Morphological Type	ρ (deg)	ϕ (deg)	v_{HELIO}	Substructure Association	Velocity Reference	Previous Use for Tan. Motion
M 32	dE	0.40	-178.87	-205 ± 3			vdMG08, vdM12
NGC 205	dE	0.61	-46.66	-244 ± 3			vdMG08, vdM12
And IX	dSph	2.69	43.42	-209 ± 3		T12	vdMG08, vdM12
And XVII	dSph	3.22	-18.19	-251 ± 2		C13	
And I	dSph	3.28	169.87	-380 ± 2		K10	vdMG08, vdM12
And XXVII	dSph	4.23	-12.70	-539 ± 4		C13	
And III	dSph	4.97	-163.12	-344 ± 10		T12	vdMG08, vdM12
HEC13	GC	5.04	142.06	-366 ± 6	Stream C	V14	
PAndAS-12	GC	5.06	-64.15	-472 ± 5	NW stream	V14	
H15	GC	5.41	-174.58	-367 ± 10		V14	
And X	dSph	5.61	48.91	-164 ± 3		K10	vdMG08, vdm12
PAndAS-52	GC	5.71	75.85	-297 ± 9		V14	
H10	GC	5.74	-166.17	-352 ± 9		V14	
B518	GC	5.74	-110.07	-200 ± 48		G07	vdM12
And XXV	dSph	6.02	-20.97	-107 ± 1		C13	
PAndAS-11	GC	6.09	-54.30	-447 ± 13	NW stream	V14	
PAndAS-07	GC	6.29	-102.77	-452 ± 18	SW cloud	V14	
PAndAS-14	GC	6.31	-135.14	-363 ± 9	SW cloud	V14	
PAndAS-08	GC	6.46	-114.96	-416 ± 8	SW cloud	V14	
PAndAS-10	GC	6.59	-51.08	-435 ± 10	NW stream	V14	
PAndAS-09	GC	6.65	-52.33	-444 ± 21	NW stream	V14	
And XV	dSph	6.84	114.86	-323 ± 5		T12	vdM12
PAndAS-06	GC	6.85	-83.47	-327 ± 15		V14	
And XII	dSph	6.96	171.95	-557 ± 1	In-falling?	C13	vdMG08, vdM12
PAndAS-54	GC	7.01	103.57	-336 ± 8		V14	
PAndAS-53	GC	7.02	103.85	-253 ± 10		V14	
NGC 185	dE	7.10	-5.08	-202 ± 7			vdMG08, vdM12
H27	GC	7.31	136.68	-291 ± 6		V14	
B519	GC	7.35	165.68	-268 ± 47			vdM12
PAndAS-05	GC	7.36	-65.74	-183 ± 7		V14	
NGC 147	dE	7.43	-12.30	-193 ± 3			vdMG08,vdM12
And XXVI	dSph	7.45	-25.30	-261 ± 3		C13	
And XI	dSph	7.50	174.27	-427 ± 3		C13	vdM12
PAndAS-56	GC	7.56	81.73	-239 ± 8		V14	
And XIX	dSph	7.71	-141.94	-111 ± 1		C13	
PAndAS-50	GC	7.81	24.06	-323 ± 7		V14	
And V	dSph	8.03	35.34	-403 ± 4		K10	vdMG08, vdM12
And XXIV	dSph	8.21	48.65	-128 ± 5		C13	
PAndAS-02	GC	8.40	-82.80	-266 ± 4		V14	
And XXX	dSph	8.45	-6.80	-139 ± 6		C13	
And XIII	dSph	8.46	166.91	-185 ± 8		T12	vdM12
MGC1	GC	8.50	168.62	-355 ± 7		V14	vdM12
PAndAS-57	GC	8.52	90.25	-186 ± 7	Eastern Cloud	V14	

Table 3.1 (cont'd)

Name	Morphological Type	ρ (deg)	ϕ (deg)	v_{HELIO}	Substructure Association	Velocity Reference	Previous Use for Tan. Motion
PAndAS-01	GC	8.70	-71.01	-333 ± 21		V14	
PAndAS-58	GC	8.74	89.35	-167 ± 10	Eastern Cloud	V14	
And XXI	dSph	9.00	-78.35	-362 ± 1		C13	vdM12
PAndAS-04	GC	9.12	-44.90	-397 ± 7	NW stream	V14	
And XX	dSph	9.24	-128.76	-456 ± 3		C13	
And XXIII	dSph	9.28	102.13	-237 ± 1		C13	
And XVI	dSph	9.50	158.05	-367 ± 5		T12	vdM12
And II	dSph	10.32	136.84	-188 ± 3		K10	vdMG08, vdM12
PAndAS-48	GC	10.34	159.73	-250 ± 6		V14	
And XIV	dSph	11.71	170.50	-478 ± 5	In-falling?	T12	vdMG08, vdM12
And XXIX	dSph	13.73	-136.51	-194 ± 1		T13	
M 33	dSph	14.78	131.79	-180 ± 1			vdMG08, vdM12
And XX	dSph	16.06	141.61	-129 ± 2	M33	C13	vdM12
And VII	dSph	16.17	-47.99	-307 ± 2			vdMG08, vdM12
IC 10	dIrr	18.37	-9.11	-344 ± 5			vdMG08, vdM12
And VI	dSph	19.77	-143.63	-354 ± 3			vdMG08, vdM12
LGS 3	dIrr	19.89	165.42	-286 ± 4			vdMG08, vdM12
And XXVIII	dSph	27.88	-100.61	-331 ± 1	In-falling?	T13	
Pegasus	dIrr	31.01	-143.37	-182 ± 2			vdMG08, vdM12
IC 1613	dIrr	39.47	171.31	-232 ± 5			vdMG08, vdM12

Table 3.2. KPNO+Mosaic Observations in the 'R08' Ring

Field Name	Field Center RA (J2000)	Dec. J2000	Camera	UTC Date	Total Exposure Time (s) M,$T2$,$DDO51$	Observing Conditions
R08A011	00:52:43.8	+49:42:12.09	Mosaic 1	09/03/2007	900, 1800, 5400	Photometric
R08A071	01:27:40.5	+44:04:21.89	Mosaic 1.1	12/07/2010	900, 1800, 5400	Photometric
R08A101	01:26:30.0	+39:37:28.00	Mosaic 1	10/26-29/2005	900, 1800, 5400	Variable
R08A149	01:04:10.3	+33:54:02.99	Mosaic 1	10/31/2005	900, 1800, 5400	Photometric
R08A197	00:30:40.3	+33:02:59.0	Mosaic 1	11/01/2005	900, 1800, 5400	Photometric
R08A250	00:03:21.0	+37:37:43.29	Mosaic 1	09/20/2006	900, 1800, 5400	Photometric
R08A281	23:56:53.7	+42:54:44.20	Mosaic 1	09/01/2007	900, 1800, 5400	Non-Photometric
R08A311	00:05:09.9	+46:54:51.59	Mosaic 1.1	12/12/2010	900, 1800, 5400	Photometric

Table 3.3. New Keck+DEIMOS Observations in the Outer M31 Halo

Field Name	Mask Name	Mask Center RA (J2000)	Dec. J2000	MJD	UTC Date	Total Exposure Time (s)	No. of Slits	No. of Successful Redshifts	No. of Stars
R08A250	A250_1	00:03:22.75	+37:37:28.3	55775.45229	08/02/2011	3600	74	32	9
R08A149	A149_1	01:04:48.95	+33:53:05.6	55775.50392	08/02/2011	3600	68	37	20
R08A101	A101_1	01:27:13.64	+39:48:16.6	55775.56264	08/02/2011	3600	73	39	27
R08A071	A071_1	01:27:51.20	+44:00:19.5	55775.60654	08/02-03/2011	2545	61	43	41
R08A281	A281_1	23:57:29.87	+42:55:27.6	55776.44911	08/03/2011	2750	73	53	42
R08A311	A311_1	00:04:26.56	+46:57:59.4	55776.48782	08/03/2011	2760	76	50	41
R08A197	A197_1	00:30:33.72	+33:00:12.7	55776.52822	08/03/2011	3200	72	23	13
R08A011	A011_1	00:52:52.95	+49:35:24.6	55776.59196	08/03/2011	2900	81	51	50

Table 3.4. MMT Observations in the Outer M31 Halo

Field Name	Field Center RA (J2000)	Dec. J2000	MJD	UTC Date	Total Exposure Time (s)	No. of Exposures
R08A197	00:30:59.04	+33:05:21.83	55857.20926	10/23/2011	12600	7
			55860.11667	10/26/2011	5400	3
R08A101	01:26:35.89	+31:52:49.04	55883.20984	11/18/2011	9950	7
			55888.15095	11/23/2011	9900	5

Table 3.5. MMT+Hectospec Spectroscopy Summary

Field Name	No. of Unique Objects	No. of Usable Spectra	No. of Stellar Spectra
R08A197	215	166	71
R08A101	227	208	87

Table 3.6. Spectral Lines and Spectral Windows for MMT+Hectospec Measurements

Line Name	Wavelength (Å)	Spectral Window Min λ (Å)	Max λ (Å)	Comments
Redshift Measurements				
Ca H	3933.6614	3848	3998	Joint Fit with Ca K
Ca K	3968.4673	3848	3997	Joint Fit with Ca H
Hα	6562.81	6520	6625	
CaT_2	8542.32	8510	8585	
Equivalent Width Measurements				
Na D	8179.0, 8200.0	8130.0 - 8175.0	8210.0 - 8220.0	Continuum fit to a blue and red window
Ca T	8498.43, 8542.32, 8662.44	8450.0	8700.0	Lines fit over 18Åwindows

Table 3.7. Definition of $m31class$

$m31class$	Description	L Restriction	X_{CMD} Restriction
+3	secure M 31 giant	$+0.5 < L$	$0.0 \leq X_{CMD}$
+2		$+0.5 < L$	$-0.05 \leq X_{CMD} < 0.0$
+1	marginal giant	$0.0 < L \leq +0.5$	$-0.05 \leq X_{CMD}$
−1	marginal dwarf	$-0.5 \leq L \leq 0.0$	$-0.05 \leq X_{CMD}$
−2		$-0.5 \leq L$	$X_{CMD} < -0.05$
−3	secure MW dwarf	$L < -0.5$	

Table 3.8. Spectroscopic Summary of All Halo Fields

Field Name	$\langle\rho\rangle$ (deg)	$\langle\phi\rangle$ (deg)	No. of Masks	Total Stars Halo	KCC	dSph	Special Classification	Prior Publication
f109	0.65	118.93	1	145	0	0		G12
H11	0.89	130.03	2	0	133	0	GSS kcc	G12
f116	0.97	126.21	1	0	109	0	GSS kcc	G12
f115	1.06	121.99	1	37	65	0	kcc	G12
f135	1.27	147.08	1	0	85	0	GSS kcc	G12
f123	1.28	128.44	1	0	39	0	GSS kcc	G12
f207	1.28	172.22	1	0	76	0	GSS kcc	G12
H13s	1.55	169.56	2	46	144	0	kcc	G12
f130	1.62	130.85	1	41	0	0		G12
a0	2.17	127.98	3	74	0	0		G12
a3	2.39	153.64	3	0	48	0	GSS kcc	G12
mask4	2.68	124.68	1	16	0	0		G12
and9	2.69	43.18	2	34	21	34	dSph kcc	G12, T12
and1	3.26	168.91	2	0	131	92	GSS dSph kcc	G12, T12
m4	4.15	124.57	5	0	33	0	GSS kcc	G12
R04A338	4.04	-19.41	3	13	0	0		G12
a13	4.22	-93.92	4	0	35	0	GSS kcc	G12
R04A240	4.06	-116.60	3	22	0	0		G12
streamE	4.79	-50.47	2	21	0	0		G12
and3	5.00	-163.32	3	13	0	61	dSph	G12, T12
and10	5.61	48.95	2	5	0	25	dSph	G12, T12
a19	5.82	-170.23	4	15	0	0		G12
R06A220	6.21	-139.03	3	0	15	0	GSS kcc	G12
R06A310	6.36	-47.13	3	9	0	0		G12
R06A040	6.62	37.60	3	10	0	0		G12
m6	6.23	123.67	5	35	0	0		G12
b15	6.69	160.82	5	19	0	0		G12
and15	6.86	114.78	2	13	0	20	dSph	G12, T12
and12	6.96	171.62	1	3	0	2	dSph	G12, T12
streamF	6.99	-49.54	3	16	0	0		G12
and11	7.49	174.21	1	2	0	2	dSph	G12, T12
and5	8.03	35.35	4	7	0	94	dSph	G12, T12
R08A101	8.55	96.61	2	5	0	0		
and18	8.30	-59.26	1	5	0	21	dSph	G12, T12
and13	8.47	166.91	5	15	0	10	dSph	G12, T12
R08A011	8.53	11.42	1	2	0	0		
R08A250	8.42	-112.42	1	3	0	0		
R08A281	8.49	-74.92	1	1	0	0		
R08A149	8.50	148.09	1	1	0	0		
m8	8.53	122.73	2	4	0	0		G12
R08A071	8.77	68.09	1	3	0	0		
R08A197	8.62	-162.92	2	6	0	0		
R08A311	8.88	-46.89	1	2	0	0		

3.9 Acknowledgements

The authors recognize numerous helpful conversations and much appreciated support from Nelson Caldwell for the planning and execution of our MMT+Hectospec observations. We thank Perry Berlind and Mike Calkins for on-site assistance with Hectospec observations and the telescope operators Mike Alegria, Alejandra Milone, and John McAfee for hospitality and assistance during observing. We further acknowledge assistance from Jeffery Carlin in understanding the Hectospec data, and recognize the assistance of Sean Moran for custom data processing required for these analyses.

RLB received NOAO Thesis support for the KPNO-4meter imaging observations used for this work.

IRAF is distributed by the National Optical Astronomy Observatory, which is operated by the Association of Universities for Research in Astronomy (AURA) under cooperative agreement with the National Science Foundation. MMT telescope time was granted by NOAO, through the Telescope System Instrumentation Program (TSIP). TSIP is funded by NSF. Observations reported here were obtained at the MMT Observatory, a joint facility of the Smithsonian Institution and the University of Arizona. This paper uses data products produced by the OIR Telescope Data

Table 3.8 (cont'd)

Field Name	$\langle\rho\rangle$ (deg)	$\langle\phi\rangle$ (deg)	No. of Masks	Total Stars Halo	KCC	dSph	Special Classification	Prior Publication
and21	9.02	-78.41	1	0	0	4	dSph	G12, T12
and16	9.50	157.98	2	1	0	5	dSph	G12, T12
and2	10.29	136.84	11	15	0	492	dSph	G12
R11A170	11.71	170.48	3	2	0	52	dSph	G12, M07
m11	11.65	123.07	4	7	0	0		G12
R11A080	11.98	74.77	1	3	0	0		G12
R11A305	12.45	-51.44	2	8	0	0		G12
and29	13.72	-136.53	2	2	0	25	dSph	T13
and7	16.16	-47.95	5	10	0	265	dSph	G12, T12
and28	27.88	-100.61	2	6	0	15	dSph	T13

Center, supported by the Smithsonian Astrophysical Observatory.

The authors wish to recognize and acknowledge the very significant cultural role and reverence that the summit of Mauna Kea has always had within the indigenous Hawaiian community. We are most fortunate to have the opportunity to conduct observations from this mountain.

Funding for the DEEP2/DEIMOS pipelines has been provided by NSF grant AST-0071048. The DEIMOS spectrograph was funded by grants from CARA (Keck Observatory) and UCO/Lick Observatory, a NSF Facilities and Infrastructure grant (ARI92-14621), the Center for Particle Astrophysics, and by gifts from Sun Microsystems and the Quantum Corporation.

The analysis pipeline used to reduce the DEIMOS data was developed at UC Berkeley with support from NSF grant AST-0071048.

Table 3.9. Three-Dimensional Center-of-Mass Heliocentric Velocity Estimates for M31

Measurement Method	v_{LOS} km s^{-1}	v_W km s^{-1}	v_N km s^{-1}	Source
PROPER MOTIONS OF STARS:				
HST PM in the Spheroid Field	...	-179.1 ± 64.1	-122.6 ± 60.0	vdm12
HST PM in the Disk Field	...	-158.0 ± 92.4	-0.5 ± 91.3	vdm12
HST PM in the Stream Field	...	-126.3 ± 103.6	-247.5 ± 102.1	vdm12
Weighted Average of HST PMs	...	-162.8 ± 47.0	-117.2 ± 45.0	vdm12
LINE-OF-SIGHT VELOCITIES OF SATELLITES:				
M 31 Satellites & Globular Clusters	-310.2 ± 130.5	-122.6 ± 101.3	-1.0 ± 83.8	Section 2, this work
M 33 PM	-183.1 ± 16.4	-47.7 ± 88.2	70.9 ± 91.5	vdmG08
IC 10 PM	-346.1 ± 84.8	-16.2 ± 88.0	-47.3 ± 89.3	vdmG08
Outer LG Galaxies	-361.3 ± 83.6	-140.5 ± 58.0	-102.6 ± 52.5	vdmG08
Weighted Average of Satellite Tracers	-299.2 ± 45.6	-82.1 ± 32.3	-46.4 ± 36.5	
LINE-OF-SIGHT VELOCITIES OF STARS:				
M 31 Stellar Halo Members	-323.8 ± 12.6	-67.6 ± 41.8	74.8 ± 56.7	Section 5, this work
Final Weighted Average for all Techniques		-96.4 ± 22.4	-44.7 ± 25.4	

Chapter 4

Cannibalization and Rebirth in the NGC5387 System. I. The Stellar Stream and Star Forming Region

4.1 Introduction

In the hierarchical galaxy formation paradigm, the haloes of Milky Way (MW) sized galaxies are built through the accretion of less massive galaxies. In Local Group, this process has been observed as streams of gaseous or stellar material in the Milky Way (e.g. the Large Magellanic Cloud (LMC); Nidever et al. 2010, 2013b), Andromeda (e.g. M33; McConnachie et al. 2009; Wolfe et al. 2013), and in Milky-Way analogue galaxies across the Local Volume (e.g. Martínez-Delgado et al. 2010; Putman et al. 2012).

N-body modeling of minor accretion events within the ΛCDM context indicate that streams can take on a variety of morphologies, which are determined by their orbital parameters (Johnston et al. 2008, See Figure 2): "great circles" from circular orbits, "umbrellas" and "shells" from radial orbits, and "mixed" morphologies from old mergers (several Gyr) of various orbital types. Similar modeling that tracks the build-up of material in halos suggests that while all MW-type galaxies will show tidal debris in their haloes, the detailed distribution of debris depends on the specific accretion history — more specifically, the number, mass, and timing of individual accretions (Bullock & Johnston 2005).

In contrast to detailed predictions from simulations, the observational portrait of minor accretion events is far from complete, owing primarily to the inherent difficulty of detecting low surface brightness tidal features. However, several observational analogues to the canonical Johnston et al. (2008) stream morphologies have been discovered in the Local Volume (Martínez-Delgado et al. 2010), including the "great circle" morphology of NGC 5907 (Shang et al. 1998; Zheng et al. 1999; Martínez-Delgado et al. 2008) and Messier 63 (Chonis et al. 2011), the "umbrella" in NGC 4651 (Martínez-Delgado et al. 2010), and the mixed type structure in NGC 1055 (Martínez-

Delgado et al. 2010). In addition to the three canonical structures in the Johnston et al. (2008) simulations, Martínez-Delgado et al. (2010) identified additional stream morphologies, including "spikes" (NGC 5866), partial disruptions (NGC 4216), and "giant plumes" (NGC 1084), that are likely variations on the canonical forms due to the effect of viewing angle(s).

Beyond these isolated discoveries, there exist few large scale searches for tidal features that are sufficient to provide crucial feedback to simulations on either the frequency of streams or the distribution of stream properties, including stream morphology, debris mass, progenitor mass, or remnant mass. Using morphological techniques to analyze a sample of 474 galaxies in the Sloan Digital Sky Survey (SDSS) DR7 (Abazajian et al. 2009), Miskolczi et al. (2011) found that 6% of galaxies exhibit clear tidal features and 19% show faint features at a limiting surface brightness of 28 mag arcsec^{-2}. Along a similar vein, Atkinson et al. (2013) find 12% of galaxies imaged in the wide-field component of the Canada-France-Hawaii Telescope Legacy Survey exhibited tidal features, though this includes both major and minor merging events. These estimates of the frequency of tidal features are in stark contrast to those anticipated from the Λ-CDM paradigm, e.g., that *all* MW-sized galaxies should have signatures of accretion events. The disparity is largely due to the shallow surface brightness limit of imaging surveys like SDSS — most features in Bullock & Johnston (2005) have surface brightnesses exceeding 28 mag arcsec^{-2}.

Although large scale searches for tidal debris are limited, the satellite galaxies of the Local Group (LG) — those dwarf galaxies currently associated with the MW or with Andromeda — do place some constraints on the process of satellite accretion. One significant constraint is the observed morphology-density relationship in the LG (Mateo 1998), the simple observation that, with the exception of the Magellanic

System (the Large and Small Magellanic Cloud (LMC, SMC) and associated debris) and M 33, the early type dwarfs (predominantly old dwarf spheroidals, dSph) are predominantly discovered embedded within the halo of their host, whereas late type dwarfs (star forming dwarf irregulars, dIrrs) are found in relative isolation or on their first passage around their host (e.g. the LMC and SMC). Beyond the LG, morphology-density relationships exist in other host-satellite systems (Tollerud et al. 2011; Geha et al. 2012). Grcevich & Putman (2009) expanded the morphological dichotomy in the LG by noting that the majority of dwarf galaxies within ∼270 kpc of their host are *undetected* in H I surveys, meaning not only are satellites quenched for current star formation, but they have no appreciable gas content to fuel future star formation. Combined, the morphology-density relationship (Mateo 1998) and the HI disparity (Grcevich & Putman 2009) imply that the minor merger process converts gas-rich, star-forming dIrrs into gas-devoid, quiescent dSphs, as suggested by, for example, Grebel et al. (2003); Ho et al. (2012). Recent simulations also support this portrait (e.g. D'Onghia et al. 2009; Łokas et al. 2010), though the competing roles of re-ionization, star formation feedback, and gas stripping remain difficult to disentangle for individual dwarf galaxies in even the most advanced simulations.

Though the density-morphology relationship is compelling, several observational studies suggest that the observed morphological change of satellite galaxies may not only be driven by interactions with a parent galaxy. For example, studies of close (< 50 kpc) satellite-host pairs in SDSS do not show strong morphological differences between a sample of "isolated" dwarfs and close-pair satellites (Phillips et al. 2014). In the LG, a number of dSph type galaxies have been discovered at large projected radii (>200 kpc) or in a "first in-fall" scenario, most notably the satellites, AndXIV (Majewski et al. 2007), AndXVIII, AndXXVIII (Slater et al. 2011) and AndXXIX

(Bell et al. 2011). These "isolated" dSphs have had limited gravitational interaction with their parent system, suggesting that there must be another evolutionary path capable of creating gas-devoid, dispersion supported galaxies. Furthermore, the recent detection of a companion satellite to NGC 4449 (Martínez-Delgado et al. 2012) and implications of a companion satellite to IC 10 (Nidever et al. 2013a), as well as more evidence of the complex structure of the dwarf-dwarf Magellanic system (Nidever et al. 2013b), strongly suggest that dwarf galaxies, like their MW-sized hosts, may also have complex minor-minor interaction histories that could strongly impact their overall evolution.

Despite challenges to the morphology-density relationship, the observational evidence on satellite systems implies that the process of minor merging causes significant morphological changes in the satellite. Since few "in-tact" star forming satellites are found embedded in their host — and even so called "transitional" morphological types (e.g. galaxies similar to Leo T Irwin et al. 2007; de Jong et al. 2008; Ryan-Weber et al. 2008) are rare, the gas removal and associated morphological changes proceed relatively quickly compared to the "lifetime" of the average satellite in the host halo ($\sim$ several Gyrs for some dSphs). Furthermore, the morphological change must occur by a means that neither completely disrupts the satellite given the large number of "intact" satellites in the LG, nor often leaves clear signs of tidal stripping given that relatively few dSphs have significant tidal features. Interestingly, Johnston et al. (2008) found that of 153 surviving satellites in their simulations, only 21% lost more than 1% of their luminous matter but only 4% of the streams had still identifiable progenitors (e.g., bound halos). Thus, to understand fully the phase of minor merging during which gas is removed from satellites, it is necessary to identify mergers in the earliest stages of disruption.

In this paper, we present the case of the NGC 5387 system — a spiral galaxy identified to be in the rare state of an ongoing satellite accretion event based on imaging from the Sloan Digital Sky Survey Data Release 9 (Ahn et al. 2012, SDSS-DR9 hereafter). The event has two notable features, a stellar stream and blue overdensity. In Section 4.2, we present deep imaging of NGC 5387 with the Vatican Advanced Technology Telescope (VATT). In Section 4.3, we present spectroscopy of the blue overdensity to determine its detailed properties. In Section 4.4, several interpretations for the origin of the blue overdensity are presented and discussed. In a companion paper, numerical simulations are used to identify the most likely interpretation, and the implications of this system will be explored.

4.2 Revealing the Accretion Event in NGC 5387

NGC 5387 was imaged in the SDSS footprint and this imaging suggested the presence of a low surface brightness stellar stream. In Section 4.2.1, we first characterize NGC 5387 based on archival data. To confirm the stream, deeper observations were obtained with the Vatican Advanced Technology Telescope (VATT) and are described in Section 4.2.2. Analysis of the imaging includes, the surface photometry of the stream presented in Section 4.2.3 and estimation of progenitor properties from the stream morphology in Section 4.2.4. In addition to the stream, we explore the photometric properties of an over-dense blue region coincident with the projected intersection of the stream with the disk. In Section 4.2.5, we explore the photometric properties of this region.

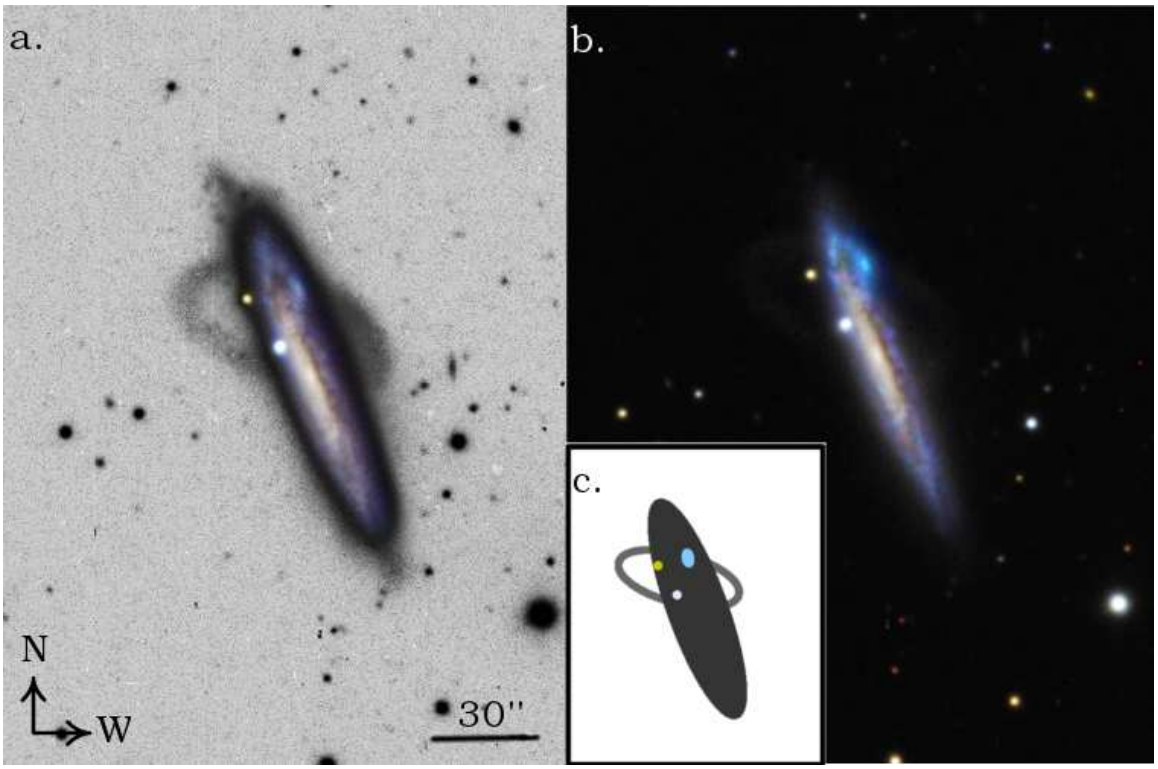

Fig. 4.1.— SDSS color image of NGC 5387; in panel a, inset in the greyscale R band image from VATT, in panel b, merged with GALEX FUV and VATT imaging, and in panel c, a schematic view of the system. The color image reveals NGC 5387 to have the features typical of a Milky Way type spiral galaxy, except for a small blue region on the north-western extent of the outer disk. The deep R band image (panel a) highlights a narrow stellar stream extending from the north-eastern outer disk to the east, with a connection to another, broader feature on the western side of the disk. The bright circular regions on disk near the stream, a yellow-orange region and a blue-white region, are both foreground stars. In panel b, the bright FUV emission at the location of the blue overdensity is emphasized and its alignment with the stellar stream. In panel c, the the NGC 5387 disk is shown in dark grey, the stream in light grey, the blue overdensity in light blue, and the two foreground stars in yellow and white. Panel c is intended to aid in the identification of features in panels a and c and does not represent an accurate physical interpretation of the system.

(a.)

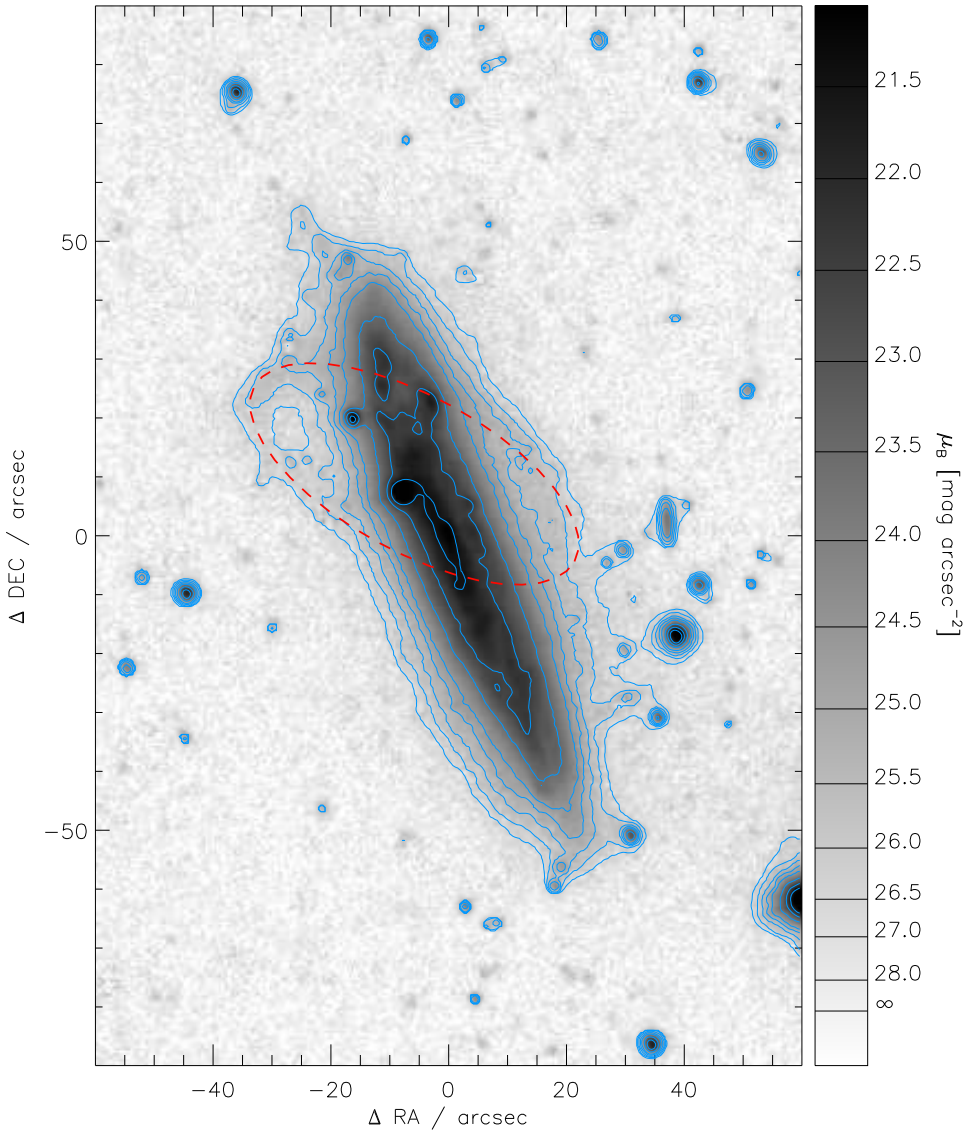

Fig. 4.2.— VATT B **(a)**, V **(b)** and R **(c)** imaging of NGC 5387. The images are astrometrically aligned and calibrated for surface brightness. The grey scale-bar on the right displays the surface brightness with asinh stretch as indicated in the sidebar. Contours (in light blue) are shown at the following surface brightness values, in mag arcsec^{-2}: (26.5, 26.0, 25.5, 25.0, 24.5, 23.5, 22.5, 21.5), (26.0, 25.5, 25.0, 24.5, 24.0, 23.0, 22.0, 21.0, 20.0), and (25.5, 25.0, 24.5, 24.0, 23.0, 22.0, 21.0, 20.0), for B, V and R respectively. An ellipse (red dashed), as described in the text, is overlaid on the stream to emphasize the stream and its alignment with the blue overdensity.

(b.)

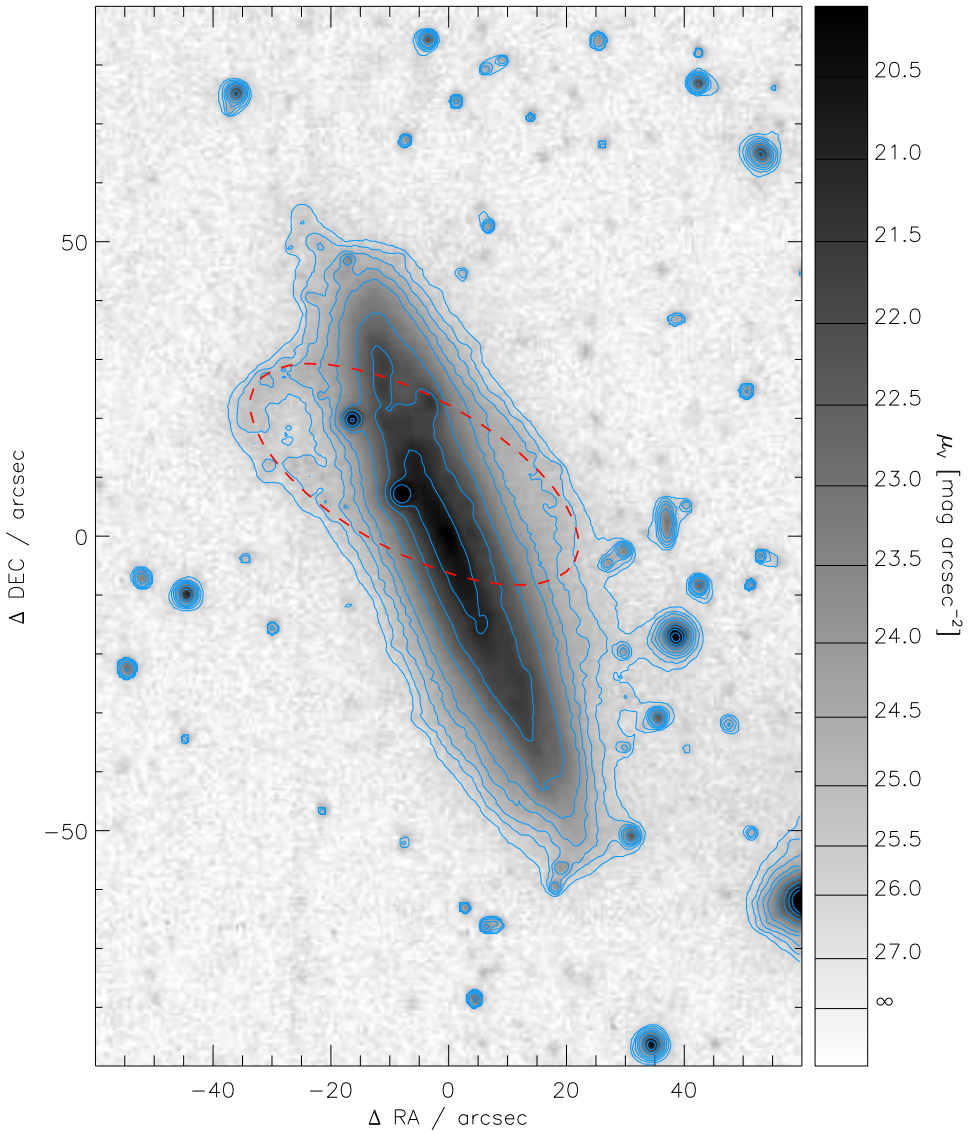

Fig. 4.2.— cont. **(b.)** VATT V imaging of NGC 5387. The grey scale-bar on the right displays the surface brightness with asinh stretch as indicated in the sidebar. Contours (in light blue) are shown at the following surface brightness values, in mag arcsec^{-2}: (26.0, 25.5, 25.0, 24.5, 24.0, 23.0, 22.0, 21.0, 20.0), for V. An ellipse (red dashed), as described in the text, is overlaid on the stream to emphasize the stream and its alignment with the blue overdensity.

(c.)

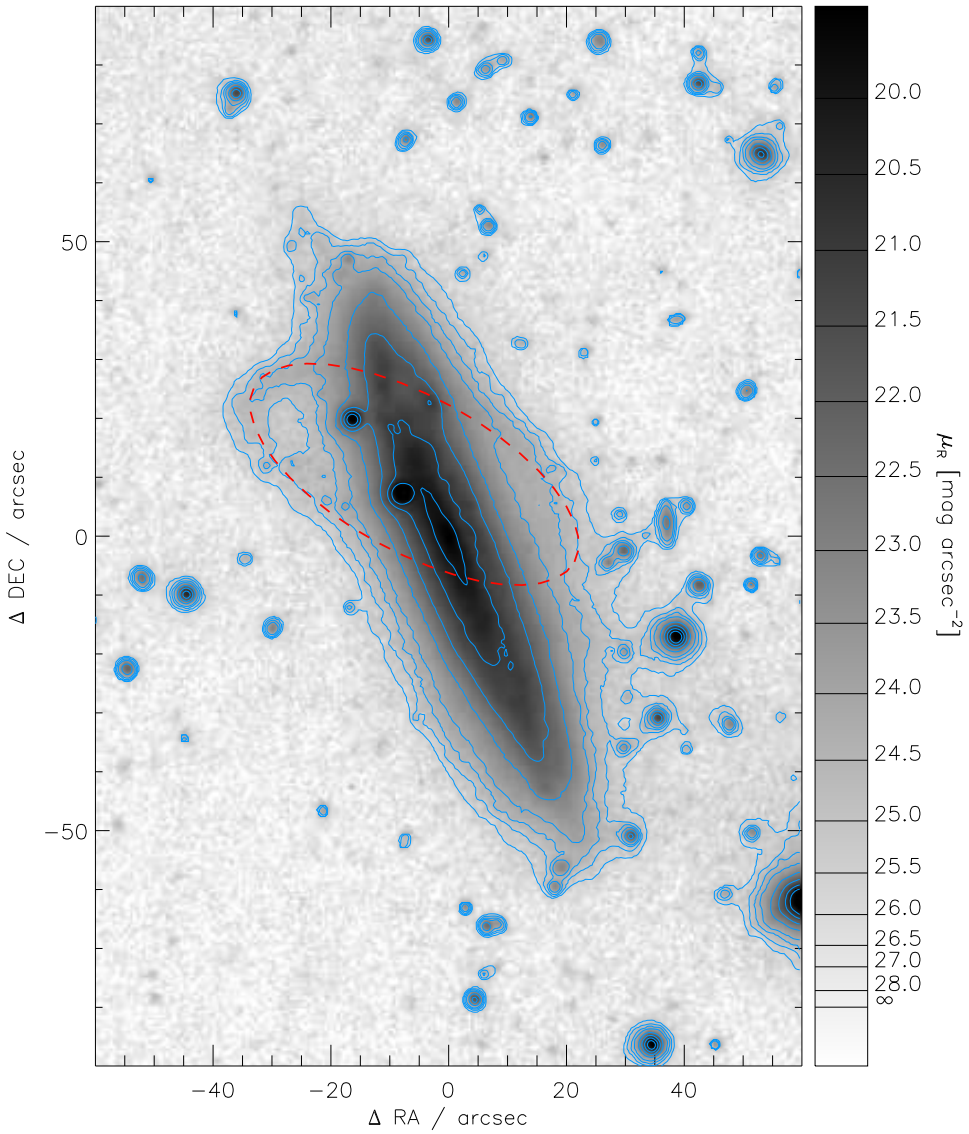

Fig. 4.2.— cont. **(c.)** VATT R imaging of NGC 5387. The grey scale-bar on the right displays the surface brightness with asinh stretch as indicated in the sidebar. Contours (in light blue) are shown at the following surface brightness values, in mag arcsec^{-2}: (25.5, 25.0, 24.5, 24.0, 23.0, 22.0, 21.0, 20.0) for R. An ellipse (red dashed), as described in the text, is overlaid on the stream to emphasize the stream and its alignment with the blue overdensity.

4.2.1 NGC 5387

NGC 5387 is an edge-on ($i = 80°$), Sbc type galaxy (de Vaucouleurs et al. 1991) with a warped disk (Sanchez-Saavedra et al. 1990). The distance to NGC 5387 galaxy is 79.3 Mpc or $(m - M) = 34.50 \pm 0.45$ (Springob et al. 2007, 2009). Assuming this distance, the galaxy has a major axis diameter of 41 (48) kpc in B (K_s) imaging (de Vaucouleurs et al. 1991; Jarrett et al. 2003). Using the maximum rotation velocity, $V_c = 162.9 \pm 3.0$ km s^{-1}, measured from the neutral hydrogen line profile, the total mass of NGC 5387 is $1.08 \times 10^{11} M_{\odot}$ (Springob et al. 2005). The total HI flux, 9.79 Jy km s^{-1}, yields a total HI mass of $1.46 \times 10^{10} M_{\odot}$ (Springob et al. 2005). Using the SDSS MPA-JHU Value Added Catalogs[1], the total stellar mass is $2.75 \times 10^{10} M_{\odot}$ (Abazajian et al. 2009; Brinchmann et al. 2004). Thus, the neutral gas fraction is $M_{HI}/M_* = 0.53$.

In the detailed spectroscopic diagnostics of Kauffmann et al. (2003), NGC 5387 is found to have no LINER or AGN component and have a central star formation rate (SFR, hereafter), SFR = 0.22 M$_{\odot}$ yr^{-1}. The global SFR for NGC 5387 can be estimated from its IRAS 100μ flux, f$_{100\mu}$=1.22 Jy $\pm$ 0.146 Jy (Moshir & et al. 1990), to be SFR(FIR) = 2.5 M$_{\odot}$ yr^{-1} using the conversion for galaxies later than Sb (Buat & Xu 1996). Overall NGC 5387 is of similar physical size as the Milky Way (MW), but is nearly an order of magnitude smaller in total mass (Boylan-Kolchin et al. 2013).

While NGC 5387 has a typical M_{HI}/M_* ratio for its stellar mass, its HI gas fraction is much larger than that of the MW (Blanton & Moustakas 2009). Likewise, the oxygen nebular abundance from the SDSS MPA-JHU VAC, 12 + log(O/H) = 9.05, while higher than average, is not an outlier on the mass-metallicity trend established by Tremonti et al. (2004). Its total star formation rate is not atypical for galaxies

[1] http://www.mpa-garching.mpg.de/SDSS/DR7/

of its type (Kauffmann et al. 2003). In its global physical properties, NGC 5387 is on the whole smaller than the MW, but is "normal" compared to galaxies of similar mass. Thus, we proceed to consider it a MW analogue galaxy.

4.2.2 New Imaging Data

Deep optical imaging was acquired for NGC 5387 at the Vatican Advanced Technology Telescope (VATT) with the VATT4k imager from UT 2012 March 21-28. The VATT4k imager has a field of view of $12' \times 12'$, and given its major axis diameter of $90''$, NGC 5387 is well contained in a single pointing of the instrument. The plate scale is $0.37''$ per pixel at the 2×2 binning mode used for these observations. The imaging data were taken in the B, V, and R filters with median seeing of $1.0''$. Individual exposures were 300s or 450s in length, with total exposure times of 8700s, 9600s, 9300s in B, V, R respectively. The data were dithered randomly $\sim 1'$ between exposures. "Off" galaxy, or blank sky, exposures were acquired at least one field of view distant from the target, but containing no significant extended objects or saturated stars. Individual exposures were of the same length as individual "on" galaxy exposures (either 300s or 450s), but the total time exposed "off" galaxy was roughly 25% of the time spent "on" galaxy.

These imaging data were processed using image processing routines in the IRAF package MSCRED following the procedures outlined in the NOAO Wide-Field Survey (NWFS) project[2]. The procedures outlined for the NWFS were adapted for the VATT4k imager, and only deviations from the standard process are described here.

The most significant deviation from the NWFS reduction is the absence of a domeflat calibration, because there is no suitable dome flat screen at the VATT.

[2] http://www.noao.edu/noao/noaodeep/ReductionOpt/frames.html

Thus, initial flat-fielding was completed using high S/N twilight exposures collected throughout the observing run in all filters. Object masks were created for each of the images and those images whose objects were well masked were median combined (typically $20-30$ per filter) to create a preliminary flat field for each filter. After application of the primary flat field, a super sky flat was created by applying the flat-field creation procedure to the science and "off" galaxy exposures. After application of the appropriate sky flats, data from the two amplifiers were merged to create a single FITS image for each frame, to which a bad pixel mask was applied to remove known image defects. All images for a filter were registered with IMALIGN and then co-added using IMCOMBINE in IRAF. The CCREJECT algorithm was applied during the stacking to remove cosmic rays and, given the large number of images in each filter, was highly successful.

The images were astrometrically registered to SDSS by cross correlating the point sources detected on the VATT images against those in the SDSS-DR9 photometric catalogs (Ahn et al. 2012). The photometric calibration is also performed by comparison to the point sources in the SDSS DR9 photometric catalog, after discarding those sources that are saturated or approached the non-linearity regime in the VATT images. The resulting zero points are corrected to include a term for the foreground Galactic extinction ($E(B-V)_{MW}$=0.03). The root mean square variation (r.m.s.) of the zero points are of order 0.01 magnitudes for B, V, R and the scatter is 0.04, 0.04, and 0.03 magnitudes about the zero point, respectively.

To estimate the depth of the VATT images, we compute the surface brightness (SB) corresponding to the pixel-to-pixel root mean square variation (r.m.s.) to obtain 27.4, 27.0 and 26.7 mag arcsec^{-2} in B, V, R respectively. The pixel-to-pixel r.m.s. is a good measure of the SB sensitivity for a single pixel in the image. However,

because we are interested in the SB averaged over many pixels, the true limit to our measurements is not represented by the photon noise in a 1-pixel scale; instead our measurements are limited by any large scale background fluctuations. Hence, we have estimated the limiting SB as the r.m.s. of the median SB determined in a series of $\sim$10″$\times$ $\sim$10″ boxes of "empty sky" in fields around NGC 5387. The corresponding values in mag arcsec^{-2} are 29.6 29.6 and 28.3 for the B, V, R images respectively.

4.2.3 A Better View of the NGC 5387 System

Figure 4.1 presents composite images of the NGC 5387 system. In Figure 4.1a, the VATT R band image is shown in greyscale with an SDSS color image of the NGC 5387 disk inset. In Figure 4.1b, the VATT R band and SDSS image are combined with GALEX FUV imaging of the region from the Deep Imaging Survey (DIS, Morrissey et al. 2007). Two key features of NGC 5387 can be identified in Figure 4.1: (i) a smooth stellar stream of "great circle" morphology (Martínez-Delgado et al. 2010), and (ii) a blue overdensity at the intersection of the stream and the disk. Both of these regions are indicated in Figure 4.1c, where the NGC 5387 disk is in dark grey, the stream in light grey and the blue overdensity as the elliptical blue region. In addition to these features, we note that the very circular blue and orange regions on the disk are both foreground stars from their spectral energy distribution (SED) in their SDSS photometry. These two stars are indicated in Figure 4.1c as the white and yellow circles, respectively. We will further describe the stream in Section 4.2.4 and the blue overdensity in Section 4.2.5.

A surface photometry analysis is performed on the VATT images for the NGC 5587 disk. Total integrated magnitudes for the NGC 5387 disk are measured by integrating the background-subtracted flux (Figure 4.2) over an elliptical aperture with semi-

major diameter 90″, corresponding to the major axis diameter (de Vaucouleurs et al. 1991), and semi-minor diameter of 25″, corresponding to its minor axis diameter (de Vaucouleurs et al. 1991). This ellipse corresponds to an R-band isophotal level of 27 mag arcsec^{-2}, i.e., $\sim 3\sigma$ above the large-scale background fluctuations. There are two sources of error in our estimates of total magnitudes; first, uncertainty in the background subtraction, and second, scatter in the photometric zero point determined from comparison to SDSS. For the former, we estimate ∼1% variations in the background across the area contained within our $\sim 3\sigma$ isophote, and for the latter the values are given in Section 2.2. The total integrated apparent magnitudes for NGC 5387 are 14.46 ± 0.04, 13.67 ± 0.05 and 13.10 ± 0.03 in B, V, R, respectively. Using the relations of Zibetti et al. (2009), the integrated colors and assuming a distance modulus, $(M - m) = 34.5$ (Springob et al. 2007, 2009), we obtain an average mass estimate of $3.13^{+1.21}_{-0.87}\times10^{10}$ $M_{\odot}$ with a 38% variation from the choice of color and reference magnitude used in the adopted M/L-color relation. The surface photometry for NGC 5387 is summarized in Table 4.1.

4.2.4 The Stellar Steam of NGC 5387

The greyscale representation of the R band imaging of Figure 4.1 clearly shows the presence of a stellar stream extending to the east of the Northern half of the NGC 5387 disk, and extending through the disk to the west.

The morphology of a stream is difficult to often interpret due to the finite surface brightness limit of the observations. More specifically, we are biased toward seeing only the brightest segments of the stream, which typically correspond to the "youngest" segment — that is those sections most recently unbound from the progenitor (Johnston et al. 2008; Martínez-Delgado et al. 2010). The surface brightness

(a.)

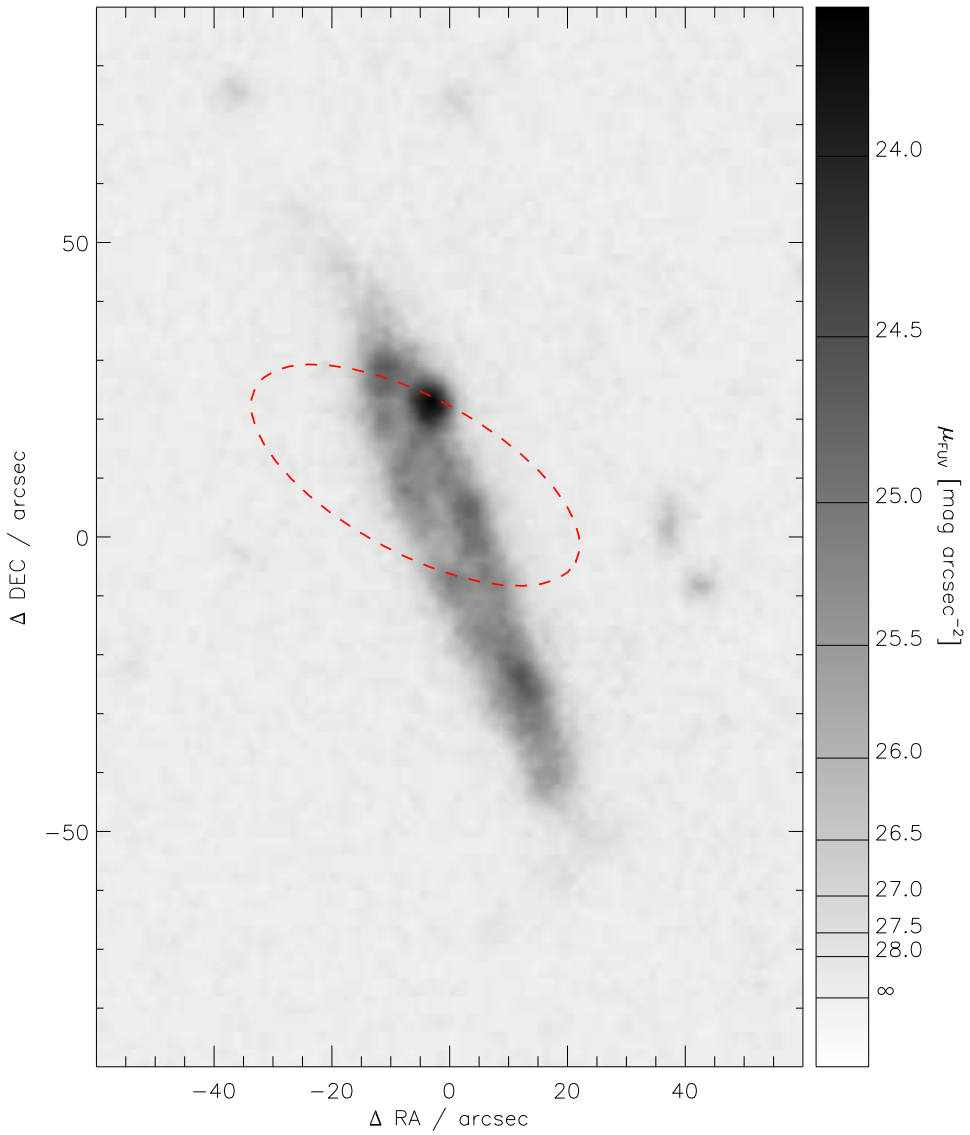

Fig. 4.3.— GALEX FUV **(a.)**, $(B-V)$ **(b.)** and $(B-R)$ **(c.)** maps of NGC 5387. As in Figure 4.2, the maps are astrometrically registered and an ellipse is over-plotted to indicate the position of the stellar stream (red dashed on the left and green dashed in the center and right panels). The blue overdensity as described in the text is very bright in the FUV image (left) and has $(B-V)$ and $(B-R)$ (center, right) colors remarkably dissimilar from the mean colors of NGC 5387. The blue overdensity is also different from the color of stream, which is overall similar to those of the NGC 5387 disk.

(b.)

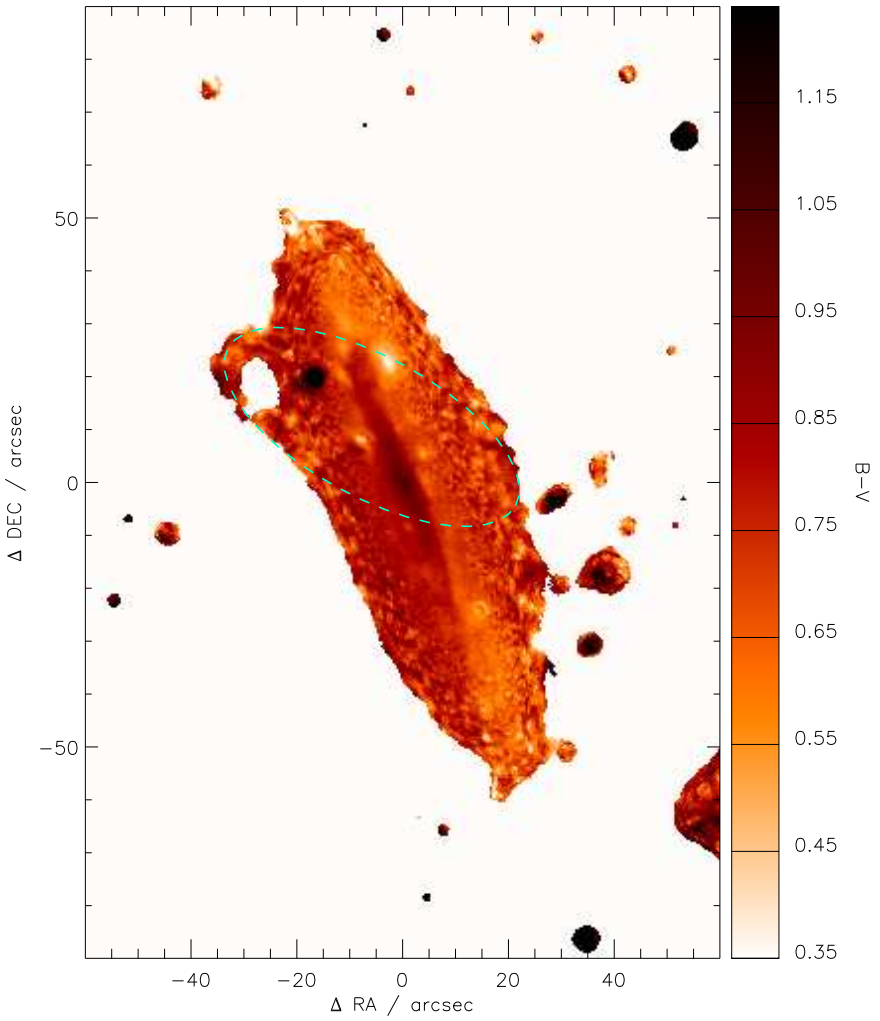

Fig. 4.3.— **(b.)** $(B-V)$ map of NGC 5387. As in Figure 4.2, the maps are astrometrically registered and an ellipse is over-plotted to indicate the position of the stellar stream (red dashed on the left and green dashed in the center and right panels). The blue overdensity as described in the text is very bright in the FUV image (left) and has $(B-V)$ and $(B-R)$ (center, right) colors remarkably dissimilar from the mean colors of NGC 5387. The blue overdensity is also different from the color of stream, which is overall similar to those of the NGC 5387 disk.

(c.)

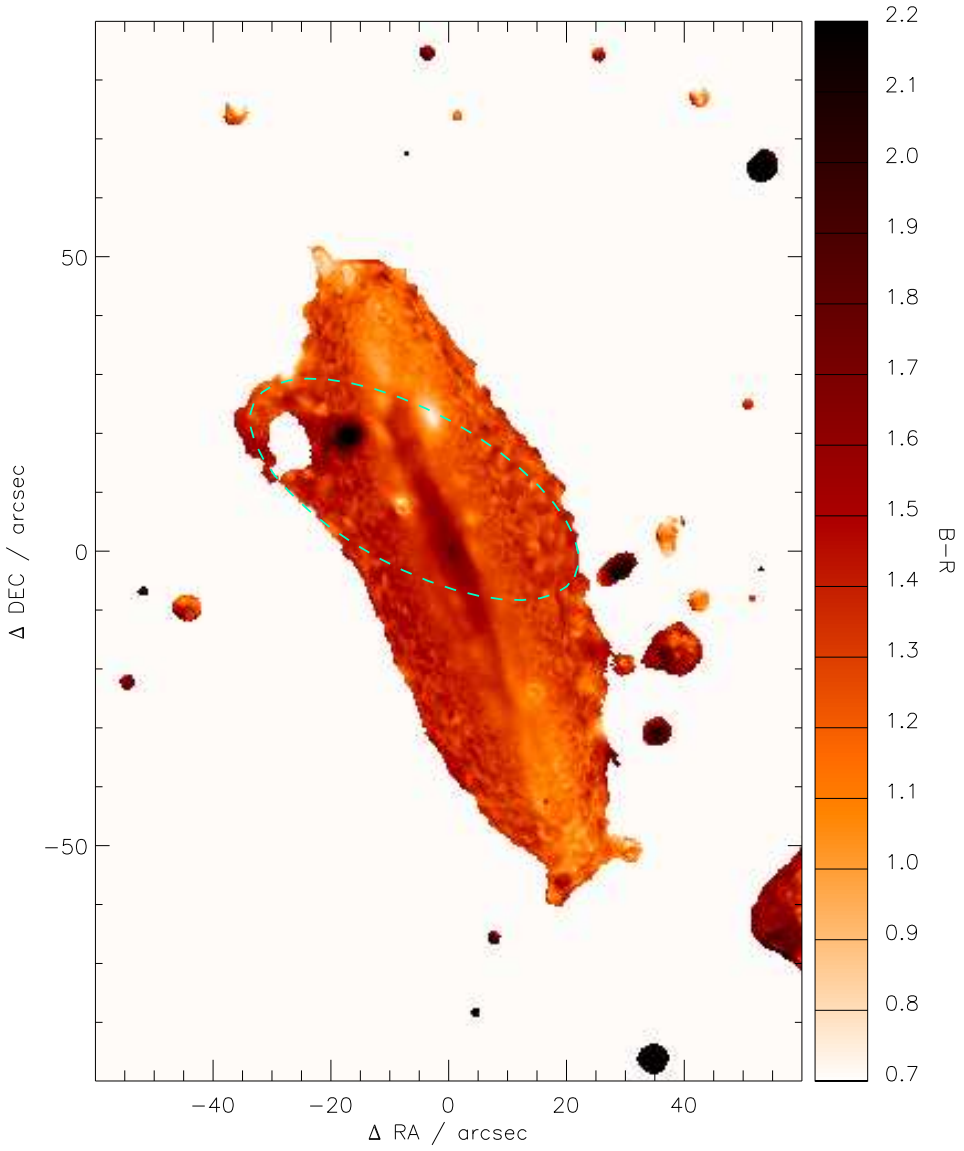

Fig. 4.3.— **(c.)** $(B-R)$ map of NGC 5387. As in Figure 4.2, the maps are astrometrically registered and an ellipse is over-plotted to indicate the position of the stellar stream (red dashed on the left and green dashed in the center and right panels). The blue overdensity as described in the text is very bright in the FUV image (left) and has $(B-V)$ and $(B-R)$ (center, right) colors remarkably dissimilar from the mean colors of NGC 5387. The blue overdensity is also different from the color of stream, which is overall similar to those of the NGC 5387 disk.

limit combined with line-of-sight inclination effects often mislead the interpretation of the stream morphology, more specifically the determination of its full angular extent, number of wraps, and its total mass. In the case of the stream in NGC 5387, we see a very clear narrow portion to the northeast of the disk and fainter segments on the western side of the NGC 5387 disk. We only identify a single wrap of the stream that can be traced for a full 360°. Given that identified segments are measured at low signal-to-noise, we cannot rule out the existence older wraps at even lower surface brightness.

The stream in NGC 5387 is most consistent with a "great circle" morphology, which implies the structure was formed from a satellite in an approximately circular orbit (Johnston et al. 2008; Martínez-Delgado et al. 2010). The stream appears to be elliptical in projection and can be described by an ellipse with semi-major diameter of 62″ (24 kpc), an axial ratio of 0.42, and a position angle 61.3° (measured from North to East). This ellipse is indicated in Figures 4.2 and 4.3. We will now determine properties of the stream and its progenitor inferred from its "great circle" morphology and measured with surface photometry.

Morphology of the Stellar Stream

From the morphology of the stream (see Figure 4.1), we can derive an estimate of the progenitor mass (m_{sat}) and "age" of the stream (t_{str}) following the analytical relations derived by Johnston et al. (2001). For the purposes of this paper the age of the stream, t_{str}, refers to the time since the accretion of the progenitor, not the age of the stellar populations comprising the stream.

Assuming a logarithmic potential for the host and $M_{NGC\,5387} >> m_{sat}$, then the

mass, m_{sat}, of the stream progenitor, is estimated by:

$$m_{sat} \sim \left(\frac{w}{R}\right)^3 \left(\frac{R_{peri}}{10\ kpc}\right) \left(\frac{v_{circ}}{200\ km/s}\right)^2 10^{11} M_{\odot} \tag{4.1}$$

where w is the width of the stream at R, R_{peri} is the radius at pericenter, and v_{circ} is the circular rotation velocity of the parent. Likewise, the age t_{str} of the streamer can be estimated as:

$$t_{str} \sim 0.01\Psi \left(\frac{R}{w}\right) \left(\frac{R_{circ}}{10\ kpc}\right) \left(\frac{200\ km/s}{v_{circ}}\right) Gyr \tag{4.2}$$

where Ψ is the angular length of the stream and R_{circ} is the radius of a circular orbit with the same energy as the true orbit.

We adopt the circular rotation velocity v_{circ} =162.9 ± 3 km s^{-1} (Springob et al. 2005). Ψ can be estimated visually from Figure 4.1 to be $\geq 360°$. Both w and R can be evaluated at any point in the stream and we choose the region of the stream with the highest apparent surface brightness (to the N of the NGC 5387 disk) such that w =11″= 4.2 kpc and R=11.7 kpc. Given the "great circle" morphology, the progenitor of the stream was most likely on a circular or near-circular orbit, and we can approximate $R_{circ} = R_{peri} = R = 12.7$ kpc (based on the ellipse in Figures 4.2 and 4.3) — this assumption implies an inclination of 65° for the stream. Changing the inclination by ± 10° results in circular radii, R_{circ}=10.1 kpc to 15.3 kpc. Substituting these values into Equation 4.1, we estimate a total progenitor mass of $4^{+2.5}_{-1} \times 10^{10}$ M$_{\odot}$, and into Equation 4.2, the formation age for the streamer of $t_{str} \sim 240^{+70}_{-40}$ Myr, where the quoted upper and lower ranges are for inclinations i=65°±10°.

Surface Photometry of the Stellar Stream

In Figure 4.2, we compare the stellar stream of NGC 5387 as observed in our three VATT filters, B, V, R. In all three optical filters the stream is detected and appears to have similar overall morphology. Overall the stream appears to be a single structure with mean surface brightness of 25.4 mag arcsec^{-2} in R. Though, we note that there are significant density fluctuations, more specifically, the stream has a maximum SB of 24.6 mag arcsec^{-2} in R and its minimum SB is indiscernible from the SB background estimate of Section 2.2 (26.7 mag arcsec^{-2} in R). By assuming a typical width of $11''$ (5.1 kpc), the geometrical parameters given in Section 2.4 and an approximately uniform surface brightness over the entire elliptical path (which cannot be verified in the overlap region with the main galaxy), we can estimate a total magnitude for the stream of ≈ 17.5 mag in R, and estimate an error of 50% due to the scale of the SB fluctuations along the stream.

To investigate the physical properties of the stream, we compute color maps from the VATT images. To do this, we enhance the original signal-to-noise ratio (SNR) in the individual pixels by performing the image adaptive smoothing introduced by Zibetti et al. (2009) using the ADAPTSMOOTH code of (Zibetti 2009). ADAPTSMOOTH performs a median filtering of the images using a circular top-hat kernel, whose size is adapted as a function of position to reach a given minimum SNR. A first pass of ADAPTSMOOTH is made in each band independently, to determine the "mask" of smoothing kernel sizes as a function of the position that provides a minimum SNR of 20. In the second pass the smoothing kernel size at a given pixel is re-determined as the maximum size over the three bands, so that the three images are smoothed consistently while ensuring the minimum SNR of 20 in all pixels. The $(B-V)$ and $(B-R)$ color maps are shown in the second and third panel of Fig. 3, respectively.

From these maps for the stream we can estimate a characteristic $(B-V)_{str}$ of 0.75, with variations between 0.6 and 0.9, and $(B-R)_{str}$ of 1.5, with variations between 1.2 and 1.7. These colors are broadly consistent with the average colors of NGC 5387, i.e., $(B-V)_{gal} = 0.79$ and $(B-R)_{gal} = 1.36$, thus implying (approximately) similar stellar populations. This observation justifies assuming the same M/L ratio for the stream as for the galaxy: the stellar mass ratio between the streamer and NGC 5387 is thus given by their luminosity ratio, i.e. ∼1:50, implying a mass for the streamer of $\sim 6^{+2.4}_{-1.7} \times 10^8\ M_\odot$. As before for the total mass of NGC 5387, the uncertainty in the mass is large due to numerous assumptions required for the estimate, but, even with these large errors, the mass is sufficiently well constrained to determine confidently that NGC 5387 is in the process of merging with a satellite companion, e.g., that this is a minor-major merger. These photometric properties are summarized in Table 4.1.

Summary of Stellar Stream Properties

The morphology of the stream implies that the progenitor was accreted within the last Gyr (t_{acr}), an age that is broadly consistent with its relatively small R_{peri}. There are no distinguishable overdensities within the angular extent of the stream, and, therefore, we do not identify a satellite remnant within the stream itself. In some known stellar streams, the progenitor is either nearly unbound or can be very elongated in the plane of the sky, as is implied by detailed simulations for the stream in NGC 5907 (Martínez-Delgado et al. 2008). Given the median seeing ($\sim 1''$) and the pixel scale, $0.38''$ per pixel, a highly distorted progenitor would be difficult to identify in our observations. Furthermore, the lack of progenitor is not uncommon, as most of the streams simulated in Johnston et al. (2008) had no identifiable progenitor. Comparing the mass of the progenitor from Equation 2 with the mass estimate of the

stream itself (Section 4.2.4), we estimate that the stream contains ∼3% of the total mass of the progenitor.

The great circle morphology of the NGC 5387 stream is similar to those identified around M 63 (Chonis et al. 2011), NGC 5907 (Martínez-Delgado et al. 2008), and NGC 4013 (Martínez-Delgado et al. 2009), but with a smaller apocentric radius and implied formation timescale. The inferred progenitor mass is comparable to that predicted for Sagittarius around the MW (Law et al. 2005), though the Sagittarius debris have multiple wraps and are thought to have formed over several Gyrs (Majewski et al. 2003), in contrast to the single wrap and short formation timescale for the NGC 5387 stream. Only one wrap of the NGC 5387 stream is detected in our observations, but we cannot rule out that there are older wraps of the stream, as was discovered for NGC 5907 when deeper observations were obtained (Shang et al. 1998; Zheng et al. 1999; Martínez-Delgado et al. 2008).

4.2.5 Properties of the Blue Overdensity

In Figure 4.1a, there is a blue region offset 23.6″ radially from the center of NGC 5387, corresponding to a projected galactocentric radius of 22.7″. The region is roughly circular with a radius of 2.2″. Given the median seeing of 1″, we are not able to resolve any sub-components to the blue overdensity and we treat it as a single region.

Using a circular aperture of 2.2″ centered on the blue over density, the total B, V, R absolute magnitudes are -14.55 ± 0.14, -14.83 ± 0.12, -15.84 ± 0.10, assuming the mean distance modulus of $(m - M)$=34.5±0.08 from independent Tully-Fisher calibrations for multiple broadband optical+NIR filters (Springob et al. 2007, 2009) and accounting for the MW reddening of $E(B-V)_{MW}$ =0.03 with a standard Cardelli et al. (1989) extinction curve for R_V =3.1. The photometric uncertainty for each

magnitude is the quadrature sum of three error sources, (i) the measurement error from the aperture photometry, (ii) the error from A_λ as scaled from $E(B-V)_{MW}$, and (iii) the error in the adopted mean distance modulus — the latter two source dominate the final quoted uncertainty. For colors, however, we compute the quadrature sum of the error in two the aperture magnitudes and the error in $E(B-V)_{MW}$, hence the uncertainty is much smaller. The blue overdensity has a $(B-V) = 0.28 \pm 0.04$ (with $E(B-V)_{MW} = 0.03$), implying $\Delta(B-V)$ from the stellar stream of $\sim$0.30. If the blue overdensity is part of the stream, then this is the first known stream with such an extreme color gradient (Δ(B-V)$\sim$ 0.3-0.6).

In Figure 4.3, we compare our optical imaging to that of the GALEX Deep Imaging Survey (Morrissey et al. 2007) to the $(B-V)$ and $(B-R)$ color maps. In Figure 4.3, it becomes clear not only that the region is much bluer than the disk of NGC 5387 and the stream, but also that the region contributes a significant portion of the FUV flux from NGC 5387. The total integrated FUV (NUV) apparent magnitude of NGC 5387 is $m_{FUV} = 17.44$ ($m_{NUV} = 16.83$) (this estimate includes the blue overdensity; no errors were reported Lemonias et al. 2011). In comparison to NGC5387, the total FUV (NUV) apparent magnitude for the blue overdensity (GALEX source J135825.0+060438) is $m_{FUV} = 18.49 \pm 0.01$ ($m_{NUV} = 18.21 \pm 0.00$). From the apparent magnitudes, the blue overdensity contributes 38% (28%) of the FUV (NUV) flux of NGC 5387. The blue overdensity is most likely a star forming region, but from the imaging alone it is impossible to determine if it is related to NGC 5387 or an overlapping foreground object.

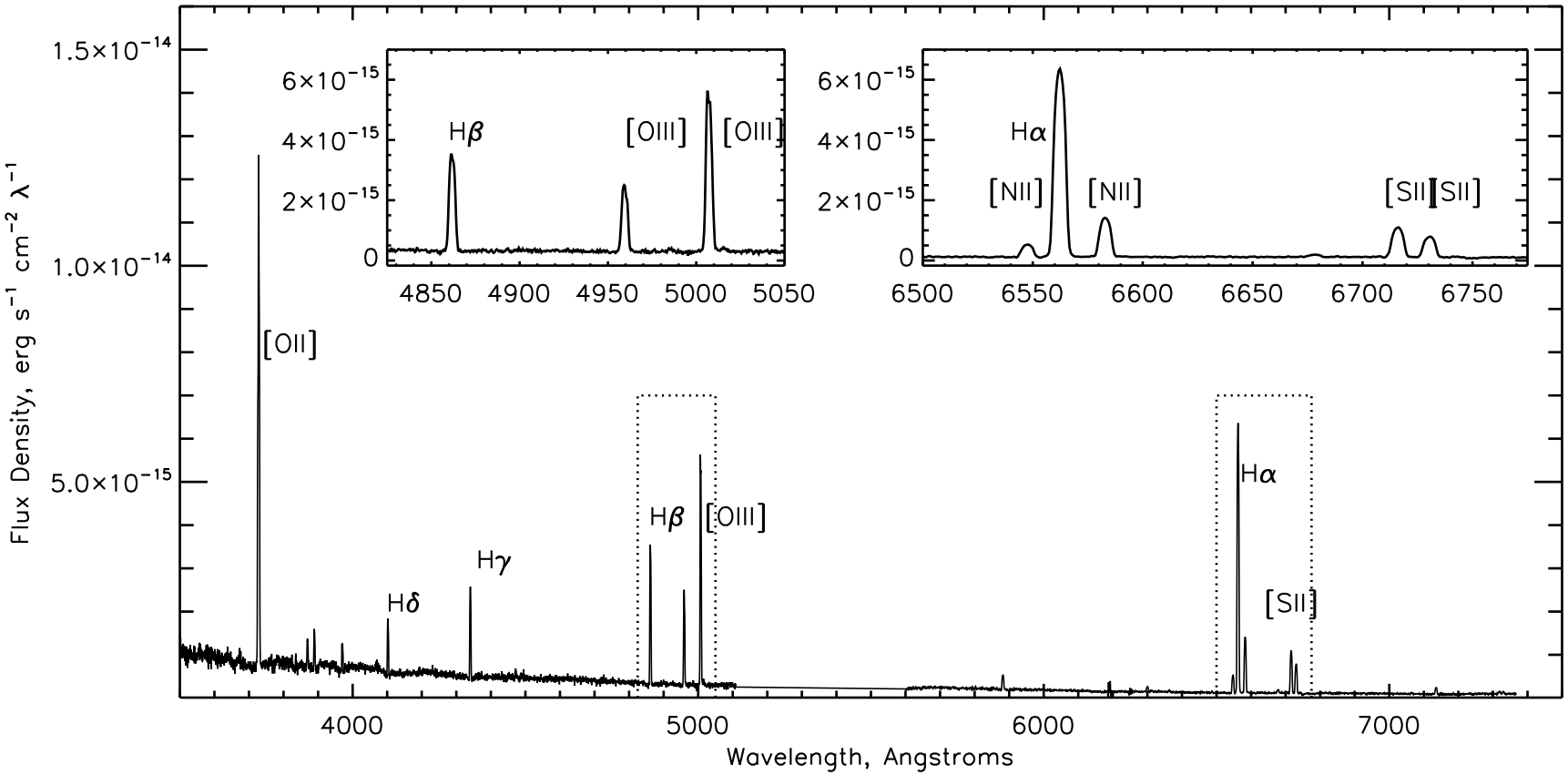

Fig. 4.4.— Rest frame wavelength LBT+MODS spectrum for the blue overdensity in the outer disk of NGC 5387, with insets of the Hα and Hβ spectral windows. The spectrum exhibits nebular emission lines consistent with an HII region.

4.3 The Bright Star Forming Region in NGC 5387

To better characterize the blue overdensity and its potential connection with the stellar stream, we obtained optical spectroscopy for the region. We will first describe the spectroscopic observations in Section 4.3.1 and our measurement procedures in Section 4.3.2. In Section 4.3.3 we describe initial measurements from the spectroscopy. We estimate the physical parameters of the blue overdensity directly from the spectra in Section 4.3.4 and from comparison to Starburst 99 models in Section 4.3.5. Lastly, we explore the mode of star formation in this region in Section 4.3.6.

4.3.1 Observations & Image Processing

Spectroscopy was obtained for NGC 5387 using the dual channel MODS1 spectrograph on the Large Binocular Telescope (LBT) (Pogge et al. 2006) on UT 2012 June 14. The spectrograph was configured with the $R = 2000$ resolution grating and a $1.0''$ slit-width, yielding a spectral range of $3200\mathring{A}$ to $10000\mathring{A}$ with mean resolution of $0.5\mathring{A}$, $0.8\mathring{A}$ per pixel for the central wavelength of the blue and red channels, respectively. Two pointings were obtained, one along the major axis of NGC 5387 (position angle $= 22°$) with central coordinates $(\alpha_{J2000}, \delta_{J2000})$ =($13^h58^m24.8^s$, $+06°04'17''$) and one parallel to the major axis offset by $5.8''$ to intersect the blue overdensity in the disk. Total exposure times were $3 \times 240s$ and $3 \times 600s$ for the two pointings, respectively.

Image processing was completed using the MODS1 python packages[3] following the standard prescription for MODS1 spectroscopic data. The one-dimensional spectra were extracted for a $2''$ region of the NGC 5387 nucleus and the blue region in the APEXTRACT package of IRAF with independent extractions for the blue and red channels. Wavelength calibrations were taken with the $0.6''$ slit and a small zero-

[3]http://www.astronomy.ohio-state.edu/MODS/Software/modsCCDRed/

point offset was calculated between the wavelength calibration spectrum and the science data using the night sky lines (the standard procedure for this instrument). Observations of the spectra-photometric standards Wolf 1346 and Hz 44 were obtained on the same night of observation and were used to spectra-photometrically correct the spectra for extinction using calibration data available in IRAF. Sensitivity functions were calculated independently for the two stars, and were averaged before application to the science spectra.

4.3.2 Spectral Measurements

The line-of-sight velocities of the galaxy from the MODS1 spectra were computed using the FXCOR routine in IRAF. An emission line template was created for emission lines in the $H\beta$ and $H\alpha$ regions smoothed by the average instrumental broadening of $3.36\mathring{A}$, which was estimated from lines in the wavelength calibration spectrum and the night sky lines in the science spectrum. The barycentric correction for the median time of each set of exposures was applied to this template.

We estimate the heliocentric velocity of NGC 5387 to be $v_{helio} = 5226 \pm 3$ km s^{-1}, well in agreement with the systemic velocity derived from its HI profile, 5216 km s^{-1} (Springob et al. 2005) and that measured from the SDSS spectrum 5226 km s^{-1} (Abazajian et al. 2009). Using the same procedure, the heliocentric velocity of the blue overdensity was measured to be 5331 ± 2 km s^{-1}.

Before estimation of emission line fluxes, we corrected the MODS1 spectra for the local Galactic extinction, $E(B-V)_{MW} = 0.03$ (Schlafly & Finkbeiner 2011; Schlegel et al. 1998), assuming $R_V = 3.1$ and applying the extinction law of Cardelli et al. (1989).

Equivalent widths for Hα and Hβ were measured using the interactive IRAF task

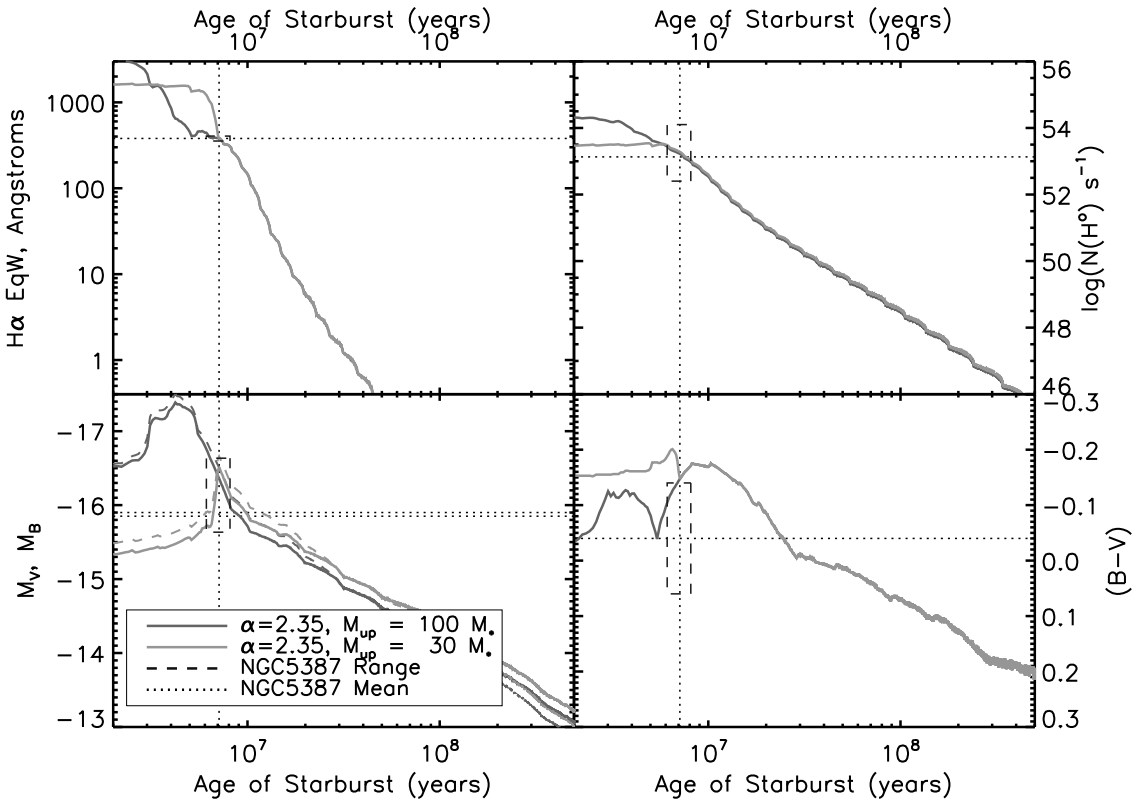

Fig. 4.5.— Comparison of the spectral properties of the NGC5386 blue overdensity to the fiducial Starburst 99 model, with a Salpeter IMF ($\alpha = 2.35$) and with upper mass cutoffs of 100 $M_\odot$ (dark grey) and 30 $M_\odot$ (grey). In the top panels, the Hα equivalent width ($EqW_{H\alpha}$, left) and the number of ionizing photons per second ($N(H^\circ)s^{-1}$, right) are used to estimate the age of the star forming region, resulting in a mean value of 8 $\times$ 10^6 years. In the bottom left panel, the age of the star forming region is compared to the total V (B) band magnitude, M_V (M_B) as the solid (dashed) thick lines. In the bottom right panel, the age of the star forming region is compared to the model $(B-V)_o$ colors to confirm the internal reddening derived from the Balmer decrement method. In each panel the the "mean" value from comparison is shown as a dotted line, and the permitted "range" of values permitted from the uncertainty in each of the the measurements are shown as a dashed box.

SPLOT. Generally, standard line profiles available in SPLOT were poor fits to the line shapes. Thus, emission line fluxes were calculated independently of SPLOT by integrating across the line profile and subtracting the best fit continuum defined individually around each emission line. The median continuum level was 3.85×10^{-15} and 9.75×10^{-16} erg s^{-1} cm^{-2} $\mathring{A}^{-1}$ for the blue and red channels respectively. There was no identifiable stellar absorption at any of the emission lines, (perhaps because we did not integrate sufficiently long to detect the underlying stellar spectral features), but the contributions from the stellar absorption to the measurements required for our work would be small. Thus, we opted not to fit a stellar absorption component to the spectra.

Flux errors were estimated by adapting the simple formulation of Berg et al. (2012, Equation 2):

$$\sigma_\lambda \sim \sqrt{(2 \times \sqrt{N} \times F_{rms})^2 + (0.02 \times F_\lambda)^2} \tag{4.3}$$

where N is the number pixels in the integration, F_{rms} is the median noise in the continuum, 0.02 is the assumed error (2%) in the summation relative to the total measured flux (F_λ). Errors on derived values are propagated using σ_λ as the flux error.

The SDSS imaging was used to design the MODS1 observational parameters. Given the SDSS pixel scale, 0.39″, and low signal-to-noise detection of the blue overdensity, the offset between the NGC 5387 major axis and the overdensity was imperfect. Furthermore, the slit was only 1″ in angular width and therefore the spectroscopic observations did not fully contain the blue overdensity. A correction was computed using FUNTOOLS[4], which uses the DS9 region style syntax to perform flux measurements with custom apertures. Using a circular aperture of 2.2″, we first

[4]https://www.cfa.harvard.edu/∼john/funtools/

calculated the total flux in the blue overdensity, used a nearby region in the disk to estimate the background contributions from NGC 5387. Then, using the MODS1 observing parameters, MODS1 target acquisition images (images taken to align the slit on target), and the spectral extraction parameters in APEXTRACT, the area covered by the slit, the area extracted in the slit, and the area subtracted as a background were determined. The fluxes then were corrected using the ratio of the total flux of the star forming region and flux extracted from the spectra. The fluxes for both the main galaxy and the emission line region were converted to the corresponding luminosity assuming $D = 79.3$ Mpc (Springob et al. 2007, 2009).

4.3.3 Spectral Analysis Methods

The full spectrum for the star forming region is shown in Figure 4.4, with insets providing zooms into the Hα and Hβ regions. The velocity of the star forming region is offset δv $= -104$ km s^{-1} from the NGC 5387 systemic velocity. This offset is well within the NGC 5387 HI profile full-width of $W = 350$ km s^{-1}(Springob et al. 2005). Thus, the blue overdensity is associated with the NGC 5387 system. Assuming the blue overdensity is at the same distance as NGC 5387, the blue overdensity is approximately 850 pc in diameter and is located 9.1 kpc from the center of NGC 5387 or 8.7 kpc projected onto the major axis with a disk height of 2.7 kpc.

Having determined the blue overdensity is a star forming region, the assumed Milky Way extinction is not sufficient to account for the extinction in the region and it is necessary to estimate the internal reddening using the Balmer decrement method. Following the prescription of Calzetti (2012) and taking representative values from Osterbrock & Ferland (2006), we estimate $H\beta/H\alpha = 4.15$, which when compared to the ideal value of $H\beta/H\alpha = 2.87$ yields $E(B-V)_{INT} = 0.35$ with an error of 0.08

(26%) estimated by propagating uncertainties from the flux measurements through our calculations. We then revise our photometry and fluxes using the extinction curve estimates for the Small Magellanic Cloud as detailed in Bianchi (2011, Table 2).

The measured reddening, $E(B-V)_{INT} = 0.35$, implies an $A_V \sim 1$, which is not abnormal for star forming regions (Reines et al. 2008, for example see Table 2) — though it is higher than might be anticipated given the strong FUV emission from the region (see Figure 4.2). Because the reddening is not abnormal, the star forming region is most likely in front of the NGC5387 disk along the line-of-sight.

4.3.4 Spectroscopic Properties of the HII Region

From the fluxes of the nebular emission lines shown in Figure 4.4, we can directly calculate a number of properties of the region, including the SFR, ionizing flux and chemical abundance. All of these values are summarized in Table 4.2. In the text we will apply our total (Milky Way + internal) extinction correction of $E(B-V)_{TOTAL}$=0.38 ±0.08, but we also include values for only the Galactic extinction in Table 4.2 for comparison to systems without an estimate for the internal extinction.

Star Formation Rate: The SFR of the blue overdensity can be derived from the Hα flux using the relationship of Kennicutt (1998a) and Osterbrock & Ferland (2006):

$$SFR(H\alpha) = 7.9 \times 10^{-42} L(H\alpha) \tag{4.4}$$

Using our Hα luminosity, 1.74 ±0.42 $\times$ 10^{41} erg s^{-1} with an 24% uncertainty of from flux and distance uncertainties, we obtain SFR($H\alpha$)= 1.77 M$_\odot$ yr^{-1} (log(SFR) = 0.25). An uncertainty of 0.43 M$_\odot$ yr^{-1} in SFR($H\alpha$) is estimated by propagating flux errors through the SFR calculation.

A second, independent estimate of the SFR can be calculated using the GALEX

FUV photometry in Table 4.2 (Morrissey et al. 2007). The reported FUV flux for the star forming region, also known as GALEX source J135825.0+060438, is 121.67 ± 0.83 μJy corrected only for Milky Way extinction[5]. We estimate a background flux based on a similarly sized region in the disk as 89.37 ± 0.67 μJy[6]. Converted to luminosity, we obtain $L(FUV) = 1.95 \pm 0.14 \times 10^{28}$ erg s^{-1}.

Following the relation of Kennicutt (1998a),

$$SFR(FUV) = 1.4 \times 10^{-28} \times L(FUV) \tag{4.5}$$

results in SFR(FUV) = 2.72 M$_\odot$ yr^{-1} (log(SFR) = 0.44), a value in reasonable agreement with that from $L(H\alpha)$. An uncertainty of 0.20 $M_\odot$ yr^{-1} is estimated by propagating the flux measurement error through the calculation.

We note that the relation of Kennicutt (1998a) assumes a constant and continuous star formation rate over a 100 Myr timescale. There is evidence in the Local Group that dwarf galaxy star formation histories are sufficiently variable, even on these relatively small timescales, to break the assumptions of Kennicutt (1998a) in the FUV to SFR conversion factor resulting in variations as large as a factor of 2 (Johnson et al. 2013).

Ionizing Flux: To better understand the mode of star formation, we also use $L(H\alpha)$ to estimate the total flux of ionizing photons, N_{LyC} in the HII region. Following from Condon (1992), for a 10^4 K gas,

$$N_{LyC} \gtrapprox 7.87 \times 10^{11} \times L(H\alpha) \tag{4.6}$$

[5]We adopt the FUV flux estimated from the NUV catalog position or the `fuv_ncat_flux` for GALEX J135825.0+060438.

[6]We use the `fuv_ncat_flux` for GALEX source J135824.6+060418, which, from inspection of the GALEX images, appears at similar intensity as the average diffuse emission from the NGC 5387 disk.

we estimate a total ionizing flux of $N_{LyC} = 1.35 \pm 0.34 \times 10^{53}$ photons, with a 25% error from the flux and distance uncertainties. Using the observations of Vacca et al. (1996) this is equivalent to ~ 1500 OV7.5 stars in our 850 pc diameter region.

Chemical Abundance: There are multiple techniques to estimate the chemical abundance of an ionized region, the most reliable being the "direct" method (e.g., that used in Berg et al. 2012)), which relies on a detection of the $[OIII]_{\lambda 4363}$ line. The $[OIII]_{\lambda 4363}$ line, however, is not detected in our spectrum to an upper limit of $4.06{\times}10^{-15}$ erg s^{-1} cm^{-2} $\mathring{A}^{-1}$, assuming a line width of $10\mathring{A}$. Thus, we opt to use the strong line calibration of Pilyugin & Thuan (2005) permits computation of the metallicity, $12 + \log(O/H)$, from strong spectral features, that while calibrated to measurements with $[OIII]_{\lambda 4363}$ does not require its detection.

The Pilyugin & Thuan (2005) method uses the spectral line ratios $R_2 = [OII]_{\lambda 3727+\lambda 3729}/H\beta$ and $R_3 = [OIII]_{\lambda 4959+\lambda 5007}/H\beta$ to estimate the excitation parameter, $P = R_3/(R_2 + R_3)$, which is correlated to the oxygen metallicity. Most notably, the calibration has upper and lower branches that diverge between $X_{23} = \log(R_2 + R_3)$ of 0.7 and 1.0. For our HII region we calculate, $P = 0.34$ and $X_{23} = 0.83$, which place the region in the transition zone between the two calibrations (see Figure 12 of Pilyugin & Thuan 2005). Thus, we opt to average $12+\log(O/H)$ calculated on both branches, for which we obtain $12 + \log(O/H) = 7.97$ for the lower branch and $12 + \log(O/H) = 8.06$ for the upper branch. We adopt $12 + \log(O/H) = 8.03 \pm 0.28$ for the metallicity of our HII region, and taking the 40% error from the Pilyugin & Thuan (2005) calibration for each of our two estimates. Given that there are numerous techniques for estimating the metallicites with differing systematics (e.g., see discussions in Skillman 1989; Berg et al. 2012), the spectral line fluxes relevant to these calibrations are presented in Table 4.3.

4.3.5 Properties Derived by Comparison to Starburst99

In addition to properties derived directly from flux measurements, star forming properties can be estimated in comparison to the fiducial Starburst 99 models (Leitherer et al. 1999, SB99, hereafter). In Figure 4.5 the model predictions from SB99 used in our analysis are given for an instantaneous 10^6 $M_\odot$ starburst in a $Z = 0.001$ metallicity gas, with a Salpeter IMF ($\alpha = 2.35$) and upper mass cutoffs of 30 $M_\odot$ (dark grey) and 100 $M_\odot$ (light grey).

Stellar Population Age: The age of the HII region can be estimated using the equivalent width of the Hα emission line. We obtain the $EW_{H\alpha} = 380\mathring{A}$ and adopt an error of $\pm$ 10$\mathring{A}$. In the top left panel of Figure 4.5, we compare our measurement (dotted lines) to the Hα EqW-age relationship in SB99. We estimate the age of the star forming region is 8×10^6 years, with a range of of 1×10^6 years permitted by the variation in the model and our uncertainty in $EW_{H\alpha}$. A similar estimate of the age was obtained using the equivalent width of the Hβ line, $EW_{H\alpha}$ =50 $\pm$ 10$\mathring{A}$.

Mass: The mass of a star forming region can be estimated by comparing the absolute V or B broadband magnitude to the magnitude-age trend in SB99, given for M_V in the bottom left panel of Figure 4.5. The SB99 models assume a mass of 10^6 $M_\odot$, but the total broadband flux scales linearly with the mass of the region. Given our de-reddened magnitude, M_V =-15.85 (Table 4.1), we estimate a total stellar mass of $\sim 2.5 \times 10^7 M_\odot$, and adopt and error of 50% on this value based on magnitude uncertainties and the range of permitted population ages. For consistency, we also estimate the mass using the M_B magnitude to obtain a similar estimate.

Comparing other Parameters: Lastly, to confirm that our SB99 estimated parameters are all self-consistent, we re-normalize the SB99 model to our assumed mass and compare to other physical parameters (Figure 4.5). First, we ensure that

the number of Lyman continuum photons is consistent with the mass of our region. As shown in the top right panel of Figure 4.5, our measured N_{Lyc} is consistent with the SB99 model at our inferred stellar population age. Second, we compare the intrinsic $(B-V)_o$ color to the age in the bottom right panel of Figure 4.5. The de-reddened color of our region, $(B-V)_o$ = -0.04 is consistent with the color of the model at this age, given a conservative error in the color and the de-reddening (shown as the color range in bottom right panel of Figure 4.5). Given the overall consistency between our suite of observational data and SB99, we are confident that, given our data, these parameters provide a reasonable description of the blue overdensity. The adopted physical parameters for the star formation region are summarized in Table 4.2.

4.3.6 Discussion of Star Forming Properties

A component to understanding the origins of the blue overdensity in NGC 5387 is to characterize the mode of star formation in the blue overdensity. We will do this by comparing our measurements for the blue overdensity to those of a number of well studied star formation regions.

First, we evaluate if the size and luminosity of the region are more consistent with a single H II region or a larger complex. In Figure 4.6, the size and Hα luminosity of the NGC 5387 H II region are compared to the sample of Kennicutt (1984); this demonstrates that the blue overdensity is both larger and more luminous than single HII regions. Instead, the NGC 5387 H II region has both a size and luminosity characteristic of "multiple H II region complexes" observed in giant spirals like M 101. As discussed by Kennicutt (1984), these regions could contain several individual 30 Doradus-class H II regions in a single symmetric envelope of ionized and neutral gas. While these star forming complexes are generally seen in large galaxies, they are also

observed in star-forming dwarf galaxies, like NGC 4449, M 33 and the LMC (Kennicutt 1984). Thus, we move forward considering the blue overdensity is composed of multiple, unresolved regions that are forming stars.

Following the example of Hunter (1999), diagnosis of the mode of star formation is akin to understanding the concentration stars within an H II region. To demonstrate, we compare 30 Doradus in the LMC and Constellation III in the Milky Way, two regions that have similar mean properties. The 30 Doradus region contains the super-star cluster R 136, a ∼2 pc sub-component that is the origin of most of the flux from the entire complex. Constellation III, in contrast, is described as a "scaled up OB association" — a large, but overall low density region of young stars. Constellation III and 30 Doradus have similar sizes and fluxes, but represent drastically different star forming environments. The observational difference between these regions is the density of high mass stars, though the comparison is complicated due to slight difference in age (30 Doradus $\lessapprox$ 8 Myr, and Constellation III $\sim$ 10 Myr).

To characterize the star forming region in NGC 5387, we can make a number of comparisons. First, we can compare the blue overdensity to 30 Doradus, for which the total extent is $R \sim$ 100pc and the total Hα luminosity is $L(\mathrm{H}\alpha)= 3.2\times10^{39}$ (Lopez et al. 2014). The blue overdensity would have to contain 54 individual 30 Doradus-like regions to produce is measured Hα luminosity (see Table 4.2) and by volume it could contain 600 such regions (assuming spherical geometry). Second, we can compare to the ensemble of super star cluster candidates in NGC 4449 identified by Reines et al. (2008, Table 5). The sample of 12 super star cluster candidates comprise a total mass of 2×10^5 $\mathrm{M}_\odot$, and produces $\mathrm{N}_{LyC} = 3.7\times10^{51}$ ionizing photons. Scaled to our total mass, 2×10^7 $\mathrm{M}_\odot$, our ionizing flux is comparable to a scaled up version of those regions in NGC 4449.

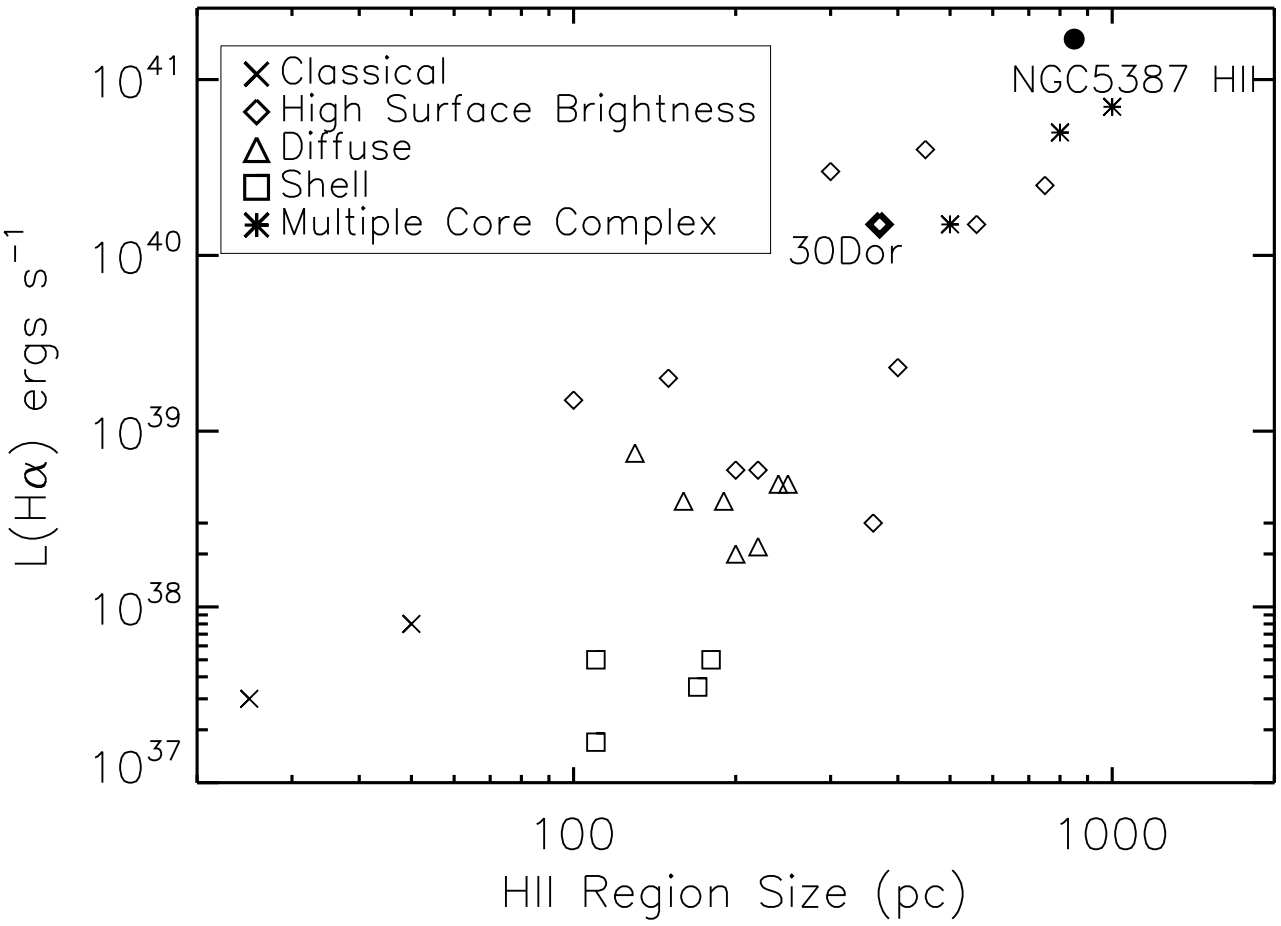

Fig. 4.6.— The observed size - Hα luminosity - type relationship for the sample of HII regions considered in Kennicutt (1984). The regions are coded by the type of HII region: multiple core complexes as stars, shell as squares, diffuse as triangles, high surface brightness as diamonds and classical as xes. The HII region in NGC 5387 is both physically larger and more luminous than the classical giant HII regions 30 Doradus in the LMC and N604 in M33. Instead, it has properties similar to the "multiple core complex" HII regions like N5471, N5461 and N5455 in M101 (stars), implying the blue overdensity is composed of multiple smaller star forming regions.

4.4 Interpretation of the Observational Data

We have presented a set of observations that confirm the existence of a stellar stream in the halo of NGC 5387 that, in projection, intersects the disk of NGC 5387 near a prominent blue overdensity. There are no distinguishable overdensities within the angular extent of the stream and we do not directly identify a progenitor within the stream itself. Spectroscopy of the blue overdensity confirms it is associated with NGC 5387. Derived properties from nebular emission lines indicate it to be a young, massive, metal-poor H II complex. These observations are consistent with a number of physical scenarios.

4.4.1 Star Formation in the Disk?

It is possible that the blue overdensity represents star formation occurring naturally in the disk, as is the case for a very massive, luminous and young star cluster in the spiral galaxy NGC 6946 studied by Larsen et al. (2001). The existence of this cluster is an example of how "violent interactions" like mergers are not a required condition to create "extreme" star forming environments in otherwise undisturbed galaxies (Larsen et al. 2001). The cluster in NGC 6846, however, has a mass of 8.2×10^5 $M_\odot$, much less massive than the blue overdensity in NGC 5387. Furthermore, the SFR in the blue overdensity measured from Hα is nearly five times that measured in the center of NGC 5387, making it a quite extreme event for the outer disk of a MW analogue galaxy. Given that $\sim$100 of the clusters studied by Larsen et al. (2001) would have to exist in an 850 pc region, this blue overdensity in NGC 5387 seems to be a much more "extreme" case than that of NGC 6946. Thus, it seems unlikely that we are seeing star formation in the disk following an in-situ mode.

Having ruled out natural star formation in the NGC 5387 disk, it is possible that

the blue overdensity is induced star formation. Generally, it is not clear what occurs when a dwarf satellite passes through the outer disk of its parent. Current insight is limited to modelling that neither provides the proper spatial resolution, nor fully implements star formation prescriptions at the level needed to distinguish if the disk is "transparent" to the stream crossing or if there is sufficient gravitational influence to induce star formation. The observation of enhanced star formation in the outer disk of NGC 5387 provides one of the first observational test cases to explore the effects of a minor merger on the outer disk of a Milky-Way analogue. To evaluate this scenario, we can explore two key questions in our observational data: (i) Are the kinematics of the blue overdensity consistent with the those of the NGC 5387 disk? (ii) Is the metallicity of the gas consistent with that of the NGC 5387 disk?

First, using V_c from the NGC 5387 HI profile (Springob et al. 2005), we can estimate the average rotational velocity of the disk at the radius of the overdensity. Using $R_{sfr} = 8.7$ to 9.1 kpc and the form of a standard rotation curve, the estimated disk motion in an edge-on galaxy should be near V_{max}, which for NGC 5387 is V_{max} = 162.9 $\pm$ 3 km s^{-1} (Springob et al. 2005). Given our uncertainty in the actual 3-dimensional position in the disk due to the inclination ($i = 77°$), we could expect to see deviation from V_{max} due to non line-of-sight motions. With a velocity offset of δv = 104 km s^{-1}, the blue overdensity has kinematics not inconsistent with being in the disk of NGC 5387, though with a relatively large dispersion.

For a basic estimation of the metallicity-radius relationship in the NGC 5387 disk, we employ the HII region metallicity-radius relationship observed in the Milky Way by Balser et al. (2011). We use their 360° relation,

$$12 + \log(O/H) = 8.866 - 0.0383 \times R_{gal}, \tag{4.7}$$

and renormalize using the metallicity of the central region of NGC 5387 from SDSS spectroscopy, $12 + \log(O/H) = 9.05$ (Tremonti et al. 2004). we estimate that at the location of the HII region, R_{sfr}= 8.7 kpc, This implies a metallicity of 12+log(O/H) = 8.73 at the galactocentric radius of the blue overdensity. The NGC 5387 HII region ($12 + \log(O/H) = 8.03$) is more metal poor than that expected in the native gas at this radius.

However, taken together it is not impossible that star formation has been induced in the outer disk of NGC 5387. We must pose several questions relating to this hypothesis. First, can such an event occur in the outer disk of a typical spiral galaxy? Second, can we explain the deviations from typical kinematic and chemical abundance trends in a spiral galaxy?

4.4.2 Tidal Dwarf Hypothesis?

Third, the blue overdensity could be formed from a gaseous component of the stellar stream intersecting the disk, or from the collision of a high velocity cloud (HVC) with the stream itself, though either of these scenarios seems highly unlikely. The formation of such a star forming region is analogous to the formation of a tidal dwarf in a major merger, though on a much smaller and less extreme scale. This "tidal dwarf" interpretation relies on there being an expelled gaseous component to this minor merger or for there to be considerable gas reservoirs in the halo of NGC 5387.

The HI content of NGC 5387 can be explored using the Arecibo 305m HI line profile of Springob et al. (2005). The beam size of Arecibo, 189″, contains the full disk of NGC 5387, including the full stellar stream of NGC 5387. The profile shows no significant distortions or other abnormal features to suggest that NGC 5387 has any significant HI content outside of the expected disk motion. The profile, however, has

an average channel width of 11 km s^{-1} and an average rms of 1.67 Jy (Springob et al. 2005), corresponding to a mass resolution of 1.3×10^9 $M_\odot$ at 80 Mpc in a single 11 km s^{-1} channel. This sensitivity may not detect a gaseous stream or large cloud. Thus, while we cannot rule out that the NGC 5387 stream has a gaseous component, there is no clear observational evidence from archival data for any abnormal HI features in NGC 5387.

On the other hand, the observed population of high velocity clouds (HVCs) in the Milky Way and Andromeda do suggest that there can be relatively large clouds of gas moving within the halo, and such gas clouds are considered a normal component of MW-sized galaxy (See Putman et al. 2012, and references therein). The Milky Way HVC population includes clouds with total gas masses greater than $10^6 M_\odot$, typical physical sizes of ∼1-2 kpc, and estimated metallicites ∼0.1 $Z_\odot$ (Wakker 2001). The total mass of even the largest of the HVCs is an order of magnitude smaller than the stellar mass of the NGC 5387 blue overdensity, 2×10^7 $M_\odot$. Additionally, the high FUV SFR indicates that the region has been forming stars for an extended period of time, 100 Myr or more, at which point an HVC would have already extinguished its gas reservoir (Lee et al. 2011). Thus, it seems unlikely that such a star forming region could be generated from an HVC collision with the stream.

4.4.3 Stream Progenitor Hypothesis?

The blue overdensity could be the progenitor of the stream. More specifically, it is possible that we have caught the satellite galaxy soon after its passage through the disk, but it is the satellite itself, not the disk, that is currently undergoing star formation. Given that progenitors of the stream should be detected along the orbit of the stream, the blue overdensity is a strong candidate for the progenitor. Typically,

when progenitors can be connected to a stellar streams, those progenitors are already gas poor and contain no appreciable on-going star formation or very young (< 1 Gyr) stellar content, though we do note that there is a 2 Gyr population in the Sagittarius dSph (Siegel et al. 2007). Thus, for most observed stream progenitors there is little to no gradation in color along the stream; the progenitor and the stream are largely indistinguishable in color. In fact, in a search for MW-LMC analogue systems (within a 60 Mpc volume), many systems have been identified with long stellar streams or with tidal distortions in the satellite, but none have exhibited strong color gradients (Martínez-Delgado et al., in prep.). If the blue overdensity is the progenitor of the stream, then this is the first minor merger to be detected with a strong a color gradient.

A clear morphological analogue to NGC 5387 is the NGC 5899 system, which also contains a red stellar stream in its outer disk. The progenitor of the stream in NGC 5899 is identified as a highly distorted overdensity along the stream near the inferred apo-centric radius (Martínez-Delgado et al., in prep.). Because a satellite spends a large fraction of its orbit at apo-center, most satellites are discovered at or near their apo-centric radii, typically far from the disk of the parent galaxy. The blue overdensity, however, is located in front of the NGC 5387 disk in projection. If the blue overdensity is the progenitor, it is likely detected at or near its pericentric radius, its closet approach to the NGC 5387 disk, i.e., an unlikely position.

Many dwarf spheroidal satellites in the Local Group show periodic episodes of enhanced star formation with a cadence similar to their orbital parameters (Dolphin et al. 2005). It is, however, exceedingly rare to find a star forming satellite in the halo of its parent (Geha et al. 2012), to find any significant gas reservoirs in satellite galaxies (Grcevich & Putman 2009), or to find close satellites with colors similar to

the LMC (Tollerud et al. 2011). Taken together, the relative scarcity of star forming dwarf satellites implies that the removal of gas from satellite galaxies is highly efficient, occurring very quickly relative to the survival timescale of the progenitor. If the blue overdensity is the progenitor for the stream, then it, as a dwarf satellite, presents exceptionally rare characteristics.

One of the properties of the blue overdensity is the discrepancy between the SFR estimated from the Hα and FUV luminosity. The Hα luminosity is most sensitive to the highest mass stars whose lifetimes are very short (<10 Myr), and, therefore, this SFR indicator traces the most recent star formation. In contrast, the FUV SFR can is sensitive to stellar populations as old 100 Myr, and the estimated FUV SFR implies that the blue overdensity has been forming stars for at least the past 100 Myr, a timescale smaller than the inferred timescale for the formation of the stream. Thus, the orbit for progenitor of the stream could have induced star formation enhancements prior to the < 10 Myr population traced by the Hα equivalent width. Not only could these two indicators trace slightly different populations, but also the application of the UV SFR conversion factor could be inappropriate for the blue overdensity, as it assumes a constant and continuous SFR for $\sim$100 Myr. Regardless, the typical SFR for a dwarf galaxy of the same mass, traced by the total B magnitude M_B, is 0.03 $M_\odot$ yr^{-1}, as estimated from the Local Volume Legacy Survey(Kennicutt et al. 2008). Thus, the both the $L(H\alpha)$ and $L(FUV)$ SFR measurements of the blue overdensity are enhanced compared to dwarf galaxies with similar properties. In addition to being consistent with timescales implied from the SFR indicators, the stream progenitor hypothesis is also consistent with the low metallicity measured for the blue overdensity, and, given the mass of the stream debris, the small mass of the region.

The stream progenitor origin of the blue overdensity is compelling because this interpretation is consistent with both the physical parameters of the blue overdensity and from the merger properties inferred from the stellar stream. If the blue overdensity is the progenitor of the stream, then we are observing a galaxy undergoing a period of significantly enhanced star formation during a minor merger. Although the observational evidence for some enhancement of star formation in such events is inferred form the star formation histories of Local Group galaxies (Dolphin et al. 2005), such a large enhancement has not been previously observed for a minor merger nor has such an enhancement been predicted in numerical simulations.

Thus, we must pose several questions relating to this hypothesis. First, can a dwarf galaxy maintain its gas reservoirs through a merger having a relatively small pericentric radii? Second, can the dwarf form stars at the measured SFR and over the time scales implied by the FUV SFR?

4.4.4 Chance Alignment?

Lastly, it must be considered that the stellar stream and the blue overdensity are a chance alignment — that the physical origins of the stream and the blue overdensity are unrelated. It is clear that the stellar stream is an accretion remnant, and, given its redshift, the blue overdensity would have to be a second satellite of dwarf Irregular type within NGC 5387 system. This two satellite scenario, however, is a very low probability event. First, the NGC 5387 stream has a relatively high surface brightness, 24.5 mag arcsec^{-2}, compared both to the known sample of stellar streams (Martínez-Delgado et al. 2010; Miskolczi et al. 2011) and to those streams in the simulated halos of Bullock & Johnston (2005). Second, star forming satellites within close to their host are exceptionally rare. In a sample of close host-satellite pairs in SDSS, Tollerud et al.

(2011) found only 10% of MW analogues had a satellite within 50 kpc, and of those only 20% of those are bluer than M33, 1.3% bluer than the LMC. NGC 5387 would be accreting two of its largest satellites within ∼1 Gyr of each other and both of those systems are exceptional in their properties. Thus, we find it statistically unlikely that the blue overdensity is independent of the stellar stream given the statistics, both observed and simulated, on such events individually.

4.4.5 Discussion of Interpretations

In this Section, we have considered four interpretations of our observational data on the blue overdensity of NGC 5387: (i) disk star formation (induced or in situ), (ii) a tidal dwarf analogue system, (iii) a star burst in the stream progenitor, and (iv) a chance alignment of two unrelated accretion events. Using our observational evidence and modeling NGC 5387 based on radial trends in the Milky Way, we have found that both the tidal dwarf and the chance alignment scenarios are highly unlikely. The remaining two scenarios, merger-induced star formation either in the parent disk or the stream progenitor, while better fits to our observational data, are physical situations that have neither been directly observed, nor modelled sufficiently to inform our interpretation. It remains unclear if the passage of a satellite galaxy through the outer region of a parent disk could induce star formation of this degree — even though there are examples of satellites in the Local Group that may have passed through their parent's disk in the recent past (Athanassoula & Beaton 2006; Majewski et al. 2003). To further understand our observations, we require numerical modeling to determine if either of our two preferred scenarios are feasible. These simulations and a further exploration of the NGC 5387 system will be presented in a companion paper.

4.5 Summary

Our deep VATT observations of NGC 5387 show a stellar stream in its halo that interests the NGC 5387 disk near a blue overdensity. Remarkably, both features were first discovered in SDSS, showing that streams of a 1:50 mass ratio can be visually identified in SDSS, even where other search techniques fail (Miskolczi et al. 2011). The measured properties of NGC 5387, the stellar stream, and the blue overdensity are given in Tables 4.1 and 4.2.

The stellar stream has a median surface brightness of $R \sim$24.5 mag arcsec^{-2} and a total magnitude, $R = 17.5$. The stream subtends 360° and wraps around the disk of NGC 5387, with a width of 11″ (4.2 kpc). Though there are large SB variations, the stream appears physically smooth overall with no clear overdensities consistent with the progenitor of the stream. Lower surface brightness wraps of the stream are ruled out to our surface brightness sensitivity limit of 28.3 mag arcsec^{-2}. The stream is red in color, $(B-V) \sim$0.7, suggestive that it is comprised primarily of old stellar populations. The total stellar mass in the stream is approximately 6×10^8 M$_\odot$ and the stream appears to have formed in ∼240 Myr from a progenitor with a total mass 4×10^{10} M$_\odot$.

In contrast to the stellar stream, the blue overdensity is blue in color, $(B-V) = 0.28$ (for $E(B-V) = 0.03$), and FUV bright, implying that it is actively forming stars. While the blue overdensity can be associated with the NGC 5387 system, we cannot confidently associate it with the stellar stream. If it is associated with the stream, however, this is the largest color gradient observed in accretion debris (Martínez-Delgado et al. 2010) and implies that it is possible for a satellite core to maintain its gas at least ∼240 Myr into the merging process. Numerical simulations to explore the relationship between these two features will be presented in a companion paper.

While the relationship between the overdensity and the stellar stream remains indeterminate, our classification of the blue overdensity as a star forming region is clear. The blue overdensity is ∼850 pc in diameter, metal poor ($12+\log(O/H)$=8.03 ±0.28), and has a star formation rate of 1.19 ±0.43 $M_\odot$ yr^{-1} from $L(H\alpha)$ or 2.72 ±0.20 $M_\odot$ yr^{-1} from $L(FUV)$. The stellar mass for the region is 2.5±1.3×10^7 $M_\odot$ and the age of the stellar population is ∼ 8±1 Myr, though the $L(FUV)$ implies the region could have been forming stars for at long as 100 Myr (Lee et al. 2011).

A comparison of the blue overdensity to H II regions in the nearby Universe (Figure 4.6) implies that it is most likely composed of several individual H II regions that we are unable to distinguish due to the seeing (1″) and the VATT spatial resolution (0.38″ per pixel) of current imaging data. Furthermore, the region is producing ionizing photons comparable to that produced by the entire super star cluster population in NGC 4449 (scaling to total mass), i.e., a dwarf galaxy forming stars at twice the rate of the LMC (Reines et al. 2008). Thus, we infer that the star formation mode in this region is akin to those modes observed in nearby star-burst dwarf irregular galaxies.

Combining all of our observational data, there are four possible interpretations: (i) the blue overdensity represents star formation induced in the disk by the minor merger, (ii) the blue overdensity is a dwarf formed during the interaction, (iii) the blue overdensity is the galaxy remnant of the progenitor of the stream in a burst phase, and (iv) the blue overdensity is an unrelated object. After careful consideration, we reject both the tidal dwarf (Section 4.2) and the chance alignment scenarios (Section 4.4). Thus, the blue overdensity most likely represents star formation induced by a minor merger – either in the disk of the parent or in the progenitor of the stream. Neither phenomenon has been directly observed previously for an accretion event of this size. Given the similarities of the blue overdensity to NGC 4449 and the enhanced

SFR in FUV (sensitive to SF of age ∼100 Myr), the blue overdensity is most likely the progenitor of the stream caught in a burst phase. Confirmation of this interpretation via detailed simulations and a full exploration of the implications of the NGC 5387 system will be presented in a companion paper.

Table 4.1. Photometric Properties of the NGC 5387 System

Photometry Property	NGC 5387 Total	Stellar Stream	Blue Overdensity E($B-V$)=0.03	Blue Overdensity E($B-V$)=0.35
M_{FUV}	-17.06 ± >0.08 (1)	...	-16.39 ± 0.38 (2)	...
M_{NUV}	-17.67 ± >0.08 (1)	...	-16.53 ± 0.25 (2)	...
M_B	14.46 ± 0.04	∼19	-14.55 ± 0.14	-15.90 ± 0.32
M_V	13.67 ± 0.05	∼18.1	-14.83 ± 0.12	-15.85 ± 0.25
M_R	13.10 ± 0.03	17.5	-15.04 ± 0.10	-15.82 ± 0.19
$(B-V)_o$	0.79	0.6-0.9	0.28 ± 0.04	-0.04 ± 0.08
$(B-R)_o$	1.36	1.2-1.7	0.50 ± 0.05	-0.08 ± 0.11
M_*	$3.13^{+1.21}_{-0.87}\times10^{10}$ $M_\odot$	$6^{+2.4}_{-1.7}\times10^{8}$ $M_\odot$	...	...
M_{tot}	1.1×10^{11} $M_\odot$	4×10^{10} $M_\odot$	...	...

Table 4.2. Spectroscopic Properties of the NGC 5387 System

Property	NGC 5387 Total	Blue Overdensity E($B-V$)=0.03	Blue Overdensity E($B-V$)=0.35
v_{los}	5226 km ± 3 km s^{-1}	5331 ± 2 kms^{-1}	5331 ± 2 km s^{-1}
M_*	3×10^{10} M$_\odot$ (1)		2×10^7 M$_\odot$
$12+\log(O/H)$	9.05 (2)	8.04 ± 0.28	8.03 ± 0.28
Age	...	8 ± 1 Myr	8 ± 1 Myr
L(Hα)	...	9.97 ±1.73 ×10^{40} ergs s^{-1}	2.24 ±1.73 ×10^{41} ergs s^{-1}
SFR L(Hα)	0.22 M$_\odot$ yr^{-1} (3)	0.53 ±0.19 M$_\odot$ yr^{-1}	1.19 ±0.43 M$_\odot$ yr^{-1}
L(FUV)	...	3.0 ±0.24 ×10^{26} ergs s^{-1} (4)	1.95 ±0.14 ×10^{28} ergs s^{-1}
SFR L(FUV)	...	0.04 ±0.0034 M$_\odot$ yr^{-1}	2.72 ±0.20 M$_\odot$ yr^{-1}
N_{LyC}	...	7.83 ±1.88 ×10^{52} photons	1.35 ±0.32 ×10^{53} photons

Table 4.3. Spectral Line Fluxes for the NGC 5387 Blue Overdensity

Spectral Feature	Flux ×10^{-15} (erg s^{-1} cm^{-2}) λ^{-1} E($B-V$)=0.03	Error E($B-V$)=0.03	Flux ×10^{-15} (erg s^{-1} cm^{-2} λ^{-1}) E($B-V$)=0.35	Error E($B-V$)=0.35
$[OII]_{\lambda 3727\AA+\lambda 3729\AA}$	103.34	7.75	465.83	34.28
Hβ (λ4861$\AA$)	31.89	4.41	103.84	14.38
$[OIII]_{\lambda 4959\AA}$	22.13	5.00	69.82	15.65
$[OIII]_{\lambda 5007\AA}$	54.31	5.45	169.14	16.80
Hα (λ6563$\AA$)	132.51	30.52	298.46	68.70

Chapter 5

Cannibalization and Rebirth in the NGC5387 System.

II. Modelling and Implications

5.1 Chapter Summary

NGC 5387 is an edge-on spiral galaxy with a stellar stream that, in projection, intersects its disk at a region, that is actively forming stars at a rate of 2 $M_{\odot}$ yr^{-1}. As presented in Beaton et al. (2014), there are two likely potential origins of the star forming region, (i) star formation in the NGC 5387 disk induced by the passage of the stream progenitor through the disk, and (ii) star formation in the stream progenitor induced by the interaction. Neither of these scenarios have been directly observed in a merger of this mass ratio. We explore the viability of these scenarios via numerical simulations to conclude that the region is most likely the remnant of the stream progenitor, which implies that we have caught this event at a unique phase. We obtain a better understanding of this conclusion via comparison to nearby star-forming galaxies in the Local Volume Legacy Survey (LVLS) and to Milky Way-LMC analogues in the Sloan Digital Sky Survey footprint. Lastly, we apply galaxy morphology metrics to the images of NGC 5387 to understand how this galaxy would be classified in a "blind" morphology survey, and find the *FUV* morphology is consistent with a merger of a significantly larger mass ratio.

5.2 Introduction

In the Λ-CDM paradigm, large galaxies like the Milky Way are formed via the the hierarchical merging of numerous less-massive galaxies. This prediction is broadly confirmed by observations of satellite galaxies and stellar debris in the haloes of the Milky Way (MW) and Andromeda (M 31) in the Local Group, as well as in more distant galaxies (e.g., Martínez-Delgado et al. 2010; Miskolczi et al. 2011). There are two pressing discrepancies between the predictions of Λ-CDM and detailed compar-

isons to the satellite galaxies in the Local Group: (i) the missing satellites problem — the overall deficit of observed satellite galaxies of all masses as compared to simulations (e.g., Moore et al. 1999), and (ii) the too big to fail problem — that the most massive satellites have mass densities inconsistent with their counterparts in simulations (Boylan-Kolchin et al. 2010, 2012). The solutions to both problems require detailed observations probing the evolution of the baryonic components of satellite galaxies to properly insert the "astro-physics" of galaxy formation into the physics of the Λ-CDM paradigm. Regarding the "missing satellites", tests on the stellar content of surviving dwarf galaxies, most notably their star formation histories and chemical enrichment patterns, may provide insight into how reionization and SN feedback impact small galaxies with shallow potential wells (Alvarez et al. 2009). For "too big to fail," the structure of satellite galaxies must be probed to large radii and low surface brightnesses to diagnose how gravitational harassment influences the re-ordering of mass within them (Zolotov et al. 2012). Thus, detailed observational efforts probing the evolution of the baryonic components of satellite galaxies are necessary to resolve this problem.

Here we present an investigation of one such merger that probes the evolution of the baryons within the dwarf satellite, that of NGC 5387, its stellar stream and a star-forming blue overdensity as discovered in Beaton et al. (2014, Paper I, hereafter). To motivate the aims of this work, we first summarize the observations of NGC 5387 from Paper I in the following section.

5.2.1 Summary of Observational Data in Paper I

In Paper I, the NGC 5387 system was found to contain a low surface brightness stellar stream (mean(μ_R) = 25.4 mag arcsec^{-2}) and a blue overdensity ($B - V$ =

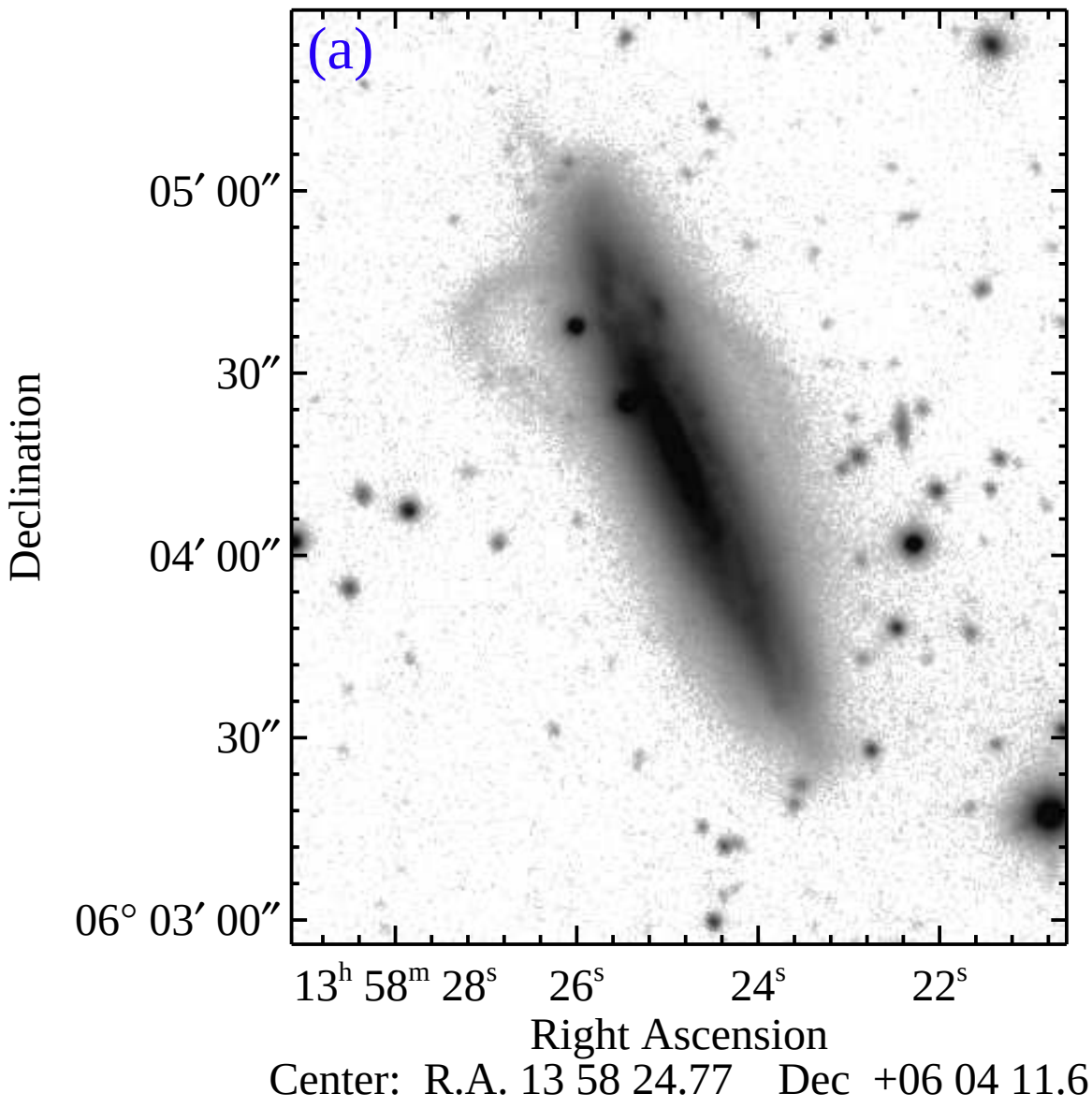

Fig. 5.1.— The NGC 5387 system. **(a)** VATT R image of NGC 5387 that shows the low sufrace brightness stellar stream. **(b)** GALEX FUV image of NGC 5387 that shows the very bright star forming region in the disk, which is coincident (in projection) with the intersection of the stream and the disk.

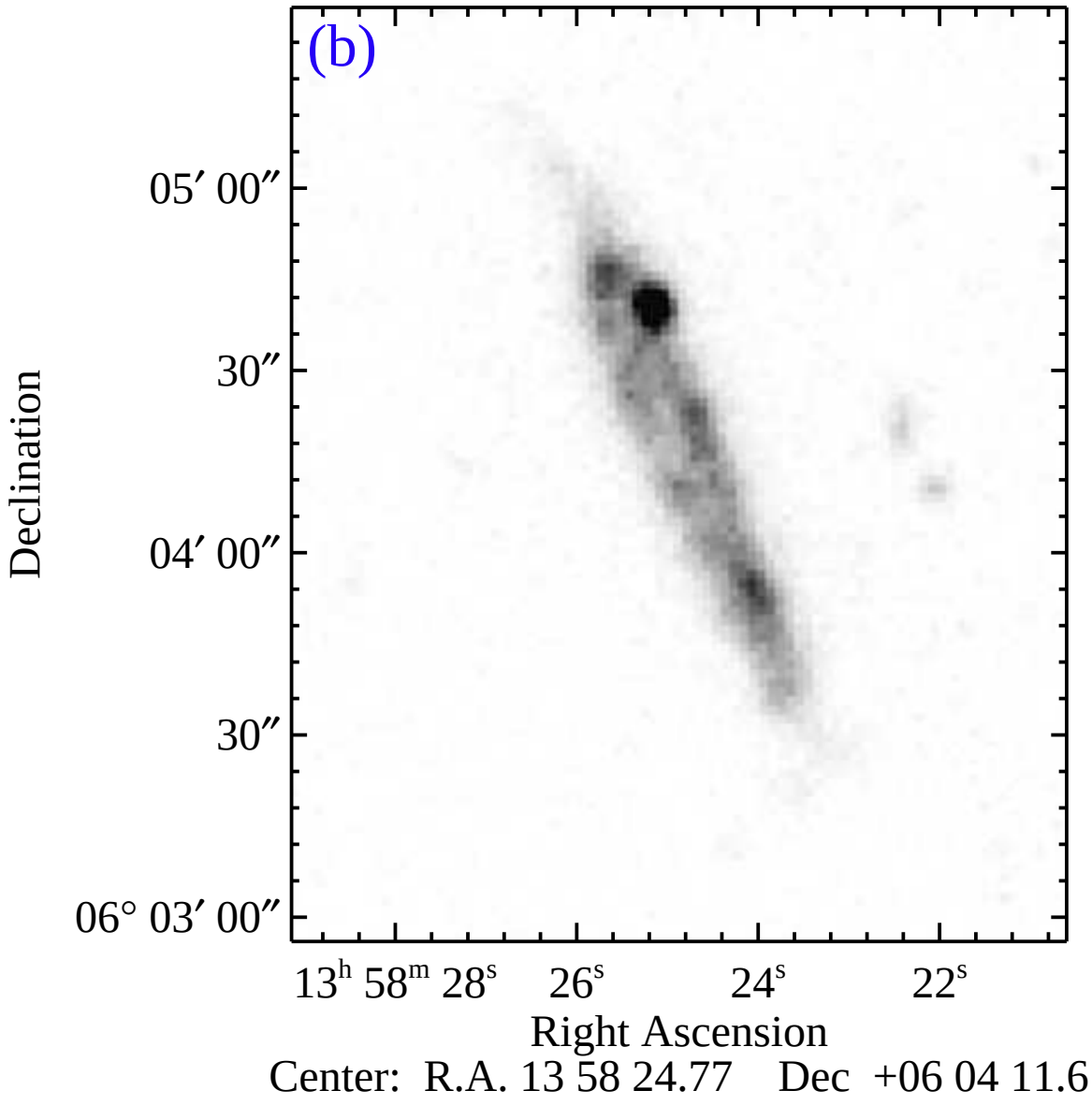

Fig. 5.1.— cont. The NGC 5387 system. **(b)** GALEX FUV image of NGC 5387 that shows the very bright star forming region in the disk, which is coincident (in projection) with the intersection of the stream and the disk.

0.28 ±0.04), The system has three relevant components visible in Figure 5.1a: (i) the galaxy NGC 5387, (ii) the stellar stream, and (iii) the blue overdensity. Figure 5.1b is the far ultraviolet (FUV) GALEX image of the same area as Figure 5.1a, which emphasizes the blue overdensity. Here we summarize the physical properties for each of these components as determined from the observational data presented in Paper I.

NGC 5387: NGC 5387 is an edge-on ($i = 80°$) Sbc galaxy with total mass 1.08×10^{11} $M_\odot$ and a maximum rotation velocity V_{max} = 169.3 km s^{-1} (Springob et al. 2005). As compared to the ∼78000 member spiral galaxy sample in the Sloan Digital Sky Survey footprint (SDSS: Blanton et al. 2005; Blanton & Moustakas 2009), NGC 5387 is overall "average" in its global properties, including its star formation rate (SFR), total metallicity, and neutral gas fraction. Given its total mass and overall morphology, NGC 5387 can, for general purposes, be considered an analogue to the Milky Way.

The Stellar Stream: In projection, the stellar stream is of "great circle" type morphology (Johnston et al. 2008) and appears to subtend ≥ 360° around NGC 5387 to the surface brightness limit of the optical imaging (Paper I). The circular radius of the stream is approximately 11.7 kpc, though we note that the three dimensional orientation of the stream is challenging to constrain. The stream has a $B - V$ color ranging from 0.6 to 0.9, implying it is composed primarily of older stellar populations. The morphology of the stream places direct constraints on both the formation timescale of the stream and the total mass of the stream progenitor (Johnston et al. 2001). Following the analytical relationships of Johnston et al. (2001) the formation timescale is ∼ 240 Myr and the total mass of the progenitor satellite as ∼4× 10^{10} $M_\odot$. Thus, the progenitor of the stream can be considered intermediate in mass between the Large and Small Magellanic Clouds (LMC and SMC, hereafter)

and to have begun disrupting relatively recently.

THE BLUE OVER DENSITY: The blue overdensity is located at the intersection of the stellar stream and the NGC 5387 disk at a galacto-centric radius of ∼8.7 kpc (or 9.1 kpc projected onto the disk plane). The region is elliptical in shape and has a major axis length of approximately 850 pc (2.2″). We note that position of the region, e.g., superimposed on the disk of NGC 5387, makes these shape parameters challenging to constrain. The region is very blue compared both to the mean colors of the NGC 5387 disk and those of the stellar stream. The region contributes 38% of the total integrated FUV flux of NGC 5387 (see Figure 5.1b). From optical spectroscopy, the blue overdensity has SFR(Hα) = 1.2 $M_\odot$ year^{-1} and SFR(FUV) = 2.4 $M_\odot$ year^{-1}, though the SFR prescriptions may not be appropriate for the "bursty" star formation histories typically observed for dwarf galaxies (e.g., Johnson et al. 2013). Compared to H II regions in the Local Volume, the blue overdensity is both physically larger and more luminous, which suggests that it is likely composed of several unresolved sub-components, instead of one large region. From comparison of properties derived from its optical spectrum to models produced by Starburst99 (Leitherer et al. 1999, SB99), the youngest stellar population has a mean age of 8 Myr and the region has a total mass of 2×10^7 $M_\odot$. The region has a gas phase metallicity similar to that of the SMC (12 + log(O/H)=8.04). Thus, the blue overdensity has overall star formation properties akin to entire dwarf starburst galaxies, but is more compact and of a lower total mass.

Four interpretations were posited in Paper I to explain the blue overdensity, two of which were immediately ruled out: (i) that the stream and blue overdensity are independent merger events, and (ii) that the blue overdensity was formed from a collision between the stream and a high velocity cloud. The two most likely interpretations

of the blue overdensity are (i) that it is a region of enhanced star formation in the outer disk of NGC 5387 induced by the minor accretion event, or (ii) that it is the progenitor of the stellar stream undergoing a period of enhanced star formation as a result of its interaction with NGC 5387. The latter interpretation is more consistent with the kinematical and chemical data for the region, but the former can not be conclusively ruled out without additional observations.

The goal of this work is to explore the viability of either of the two preferred scenarios of Paper I with numerical simulations. Explorations of other scenarios are beyond the scope of the work presented here. These simulations are described in Section 5.3 and the best matching model is described in detail in Section 5.4. We explore the conclusions of the simulations by comparing the properties of NGC 5387 to those of galaxies in the Local Volume Legacy Survey (LVLS) in Section 5.5.2 and to MW-LMC analogues in Section 5.5.3. Global morphological classification metrics are applied to the optical and UV imaging for NGC 5387 and compared to large morphological studies in Section 5.5.4. The work is discussed and summarized in Section 5.6.

5.3 Simulations of the NGC5387 System

To understand the NGC5387 system and distinguish between competing observational hypotheses, we use a set of numerical simulations described in Section 5.3.1. In assessing these simulations, we not only ask whether each of the scenarios can be qualitatively recreated, we also ask how well either scenario can match the detailed observational data of the NGC 5387 system. From this process, we come to the best interpretation given the current observational data and propose observational tests that can be used to create more detailed models in Section 5.4.

In this section, we first summarize the specific observational criteria any simulations must reproduce to recreate the NGC 5387 system:

1. The interaction of a single dwarf satellite must be able to produce the stream and blue overdensity approximately 240 Myr into the interaction. The dwarf satellite must have properties similar to those estimated for the stream progenitor from the stream morphology.

2. The overall morphology of the stream must be reproduced. More specifically, the stream must subtend at least 360° and have the general appearance of the stream given in Figure 5.1. From the color of the stream, it must also be composed of intermediate to old stellar populations, akin to those in the halos of dwarf galaxies.

3. The stream must intersect the disk, in projection, at a region of recent star formation, albeit the star formation can physically be within the gas disk of the parent or the satellite. This region must be offset in its line-of-sight velocity from both the systemic velocity of NGC 5387 and that anticipated at ∼9 kpc from a simple rotation curve applied to NGC 5387 (see discussion in Paper I for details). The observed velocity offset between the blue overdensity and the systemic velocity of NGC 5387 is $\delta v_{los} = -104$ km s^{-1}.

4. The blue overdensity must be forming stars at a rate that is enhanced compared to the underlying stellar disk and contain relatively young stars, < 10 Myr old compared to those both in the stream and in the underlying stellar disk.

(a.)

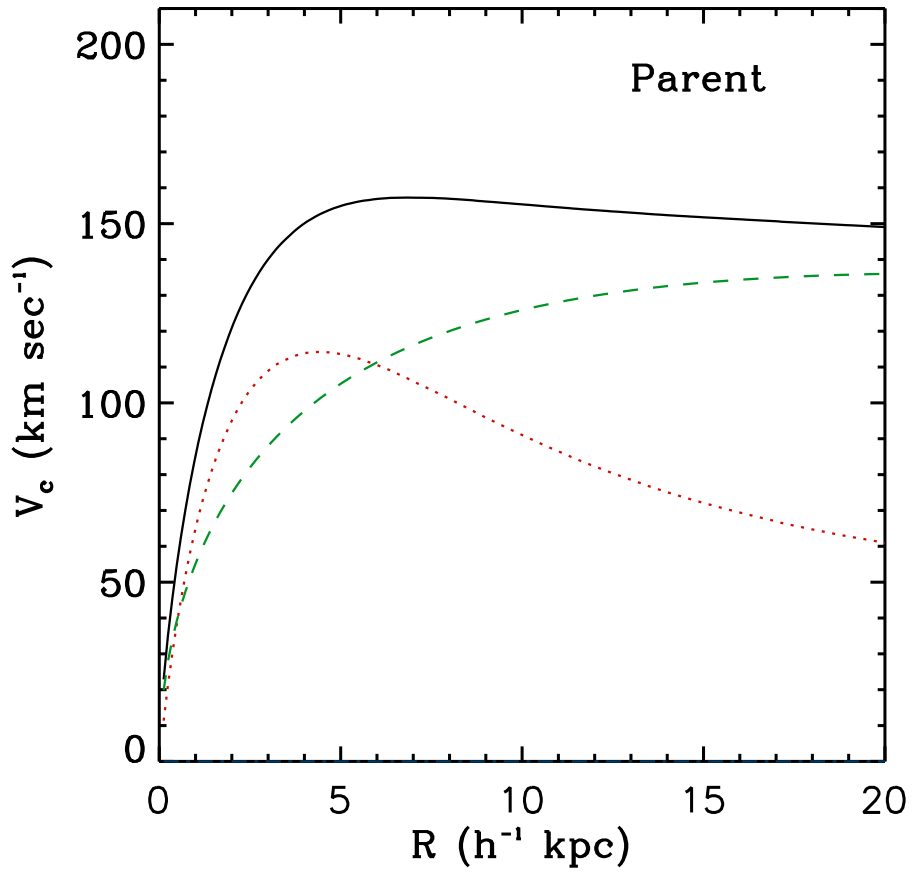

Fig. 5.2.— The initial rotation curve is plotted for the model versions of **(a.)** NGC5387 and **(b.)** its satellite. The different lines indicate the contribution from the dark matter halo (green, dashed) and the disk (red, dotted). The solid black line indicates the total rotation curve for either system. The satellite galaxy is placed on an eccentric orbit (e=0.7) about NGC5387, with a pericenter distance of 3 kpc and the apocenter at 15 kpc.

(b.)

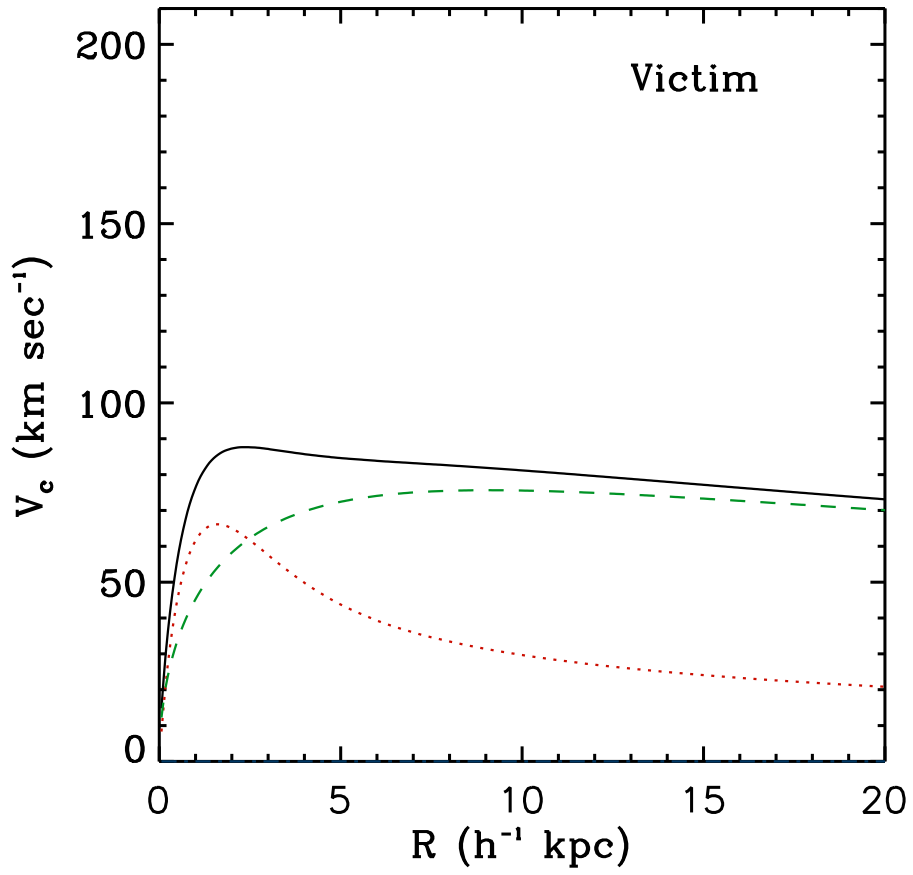

Fig. 5.2.— cont. **(b.)** The initial rotation curve is plotted for the model versions of the NGC5387 satellite. The different lines indicate the contribution from the dark matter halo (green, dashed) and the disk (red, dotted). The solid black line indicates the total rotation curve for either system. The satellite galaxy is placed on an eccentric orbit (e=0.7) about NGC5387, with a pericenter distance of 3 kpc and the apocenter at 15 kpc.

5.3.1 Numerical Methods

Our numerical simulations were performed with GADGET3, a parallel TreePM code based on smoothed-particle hydrodynamics (SPH) technique. A detailed description of the code is available in the literature (Springel 2005). Here, we note the essential features relevant to the questions posed here.

Star formation is implemented with the effective two-phase model of Springel & Hernquist (2003). We adopt the same initial parameters as used in that paper, more specifically a threshold gas number density for star formation of $N_h = 0.13\,\mathrm{cm}^{-3}$. The star formation time-scale is assumed to scale with mass density as $t_{sf} \sim \rho^{-0.5}$, which is functionally normalized to 2.1 Gyr at the threshold density (ρ_h). This formulation matches the empirical relation between the gas surface density and star formation rate for nearby galaxies (Kennicutt 1998b). The energy associated with supernovae heats the multi-phase medium and thereby regulates star formation, but in the model implementation used here this feedback is not sufficiently strong to drive significant gas outflows.

We note that the adopted star formation prescription may be too simplistic for a highly detailed study (Hopkins 2013). However, the two purposes of these simulations are (i) to determine *if* the passage of a satellite galaxy through the stellar and gas disk of a larger galaxy can create enhanced star formation and (ii) to identify where that star formation would occur within in the galaxy-satellite system. Thus, concerns over the specific star formation prescription are not likely to influence qualitative comparisons between the observational data and the simulations. A detailed quantitative assessment would require not only adaptations of the simulation methodology, but would also require a more detailed observational portrait and, taking into account the available data on the system, is beyond the scope of this work. Given the con-

cerns expressed in Hopkins (2013), we consider how our adopted prescriptions could influence our results in Section 5.4.

In addition to the concerns over the star formation prescription of Springel & Hernquist (2003), the reliability of SPH for cosmological simulations has been challenged by Agertz et al. (2007), Junk et al. (2010), Read et al. (2010), Vogelsberger et al. (2012) and Sijacki et al. (2012). However, comparisons between SPH and calculations done with the moving mesh code Arepo show good agreement for applications involving individual galaxy collisions, at least when the sub-resolution model mentioned above is used to represent star-forming gas (Hayward et al. 2014) — which is the situation described here.

5.3.2 Setting the Initial Conditions

The system in our models consists of a parent galaxy with properties similar to NGC5387 and a companion satellite on an orbit that takes it through the disk of the parent. Both the parent and the satellite galaxies consist of a dark matter halo and a rotationally supported disk of stars and gas. The parameters describing each galactic structure are independent of the other components. Models are constructed in a manner similar to the approach described by Hernquist (1993) and Springel (2000). The initial conditions for the construction of the galaxies used in our numerical models are summarized in Table 1. Here, we summarize the relevant setup for our simulations.

We model the dark matter mass distribution of each galaxy with a Hernquist (1993) model, with cumulative mass distribution,

$$M(< r) = \frac{M_{\rm DM} r^2}{(r+a)^2}. \tag{5.1}$$

In this equation, a is the radial scale length related to the scale radius, r_S, of the cor-

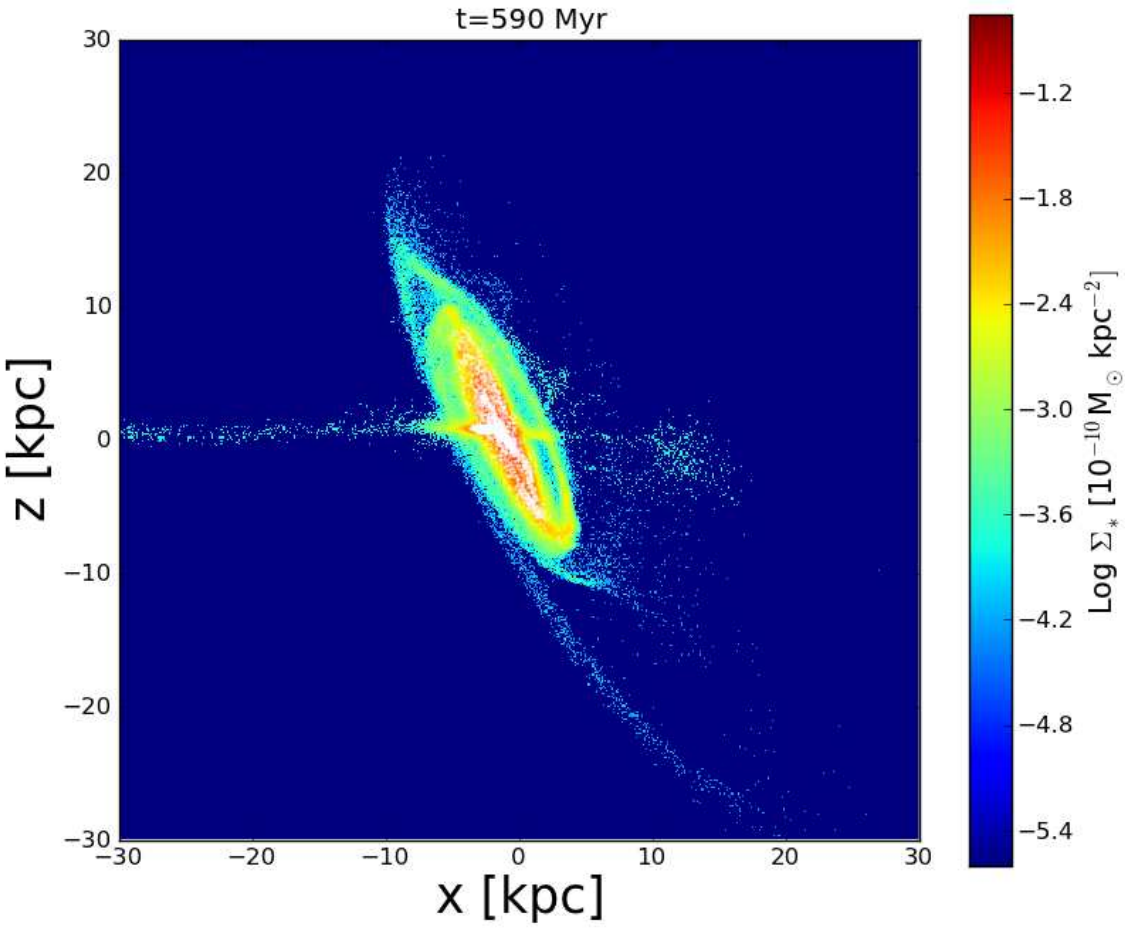

Fig. 5.3.— Snapshot of the best match simulation to the observational data of NGC 5387 occurring 590 Myr into the interaction. The satellite galaxy encountering the larger system at the second passage though the disk. As described in the text, a brief episode of enhanced star formation occurs in the inner parts of the satellite galaxy and in the parent disk along the spiral arms. Only stars are displayed in the images and their colors are scaled to the stellar surface density. Stars that were formed recently are over-plotted as white particles.

responding NFW halo ($r_S = R_{200}/C$; Navarro et al. (1996b) as described in Springel (2005)):

$$a = r_S \sqrt{2\left(\ln(1+C) - \frac{C}{1+C}\right)}, \tag{5.2}$$

where C is the concentration parameter. The adopted values for C and a are given in Table 1.

The model for the parent galaxy has a total mass of $4\times\ 10^{11} h^{-1}$ $M_\odot$ with a peak velocity of v_{peak} = 160 km s^{-1}, similar to that observed for NGC 5387 (Springob et al. 2005). The satellite galaxy has v_{peak} = 85 km s^{-1} and a total mass of $\sim 5 \times 10^{10} h^{-1}$ $M_\odot$, making it intermediate between the Large and Small Magellanic Clouds in its overall properties, which is consistent with the observed properties of the stream progenitor. The mass ratio between the parent and the satellite galaxy is approximately is 1:10 and the ratio of the peak velocities is 1:2.

The parent and satellite galaxy are modeled by a gaseous disk with a scale length two times larger than that of the stellar component. Our adopted scale length is 2 kpc for the stellar disk and its scale height (z_o) is taken as 10% of the disk scale length, and the modeled scale height of the parent stellar disk is initially $z_o = 0.2$ kpc. The scale height for the gaseous disk is determined by self-gravity and the pressurization of the ISM, as prescribed by the effective equation of state (Springel & Hernquist 2003).

The number of particles of each simulated component (gas, stars, or dark matter) are chosen such that the mass resolution per particle of a given type is roughly the same for both galaxies. The satellite galaxy is placed on an eccentric orbit ($\epsilon = 0.7$) about the parent, with a pericenter distance of $R_{peri} = 3$ kpc and the apocenter at $R_{apo} = 15$ kpc, which were selected based upon the measured physical parameters of the stream.

5.4 Simulation Results

Preliminary evaluation of the simulations is motivated focused on reproducing the following morphological observations: (i) a stream of old stars around NGC5387 and (ii) the enhanced star formation in its intersection with the galaxy disk. The remaining observables are only evaluated for those models meeting the morphological criteria. Figure 5.3 is a snapshot of our "best" model of the NGC 5387 system caught at t ∼590 Myr, a timescale for the interaction that is within the uncertainty of the estimate presented in Paper I. There are notable consistencies between the model and the available observational data previously summarized — there is a stellar stream with $R_{apo} \sim 10$ kpc, region of enhanced star formation at the intersection of the parent disk and the stream. The star formation in Figure 5.3 occurs *within* the progenitor of the stream debris. More specifically, the satellite galaxy is undergoing a brief episode of enhanced star formation in its inner regions at the second passage though the disk of the parent system. Young stars formed during the interaction are over-plotted in white in Figure 5.3.

In the following sections, we address each of the major observations of the NGC 5387 system and the ability of the preferred model to reproduce the the observational data. Where there is some ambiguity, we discuss limitations in both the observations and the simulations that have the potential to alter the interpretation. Then, we describe the evolution of our model until the satellite galaxy is no longer identifiable, which associates the NGC 5387 merger with other "late-stage" (>several Gyr) mergers in the Local Group. Lastly, we summarize the conclusions that can be drawn from the results of the simulation.

5.4.1 Stream Morphology

The stellar stream is the natural outcome of the tidal interaction between the satellite galaxy and NGC 5387. The stellar stream shown in Figure 5.3 is qualitatively in good agreement with the observational data, although the match is not perfect. The model stellar stream does not contain a significant young stellar population, consistent with the actual colors of the stream from surface photometry. Slightly different choices of orbital parameters do not dramatically change the overall physical picture of the stream. Thus, we conclude the model is able to reproduce qualitatively the observed characteristics of the stellar stream in NGC 5387.

5.4.2 Line of Sight Velocity

The dynamics of best fit model (Figure 2) can be compared to the observational line-of-sight velocity for the blue overdensity. First, the simulated galaxy is oriented identical to the plane-of-sky position angle and the inclination angle of NGC 5387. We simulate the spectroscopic observations by measuring the distribution model particles as projected onto a line-of-sight that matches both the observed orientation of the stellar stream. From the relatively small A_V of the star forming region measured from optical spectroscopy ($A_V \sim 1$), it is most likely that the star formation region is located on the near side of the NGC 5387 disk and we place the (star forming) progenitor on the near side of the simulated disk. This procedure simulates the placement of a slit over the blue overdensity as was done for the spectroscopic observations (see description in Paper I).

Figure 5.4 displays the the mean line of sight velocity for all particles in the model star forming region is δv_{los} = -104 km s^{-1}. The overall velocity dispersion of the particles (Figure 5.4) is consistent with a progenitor satellite galaxy with an

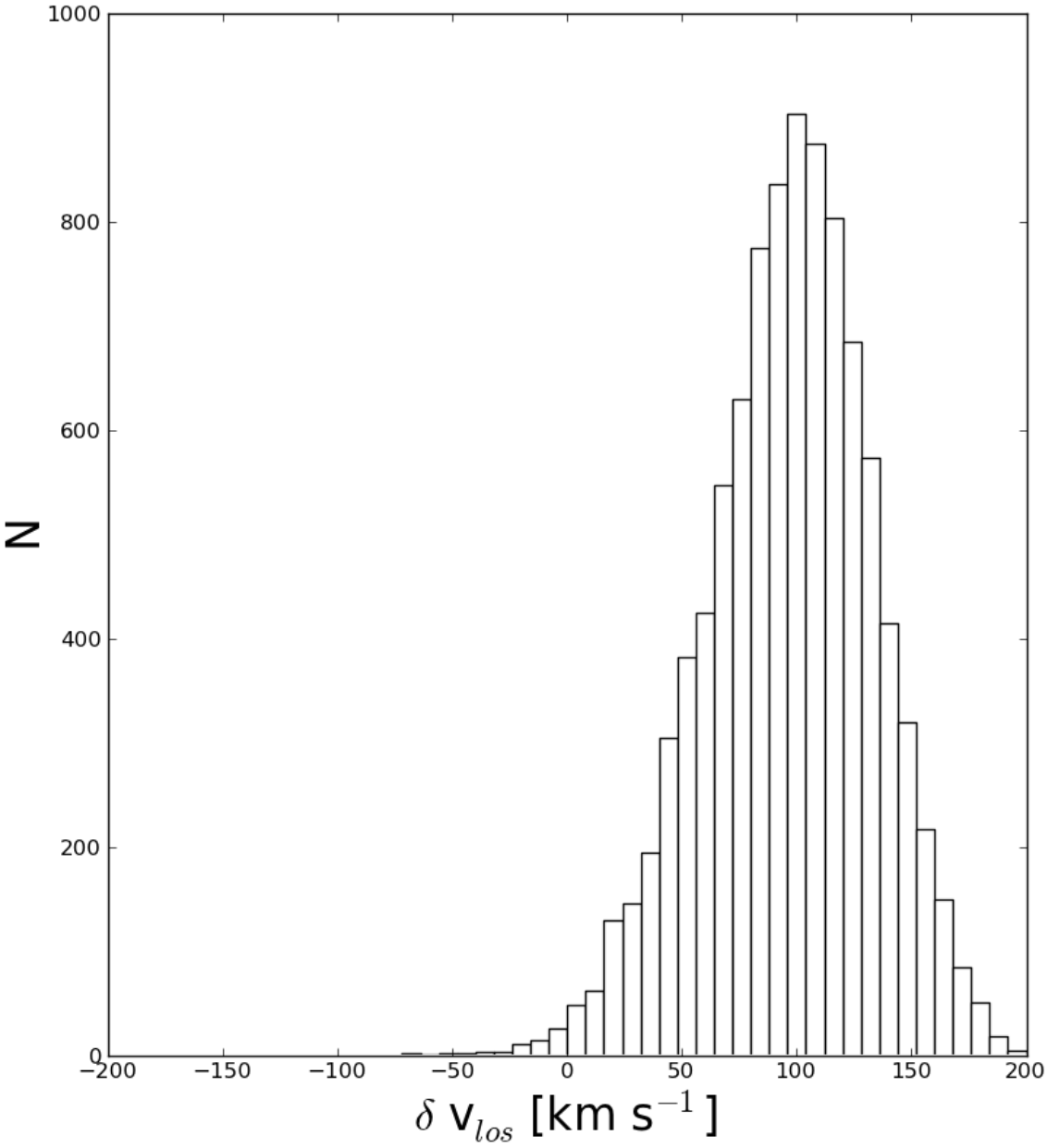

Fig. 5.4.— Marginal distribution of the particle velocities within the simulated star forming region relative to the parent galaxy. The simulated parent galaxy is placed at the position angle of NGC 5387 and rotated such that the stream orientation agrees with that observed around NGC 5387. The three dimensional velocities for particles within the stream are then projected along this line-of-sight to build the marginal distribution. This distribution is made for the simulation given in Figure 5.3 at the time where the satellite makes its the second passage about its parent. This mean velocity shows broad agreement with the observed velocity of the HII region relative to NGC 5387, $v_{los} = -104$ km s^{-1}.

initial mass given in Table 1, which has undergone to mass loss both from tides and heating of stars due to disk shocking during its interaction (D'Onghia et al. 2010a). We repeated the same simulation with the initial disk of the satellite galaxy oriented differently with respect the parent disk galaxy and measured a similar value for v_{los}. Thus, our best match model is able to reproduce the observed kinematical data.

5.4.3 Disk Star Formation?

The model that best reproduces the observational data for the NGC 5387 system supports the interpretation that the blue overdensity is the progenitor of the stream undergoing a brief star formation enhancement as a result of its interaction. It is important, however, to discuss briefly our attempts to produce the alternate interpretation, albeit that model is not explicitly shown here.

In all of our attempts to recreate the blue overdensity in the stellar disk, the disk star formation is never concentrated into a $\sim$1 kpc region, but rather is spread along the spiral arms within the disk. Moreover, the intensity of the star formation that we are able to induce in the disk is never of the intensity observed for the blue overdensity. These two differences, the intensity of the star formation and the area is subtends, are sufficient to conclude that we are unable to reproduce the blue overdensity as star formation in the disk in our simulations. It is, however, interesting to note that in our preferred model (Figure 5.3), the disk galaxy too has some recent star formation out to several kpc.

There are a few limitations in our methods that can explain the difficulty to produce a suitable star forming region in the disk. First, the limited spatial resolution of the simulations in the satellite galaxy limits our ability to properly describe the gas cooling within a few parsecs. Second, stellar feedback in the form of galactic

winds is not employed in our simulations and a different star formation description could be more appropriate and reduce the discrepancies noted here. Lastly, the true three-dimensional orientation of the structures in NGC 5387 is unknown. It is possible that the edge-on orientation of the NGC 5387 disk (i=80°), could produce an apparent alignment of the spatially distinct star formation regions produced in our disk star formation scenario. If this is the case, then high spatial resolution imaging at high contrast of the NGC 5387 disk would have the potential to resolve the 2.2″ blue overdensity into its component HII regions. Given the prediction of the disk star formation model, if sub-components within the overdensity are detected, then their spatial distribution, compact or distributed, would help to distinguish the two scenarios.

5.4.4 Starburst in the Satellite Remnant?

Starbursts observed in L_* galaxies are typically found in their innermost regions (e.g., within ∼1 kpc of galactocentric radius), with typical physical extents of order one tenth the size of the host galaxy. Despite the small physical size, they are converting gas into massive stars at a rate that exceeds that found throughout the rest of the host galaxy by a factor of ∼10. In normal star-forming galaxies like our own Milky Way, the star-formation rate is a ∼1 $M_\odot$ year^{-1} averaged across the Galactic disk. Thus, for an L_* galaxy, the star-formation rate would be 10 $M_\odot$ year^1 in a region with a radius of 0.5 kpc. This definition for relatively large galaxies is often challenging to scale to galaxies of different masses and especially to different Hubble types. A more objective criterion is to use the specific star formation rate (sSFR, hereafter), which is a logarithmic ratio of the star formation rate compared to the total stellar mass of the galaxy, with a Δ(sSFR) > 1 for objects of comparable mass, corresponding to a

star burst. Thus, for a dwarf galaxy of approximate LMC mass, a star burst would be SFR > 0.5 $M_\odot$ year^{-1}.

We measured the intensity of the burst of the satellite galaxy in the simulation as the total mass of stars formed in the star forming event relative to the length of the event and the approximate area in which the stars were formed. In our best-match simulation (e.g., that of Figure 5.3), the total mass of new stars is 10^6 $M_\odot$ within a 0.5 kpc region with a duration of approximately 20 Myrs. This corresponds to an average SFR of 0.5 $M_\odot$ year^{-1} over the duration of the star forming event, which is a factor of 2-4 lower than that observed in the NGC 5387 overdensity. The limitations in our simulation methods discussed with respect to disk star formation undoubtedly add uncertainty in our comparison.

Moreover, in addition to the star formation at the current epoch, our simulations show enhanced star formation in the satellite galaxy *after each* of its disk passages, as is shown by the white points the panels of Figure 5.5. Thus, perhaps a more pressing question is if our simulation adequately reproduces the ability of a dwarf galaxy to retain its gas after impacting the disk of its parent. In this case, the distribution of the HI gas in the system — and the associated kinematics — would provide great insight to resolve this concern.

5.4.5 Evolution of the System

Finally, we describe the overall evolution of the stream progenitor over its interaction with NGC 5387. Figure 5.5 presents several discrete time steps from the first in-fall of the galaxy in panel a, which is set to be $t = 0$ Myr. to when it is completely disrupted in the model in Figure 5.5g ($t = 1950$ Myr). The tidal tail becomes visible in Figure 5.5b, and is produced by the fact that stars rotating in the progenitor disk of the

satellite – in interaction with a system 10 times more massive – strongly *resonate* and are pulled into elongated shapes by the gravitational field of the larger galaxy(Toomre & Toomre 1972; D'Onghia et al. 2009, 2010b). Given the mass ratio between satellite and parent galaxy of 1:10 and the highly eccentric orbit makes the smaller system to merge into the larger galaxy after just three passages, approximately after 2 Gyrs from the beginning of the simulation. The best match to the morphology of the stream, occurs at approximately t =590 Myr Figure 5.3 or, slightly later in Figure 5.5c, in reasonable agreement with the analytical timescale estimated from the morphology of the stellar debris (Paper I).

The progenitor system is last identifiable in Figure 5.5d (t =975 Myr). In the last stages, Figures 5.5e, Figure 5.5f, and Figure 5.5g, the satellite becomes indistinguishable from the larger system and some of the material has been thrown far away from the identifiable extent of the satellite remnant. The stellar debris form several arcs and shells of stars extending to R_{proj} ∼30 kpc into the simulated galaxy. The debris have a "hot" or "warm" velocity dispersion similar to that observed in the "spheroid" or "halo" of nearby disk galaxies.

As noted previously, enhanced star formation occurs after each passage of the satellite galaxy through the disk of NGC 5387, and only ceases at ∼1 Gyr (Figure 5.5d) and several passages through the disk. Thus, there are several times in the simulation that qualitatively agree with the enhanced star formation, but the best morphology to the observed stellar stream occurs just after the second passage. Observations to a deeper limiting surface brightness may reveal additional debris features that could better match to a later passage.

While there are multiple enhancements of the star formation, each is sustained for a relatively brief period of time (10's Myr) compared to the time between passages

($\sim$ 100 Myr) and its total survival time in its parent halo ($\sim$ 1 Gyr). For the current burst, this timescale is approximately 20 Myr in the model (with the numerical caveats mentioned previously). Thus, the satellite would only be observable in a burst phase for $\sim$10% of the time it is identifiable within the parent halo. Moreover, its "quenching timescale" is approximately 1 Gyr.

5.4.6 Summary

The simulations were able to reproduce the overall morphology of the NGC 5387 system, confirming that all of the aspects of the NGC 5387 system can be reproduced with the interaction of a single disky dwarf satellite. The best-match simulation has remarkable similarities to the observational data, considering both observational bias, observational errors, and the potential impacts from assumptions made in the initial conditions of the simulation. The simulations were not able to produce a spatially compact, star forming region within the disk of the simulated NGC 5387, but were able to produce star formation within the satellite itself in qualitative agreement with the observations of the blue overdensity.

From the simulations, we draw several conclusions: (i) the specific features of the NGC 5387 system can be formed via the interaction of a single satellite galaxy intermediate in mass between the SMC and the LMC, (ii) the blue overdensity is most likely the remnant of the progenitor of the stream undergoing a burst of star formation, (iii) the satellite merger in NGC 5387 has been "caught" at a unique phase of its merging, a time when it is forming stars ($\sim$ 10% of its merger).

(a.)

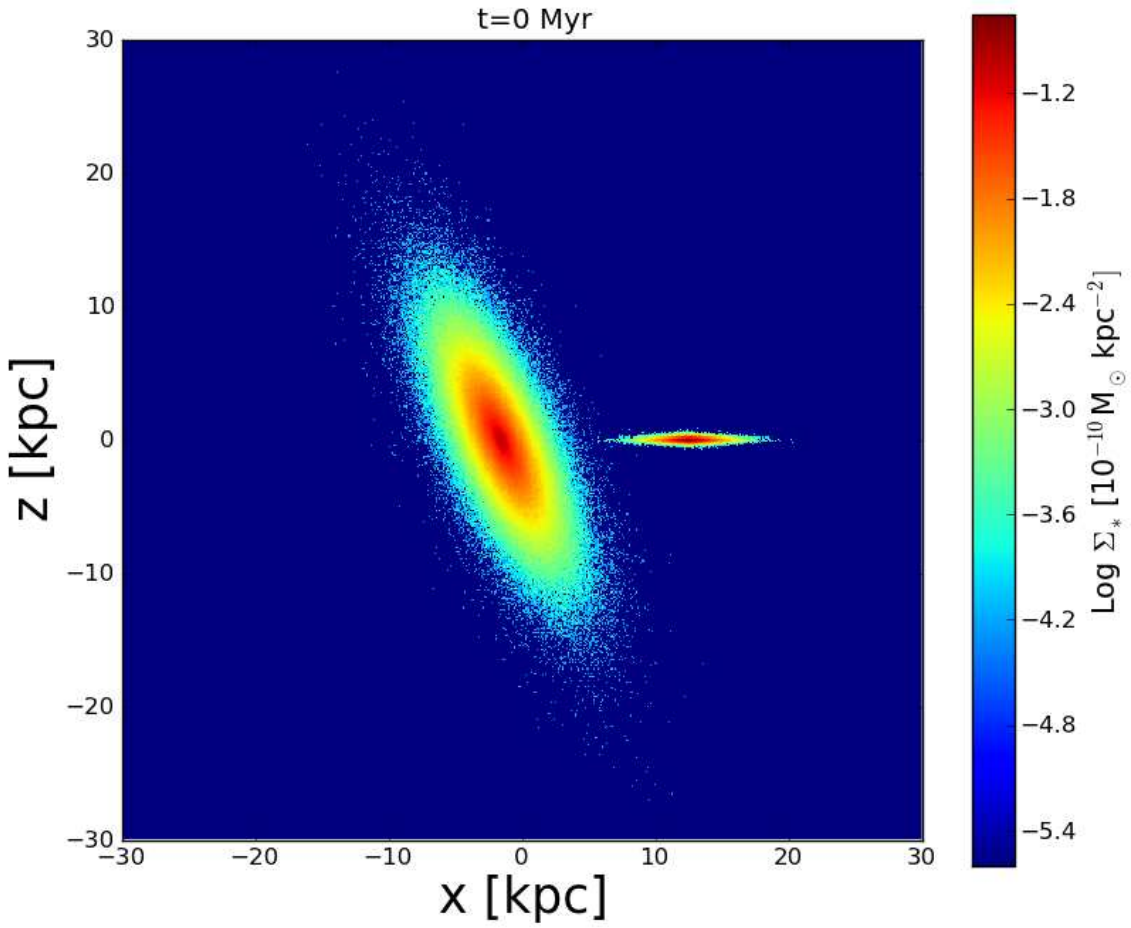

Fig. 5.5.— Time evolution of the satellite interacting with the parent from its first infall until its destruction. Only stars are displayed. The color bar is stretched to track the logarithm of surface density expressed in units of 10^{10} $M_\odot$ kpc^{-2}.

(b.)

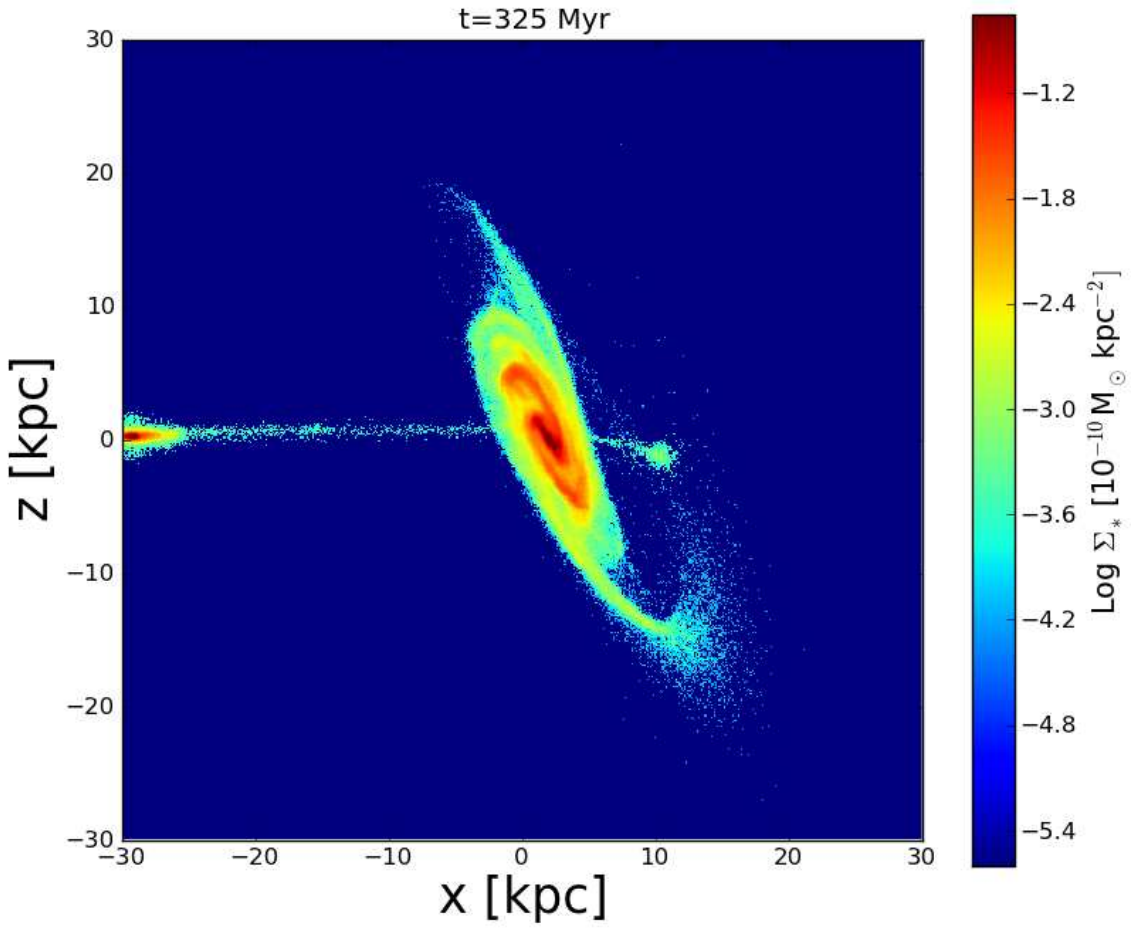

Fig. 5.5.— cont. Time evolution of the satellite interacting with the parent from its first infall until its destruction. Only stars are displayed. The color bar is stretched to track the logarithm of surface density expressed in units of 10^{10} $M_\odot$ kpc^{-2}.

(c.)

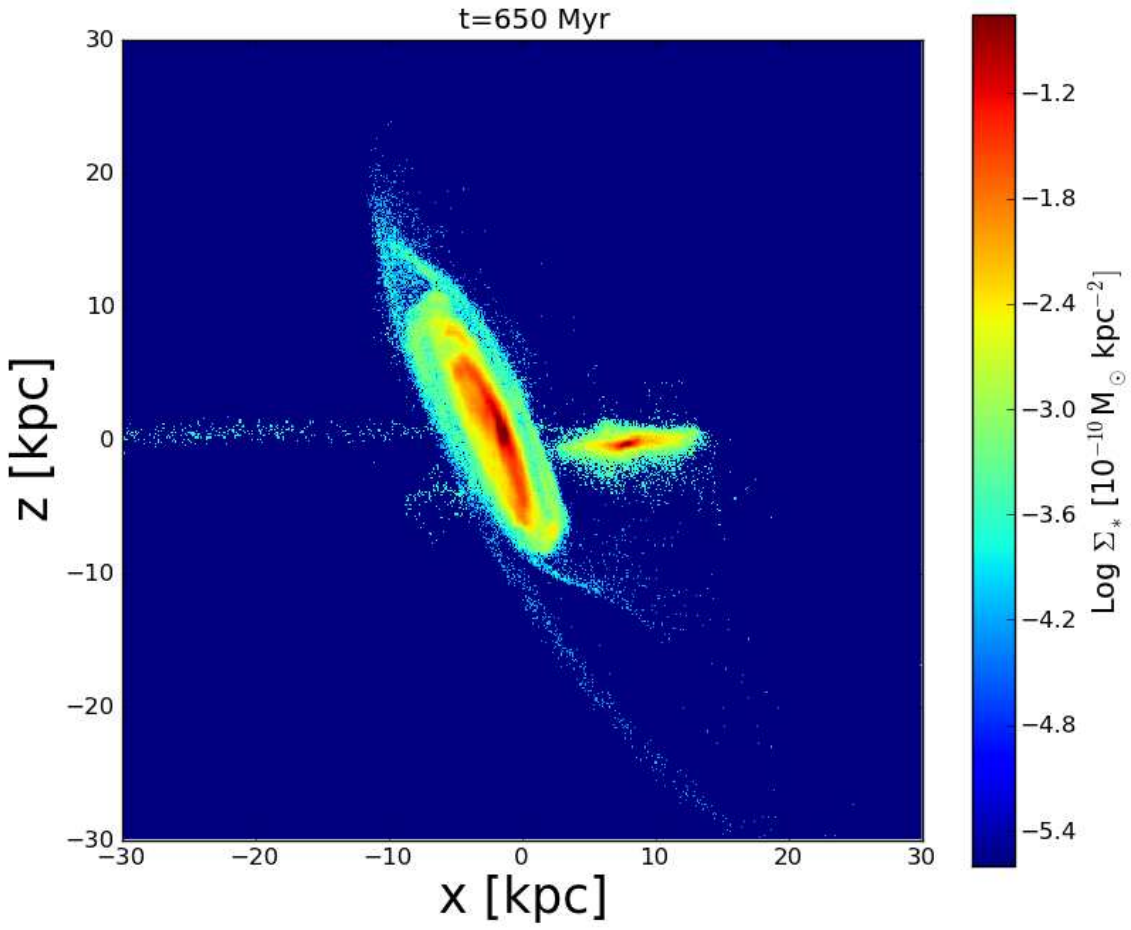

Fig. 5.5.— cont. Time evolution of the satellite interacting with the parent from its first infall until its destruction. Only stars are displayed. The color bar is stretched to track the logarithm of surface density expressed in units of 10^{10} $M_\odot$ kpc^{-2}.

(d.)

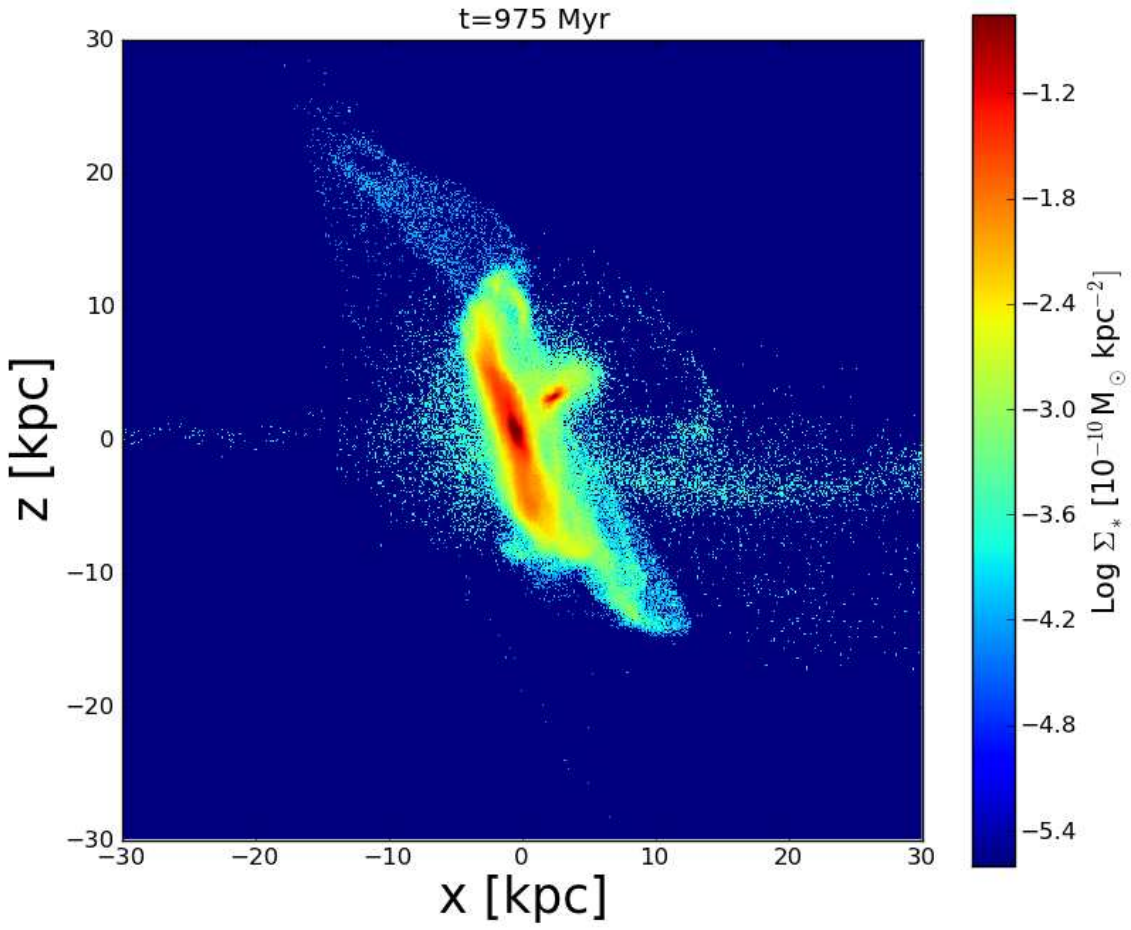

Fig. 5.5.— cont. Time evolution of the satellite interacting with the parent from its first infall until its destruction. Only stars are displayed. The color bar is stretched to track the logarithm of surface density expressed in units of 10^{10} $M_\odot$ kpc^{-2}.

(e.)

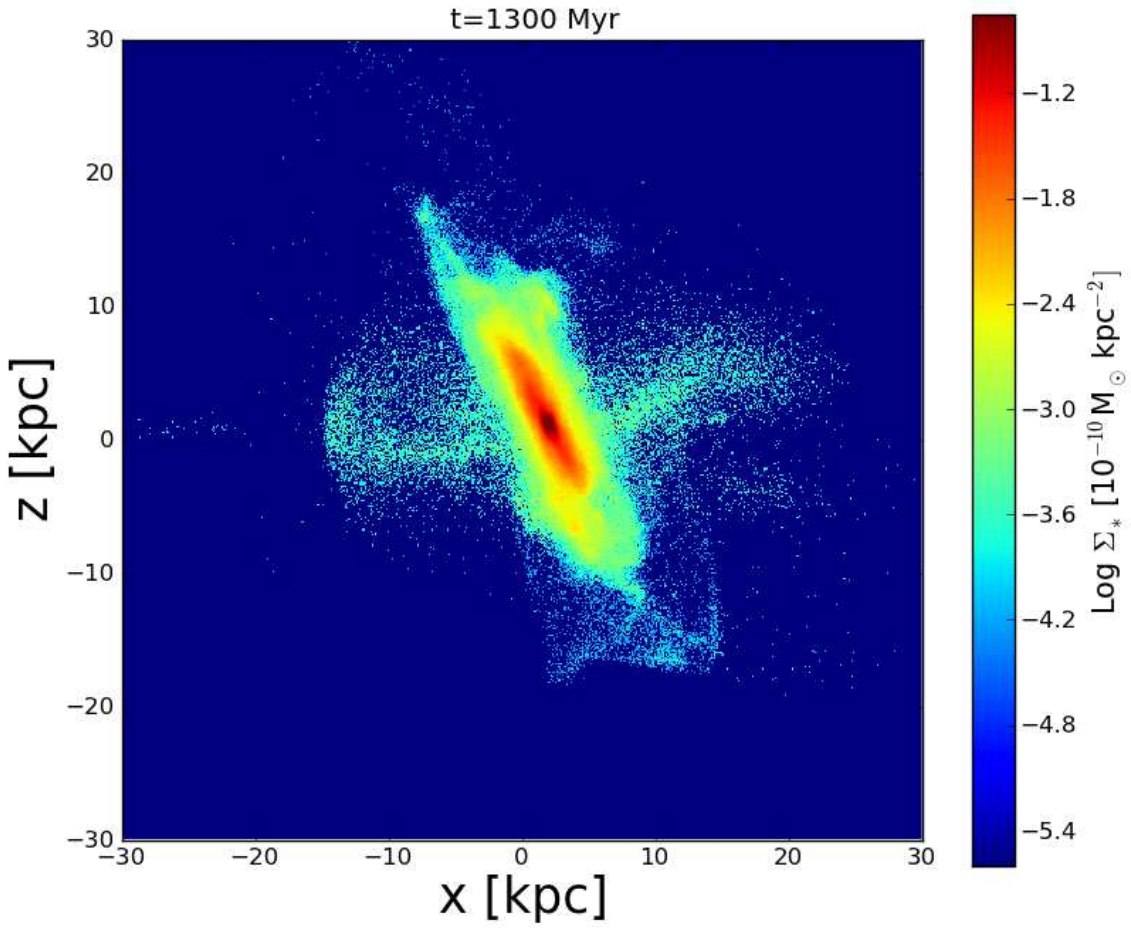

Fig. 5.5.— cont. Time evolution of the satellite interacting with the parent from its first infall until its destruction. Only stars are displayed. The color bar is stretched to track the logarithm of surface density expressed in units of 10^{10} $M_\odot$ kpc^{-2}.

(f.)

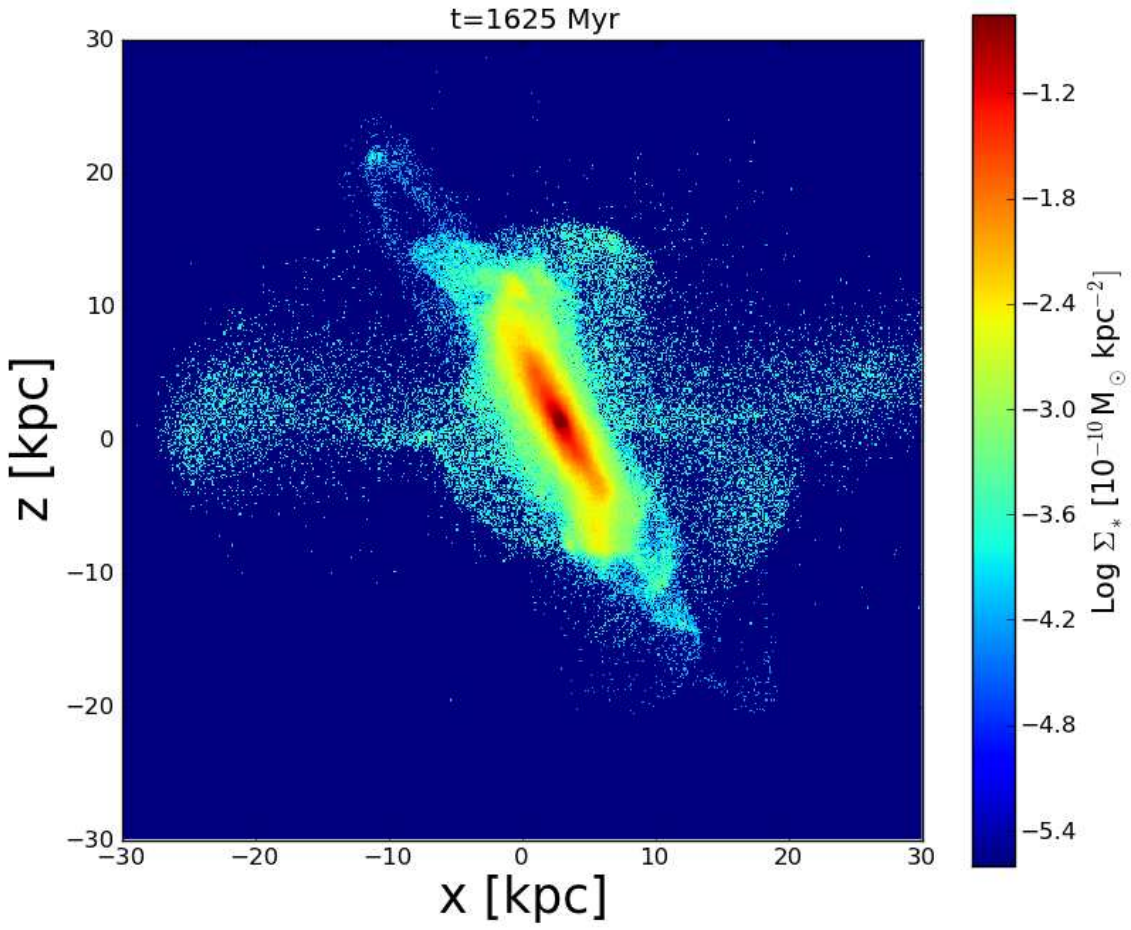

Fig. 5.5.— cont. Time evolution of the satellite interacting with the parent from its first infall until its destruction. Only stars are displayed. The color bar is stretched to track the logarithm of surface density expressed in units of 10^{10} $M_\odot$ kpc^{-2}.

5.5 Comparison to Literature Observations

The simulations undertaken in Section 5.3 and described in Section 5.4 broadly support the conclusion of Paper I that the blue overdensity is the remnant of the progenitor of the stellar stream. In addition, the simulations were able to draw additional inferences about the satellite merger. It is the goal of the sections to follow to determine if these inferences are valid in comparison to existing observational datasets. In the following discussions and figures, we will refer to the blue overdensity as NGC 5387 A for simplicity.

As summarized in Paper I, the color gradient between the progenitor and the stream is unique among current samples of stellar streams in this mass and surface brightness regime (Martínez-Delgado et al. 2010; Miskolczi et al. 2011). Furthermore, while new gas-rich dwarfs have been discovered in the vicinity of the Local Group that are currently forming stars (e.g., Leo P, Giovanelli et al. 2013), none have stellar debris that confirm cannibalization by their parent as the impetus for the star formation. While HI debris may be present, those can be a result of dwarf-dwarf interactions, as in IC 10 (Nidever et al. 2013a), or from fly-by encounters, as is posited for some Local Group transitional type galaxies (Teyssier et al. 2012). It could be argued, however, that relatively few systems have been imaged to the surface brightness limit necessary to detect such stellar debris (e.g., > 27 mag arcsec^{-2}; Martínez-Delgado et al. 2010; Miskolczi et al. 2011).

In Section 5.5.1, we compare the specific details of the simulation results to well studied Local Group disrupting satellites. In Section 5.5.2, we ask if the mean properties of NGC 5387 A are consistent with being the remnant of a dwarf galaxy by comparison of its properties to the Local Volume Legacy Survey (LVLS) of star forming galaxies within 11 Mpc (Kennicutt et al. 2008; Lee et al. 2011). We further

identify aspects of the NGC 5387 A that are unique in comparison to the LVLS. In Section 5.5.3, we ask whether the properties of the NGC 5387 A merger are consistent with being caught at a rare point in the evolution of a merging system by comparison to the sample of MW-LMC analogue close pair systems in the SDSS volume from Tollerud et al. (2011). Again, we identify additional aspects of the NGC 5387 merger that are unique in comparison to this sample. Combined with the comparison to LVLS, these criteria serve as a means to seek out analogues to NGC 5387. Third in 5.5.4, we ask if there is a more efficient means to identity systems such as NGC 5387 by applying the Conselice (2003) morphological classification metrics to the images of NGC 5837. We compare its parameterization to empirical distributions to determine both the Hubble type and the evolutionary state (e.g., normal, merger, starburst). We infer from these comparisons how systems similar to NGC 5387 are interpreted at much larger distances.

5.5.1 Comparison to Local Group Satellite Mergers

Young Stars in Sgr

Siegel et al. (2007) derived the star formation history (SFH) for the core of the Sagittarius dwarf Spheroidal (dSph) using deep precision photometry from the Advanced Camera for Surveys (ACS) on the Hubble Space Telescope (HST). This work discovered the presence of blue loop stars, clear evidence for a young stellar population in the core of Sgr. The CMD signature for this population was weak within the relatively small footprint of the ACS ($\sim$ 1% of the king core area; Majewski et al. 2003), and was difficult to trace amongst the other older stellar populations. The age of the population was difficult to constrain better than between 100 and 800 Myr. State of the art modelling suggests that Sgr dwarf has come within 15 kpc of the Galactic

center three times in its 8 Gyr interaction (Law & Majewski 2010), implying that it has passed through the HI disk of the Galaxy if not the stellar disk itself (Carraro et al. 2014). Furthermore, the Siegel et al. (2007) SFH also shows evidence for earlier, discrete star forming events throughout the 8 Gyr interaction history (Law & Majewski 2010).

From the example of Sgr, there is at least one observational example of a satellite experiencing disk passages and retaining a gas reservoir sufficient to fuel later star forming episodes. Thus, while there are assumptions in the simulations that may impact our quantitative comparison to the observational data, there is indirect support for the qualitative portrait from the simulations.

Disk Galaxy Debris

Toward the end of the merger, the stellar debris form arcs and shells of stars that morphologically resemble those of the Great Southern Stream in M 31 (Ibata et al. 2001; Ferguson et al. 2002). Deep ACS CMDs indicate that the stream and the spheroid of M31 are similar in their overall stellar content, albeit the stream is, on average, $\sim$ 1 Gyr younger than the spheroid (Brown et al. 2006a,b). This similarity implies that the two structures, if not actually related, may have similar origins. Unlike the SFH for Sgr, however, the Brown et al. (2006a) data were not constrained to trace the evolution of a singular component, and thereby do not elucidate the overall evolution of the GSS progenitor akin to that summarized for Sgr or explored here for NGC 5387.

Simulations attempting to reconstruct both the stellar density and morphology of stream debris and their kinematical signatures, predict the progenitor of the GSS would need to be a relatively massive satellite with rotational support (Fardal et al.

2008, 2012). The rotation of the progenitor is necessary to produce the numerous arcs, shells, and shelves observed across the inner halo of M 31. Indeed, detailed kinematic studies of the M 31 inner halo find kinematically cold debris, overall consistent with the GSS in many of pencil beam probes of the inner halo (Gilbert et al. 2012).

In Fardal et al. (2012), the GSS signatures were traced through the extensive inner debris field of the M 31 stellar halo, demonstrating how a single satellite merger can, effectively, dominate the inner halo. By comparison to the evolution of the NGC 5387 merger (Figure 5.5), this would also be the case in the final stages of NGC 5387. Interestingly, the merger timescale for the GSS $\sim$ 1 Gyr is similar to what is estimated for the full destruction of the NGC 5387 stream progenitor. While the age data are not currently available on a large scale for the GSS, the qualitative portrait from our simulations is similar. Moreover, a search for young star in the GSS debris may be motivated.

5.5.2 NGC 5387 Compared to Local Star Forming Galaxies

The Local Volume Legacy Survey (LVLS) is a pan-chromatic portrait of star-forming galaxies within 11 Mpc (Kennicutt et al. 2008). By combining deep ground-based Hα (Kennicutt et al. 2008) imaging with space based *Spitzer* and GALEX imaging (Lee et al. 2009, 2011), the survey has provided deep insight, not only into the differences between these star formation tracers, but also how the techniques are complementary metrics to understand the recent star formation history (i.e., few 100 Myr, Lee et al. 2009, 2011). In addition to these primary data associated with the LVLS, the sample of galaxies has also been probed for its gas-phase metallicities (Berg et al. 2012) and has corresponding broad band optical imaging. The survey is volume limited to 11 Mpc and thereby over-samples dwarf galaxies compared to larger, Milky-

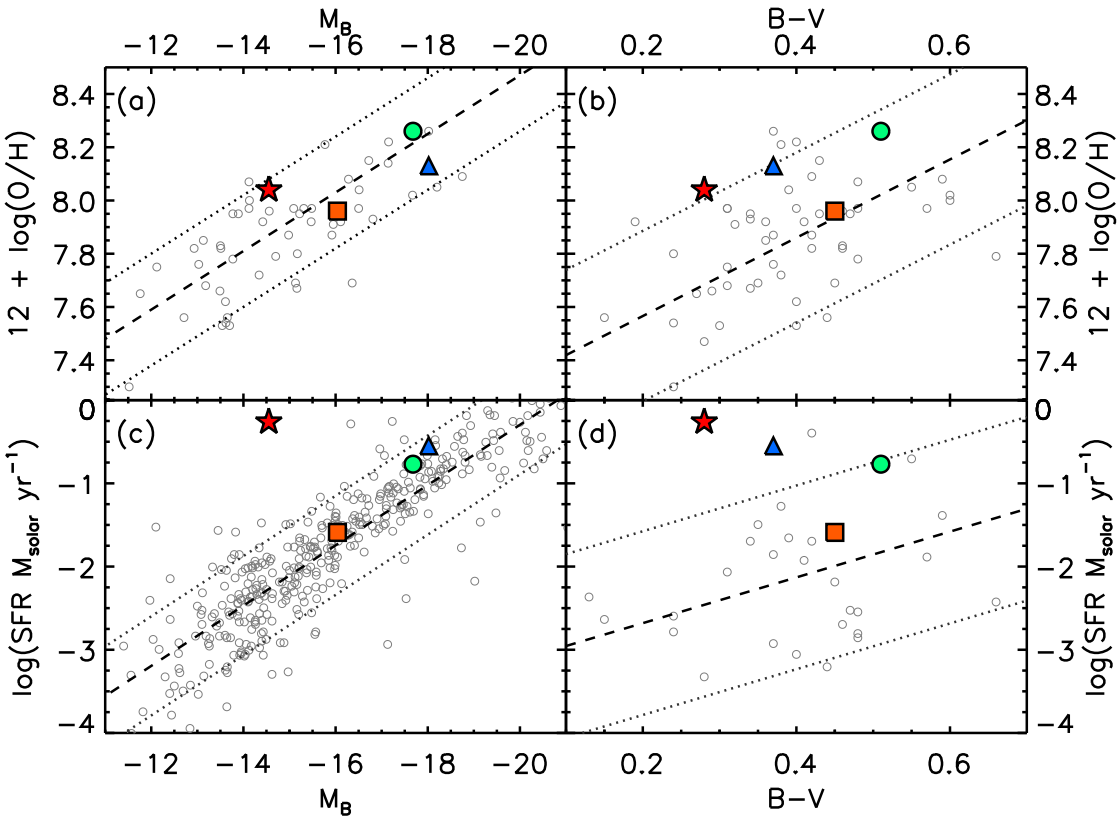

Fig. 5.6.— Comparison of the properties of NGC 5387 A (red star; Paper 1) to the sample of galaxies in the Local Volume Legacy Survey (LVLS, small grey circles Kennicutt et al. 2008; Berg et al. 2012) and to the LMC (large green circle), SMC (large orange square) and to NGC 4449 (large blue triangle). The top panels compare the nebular oxygen abundance (12+log(O/H)) to **(a)** the total B magnitude (M_B) and **(b)** the $B-V$ color. The bottom panels compare the star formation rate (SFR) from L(Hα) to **(c)** the total B magnitude (M_B) and **(d)** the $B-V$ color. Trend lines (dashed) and 1σ ranges (dotted) are given for each panel.

Way analogue type galaxies. Given the pan-chromatic data currently available for NGC 5387 and NGC 5387 A (Paper I, summarized in Section 5.2.1), the LVLS is an ideal sample to compare our data for NGC 5387.

The mass-metallicity relationship for dwarf galaxies has been shown to be remarkably robust for spectroscopically determined stellar abundances and masses derived from velocity dispersion profiles (Woo et al. 2008; Kirby et al. 2013b) in non-star forming systems. Thereby, it is a useful tool to identify abnormal events in the long-term star formation history of a system. For example, Kirby et al. (2013a) compared the stellar abundance and dynamical mass of Segue 2 against this relationship and found it to be much more metal rich than other galaxies of comparable mass. By assuming that Segue 2 originally had a mass consistent with its metallicity, Kirby et al. (2013a) inferred that Segue 2 had lost up to 95% of its total mass in interaction with the Milky Way. Given our current interpretation of NGC 5387 A, our aims to understand NGC 5387 A are similar.

For both LVLS and NGC 5387 A, however, there are no stellar spectroscopic abundances, nor dynamical masses. Thus, the relationship of Woo et al. (2008) and Kirby et al. (2013b) can not be applied directly. In their study of the low luminosity galaxies in LVLS, however, Berg et al. (2012) also noticed a trend analogous to that of Woo et al. (2008) between the nebular abundance, 12 + log(O/H), and the total B broadband magnitude (M_B), fitting for the following relationship:

$$12 + \log(O/H) = 0.11(\pm 0.01) \times M_B + 6.27(\pm 0.21) \tag{5.3}$$

Berg et al. (2012) further argued that in cases where the nebular abundance could not be measured using the "direct" method (i.e., from oxygen lines), the relationship was more robust than using indirect spectroscopic methods (i.e., using line ratios propor-

tional to overall abundance; see discussion in Paper I), albeit with an assumption that the galaxy has not had significant interactions that could have removed a fraction of its mass. As such, the relationship of Berg et al. (2012) can be used analogously to that of (Woo et al. 2008; Kirby et al. 2013b) for star forming galaxies.

In Figure 5.6a, nebular abundance is plotted against M_B (only corrected for extinction from the Galactic foreground) for the LVLS low luminosity sample of Berg et al. (2012) (open grey circles) with Equation 5.3 over plotted (dashed line) with the 1-σ range given (dotted lines). Data for those dwarf systems previously compared to the blue overdensity are as follows: the LMC (green circle), SMC (red square), and NGC 4449 (blue triangle) where are all values are those of Berg et al. (2012). The value for NGC 5387 A is indicated by a red star.

Overall, the metallicity of NGC 5387 A is consistent with those of galaxies of similar M_B, albeit at the edge of the 1-σ range of Equation 5.3. Thus, for its M_B its metallicity is not abnormal, e.g., as was the case in Segue 2. To bring NGC 5387 A closer to the relation, it would need to be slightly brighter (e.g., slightly more massive), which is consistent with our measurement that at least 6×10^8 $M_\odot$ of the galaxy has been stripped and now forms the stellar stream (Paper I). In comparison, the total stellar mass of the LMC (SMC) is $\sim$ 870 (3.1)$\times10^8$ $M_\odot$ with an addition 5 (5.6)$\times10^8$ $M_\odot$ in neutral gas (van der Marel et al. 2009). Thus, a not inconsiderable portion of the stellar mass of NGC 5387 A can be inferred to have been already stripped.

Given the high FUV flux in NGC 5387 A (38% of the total integrated flux of NGC 5387), M_B may not be the most appropriate broad-band magnitude to utilize as a mass tracer. In Figure 5.6b, the nebular abundance is plotted against the $B-V$ color with the appropriate data for the LMC, SMC, NGC 4449, and NGC 5387 A highlighted as in Figure 5.6a. A trend-line (dashed) and 1-σ variation (dotted) are

drawn for illustrative purposes only. In Figure 5.6b NGC 5387 A is, again, just at the 1-σ variation for the LVLS low-luminosity sample, bluer than what would be expected. It is interesting to note that the LMC and NGC 4449, both dwarf galaxies considered to be in a starburst phase, are also "bluer" than what would be anticipated from their nebular metallicities, whereas the SMC, a galaxy not considered to be in a starburst phase, is consistent with the mean relation. At the very least, the larger scatter in the $B - V$ distribution implies that when trying to make inferences to the mass-metallicity relationship using a broad-band magnitude as an observable for mass, some care should be taken in selecting the most appropriate magnitude as a proxy for total mass.

In Figure 5.6c, the star formation rate derived from Hα luminosity is shown against the total M_B magnitude, where data for the LVLS galaxies (open grey circles) is from the photometric study of Kennicutt et al. (2008). As discussed previously, galaxies are considered to be in a "starburst" if their sSFR is enhanced. To mimic the sSFR criterion, Figure 5.6c compares log(SFR) to the total M_B magnitude, as in the other panels of Figure 5.6, data for the LMC, SMC, NGC 4449, and NGC 5387 A are highlighted and a trend-line (dashed) with 3-σ range (dotted) is shown and we can compare the star formation rate of NGC 5387 A to galaxies of similar overall stellar mass. For the magnitude from $-14.3 < M_B < -14.8$, the mean star formation rate is log(SFR)=-2.45 with a standard deviation of log(SFR)=0.6 over the same range. NGC 5387 A is $\Delta(\log(\mathrm{SFR})) = 2.19$ from the mean star formation rate for galaxies of similar magnitude, i.e. NGC 5387 A is forming stars more than 100 times the rate seen in galaxies of comparable B magnitude and is $\sim$3.5σ from the relation. However, were NGC 5387 A similar in total magnitude to NGC 4449 it would be just out of the 1σ range the relation demonstrated by the LVLS sample.

Interestingly, not only is the SFR of NGC 5387 A enhanced compared to mean value for its magnitude, but it is also enhanced compared to the LMC, SMC and NGC 4449, whose properties are all within the 3-σ range of the LVLS relation. In Figure 5.6d the log(SFR) is plotted against $B-V$, with trend-lines and highlighting as in the other panels. Again, the SFR for NGC 5387 A is extreme, but only slightly more so than NGC 4449.

Conclusions from Comparisons to the LVLS

1. We find no direct analogues to NGC 5387 A in the LVLS sample, nor are the LMC and SMC reasonable comparison galaxies. Interestingly, the properties of NGC 4449 are, on the whole, similar to that of NGC 5387 A, albeit NGC 4449 is several magnitudes brighter. NGC 4449 is a dwarf starburst with a recently discovered stellar stream from one of its satellites (Martínez-Delgado et al. 2012). Moreover, the star formation in NGC 4449 is dominated by compact, highly energetic star forming regions known as super star clusters (Reines et al. 2008), unlike in the LMC or SMC (though there are some brighter clusters in those systems). Thereby, NGC 4449 may be the most appropriate analogue to NGC 5387 A, but is itself a cannibalizing and in-tact galaxy.

2. The overall nebular abundance of NGC 5387 A is in overall agreement with the mass-M_B relationship from Berg et al. (2012). This suggests the gas excited by the young stars in NGC 5387 A has been chemically enriched similar to that in dwarf galaxies of comparable mass. Thereby, our interpretation of NGC 5387 A as the remnant of a disrupting galaxy is observationally supported. Were its metallicity drastically different from that anticipated by the mass-M_B relation, then more exotic interpretations could be more plausible.

3. The comparison to LVLS verifies that NGC 5387 A is unique and supports the conclusion of the modelling that the merger has been caught at a very special time in its evolution. However, the sample of the LVLS is limited and only spans a few MW sized galaxies, and thereby dwarf galaxies capable of an interaction with a MW host. Thus, in the next subsection we expand our comparison to the volume of SDSS.

5.5.3 NGC 5387 Compared to MW-LMC Analogues

Tollerud et al. (2011) searched the Sloan Digital Sky Survey (SDSS) Data Release 7 (Abazajian et al. 2009) for spectroscopically confirmed isolated close-pair systems with properties similar to the Milky Way LMC (MW-LMC, hereafter) close-pair system. The primary goal of Tollerud et al. (2011) was to compared observed and predicted frequencies of L_* galaxies, e.g., L_{MW}, with single, massive satellite companions (e.g., L_{LMC}). Although this goal is slightly different than ours, the work produced an ideal sample of confirmed satellites over a more representative volume than the LVLS (See Tollerud et al. 2011, Section 5 for more details), more specifically, to $z \sim 0.0342$. Moreover, the specific selection criteria of the Tollerud et al. (2011) sample to isolate $L_{MW} - L_{LMC}$ pairs is exceptionally useful given the mean properties of NGC 5387 and the progenitor of its stream are similar to those of the MW-LMC. Of particular interest to our discussion here was the comparison of the dwarf satellite's color, in this case $g' - r'$, between those in a close pair and isolated dwarfs of a similar mass.

Since Tollerud et al. (2011), there have been other groups performing similar analyses on subsequent SDSS data releases, e.g., studies of the colors or SFR of dwarf galaxies as a function of their distance from a primary, that have found similar overall results as Tollerud et al. (2011). Of note, Geha et al. (2012) identified "quenching"

radius for dwarf satellites compared to isolated field dwarfs and Phillips et al. (2014) generalized this analysis using the sSFR, to tie the dwarf satellite quenching to effects observed for larger galaxies in groups and clusters. However, only Tollerud et al. (2011) focused specifically on host-satellite pairs of similar mass ratio as the MW-LMC, which, as presented in Paper I, is a mass ratio analogous to NGC 5387 and the progenitor of its stream.

The $g' - r'$ Color of NGC 5387 A

Before comparing NGC 5387 A to the close pair sample, its $g' - r'$ color must be determined. While NGC 5387 is included in the SDSS footprint, the blue overdensity is not explicitly included as a source in the SDSS photometric catalog. Moreover, our follow-up imaging (Paper I) is not only deeper, but better resolved than that of SDSS, which permits an overall better estimate of the total magnitudes. Therefore, we choose to estimate colors by adapting our B, V, R photometry to the corresponding SDSS filters. For the NGC 5387 stream progenitor, we convert our $(B - V)$ color $(B-V = 0.28\pm0.05)$, dereddened for the Milky Way foreground, to $(g'-r')$ following the Jester et al. (2005) conversion between SDSS and Johnson filters for stars with $R_C - I_C < 1.15$, given by:

$$(g' - r') = 1.02 \times (B - V) - 0.22 \tag{5.4}$$

with an root mean square scatter of 0.04. The result for NGC 5387 A is $(g' - r') = 0.042 \pm 0.06$. We note that the Jester et al. (2005) transformation may not be the most ideal for the blue overdensity, because it is composed of very young (< 10 Myr) stars. The transformation does, however, provide a reasonable estimate of $(g' - r')$ color for our comparison to Tollerud et al. (2011).

We adopt the average value for the LMC ($(g'-r')$=0.28) directly from Tollerud et al. (2011). Given the similarity in the star forming properties of NGC 5387 A and NGC 4449 demonstrated in the previous section, we will also use this galaxy as a comparison in Figure 5.6. We adopt the $(g'-r')$ color for NGC 4449 ($(g'-r')$=0.34) as calculated from the broadband fluxes given in the NYU-Value Added Galaxy Catalog (Blanton et al. 2005) from the Sloan Digital Sky Survey Data Release 6 (Adelman-McCarthy et al. 2008).

Figure 5.7a is adapted from Tollerud et al. (2011, their Figure 11) and compares the $(g'-r')$ distribution for the 342 member close-pair sample (filled grey histogram) to that of the control or isolated dwarf sample of 28,000 members (dashed black histogram). In Figure 5.7a, the color for NGC 5387 A, the LMC, and NGC 4449 are indicated as bold black arrows with light grey dashed lines. As in Tollerud et al. (2011), the LMC ($g'-r'$=0.27) is bluer than 98% of the SDSS MW-LMC analogue systems in SDSS (96% of the controls). NGC 4449 ($g'-r'$=0.34) is bluer than 91.5% of SDSS MW-LMC analogues and 86.3% LMC analogues in the field. NGC 5387 A ($g'-r'$ =0.08) is bluer than 100% of both the SDSS MW-LMC analogues and the LMC analogues in the field.

As was the case in comparison to the LVLS, the blue overdensity remains unusual in its color compared to the SDSS sample of MW-LMC analogues. As shown by Paper I in comparison to an Starburst99 model, the blue overdensity, when corrected for internal extinction (not applied here because such measurements are not available for all galaxies) has the appropriate color for a 10 Myr population. Thus, what may be most unusual for NGC 5387 A is the degree to which its extremely young stellar populations ($<$ 10 Myr) *dominate* its total integrated color, unlike the other galaxies in the sample which are known to have significant intermediate and old

stellar populations. The extreme "blueness" of NGC 5387 A could be caused, at least in part, to two factors: (i) its location superimposed on the disk, making it only feasible to trace its photometric properties by the unusual blue color itself, and (ii) its interaction with NGC 5387, which has already stripped a considerable amount of its luminous mass into the >360° stellar stream. Whereas there are no means to address the former complication in current data, we address the potential effect of the latter in the following subsection.

Approximating the Color of the 'Complete' Progenitor

We apply the Jester et al. (2005) transformation to our $(B-V)$ color of the NGC 5387 stellar stream ($B-V=0.9$, although with variation along the stream, Paper I) to obtain $(g'-r')=0.75$. The color of the stellar stream is indicated as an arrow in Figure 5.7b. The NGC 5387 stream ($g'-r'$ =0.75) is bluer than 8% of MW-LMC analogues and 7% of control galaxies. Thus, the stellar stream appears "typical" or even "redder" than those satellites considered "red". And so, we can now ask if the galaxy were not being tidally stripped, what would the effective color of the progenitor be? Assuming that NGC 5387 A and the stellar stream were once part of the same system, we add the integrated flux of NGC 5387 A to that of the stream to approximate a scenario in which the NGC 5387 A star forming complex is embedded within a stellar halo.

Assuming a distance modulus, $m-M=34.5\pm0.45$ (79.3 Mpc; Springob et al. 2009), the absolute magnitudes of the stream are $M_{B,stream}=-15.5$ and $M_{V,stream}=-16.4$ (Paper I). We then can add the fluxes of the blue overdensity to that of the stream to determine its effective magnitudes and luminosities if the systems were still in tact. For NGC 5387 A, the magnitudes are $M_B=-14.5$ and $M_V=-14.83$ (Paper

I). By converting the magnitudes into flux units, assuming the same zero point, and summing the resulting fluxes, we derive total approximate magnitudes for the stream *and* NGC 5387 A of $M_{B,combined} = -15.8$ and $M_{V,combined} = -16.2$, which results in $B - V = 0.77$. Using Equation 5.4, we obtain $(g' - r')_{combined} = 0.60$.

The resulting color is compared to the Tollerud et al. (2011) secondaries and field dwarf galaxy catalogs in Figure 5.7b and found to lie in or near the "trough" between the peaks for the blue and red secondaries. The combined NGC 5387 stream + NGC 5387 A is bluer ($g' - r'$ =0.60) than 52% of MW-LMC analogues and 38% of LMC analogues in the field. Thus, if we were observing a field galaxy or a secondary with this level of star formation superimposed on an old stellar population, the galaxy would not be identified as abnormal as implied by previous comparisons.

Discussion

We have compared the color of the blue overdensity to the LMC-analogues in the SDSS DR7 (Tollerud et al. 2011; Abazajian et al. 2009) and found it to be abnormally blue for MW-LMC pairs. If we compare the color stellar stream to this sample sample, however, it appears typical of "red" LMC-analogues. To mimic the appearance of the galaxy if it were not being tidally stripped – but had the same compact star-forming region, we combine the B and V fluxes of the stream and blue overdensity and find a net color that is consistent with the median color of the MW-LMC analogues in the Tollerud et al. (2011) sample.

From these analyses, we can draw several conclusions. First, what is abnormal about the blue overdensity is that the young < 10 Myr stellar population is its most luminous population even into the reddest of our optical broadband filters. This could be an effect of the tidal stripping, which has removed a large fraction of the overall

(older) stellar mass from the stream progenitor. Were this galaxy, now disassembled, to be found intact — either in the field or at a larger radius in the halo — its overall color would not appear unusual. We conclude that broadband colors alone may not be a sufficient criterion to identify dwarf galaxies in abnormal evolutionary states. For the identification of dwarf satellite galaxies as lower mass analogues of "green valley" objects detected in groups or clusters, however, a broadband color approach may be effective.

Despite the overall similarity of the total integrated colors of the simulated progenitor to intact star forming dwarf systems, there are considerable differences when considering the morphology of our simulated object. Even if embedded within a galaxy halo, the star forming region would still be relatively compact, entirely contained within a diameter of 850 pc, for its luminosity. In contrast, irregular type dwarf galaxies tend to have clumpy star formation distributed across their visible extent (See Mateo 1998, for a review of dwarf morphologies). Thus, what may considered truly abnormal in NGC 5387 A is the concentration of relatively intense star formation (for a dwarf galaxy) to a relatively small volume. This is, however, broadly consistent with the tidal stripping scenario, because if the blue overdensity is the remnant of the stream progenitor (as suggested by our models), then the only gas not previously removed during the interaction would tend to be confined within the deepest part of the potential well.

We note, however, that an essential criterion for the selection of the Tollerud et al. (2011) sample is that the secondary galaxy be cleanly distinguished from its parent. As described in Tollerud et al. (2011), in practice this criterion meant removing bright HII regions found within the disk of a spiral galaxy because without additional data, it was not clear if these regions were galaxies or bursts within the parent.

In particular, Tollerud et al. (2011) discusses the known limitations of the SDSS photometric pipeline both to distinguish between objects super-imposed upon one another and, even if distinguished, to classify these objects. Though this may be a small effect for the Tollerud et al. (2011) sample, it does limit the ability to assess instances of objects similar to NGC 5387 A. This limitation provides motivation for the efforts described in the next subsection, in which we apply morphological criteria to the light distribution of the parent galaxy.

5.5.4 Morphological Metrics Applied to NGC 5387

A common method to automatically identify merging systems or otherwise atypical systems in large imaging surveys is to identify peculiar morphologies in the two dimensional light distribution. One such technique pioneered by Conselice (2003) was developed and found to yield meaningful and comparable results for galaxies in the near-field and to $z \sim 3$ (see review in Conselice 2014). This system, known as CAS, uses three characterizations of the light distribution, the concentration (C), the asymmetry (A), and the clumpiness (S).

The concentration index (C) is a ratio of the total light in the inner to outer parts of a galaxy, which uses the Petrosian radius $\eta(R)$– the radius at which the ratio between the surface brightness at that radius ($I(R)$) is a specified fraction of the total surface brightness *within* that radius. The Petrosian radius has the advantage of being applicable to a wide number of systems over a wide range of redshifts (see Conselice 2014) The asymmetry index (A) is a comparison of a galaxy to its own profile rotated by 180° . The clumpiness index (S) is a measure of the relative amount of light that is found in clumps compared to that found in smooth components, which is computed by removing smooth structure using a large scale median filter (spatial size set by

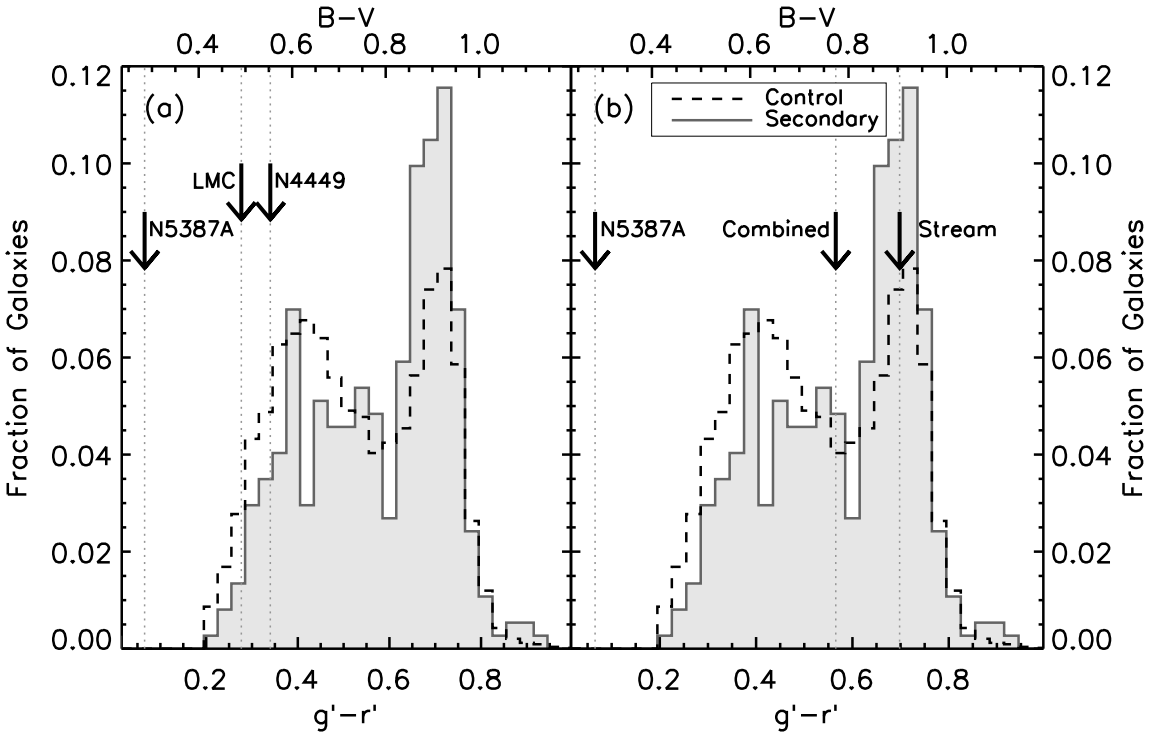

Fig. 5.7.— The distribution of the g′-r′ color for MW-LMC analogues ("secondary," grey filled histogram) and for LMC-analogues in the field ("control," dashed black) from the identification techniques of Tollerud et al. (2011) from the SDSS DR7 (Abazajian et al. 2009) compared to colors of in **(a)** NGC 5387 A, the LMC, and NGC 4449 and in **(b)** NGC 5387 A, the stellar stream around NGC 5387, and the combined photometry for the two objects, all of which are indicated with bold arrows.

$\eta(R)$). Further details of this system and its applications can be found in the review of Conselice (2014).

The CAS technique is ideal for blind application because, by design, it requires no detailed prior assumptions on galaxy morphology, e.g., early-type versus late-type, and is largely robust to systematics of the imaging, e.g., the plate scale and seeing. The CAS technique has been fundamental in explorations of the morphological evolution of galaxies from z$\sim$3 to the present in the GOODS-N and CANDELS fields (among others) – specifically because it requires no a priori galaxy classification and is robust to the size scale probed in an individual image.

Application of CAS to NGC 5387

Application of the CAS metrics to the imaging presented in Paper I was computed using a CAS implementation for the IRAF environment specialized for local galaxies (C. Conselice, private communication). The images were prepared for the code using the following steps: (i) rotation of the galaxy to an effective position angle of 0°; (ii) subtraction of foreground stars and background galaxies; and (iii) determination of a "clean" region in which to calculate the noise statistics and background measurements required by the CAS code. The image rotation was performed with SCAMP and SWARP to remove the on-sky position angle of NGC 5387. Subtraction of foreground stars and background galaxies for each image was performed interactively using the feature in the IRAF routine IMEXAM. Regions of size appropriate to the visible extent of a star were replaced with a background appropriate for that region. Care was taken for the two bright foreground stars in the disk of NGC 5387 (see Figure 5.1), and pixels in these regions were replaced with the mean brightness value for the pixels symmetrically placed across in the plane of the galaxy. The background

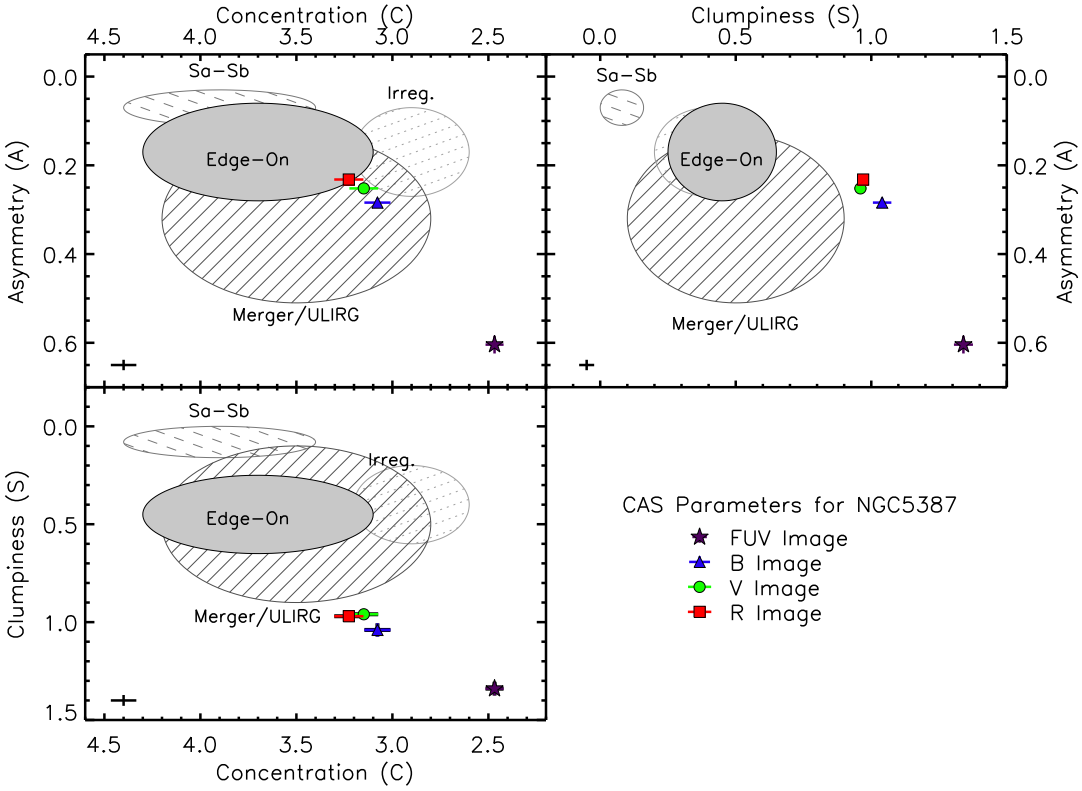

Fig. 5.8.— Comparison of the CAS parameters for NGC 5387 imaging data to the morphological parameter space empirically identified by Conselice (2003). In the **(a)**, concentration (C) is plotted versus asymmetry (A), the **(b)**, clumpiness (S) is plotted versus asymmetry (A), and in the **(c)** concentration (C) is plotted versus clumpiness (S). Filled ellipses represent the 1σ range for early type disks (Sa-Sb; light grey dashed), dwarf irregular galaxies (light grey dotted), ULIRGs (grey solid lines), and for edge-on disks (filled grey) in each panel. The parameters derived for NGC 5387 are presented for *FUV* (purple star), *B* (blue triangle), *V* (green circle), and *R* (red square) in each panel. Error bars are drawn on each point, but often are smaller than the points themselves. The mean error for the NGC 5387 parameters is illustrated in the lower right of each panel.

region specified for the CAS code was chosen to be as free from the source removal process previously described. The CAS procedure was run on each of the four images of NGC 5387 (FUV, B, V, and R) with the resulting values and errors for the CAS parameters given in Table 2. We proceed to compare the values for NGC 5387 to the empirical parameter spaces defined by Conselice (2003) for morphological classification.

The Morphology of NGC 5387 in CAS space

Conselice (2003) used catalogs of normal and interacting galaxies to identify empirically the regions of CAS parameter space inhabited by distinct morphological types. Since NGC 5387 is an Sbc edge-on spiral, it is meaningful to compare its structural indices to the mean and 1σ variations for edge-on disks in Conselice (2003).

In Figure 5.8, we compare the results of the CAS analysis to the demonstration sample of Conselice (2003) used to identify the spaces occupied by different morphological types. In each of the panels of Figure 5.8, the 1-σ ranges are drawn as ellipses for Sa-Sb type galaxies (light grey dashed hashing), irregular galaxies (light grey dotted hashing), edge-on galaxies (solid hashing), and ULIRGs (grey dashed hashing). We note that the ULIRGs are used in a morphological sense, i.e., to identify spaces for irregular and merger morphologies, and not for a luminosity criteria. For consistency with Conselice (2003) we maintain the name 'ULIRG' for this region of parameter space. The CAS values for NGC 5387 A are given for FUV (purple star), B (blue triangle), V (green circle), and R (red square).

In Figure 5.8a, the asymmetry (A) and concentration (C) parameters are compared. The optical CAS parameters for NGC 5387 fall just outside of the 1σ range for both edge-on and irregular systems in a space degenerate with ULIRGs/Mergers.

In contrast, the CAS parameters for the FUV imaging are completely outside of the 1σ ranges. In Figure 5.8b, the asymmetry (A) and clumpiness (S) parameters are compared. The CAS parameters derived from both optical and FUV imaging fall out of the 1σ ranges for all morphologies, primarily due to the large "clumpiness" value. The CAS parameters from optical, however, are within the 2σ range for edge-on, irregular, and ULIRG galaxies. In Figure 5.8c, the clumpiness (S) and concentration (C) parameters are compared. Again, the CAS parameters from both optical and FUV fall outside of the 1σ ranges, particularly due to the large clumpiness (S) parameter. The clumpiness (S) parameter, however, has been found to be the least reliable of the three parameters

In summary, the the CAS parameters from the optical imaging (B, V, R) are broadly similar to those of edge-on, irregular or ULIRG/Mergers type morphologies with the strongest deviation occurring in the clumpiness parameter. In contrast, the CAS parameters from the FUV imaging are inconsistent with any particular morphological type studied in Conselice (2003). This difference, however, could largely be due to the morphological differences seen between star forming galaxies in the optical and FUV, an effect that has been explored and is often taken into account using a set of corrections to the CAS parameters to account for the morphological k-correction between rest frame optical and FUV imaging. The offsets, however, are not sufficiently large to account for the variation. Thus, the CAS parameters, explored in a pure morphological sense, indicate that the FUV light distribution is abnormal. We explore the evolutionary state classification in the following section.

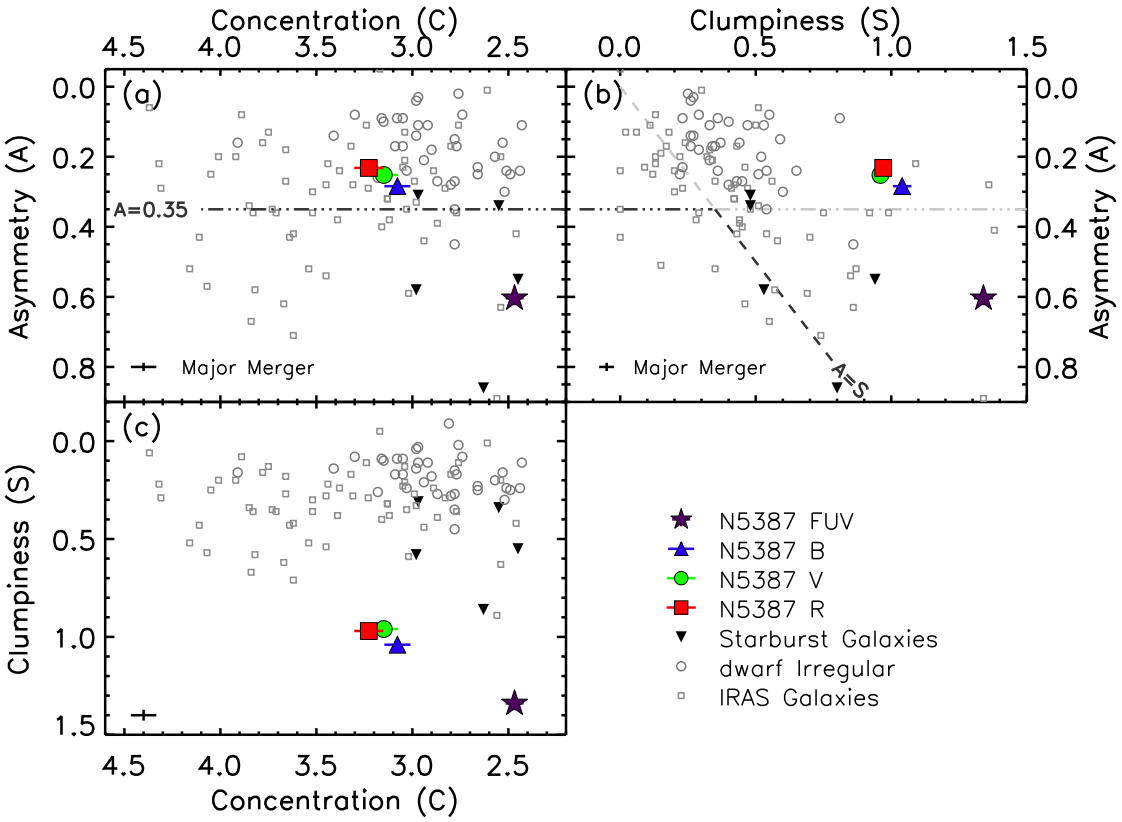

Fig. 5.9.— CAS morphology metrics for NGC 5387 (indicated as in Figure 5.8) compared to data from Conselice (2003) for starbursts (filled triangles), dwarf irregulars (grey open circles), and IRAS galaxies (grey open squares), which are used to identify empirically the evolutionary state in CAS space. **(a)** Asymmetry (A) versus concentration (C). Major-mergers (mass ratio > 1:4) are identified by the cut A > 0.35 (dot-dash line). **(b)** Asymmetry (A) versus clumpiness (S). In addition to the A> 0.35 cut applied in (a), an additional criterion, $A > S$ (dashed) is used to distinguish between clumpiness due to many H II regions and due to major mergers. **(c)** Clumpiness (S) versus concentration (C).

Merger or Non-Merger?

The panels of Figure 5.9 are identical to those of Figure 5.8, except in lieu of showing the empirical spaces for different Hubble types, the empirical spaces for evolutionary states are displayed. The CAS parameters for starburst galaxies (down triangles), dwarf irregulars (open circles), and IRAS ULIRGs (open squares) were used by Conselice (2003) to define regions in the concentration-asymmetry (C-A) and the clumpiness-asymmetry (S-A) parameter spaces consistent with merging systems. In Figure 5.9a, the C-A plane is shown. Based largely on the location of the ULIRG galaxies (open squares) in comparison to the dwarf irregulars (open circles), Conselice (2003) defined a conservative limit for major-mergers (1:4 mass ratio) at A $>$ 0.35 (dot-dash line). The CAS parameters for NGC 5387 derived from optical imaging are very near to the major-merger cut-off, whereas the CAS parameters for NGC 5387 in *FUV* would be classified as a major-merger in this space. As in the previous subsection, the morphological k-correction offsets from, do not strongly alter this impression. We note, however, that the CAS parameters for the *FUV* imaging are similar to several of the starburst galaxies, which would be expected to have many compact star forming regions across their visible extent that can "mock" the appearance of a disturbed morphology.

The overlap between starburst galaxies and major-mergers was the motivation for the additional classification metric demonstrated in Figure 5.9b in the C-S plane. As in Figure 5.9a, the A$>$0.35 cut is given as a dot-dash line. In the C-S plane the additional criterion of asymmetry being larger than the clumpiness is employed (demonstrated as the dashed line for $A = S$). due to the overall loss of resolution for more distant objects Thereby, the major-mergers ($>$1:4 mass ratio) are identified in the bottom left corner of Figure 5.9b. With the addition of this criterion, the CAS

parameters for NGC 5387 derived from the *FUV* imaging would not be classified as a major-merger, as implied from the C-A plane. Although no merger criteria were defined for the C-S plane, the plane is shown in Figure 5.9c. Here, both the optical and *FUV* derived CAS parameters fall outside of the range spanned by the demonstration dataset of Conselice (2003).

It is interesting to note, however, that the A > S criterion is commonly relaxed in application to datasets at higher redshifts due to the overall loss of resolution for more distant objects. As previously discussed, the morphological k-correction and the behavior of galaxies artificially shifted to higher redshifts most affect the clumpiness (S) parameter (**?**). This is, often, due to the relatively small number of pixels spanning the galaxies observed in higher redshift samples. Thus, *if* NGC 5387 were observed at a larger redshift (with the various statistical correction applied), it would most likely be classified as a system undergoing a major-merger (>1:3) or intermediate-merger (1:3>1:6), when it is in fact at most ∼1:10 merger, a mass regime often termed "micro-merger". detailed observations of the Sgr dSph.

Discussion of CAS Comparisons

The CAS galaxy morphology criteria were applied to the optical and *FUV* imaging of NGC 5387 following the prescription developed in Conselice (2003). The results (Table 2) were compared to the empirical spaces defined by Conselice (2003) for the diagnosis of galaxy morphology (e.g., Hubble Type) and for evolutionary state. For all planes, the CAS parameters from optical imaging were found to be consistent with a mildly irregular edge-on system or a ULIRG/Merger. From inspection of Figure 5.1, this characterization from the broad band optical imaging is qualitatively accurate. In contrast, the CAS parameters derived from *FUV* imaging were consistent

with no Hubble Type studied in Conselice (2003), but were consistent with starburst or ULIRG/Merger systems — even with appropriate corrections for the pass-band. Thus, in blind application of the CAS system, perhaps the most conservative of the morphological classifications, the *FUV* light distribution of NGC 5387 is flagged as a major-merging (>1:4) system. Given the overall robustness of the CAS system for galaxies to redshift z∼3, the *FUV* CAS parameters for NGC 5387 imply that it is possible to detect "minor" (∼ 1:10 mass ratio) or even "miniscule" mergers (<<1:10 mass ratio) in a starburst phase phase similar to NGC 5387 A. Phrased slightly differently, the 'clumpy' appearance of rest frame *FUV* light distributions need not be caused by major mergers, albeit there is only a short time frame over which a "micro-merger" maintains this morphological appearance.

5.6 Summary

In this work, we use a the observational data presented in Paper I to understand better the NGC 5387 system. First, we use detailed numerical simulations to explore the two preferred interpretations of the NGC 5387 system, more specifically that star formation is induced by a minor accretion event either (i) in the disk of NGC 5387 or (ii) in the progenitor of the stellar stream.

We find the following:

1. The overall morphology of the stellar stream is reproduced with a 1:10 mass ratio merger that starts on a radial orbit and, on its first pass, intersects the disk in its inner parts. The best match to the stream morphology occurs t =590 Myr years into the merger just after its second disk passage.

2. The companion galaxy maintains some gas reserves during its disk passages and

begins to form new stars after each disk passage approximately when it is at its apocentric radius.

3. Star formation can be induced by the event in the galaxy disk, but in our simulations this star formation is not concentrated in a small angular region. In contrast, the companion galaxy is able to produce stars both in a concentrated region and at a rate comparable to the observations of the blue overdensity.

Since the uncertainties in the star formation prescriptions of the modelling may be important, we cannot definitely rule out that the NGC 5387 star formation is in the disk. In the scope of the work presented here, however, this scenario cannot reproduced to match the observations of NGC 5387. The *most likely* interpretation of the NGC 5387 A (blue overdensity) is star formation within the remnant of the stream progenitor. Comparisons to galaxies in the Local Group, Local Volume, and SDSS MW-LMC pairs produce no similar systems. The star formation history of the Sagittarius dSph, however, does reveal that particular galaxy has formed stars in multiple bursts over its 2.5 to 3.0 Gyr interaction with the MW, including a $\sim$13.5 kpc passage through the Milky Way disk (Law & Majewski 2010). Thus, although there is no direct evidence for similar scenarios, there are indirect clues in the star formation histories of disrupting satellites in the Local Group. Further refinements to the interpretation of the NGC 5387 system require constraints from observations at higher resolution and those that constrain the gas kinematics.

Although there are uncertainties in our physical interpretation, the NGC 5387 system was compared to other samples. NGC 5387 A was found to be abnormally blue, both compared to the LVLS and to the MW-LMC pairs in the SDSS volume. We postulate that the abnormal color is due to the dominance of the young (< 10 Myr) stellar component in the tidally stripped satellite remnant. This dominance

is, in part, due to difficulties tracing the component superimposed on the disk of NGC 5387. With at least 5×10^8 $M_\odot$ of stellar mass already stripped, NGC 5387 A has lost a significant portion of its overall old and red populations (equivalent to the entire stellar mass of the SMC). By co-adding the flux from the stellar stream and NGC 5387 A we simulate a satellite (or field galaxy) with similar star formation properties and a relatively intact stellar halo. The combined color of the system is consistent with that of the green valley between the red and blue peaks in the distribution of MW-LMC analogues in SDSS.

Given the limitations discussed for the comparison samples, we cannot directly conclude that the merger in NGC 5387 is not necessarily a rare event, only that no analogues are detected in our efforts. Both the simulations and the comparison to observational samples suggest that the accretion of NGC 5387 A has been "caught" at a rare time in its evolution — a relatively brief period in which it is forming stars at a large rate. The high star formation rate and the relatively large and concentrated high mass stellar content imply a very "extreme" star forming environment in the remnant of the stream progenitor. If all satellite galaxies of similar mass and orbital parameters experience a phase similar to NGC 5387 A (and potentially Sgr), then this phase could contribute significantly to the overall depletion of gas in satellite systems observed in the Local Group (Spekkens et al. 2014, Beaton et al. in prep.).

Exploration of the later evolution of the simulated NGC 5387 system indicate that additional star formation bursts due occur and are correlated with disk passages of the system. Furthermore, the late-time evolution of the NGC 5387 accretion event produced a stellar debris field similar in overall morphology to that of the Great Southern Stream in M 31. Although the progenitor for the GSS has not been identified, detailed modeling — which takes into account star count maps, kinematics,

and basic chemical content — are consistent with a satellite progenitor with similar overall properties to the inferred original state of NGC 5387 A. The similarity suggests that some young to intermediate age content (1 to 5 Gyr) may be found within these debris.

The morphological classification technique of Conselice (2003), sensitive to identification of both the morphological type and evolutionary state, were applied to NGC 5387. The CAS parameters for NGC 5387 derived from optical imaging were consistent with its edge-on Sbc morphology and as a minor merger. In contrast, the parameters derived from the *FUV* light distribution were inconsistent with the Hubble Types included in Conselice (2003) and would be classified as a major merger and/or star-bursting galaxy.

5.6.1 Final Remarks

Although this attempt to understand the NGC 5387 system has not conclusively identified the nature of the blue overdensity, it does provide insight into the evolution of satellite galaxies within hierarchical galaxy assembly. Our models indicate that we are seeing the NGC 5387 merger at a short-lived period of the merger — regardless of where the star formation is occurring physically. Not only have we captured NGC 5387 A *during* a burst, it has been caught just after the most energetic signatures of the most massive stars have faded (e.g., it would not be identified by massive star signatures, e.g., Wolf Rayet emission lines), but while it is still contains sufficiently massive stars to produce significant Hα luminosity. That there are no currently identified analogues is most likely because star formation in the accreting dwarf during minor-major mergers proceeds in discrete bursts (e.g., as detected in Sgr) and can only be Hα bright for a short time (< 10 Myr). This interpretation is qualitatively

in agreement with assessments of the 'bursty' star formation histories of Local Group galaxies when compared with orbital properties (Dolphin et al. 2005).

The lack of systems with similar characteristics in the Local Volume (e.g., LVLS), or the SDSS Volume, makes it unclear how often a satellite merger might experience an extreme star formation event. The overall "bursty" nature of Local Group dwarf galaxy star formation histories implies there is a "universality" to sudden bursts of star formation (Grebel et al. 2003; Dolphin et al. 2005). Thus, efforts to understand the galaxy-morphology relationship in terms of gas removal (Grebel et al. 2003) must include *not only* the stripping of the galactic hot gas halo, but also the potential effects of "extreme" starbursts in the dwarf galaxies akin to that of NGC 5387. Additional observations that probe the energetics of the interstellar medium in and around NGC 5387 A, including high spatial resolution HI maps and large dynamic ranges Hα, could reveal how the extreme star formation contributes to the gas depletion of dwarf satellite galaxies (Geha et al. 2012).

Using the numerical simulations as a guide, NGC 5387 A produces at least $\sim 10^7$ $M_\odot$ of stars in the bursts during its interaction with the parent. This is approximately 10% of its inferred stellar mass. These bursts occur in an overall dense and compact mode of star formation — more similar to modes of super star clusters commonly associated with major gas-rich mergers than that observed in the disks of galaxies (see discussion in Paper I). Since super star clusters are considered the precursors to locally observed globular clusters or massive open clusters, local clusters observed with anomalous properties — either in chemical abundance patterns or systemic velocities — could have formed during bursts similar that of NGC 5387 A before being assimilated into the host.

Extending our comparison to a cosmological volume, however, finds the over-

all galactic morphology of NGC 5387 in the *FUV* similar to the rest-frame *FUV* morphologies of galaxies in what is considered "more active" phase of hierarchical assembly. This suggests that some of the irregular morphologies observed at cosmological distance could be attributed to mergers of the ∼1:10 mass ratio, rather than those in the intermediate- or major-major $> 1:10$ and $>$ 1:4 regimes, respectively. Given the increased incidence of mergers of all mass scales at higher redshift, finding NGC 5387 A analogues may be easier to identify for study. Additional work to determine the potential for star formation within minor mergers — and the particular properties of that star formation — are needed to evaluate more completely the inferences posed here.

5.7 Acknowledgements

We thank Christopher Conselice for access to the appropriate implementation of his CAS morphology codes. RLB and ED thank the the Aspen Center for Physics and NSF Grant #1066293 for hospitality during the writing of this manuscript. We acknowledge helpful discussions during a November 2013 Yale Galaxy Lunch and a February 2014 NRAO+UVA Galaxy Evolution Discussion that assisted in our interpretations.

Table 5.1. Initial Conditions for Merger Simulations

Property	Parent Galaxy	Satellite
M_* ($M_\odot$)	1.6×10^{10}	1.5×10^9
M_{gas} ($M_\odot$)	8×10^9	5×10^8
M_{halo} ($M_\odot$) [a]	4×10^{11}	5×10^{10}
R_{200} (kpc)[b]	120	60
C[c]	9	12
a (kpc)[d]	22.3	9
Stellar Disk scale length (kpc)	2.0	1.0
Spin parameter λ	0.035	0.035
Gravitational Softening Gas/Stars (kpc)		0.1
Gravitational Softening Halo (kpc)	0.2	0.2
N_{stars}	2×10^6	2.5×10^5
N_{gas}	1×10^6	1×10^5
N_{halo}	2×10^6	2×10^5

[a]The ratio of halo mass to the assumed Hernquist dark matter profile. The total mass of the galaxy is then $M_{total} = M_{halo} + M_* + M_{gas}$.

[b]The radius where the average enclosed density is 200 times the critical density of the Universe.

[c]Concentration parameter of the dark matter halo following Springel (2005).

[d]The scale radius for the Hernquist profile assumed for the dark halo.

Table 5.2. CAS Morphology Parameters for NGC 5387

Image Band	Petrosian Radius	Concentration (C)	Asymmetry (A)	Clumpiness (S)
$Far-UV$	189.1	2.47 ± 0.05	0.60 ± 0.02	1.34 ± 0.04
B	156.0	3.08 ± 0.07	0.28 ± 0.01	1.04 ± 0.03
V	146.0	3.15 ± 0.08	0.25 ± 0.01	0.96 ± 0.02
R	157.4	3.23 ± 0.08	0.23 ± 0.01	0.97 ± 0.02

Chapter 6

Summary and Future Work

6.1 Executive Summary of Chapters:

Because of their long dynamical timescales, stellar halos provide unique insight into the formation and evolution of galaxies because the signatures of hierarchical mass assembly are readily accessible for study — albeit at exceptionally low surface brightnesses and over large angular scales for nearby systems. Recent detailed hydrodynamical and N-body simulations, carried out within the framework of a ΛCDM cosmogony, are sufficient to track the formation of Milky Way-sized galaxies. It is clear from these simulations that stars within the halo can have multiple, distinct origins: (i) through accretion of satellite galaxies, (ii) via *in situ* formation, or (iii) by being dynamically kicked out of the inner Galaxy. Each mechanism for contributing halo stars imparts a specific expected age and chemical pattern distribution. In the Milky Way, studies of these populations are complicated by our internal perspective, both in that multiple structural components are super imposed along the line-of-sight and that distances to potential halo substructures are challenging to measure. On the other hand, the Andromeda galaxy (M31) offers the ideal combination of an external perspective and relative proximity that lends it more easily to a detailed star-by-star (at least for evolved stars that can be resolved), but global view. Over more than a decade of work the SPLASH (Spectroscopic and Photometric Landscape of Andromeda's Stellar Halo) team has used a powerful combination of KPNO/4-m+Mosaic optical (M, T_2, $DDO51$) imaging with follow-up Keck/DEIMOS spectroscopy across the halo of M31 and its satellite system to discover the true metal-poor halo of M31 and measure its key properties — surface brightness profile, substructure, kinematics, metallicity — to 2/3 of the virial radius or $R_{proj} \sim 200$ kpc.

In this thesis, we have expanded upon these primary SPLASH goals to understand other aspects of the M 31 halo and to extended this type of work to another

spiral galaxy at large distances (summarized in Chapter 1). In Chapters 4 and 5, the NGC 5387 system was explored. NGC 5387 is a Milky Way/M 31 analogue seen at near edge-on inclination. It also contains an identified stellar streams and a curious blue over-density seen in surface photometry. The physical parameters of this system, derived via a combination of multi-wavelength deep imaging and optical spectroscopy, are consistent with a recent "micro-merger" (mass ratio 1:10 or even more extreme mass ratios), with progenitor properties similar to those of that inferred for the Great Southern Stream in M 31 (Fardal et al. 2008). From the length and morphology of the stream around NGC 5387, it can be estimated that the satellite has been disrupting for approximately t =300 Myr. While the stream itself is red — implying it is comprised primarily of old stellar populations, at the intersection of the stream and the disk of NGC 5387 is a blue overdensity that contains 38% of the total integrated FUV flux of the NGC 5387 system (Chapter 4). After modeling (Chapter 5) and comparison of its photometric and spectral properties to H II regions (Chapter 4) and dwarf galaxies (Chapter 5), the best interpretation of the blue overdensity is that of the surviving portion of the progenitor, actively forming stars. In both of the two most prominent tidal debris features in the haloes of the Milky Way and M 31, the Sagittarius Stream in the former and the Great Southern Stream in the latter, there is evidence for surprisingly large fractions of young (t <2 Gyr) and intermediate (t $\sim$ 2-10 Gyr) age stellar populations. In the NGC 5387 "micro-merger" we find an analogue to these systems caught exceptionally early in its merging process (300 Myr); thus, the NGC 5387 interaction provides a view into the earliest stages of <1:10 mass ratio mergers (e.g., micro-mergers) that hereto has been absent from the observational accounting of such events.

In Chapter 3, we presented the full observational expanse of the SPLASH project

for the first time — including all 72 photometric fields approximately 75% of which have corresponding spectroscopic follow-up. The ability of the Washington+$DDO51$ photometric system to identify candidate M 31 red giant stars is exploited to double the number of confirmed kinematical member stars beyond $R_{proj} \sim 120$ kpc — a surface brightness > 31 mag^{-1} arcsec^{-2}. This is substantially more than in any other halo — including those known identified within our own Milky Way. In addition, we expand the number of sight lines with kinematic confirmation in the "smooth" halo (i.e., fields without dwarf satellites) at these radii from four in Gilbert et al. (2012) to twelve, including the detection of M 31 red giant stars spanning the full azimuthal range at $R_{proj} \sim$120 kpc. As part of this work, we exploited wide-field multi-plexing spectrographs that are better matched to the anticipated stellar densities in the outer halo. Although the resulting kinematical and chemical measurements obtained with the MMT+Hectospec are at overall lower precision than those obtained with the workhorse spectroscopic instrument of the SPLASH project, Keck II +DEIMOS, the former combination is well suited to this application — the exploration of a low density population for which only modest (5-10 km s^{-1}) precision is needed in contrast to, for example the detailed kinematical precision required to accurately model either dwarf satellites (e.g., Ho et al. 2012; Tollerud et al. 2012) or detangle the complex, multiple component inner halo/spheroid (e.g., Gilbert et al. 2009a). With instruments like the Hectospec (among others), the potential to continue exploring the M 31 halo to large radii at high efficiency is expanded.

With the increased sampling at large projected radii, and making use of serendipitous halo star detections in our M 31 dwarf satellite campaign (Tollerud et al. 2012), we built the full spectroscopic database for SPLASH and apply it to the measure the tangential motion of M 31 from the line-of-sight velocities of individual halo member

stars, resulting in a measurement broadly in agreement with other statistical and direct measurement techniques. The effort is an important first step toward using the unique SPLASH dataset to model the dynamics of the M 31 stellar halo to large radii — with far better sampling than similar efforts relying on sparse azimuthal and radial sampling provided by the globular cluster and/or dwarf satellite systems, whose members often have unclear associations with substructure or are suspected of being on first infall.

6.2 Future Work

This expanded SPLASH aims primarily at a *description* of the M 31 stellar halo, which — although providing powerful evidence for the dominance of the hierarchical assembly for halo formation and, in comparison to the substructure known in the Milky Way, variance in stellar halo parameters due to distinct accretion histories (i.e., cosmic variance) — does not provide extensive discriminating power *between* the specific predictions of halo formation scenarios stemming from the growing body of cosmologically driven Λ-CDM modeling of Milky Way sized galaxies. For example, while it is clear that the hierarchical accretion of satellites plays a large role in the formation of the stellar halo, it is not feasible to measure the role of the *in-situ* halo formation, e.g., that during any initial monolithic collapse, from the distribution of the old stellar population (stars of t_{age} >10 Gyr), that could also have come from satellite accretion. Thus, while the SPLASH and PAndAS projects have provided our first detailed portrait of a stellar halo outside of our own Milky Way, the next generation science questions can only be answered by observational approaches that produce data products capable of better constraining the *details* of halo formation. In practice, our understanding of galaxy formation — as inferred from resolved

stellar populations — advances due to the interplay of numerical simulations and observations. Thus, the future work detailed here is guided based on the numerical simulations that were summarized in Chapter 1, in particular the age-dependent "phase space" characteristics demonstrated by the panels of Figure 1.1.

Thus, the SPLASH project has been extended to add two significant new dimensions critical to piecing together the evolution of M31's halo: the age distribution and chemical enrichment history of halo field stars and satellites. Four distinct approaches based on newly developed as well as traditional techniques will provide independent, but complementary, assessments of the star-formation/enrichment history of present and future M31 halo stars:

1. The exploitation of a large database of wide-field, near-infrared (J, K_s) imaging in our established Mosaic/DEIMOS halo fields to constrain the intermediate-age fraction through studies of asymptotic giant branch (AGB) stars in the M31 halo and satellite galaxies. These data are being obtained through an approved NOAO survey program now in its third year of data collection with the NEWFIRM instrument on the KPNO 4-m telescope (PI: Beaton & GuhaThakurta), with photometric AGB identification techniques being tested in the Ph.D. Thesis of Katherine Hamren (UC-Santa Cruz).

2. We will undertake the first systematic survey for Anomalous Cepheids in the M31 satellites. Anomalous Cepheids are evolved, several solar mass stars believed to be from intermediate-age populations. The required multi-epoch photometry for the 20 satellites in the SPLASH sample are being obtained through a combination of SPLASH data products, public archival datasets, limited access archival datasets (e.g., from the Large Binocular Telescope), and new observations via public (KPNO+Mosaic; PI: Beaton) and (*potentially*) private

access facilities (WIYN+pODI/ODI).

3. Isochrone fitting is a traditional age-dating methodology, but one whose application to distant systems for which only bright stars are accessible is complicated by the age-metallicity degeneracy of the red giant branch (RGB). Recent recalibration of the conversion between the infrared Calcium Triplet (e.g., Ho et al. 2014, and references therein), provides the application of this technique broadly to our existing database or via the co-addition of individual spectra at low S/N for multiple stars with similar stellar type (as determined by color). With spectroscopic metallicities of individual member stars, we aim to break this degeneracy and recover sensitivity to age for M31 satellites in optical+NIR CMDs.

4. It is well known that information on relative ages is imprinted in chemical abundance patterns due to the interplay of the specific star formation history and the timescales for the activation of different nucleosynthetic pathways. The primary access to this information stems from the measure of $[\alpha]$-abundances, which is now feasible for either co-added spectra (Yang et al. 2013) or directly from high S/N observations of confirmed member stars (Vargas et al. 2013, 2014). This additional chemical information is a key aid in using halo stars to distinguish between formation scenarios, each of which is expected to yield a different chemical abundance pattern.

With these four programs adding constraints on the stellar age distribution and chemical enrichment history in M31's halo to the already extensive body of work on the stellar halo, we will obtain the critical missing piece for testing halo formation models within the context of ΛCDM. In the remainder of this chapter, the details of

these future efforts, which are expected to be my primary research for the coming years, will be laid out in detail. Sections 6.3, 6.4, and 6.5 discuss the observations and techniques required to make these measurements. The proposed program of study — currently in the third year of data collection — is summarized in Section 6.6, with comments on its logical expansion in the next era of space and ground based telescopes.

6.3 Age Distributions from Asymptotic Giant Branch Stars

The primary avenue for deriving a global mapping of the ADF for the M31 field capitalizes on the age sensitivity of AGB sub-type in NIR, ($J - K_s$, K_s) CMDs, as illustrated in Figure 6.1. Molecular absorption features in the atmospheres of AGB stars give the NIR CMD strong leverage for distinguishing intermediate age stellar population from older ($\gtrsim$ 10 Gyr) and younger ($\lesssim$100 Myr) stars. In the NIR, AGB stars not only are more separated from the RGB than in the optical, but can also be separated into sub-types, C vs. O-rich, that are tracers for the mass, and therefore age, of the AGB population (Marigo et al. 2008). For AGB stars, the J-band ($\lambda \sim$ 1-2 μm) in particular is dominated by strong molecular absorption features (TiO in O-rich AGB stars, and CN and C_2 in C-rich AGB stars) that are strongly dependent on the mass of the star. These absorption features vary due to the strength of the thermal pulses that bring material from the stellar core into the atmosphere. Low-mass AGB stars have relatively weak pulses that produce limited carbon dredge-up and, as a result, low-mass AGB stars are bluer and fainter. Medium-mass AGB stars have more efficient thermal pulsations that do dredge-up significant amounts of

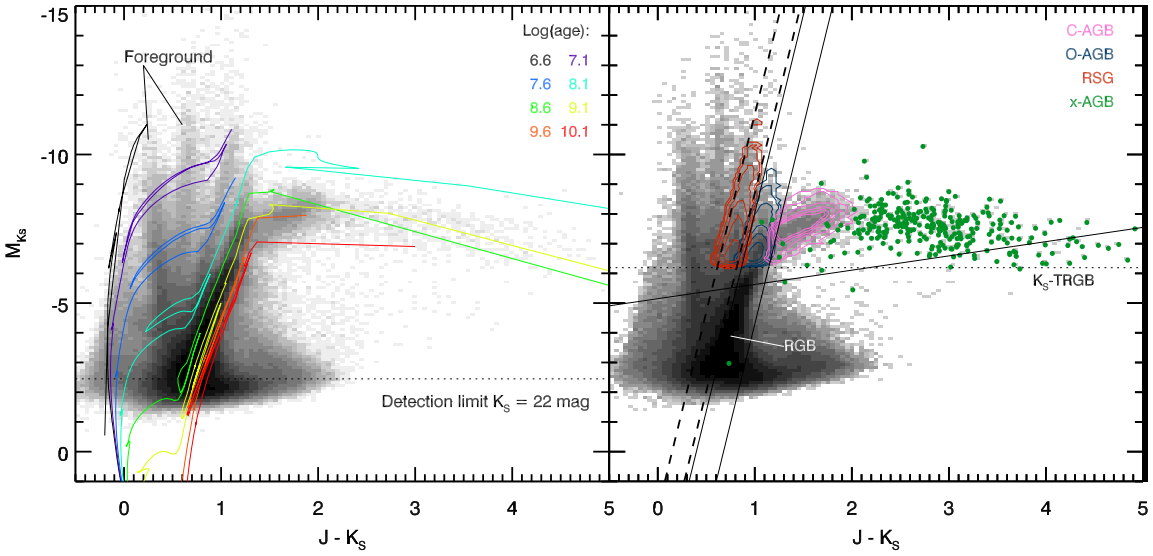

Fig. 6.1.— Near-infrared (2MASS) color-magnitude diagrams of evolved stars in the LMC (**left panel**) and SMC (**right panel**). The average metallicity of the LMC and SMC is [Fe/H] ~ -0.3 and [Fe/H] ~ -0.7, respectively, and these values straddle the mean metallicity of the inner ($R < 30$ kpc) halo of M31. The outer halo of M31 ($R > 30$ kpc) is more metal-poor than the SMC and is expected to be older on average. The colored lines in the left panel show isochrones of different ages, illustrating the age discrimination power of NIR CMDs; the horizontal dotted line shows the 3σ limiting magnitude of our proposed NEWFIRM survey. Solid and dashed lines in the right panel show the rough separation between different categories of evolved stars of different ages and metallicities (Boyer et al. 2011b).

carbon, making these stars brighter and redder "carbon" type AGB stars. The most massive AGB stars undergo "hot bottom burning," which makes them much brighter than the other AGB stars, but also prevents effective carbon dredge-up, leaving these stars blue in NIR colors. (Marigo et al. 2008).

A NIR imaging survey is a very effective means to exploit this age sensitivity of AGB stars (Figure 6.1). Compared to RGB stars, AGB stars in a stellar system are more luminous, and thereby become the brightest objects in the NIR CMD. While in optical CMDs some classes of AGB stars can be distinguished from RGB stars, there is no discriminating power in optical CMDs to classify — or age — the AGB population (Marigo et al. 2008). Admittedly, in the NIR there are still many early-AGB stars that are indistinguishable from the RGB branch, but the AGB stars most readily identified in NIR CMDs are most interesting from our standpoint: those that are thermally pulsating, show age (mass) variation, and lie above the TRGB (Boyer et al. 2011b; Marigo et al. 2008). In NIR CMDS, we expect to be able to differentiate intermediate-age stellar populations ($2 - 10$ Gyr) from old stellar populations (> 10 Gyr; see Figure 6.1). This level of age constraint is sufficient to get strong handles on the questions outlined above. A wide-area, NIR imaging survey is the only reasonable way to assess the distribution of intermediate-age versus old stellar populations on the *global scale* necessary to understand the ADF in the M31 stellar halo.

The "M31-Asymptotic Giant Extended Survey" (M31AGES; Co-PIs P. Guhathakurta and R. Beaton), begun in fall 2012, has been granted long term status with a total of 34 nights on the KPNO 4-meter over three M 31 observing seasons. M31AGES is undertaking a NIR imaging survey with the NEWFIRM infrared imager of 72 fields spread throughout M31's halo (Figure 6.2). KPNO/4m+NEWFIRM is an ideal telescope-instrument combination that balances the complementary needs of field-

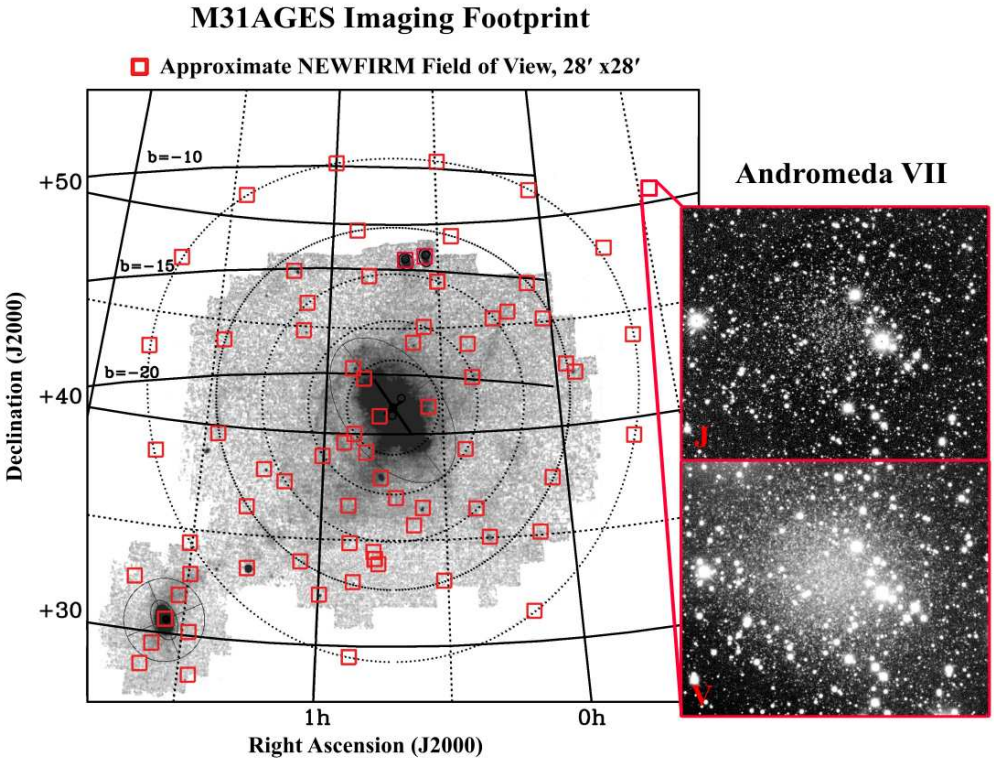

Fig. 6.2.— **Left:** Our survey fields (red boxes) against the PAndAS star-count map (Richardson et al. 2011). We are obtaining NEWFIRM J and K_s images for each of our 72 fields with existing Mosaic M, T_2, and $DDO51$ imaging. Dashed circles represent projected distances from M31's center of 30, 60, 90, 120, and 165 kpc. Our NEWFIRM survey targets 20 dwarf spheroidals, 2 dwarf ellipticals, M33 and 49 pointings across the M31 stellar halo. **Right:** Inset comparing Andromeda VII in NIR (J, top) and optical ($\approx V$, bottom).

of-view ($28' \times 28'$), imaging depth, and image quality that well match the existing SPLASH KPNO-4m +Mosaic optical survey ($FOV = 36' \times 36'$). The SPLASH survey fields (Figure 6.2) were selected to address three primary science categories: (i) known M31 dSph satellites, (ii) existing halo substructure, and (iii) azimuthal and radial coverage of the smooth halo that probes the overall stellar content of the M31 halo to $2/3R_{virial}$. Our primary goal to reconstruct the age-distribution of the M31 halo is actually and effort to back out its overall formation history, thus each of these three sets of fields is crucial to the task because each traces a different stage of its formation. Since dSphs are objects being accreted into the larger halo, intact dSphs represent "future" accretion events. Existing substructure, like the GSS and Streams E and F (Ibata et al. 2007; Tanaka et al. 2010), represent snapshots of ongoing accretion events, whereas the remaining fields, distributed for uniform radial and azimuthal coverage, probe both the underlying smooth halo (e.g., the 'in-situ' halo) and those accretions that have been fully assimilated into the halo.

The SPLASH and M31AGES footprint balances the complementary needs for a wide-area survey sampling a range of diverse halo environments with the depth required to probe the AGB (Figure 6.2). Existing NEWFIRM data obtained with median seeing (FWHM = $1.05''$) and sky brightness conditions have shown that the instrument reliably reaches a 3σ detection limit of (J, K_s) = (23.1, 22.0) in our standard integration times — detection limits are well matched to what is required to discriminate the old and intermediate stellar populations in the M31 stellar halo (Figure 6.1) and demonstrated for the M31 satellite Andromeda VII in Figure 6.3. The combined NIR and optical imaging will allow, *for the first time*, an estimate of the age distribution of stars in fields spanning the full extent of M31's stellar halo. M31AGES builds on a wealth of data and experience acquired over the past

decade of M31 studies, and can be integrated into the broader portrait of M31's stellar halo already in hand from optical imaging, spectroscopy and high-resolution models of Milky Way sized galaxies in a Λ-CDM cosmogony. We posit that this observational program has the potential to *not* just be a simple incremental increase in our knowledge of M31's stellar halo. Rather, they will fill a gap in our current understanding of how stellar halos form: measurement of the age distribution of halo stellar populations on a global scale.

6.3.1 Ancillary Benefits of the NEWFIRM Survey

Though our primary goal for obtaining the NIR imaging is the age discrimination provided by the AGB stars, we accrue several additional benefits of adding these data to our expansive optical database:

• ***Improved Isolation of M31 Stars:*** The surface brightness of M31's halo is extremely low at the largest radii (Gilbert et al. 2012), such that the number density of M31 RGB stars is *significantly* smaller than that of foreground Milky Way stars and background galaxies. Background galaxies are removed using morphological criteria. The existing optical observations have been optimized for separating giants in M31 from foreground dwarf stars in the Milky Way: the $M - DDO51$ index, in combination with a color tracking stellar effective temperature, is a useful dwarf/giant discriminant (see Figure 6.3c Majewski et al. 2000). While $M - T_2$ has proven to be reasonably effective for dwarf/giant separation, an increased color baseline adds significant discriminant for the separation of the two populations. Adding NIR photometry for $M - K_s$ colors ($\approx(V - K_s)$) improves Milky Way dwarf star foreground removal by a factor of three (compare the color axis in panels Figure 6.3c and Figure 6.3d).

Well-calibrated **optical + NIR photometric catalogs** are derived for each of the 72 M 31 halo fields, which, pursuant to the agreement of a NOAO Survey Program, will be made available to the community at large. M31AGES includes 23 of M31's dwarf satellites (20 dSphs, 2 dEs, 1 dSpiral). The released photometry is an invaluable resource for identifying RGB stars in these low surface brightness galaxies. Substructure resulting from mergers is most clearly seen in phase space, which requires measurement of velocities. The optical + NIR catalogs will allow us and the community at large the ability to identify a pure sample of M31 red giants to make the most efficient use of precious 8-10m telescope time for follow-up spectroscopy. The Milky Way foreground star catalog will be interesting in its own right for studying the Galactic structure. The study of the M31 halo by our survey complements the study of the M31 disk by the Local Group Survey and the Panchromatic Hubble Andromeda Treasury (PHAT) multi-cycle HST program. We will doubtless find many other unexpected uses for our photometric catalog.

• ***Improved Estimates of $T_{\rm eff}$ for Individual Stars:*** The SPLASH project has undertaken an extensive spectroscopic survey of RGB stars. Although individual RGB spectra lack the S/N needed to measure the abundance of α-elements, we have had success in measuring the average [α/Fe] of co-added spectra of groups of stars (Cheng et al. 2012; Guhathakurta et al. 2012; Yang et al. 2013). [α/Fe] traces the relative previous enrichment from Type Ia versus Type II supernovae and is a crucial component of chemical tagging studies. In tidal debris streams, a measurement of the α-abundance can provide a rough estimate of the timescale between the onset and cessation of star formation in the satellite, and can thus provide an estimate of the time of infall into the M31 system. Measuring [α/Fe] from co-added spectra works best when stars within a narrow range of metallicities and ages are co-added. The

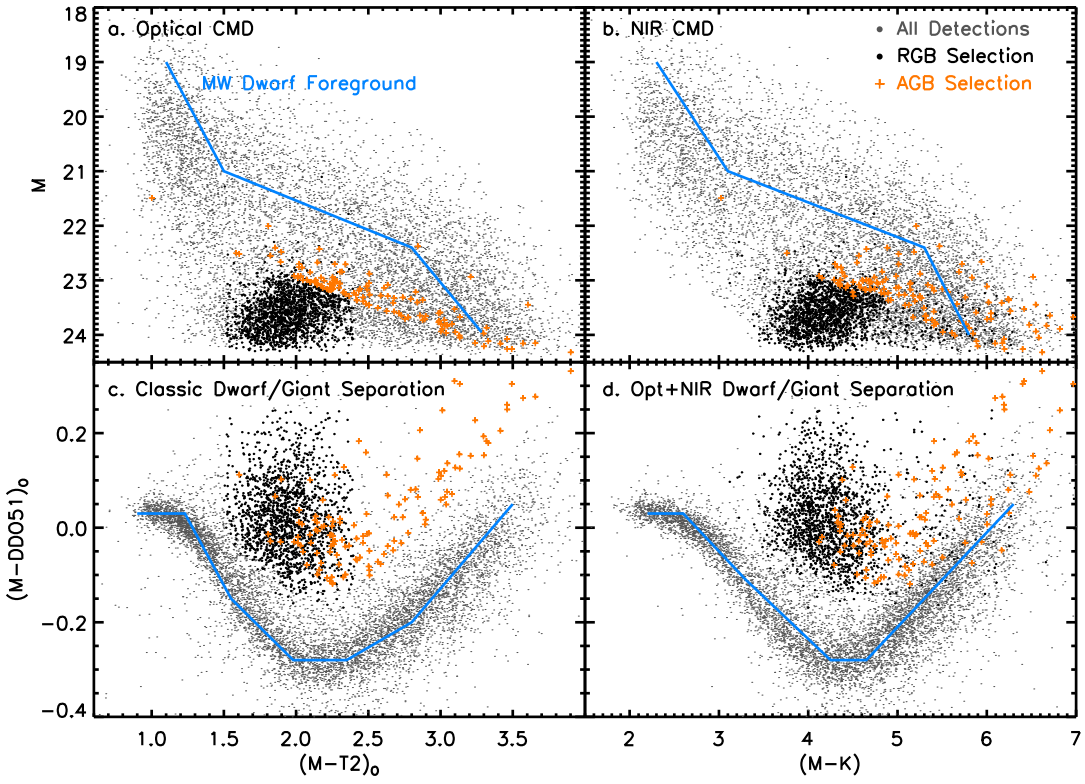

Fig. 6.3.— Example of optical (**left**) and merged optical+near-infrared (**right**) data for Andromeda VII ($b = \quad -10°$). **(a)** the optical SPLASH (M,$M-T_2$) CMD is compared to **(b)** the optical+NIR CMD (M,$M-K_s$). **(c)**, the Washington+$DDO51$ dwarf/giant separation technique is demonstrated (Majewski et al. 2000) and **(d)** demonstrates improved dwarf/giant separation due to increased temperature sensitivity of the $M-Ks$ color (note that while the color axis has greatly expanded, the average photometric color error is the same in both diagrams). In each panel, we highlight: (i) the Milky Way foreground sequence (blue), (ii) RGB isolation via Majewski et al. (2000) (black), and (iii) OPT+NIR AGB identification following the example Cioni & Habing (2003) for the LMC (orange).

NIR based stellar age estimates will also improve our grouping of similar stars for spectral co-addition. Most importantly, the proposed NIR observations will allow us to measure precise $T_{\rm eff}$ for individual stars from $M - K_s$ colors (compare the axes on the left and right panels of Figure 6.3). Precise knowledge of $T_{\rm eff}$ is critical for abundance determination; we currently estimate $T_{\rm eff}$ from the M, T_2 photometry (Figure 6.3a). However, $V-K$ color ($\approx (M-K_s)$) has long been the gold standard for measuring $T_{\rm eff}$, and will significantly improve our ability to make accurate abundance estimates (Figure 6.3b).

• ***Lower Dust Sensitivity in CMDs:*** Currently, low-spatial resolution (Schlegel et al. 1998) dust maps are used to estimate the foreground Milky Way reddening correction for each SPLASH pointing. Less dust-sensitive NIR CMDs will reduce systematic uncertainties in comparing CMDs to theoretical isochrones, from which photometric metallicities are derived. Additionally, the NIR imaging can be combined with *Spitzer*+IRAC imaging for the M31 satellites to derive the *total* line-of-sight reddening to *individual* stars using Majewski et al. 's RJCE technique (Majewski et al. 2011; Nidever et al. 2012) and estimate the mean internal reddening for each satellites. Deep IRAC photometry of the M31 dSph population, suitable for application of RJCE, is already being obtained (Boyer et al. 2011a, 2012).

• ***Insight into Foreground Milky Way Substructure:*** Our observational program includes a plan for taking NIR images with a large dynamic range in the final photometry — spanning the bright limit of very short exposures to the depth required for our CMDs. The bright end of this range permits ancillary studies of foreground Milky Way substructure — in particular the Triangulum-Andromeda overdensity that spans the full spatial range of the SPLASH footprint (Majewski et al. 2004; Rocha-Pinto et al. 2004; Sheffield et al. 2014; Deason et al. 2014).

6.4 Age Distributions in M31 Satellites from Anomalous Cepheids

Intrinsically low-luminosity objects, like dSphs, present significant challenges to analysis of their star formation histories because not all phases of stellar evolution are well sampled in their CMD and even those present are often swamped by foreground (Milky Way) or background (M31 stellar halo, unresolved galaxies) contaminants. Luminous variable stars, however, represent unambiguous indicators of specifically-aged, *otherwise indiscernible* populations in a stellar system; more specifically, the color magnitude signatures of stellar populations tend to be dominated, in number, by the most massive star forming events and can swamp signatures of smaller bursts that are important for the work presented here. Even in well-studied systems like the Large Magellanic Cloud (LMC), such tracers have proven invaluable for proper reconstruction of the SFH (Fiorentino & Monelli 2012). At M31 distances, the Cepheid-type variables are particularly useful due to their intrinsic luminosity — several magnitudes brighter than the horizontal branch (HB) — and can be efficiently photometered from the ground — unlike RR Lyrae which require HST temporal monitoring at M31 distance (Sandage & Tammann 2006; Mateo et al. 1995). Moreover, unlike RR Lyrae, the Cepheid-type variables can be found in intermediate to young (< 8 Gyr) populations and have observable properties — period (P), luminosity (M), color, variability amplitude (A) – that can be used to classify Cepheid sub-types correlated to the mass/age and metallicity of the parent stellar population (Sandage & Tammann 2006; Wallerstein 2002). Of key interest for the work proposed here are the low metallicity ($Z < 0.0001$) Cepheids typified by RR Lyrae-like periods ($0.3 \leq P_{AC} \leq 2.0$), but with luminosities several magnitudes brighter than RR Lyrae.

There are two well-classified sub-types: the short-period Classical Cepheids (s-pCC), which are from young (< 1 Gyr) populations, and Anomalous Cepheids (Anomalous Cepheids), which trace either old (> 10 Gyr) or intermediate age ($1 - 10$ Gyr) populations (Gallart et al. 2004).

While relatively rare, Anomalous Cepheids have been found in all dwarf galaxies that have been monitored for variable stars (Pritzl et al. 2005), with virtually all of the ∼200 known Anomalous Cepheids being members of LG dwarf galaxies (Pritzl et al. 2002; Sandage & Tammann 2006; Gallart et al. 2004; Clementini et al. 2012; Fiorentino & Monelli 2012). Only one Anomalous Cepheid has been identified in a globular cluster, that being NGC 5466 (Zinn & King 1982). Generally the Anomalous Cepheids are metal-poor, helium-burning stars with $1.5 \leq M_V \leq 0.5$ (Bono et al. 1997). Theoretical investigations into the origins of Anomalous Cepheids indicate these stars are either (1) evolved, intermediate-age (< 5 Gyr) stars, or (2) the evolved products of mass transfer in old (> 10 Gyr) binary systems, but with no definitive means to distinguish either mechanism (Bono et al. 1997). Nevertheless, the *observational* evidence better supports the interpretation that Anomalous Cepheids are metal-poor, intermediate age variables: (1) the spatial distribution of Anomalous Cepheids in the LMC shows they are not coincident with the older stellar populations (Fiorentino & Monelli 2012), (2) high-resolution spectroscopy of the star in NGC5466, the Anomalous Cepheid most likely to be formed by a binary mass transfer scenario, has found no evidence to support the binary merger origin (McCarthy & Nemec 1997), and (3) no Anomalous Cepheids have been found in any other system comprised of *only* an old stellar population (> 12 Gyr).

Thus, it appears that Anomalous Cepheids may be an ideal tracer of intermediate aged populations, at least for the M31 dwarf spheroidal satellites. As mentioned,

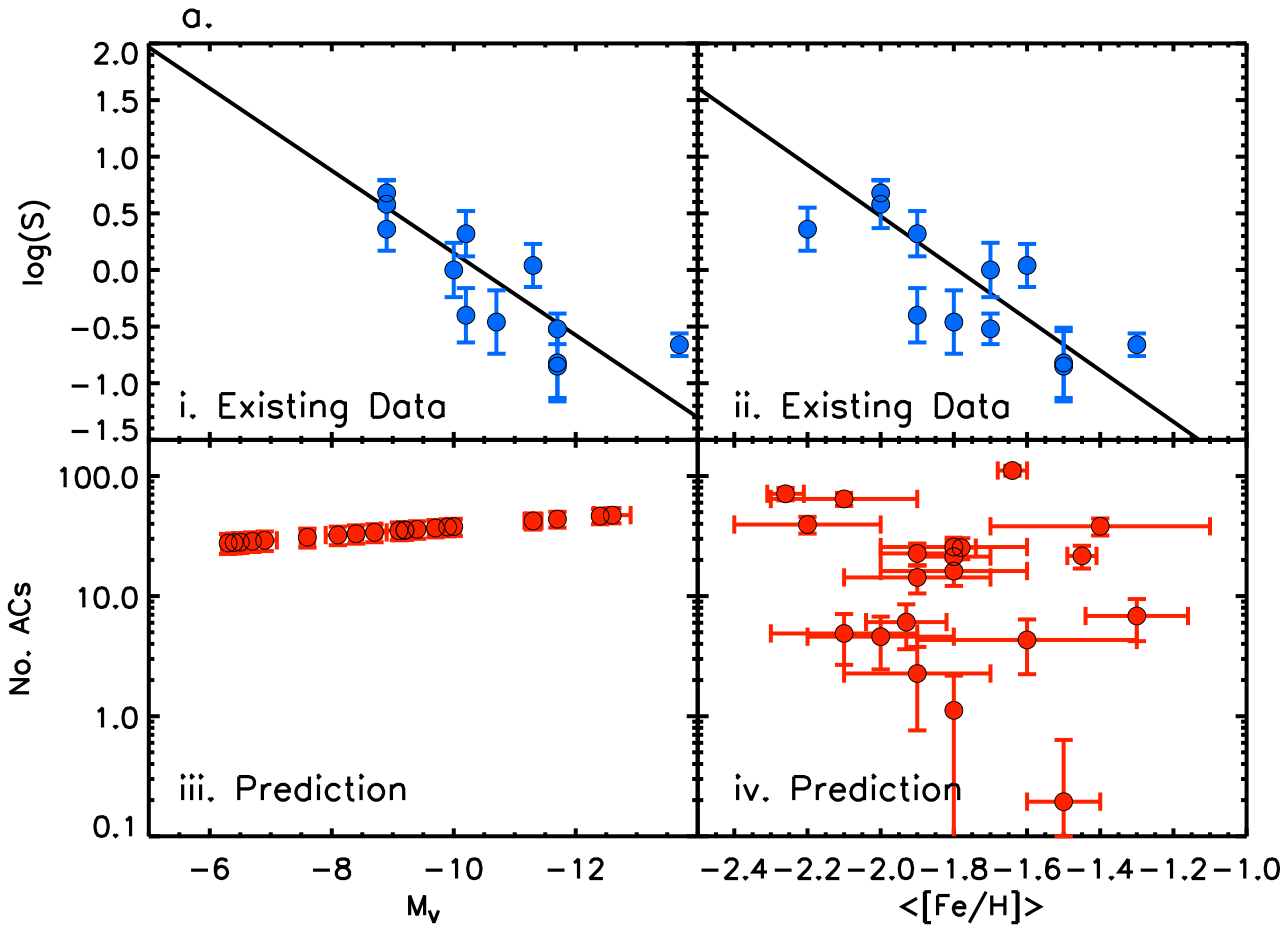

Fig. 6.4.— **a)** Observed specific frequency, $\log S$, of Anomalous Cepheids in dSph systems as a function of total V magnitude **(i)** and mean [Fe/H] **(ii)**. Empirical relationships are fit to the data (Pritzl et al. 2002). Predicted number of Anomalous Cepheids in M31 dSphs based on M_V **(iii)** and mean [Fe/H] **(iv)** (McConnachie 2012). **b)** Period-Luminosity relationship (PL) for confirmed Anomalous Cepheids in the Local Group. This figure includes the compilation of Milky Way data (Pritzl et al. 2002) (*blue*), M31 data for And01, And03, And02 and And06 (*green*) and data for Leo T (*red*) (Pritzl et al. 2002; Gallart et al. 2004). In comparison to theoretical predictions, the scatter is attributed to the mass of each individual star. Masses, however, can be derived through period-magnitude-amplitude and period-magnitude-color relationships derived from theoretical modelling.

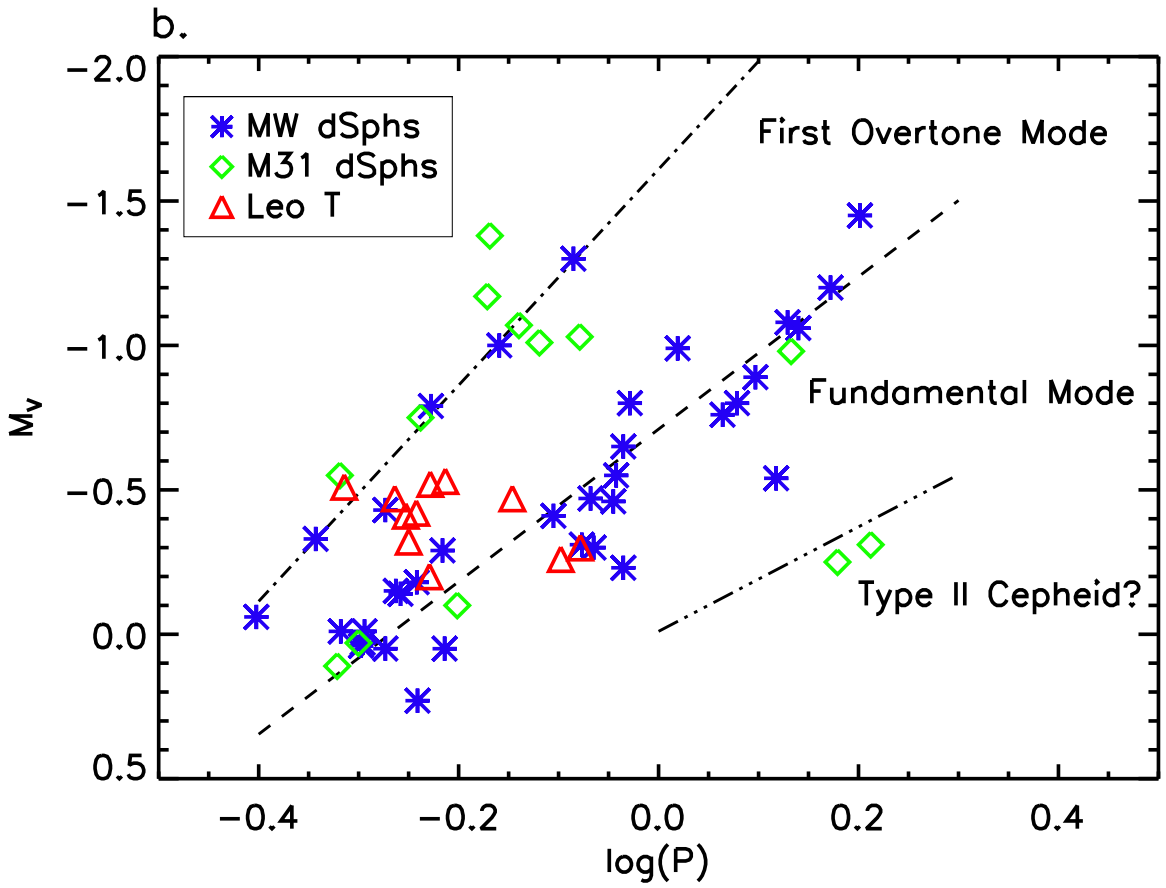

Fig. 5.4.— cont. **b)** Period-Luminosity relationship (PL) for confirmed Anomalous Cepheids in the Local Group. This figure includes the compilation of Milky Way data (Pritzl et al. 2002) (*blue*), M31 data for And01, And03, And02 and And06 (*green*) and data for Leo T (*red*) (Pritzl et al. 2002; Gallart et al. 2004). In comparison to theoretical predictions, the scatter is attributed to the mass of each individual star. Masses, however, can be derived through period-magnitude-amplitude and period-magnitude-color relationships derived from theoretical modelling.

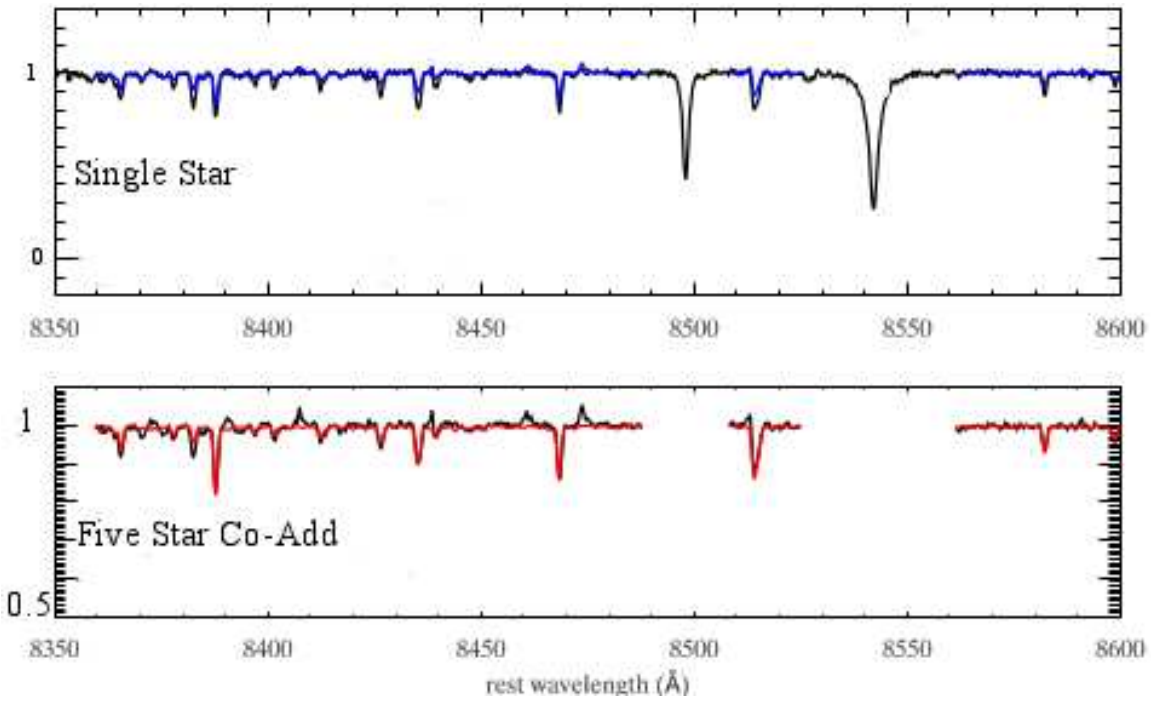

Fig. 6.5.— **Top:** Example Keck+DEIMOS spectrum for a single star in Draco (black) compared to its best fit spectral synthesis model (blue). **Bottom:** Co-added spectrum for five individual RGB stars in Draco (black) as compared to the best fit synthetic spectrum (red) (Yang et al. 2013). Regions of the spectrum found to bias the measurement technique are masked. A key part of this process is estimating the temperature (T_{eff}) and surface gravity (log(g)) of individual stars from photometry in order to co-add stars with similar physical characteristics.

Anomalous Cepheids have been found in all dSph galaxies searched for variable stars and, as shown in Figure 6.4a, the specific frequency of Anomalous Cepheids (number per $10^5 L_\odot$) is inversely correlated with dSph luminosity (M_V) and mean [Fe/H] (Pritzl et al. 2002). In the bottom panels of Figure 6.4a, relationships derived in the top panels are applied to M31 dSphs using the most recent estimates of their total luminosity and [Fe/H] (McConnachie 2012), and show that non-negligible samples of Anomalous Cepheids are expected in M31 satellites, though the two predictive measures differ on the specific numbers for each. Though Anomalous Cepheids have been identified in four of the M31 dSphs through HST imaging, the total areas surveyed represent small fractions of the total dSph (Pritzl et al. 2002, 2004, 2005) so that proportionally more Anomalous Cepheids can be found with full area coverage for these systems.

Identification of Anomalous Cepheids in the M31 dSphs and defining their light-curves requires further *optical* observations with proper time series cadences; meanwhile, because Anomalous Cepheid light curve amplitudes in the NIR are well below the photometric measurement accuracy, the NIR data (from our NEWFIRM survey) yield *mean*, static luminosities. Based on mean intrinsic Anomalous Cepheid luminosities (Figure 6.4b), the distance modulus to M31 (μ=24.4), and the projected radius of the M31 stellar halo ($R \sim 200$ kpc, or $\mu \pm 0.4$) the mean apparent V magnitude of M31 Anomalous Cepheids range over $22.5 \leq V_{AC} \leq 25.2$, with variability at the level of ~ 0.5 magnitudes. In good conditions, $V \sim 25.0$ is reliably attained in 900s exposures with 4-meter class telescopes. With careful consideration given to proper time sampling cadence for these short-period variables, optical light curves can be obtained with only modest amounts telescope time.

KPNO 4-meter + Mosaic Variable Search: Complementing the NIR imaging

program is a proposed search for Anomalous Cepheids in M31 satellites. Though tiny Anomalous Cepheid light variations make them precise standard candles at NIR wavelengths, the large optical light-curve amplitudes are needed to identify the Anomalous Cepheids and derive their periods. Guided by a previous, small area survey of four M31 dSphs (Pritzl et al. 2002, 2004, 2005), appropriate time series V imaging can be pursued. With typical Anomalous Cepheid periods of $\sim$1 day, the necessary data for all dSphs in this program can easily be collected with only moderate observational resources. A total of six nights were awarded on the KPNO-4m + MOSAIC in 2014B for this project with 50% of the allocated time lost to weather. Additional epochs were obtained for each of the twenty dSphs allowing for the identification of variable candidates to strengthen future proposals. By folding in the wealth of archival data on these objects in public (NOAO, CFHT, etc ..) and private (LBT) archives, it may be possible to produce rudimentary light curves without additional data collection.

Identification & Characterization of Variable Stars: Once the necessary optical observations are acquired, the image processing and photometric techniques developed for the optical SPLASH survey can be applied to the images. Variable stars can be identified from time series photometric catalogs using the Welch-Stetson variability index (Welch & Stetson 1993), which is sufficiently robust to work at or near the limiting magnitude of a photometric catalog and is adopted in similar searches for variable stars Pritzl et al. (2002, 2004, 2005). Light curves, from which pulsation modes can be determined, will be fit to derive periods and amplitudes using methods developed by Layden et al. (2000). The physical parameters of the variable stars can be derived using the NIR magnitudes, which better approximate the static luminosity, using theoretical Period-Magnitude-Amplitude and Period-Magnitude-Color relationships (Caputo et al. 2004; Marconi et al. 2004; Fiorentino et al. 2006).

The observed period-luminosity relationship (PLR) is reproduced in Figure 6.4b for those 50 stars with well constrained pulsation modes, separated into fundamental or first overtone (Pritzl et al. 2002). The scatter in Figure 6.4b is comparable to the scatter in the stellar mass of individual Anomalous Cepheids and observational errors for the mean optical magnitude (Fiorentino et al. 2006). Pulsation mode cannot always be determined from the light curve alone (Bono et al. 1997; Fiorentino et al. 2006), but the two modes separate rather cleanly in the PLR diagram. Once identified, masses of individual stars can be derived from the theoretical period-magnitude-amplitude (PMA) and period-magnitude-color relationships (PMC) for the given pulsation mode (Caputo et al. 2004; Marconi et al. 2004; Fiorentino et al. 2006). These relationships exist for both optical and NIR bands and with our combined optical+NIR data we will be able to average estimates from multiple PMA and PMC relationships to reduce observational scatter. Derived masses for these He-burning stars, in turn, when combined with our additional constraints (photometric and spectroscopic) on metallicity in these dSphs, provide strong indicators of the ages of these stars and the star formation episode they represent in their parent system.

6.5 Age Distributions by Breaking the RGB Age/Metallicity Degeneracy and Relative Age Distributions from [α/Fe]-[Fe/H] Patterns

There are degeneracies in determining the star formation history of any mixed-age stellar population via photometry alone. Stars with different ages and metalicities

inhabit the same area of color-magnitude space, even for multi-band photometry with a large color separation. A complete sample of stars with spectroscopically-determined metalicities can break this degeneracy, however, obtaining such a sample is prohibitively expensive. For example, while the deepest photometry available for the M31 satellites extends to stars with $R \sim 25$ the deepest spectroscopy performed with the largest telescopes are three full magnitudes brighter ($R \sim 22$). While a complete spectroscopic sample is not feasible for the proposed photometric survey, it is possible to determine spectroscopic metalicities for representative subsamples in these systems. To two novel techniques are now applicable to our work in the M 31 halo: (i) abundances determined from medium resolution spectroscopy, and (ii) abundances determined from co-added low resolution spectroscopy.

Photometric age measurements using RGB stars are limited in precision due to the age-metallicity degeneracy in the RGB branch. An increase (decrease) in metal abundance can mimic a larger (smaller) age for a stellar population. Using the spectroscopic data outlined above, we will construct metallicity distribution functions for these dSphs, thereby breaking the degeneracy inherent in photometrically-derived ages. The [α/Fe] measurements will enhance our understanding of internal chemical evolution in each dSph, because elemental abundances are an archaeological record of past star formation (Freeman & Bland-Hawthorn 2002). For example, the presence of solar-level (~ 0.0) [α/Fe] abundance ratios is indicative of a stellar population that undergoes internal chemical enrichment in a timescale at least as long as the minimum time delay for the production of Type Ia SNe, between 50$-$500 Myr after the onset of star formation. A large number of [Fe/H] and [α/Fe] measurements are now available for Milky Way dSphs. By comparing the distribution of stars in [α/Fe]-[Fe/H] space between the M31 and Milky Way dSphs, it will also be possible

to place the first constraints on the degree of similarity in chemical evolution between the member dSphs of the satellite systems of both galaxies.

Medium Resolution Spectroscopy: We are in a unique position to measure spectroscopic metalicities of individual M31 stars. Stars at M31 distance are inaccessible to traditional metallicity measurements via high resolution spectroscopy (R>20,000), and while it is possible to obtain higher S/N spectra of M31 stars via medium resolution spectroscopy (R∼5000), in the past these data have been used only to determine crude metallicities via integrated line widths. Kirby et al. (2008, 2011b,a) developed a spectral synthesis technique for medium resolution spectra that directly estimates [Fe/H] and abundances of four α-elements. Vargas et al. (2014) adapted this technique to measure abundances of stars in the M31 dwarf satellites by obtaining high S/N spectroscopy of confirmed satellite members in the SPLASH datasets (Tollerud et al. 2012). Application of this technique to such faint stars requires spectra with S/N> 20Å^{-1}, corresponding to roughly 3-6 hours of exposure time with the Keck/DEIMOS spectrograph.

The technique consists of a pixel-by-pixel matching between stellar spectra of RGB stars and a finely-spaced grid of synthetic spectra optimized for our spectral wavelength range. We measure [Fe/H] (our proxy for stellar metallicity) and [α/Fe] abundances ratios ([Mg/Fe], [Si/Fe], [Ca/Fe], [Ti/Fe]) by finding the best-matching synthetic spectrum to the data in the χ^2 sense, using only the wavelength regions sensitive to a particular element. This has been calibrated and tested extensively using measurements of stars with prior high-resolution chemical abundances, ensuring we can obtain accurate chemical information for spectra with S/N $\gtrsim$ 15 Å^{-1} (Vargas et al. 2014). We have recently obtained a large number of Keck/DEIMOS spectra with sufficient S/N for determining spectroscopic metallicities and α-element abundances

in six M31 dSphs (And V, And VII, And X, And XI, and And XVI, And XIX) and a handful of individual M31 halo stars. The dataset includes 120 previously-confirmed satellite members and 130 new candidates selected from their CMD position. After accounting for radial velocity contaminants in the newly acquired data, we anticipate a sample of ~ 170 metallicity and [α/Fe] measurements.

Co-Added Spectroscopy: An alternate to obtaining additional exposure time is to boost the total spectral S/N via the co-addition of the spectra of groups of "like" stars, where such groups are defined based on radial velocity membership in a given dSph satellite and proximity to an isochrone of a particular metallicity/age in the CMD. Tests using co-added spectra of Milky Way RGB stars of known [Fe/H] and [α/Fe] look very promising (an example is given in Figure 6.5) and indicate that it should be possible to derive detailed (but ensemble-averaged) chemical abundances for specific subpopulations in M31 and its satellites (Yang et al. 2013). This work will benefit from the new NEWFIRM survey due to the increased temperature sensitivity of the $V - K_s$ color.

The primary goal of the existing SPLASH spectroscopic database was to acquire line-of-sight velocity information required to resolve M31 kinematical components. These data, however, are of insufficient S/N to derive robust chemical abundances. though they do form the backbone of the star selection required for this aspect of the project.

6.6 Summary

In this chapter, we have placed the results of this thesis into the broader context of the SPLASH goal to characterize the stellar halo of M 31 using old stellar populations as the primary tracer. In many aspects, this work completes the immediate goals for first

generation explorations of the M 31 stellar halo, which will be surpassed by deeper wide-field observations, both with PAndAS and the proposed survey with Subaru. Not only have we probed the halo by building samples of high likelihood member stars, we have begun to probe its dynamics to large projected radii ($R_{proj} \sim 165$ kpc), which will permit the first truly *global* kinematic exploration of a stellar halo at large radii.

In this chapter, we also motivate the questions to be posed for second generation surveys of the M 31 stellar halo, which have the potential to truly transform our understanding of its formation. By constraining the ages and chemistries of the stellar populations in M 31 stellar halo, the global age fraction distribution and mean chemical evolution histories provide meaningful probes of the total formation history of M 31, not just in satellite accretion, but also from 'in-situ' and kicked-out mechanisms. Moreover, the age and chemical distributions start to tease out the progenitor properties for the fraction of accreted stars. In combination with more detailed work ongoing for the Milky Way (e.g., APOGEE and GAIA Zasowski et al. 2013), it is feasible to have the basic parameters of the two closest large galaxy halos characterized on a timescale appropriate for the era of 30-meter class telescopes, whose combined collecting area and potential for high resolution large field-of-view, will permit detailed study of the halos for other large galaxies in the Local Volume, to truly probe the universality of stellar halo structures and properties, and constrain the role of Λ-CDM in halo, and by proxy, galaxy formation.

The primary observational data product for these efforts are NIR imaging, in which evolved AGB stars, typically confused with the RGB in optical colors, have unique signatures by their mass (or age). This is the first large area probe of this nature and to this depth – albeit, a natural extension of the 2MASS 6X survey that

revealed previously "hidden" structure in the M 31 bar, bulge, and disk (**?**Beaton et al. 2007). The M 31AGES program, however, suffers from one major drawback: observational programs of this nature are difficult to carry out from the ground en masse, owing to the dominance of emission from the sky occurring for these wavelengths. Thus, to date this technique has only been applied to the SMC, LMC, and our pencil-beam survey of M 31. Expansion much beyond these initial probes is limited both by seeing, the lack of wide-field NIR instruments, and the overall sensitivity that can be obtained from the ground, even in our long integrations.

The wide field, high resolution, and sensitivity of the proposed WFIRST-ATCA mission makes it uniquely poised to survey the halos of nearby galaxies in the near-infrared. A sample such as that of the Local Volume Legacy Survey (LVLS) — all galaxies within 3.5 Mpc and all S/Irr within 11 Mpc — would be complemented by the addition of the NIR imaging to the existing sample of ground and space based UV, optical, and MIR. Thus, WFIRST-ATCA can not only build the first large sample of global stellar halo properties via the red giant branch (overall size, surface brightness profile, shape, etc.), but can also produce the first age-distribution sample via the AGB/RGB fraction. Such a dataset will be sufficient to provide crucial observational feedback to fine-tune state-of-the-art galaxy formation simulations for the relative contribution of halo formation mechanisms. Moreover, with a representative sample of galaxies — even in integrated light — we can begin to connect accretion histories to current disk structure, probing the basic "nature" versus "nurture" questions being asked for the Milky Way in terms of resolved stellar populations. In the meantime, surveys like M 31AGES demonstrate the efficacy of using NIR passbands to gain additional leverage on the most pressing questions of hierarchical mass assembly for Milky Way sized galaxies.

References

Abazajian, K. N., Adelman-McCarthy, J. K., Agüeros, M. A., Allam, S. S., Allende Prieto, C., An, D., Anderson, K. S. J., Anderson, S. F., Annis, J., Bahcall, N. A., & et al. 2009, ApJS, 182, 543

Adams, W. S. & Joy, A. H. 1917, ApJ, 46, 313

Adams, W. S. & Joy, A. H. 1922, in Publications of the American Astronomical Society, Vol. 4, Publications of the American Astronomical Society, 201

Adams, W. S., Joy, A. H., Humason, M. L., & Brayton, A. M. 1935, ApJ, 81, 187

Adams, W. S. & Kohlschutter, A. 1914, ApJ, 40, 385

Adelman-McCarthy, J. K., Agüeros, M. A., Allam, S. S., Allende Prieto, C., Anderson, K. S. J., Anderson, S. F., Annis, J., Bahcall, N. A., Bailer-Jones, C. A. L., Baldry, I. K., Barentine, J. C., Bassett, B. A., Becker, A. C., Beers, T. C., Bell, E. F., Berlind, A. A., Bernardi, M., Blanton, M. R., Bochanski, J. J., Boroski, W. N., Brinchmann, J., Brinkmann, J., Brunner, R. J., Budavári, T., Carliles, S., Carr, M. A., Castander, F. J., Cinabro, D., Cool, R. J., Covey, K. R., Csabai, I., Cunha, C. E., Davenport, J. R. A., Dilday, B., Doi, M., Eisenstein, D. J., Evans, M. L., Fan, X., Finkbeiner, D. P., Friedman, S. D., Frieman, J. A., Fukugita, M., Gänsicke, B. T., Gates, E., Gillespie, B., Glazebrook, K., Gray, J., Grebel, E. K.,

Gunn, J. E., Gurbani, V. K., Hall, P. B., Harding, P., Harvanek, M., Hawley, S. L., Hayes, J., Heckman, T. M., Hendry, J. S., Hindsley, R. B., Hirata, C. M., Hogan, C. J., Hogg, D. W., Hyde, J. B., Ichikawa, S.-i., Ivezić, Ž., Jester, S., Johnson, J. A., Jorgensen, A. M., Jurić, M., Kent, S. M., Kessler, R., Kleinman, S. J., Knapp, G. R., Kron, R. G., Krzesinski, J., Kuropatkin, N., Lamb, D. Q., Lampeitl, H., Lebedeva, S., Lee, Y. S., Leger, R. F., Lépine, S., Lima, M., Lin, H., Long, D. C., Loomis, C. P., Loveday, J., Lupton, R. H., Malanushenko, O., Malanushenko, V., Mandelbaum, R., Margon, B., Marriner, J. P., Martínez-Delgado, D., Matsubara, T., McGehee, P. M., McKay, T. A., Meiksin, A., Morrison, H. L., Munn, J. A., Nakajima, R., Neilsen, Jr., E. H., Newberg, H. J., Nichol, R. C., Nicinski, T., Nieto-Santisteban, M., Nitta, A., Okamura, S., Owen, R., Oyaizu, H., Padmanabhan, N., Pan, K., Park, C., Peoples, Jr., J., Pier, J. R., Pope, A. C., Purger, N., Raddick, M. J., Re Fiorentin, P., Richards, G. T., Richmond, M. W., Riess, A. G., Rix, H.-W., Rockosi, C. M., Sako, M., Schlegel, D. J., Schneider, D. P., Schreiber, M. R., Schwope, A. D., Seljak, U., Sesar, B., Sheldon, E., Shimasaku, K., Sivarani, T., Smith, J. A., Snedden, S. A., Steinmetz, M., Strauss, M. A., SubbaRao, M., Suto, Y., Szalay, A. S., Szapudi, I., Szkody, P., Tegmark, M., Thakar, A. R., Tremonti, C. A., Tucker, D. L., Uomoto, A., Vanden Berk, D. E., Vandenberg, J., Vidrih, S., Vogeley, M. S., Voges, W., Vogt, N. P., Wadadekar, Y., Weinberg, D. H., West, A. A., White, S. D. M., Wilhite, B. C., Yanny, B., Yocum, D. R., York, D. G., Zehavi, I., & Zucker, D. B. 2008, ApJS, 175, 297

Agertz, O., Moore, B., Stadel, J., Potter, D., Miniati, F., Read, J., Mayer, L., Gawryszczak, A., Kravtsov, A., Nordlund, Å., Pearce, F., Quilis, V., Rudd, D., Springel, V., Stone, J., Tasker, E., Teyssier, R., Wadsley, J., & Walder, R. 2007, MNRAS, 380, 963

Ahn, C. P., Alexandroff, R., Allende Prieto, C., Anderson, S. F., Anderton, T., Andrews, B. H., Aubourg, É., Bailey, S., Balbinot, E., Barnes, R., & et al. 2012, ApJS, 203, 21

Aihara, H., Allende Prieto, C., An, D., Anderson, S. F., Aubourg, É., Balbinot, E., Beers, T. C., Berlind, A. A., Bickerton, S. J., Bizyaev, D., Blanton, M. R., Bochanski, J. J., Bolton, A. S., Bovy, J., Brandt, W. N., Brinkmann, J., Brown, P. J., Brownstein, J. R., Busca, N. G., Campbell, H., Carr, M. A., Chen, Y., Chiappini, C., Comparat, J., Connolly, N., Cortes, M., Croft, R. A. C., Cuesta, A. J., da Costa, L. N., Davenport, J. R. A., Dawson, K., Dhital, S., Ealet, A., Ebelke, G. L., Edmondson, E. M., Eisenstein, D. J., Escoffier, S., Esposito, M., Evans, M. L., Fan, X., Femenía Castellá, B., Font-Ribera, A., Frinchaboy, P. M., Ge, J., Gillespie, B. A., Gilmore, G., González Hernández, J. I., Gott, J. R., Gould, A., Grebel, E. K., Gunn, J. E., Hamilton, J.-C., Harding, P., Harris, D. W., Hawley, S. L., Hearty, F. R., Ho, S., Hogg, D. W., Holtzman, J. A., Honscheid, K., Inada, N., Ivans, I. I., Jiang, L., Johnson, J. A., Jordan, C., Jordan, W. P., Kazin, E. A., Kirkby, D., Klaene, M. A., Knapp, G. R., Kneib, J.-P., Kochanek, C. S., Koesterke, L., Kollmeier, J. A., Kron, R. G., Lampeitl, H., Lang, D., Le Goff, J.-M., Lee, Y. S., Lin, Y.-T., Long, D. C., Loomis, C. P., Lucatello, S., Lundgren, B., Lupton, R. H., Ma, Z., MacDonald, N., Mahadevan, S., Maia, M. A. G., Makler, M., Malanushenko, E., Malanushenko, V., Mandelbaum, R., Maraston, C., Margala, D., Masters, K. L., McBride, C. K., McGehee, P. M., McGreer, I. D., Ménard, B., Miralda-Escudé, J., Morrison, H. L., Mullally, F., Muna, D., Munn, J. A., Murayama, H., Myers, A. D., Naugle, T., Neto, A. F., Nguyen, D. C., Nichol, R. C., O'Connell, R. W., Ogando, R. L. C., Olmstead, M. D., Oravetz, D. J., Padmanabhan, N., Palanque-Delabrouille, N., Pan, K., Pandey, P., Pâris, I., Percival, W. J.,

Petitjean, P., Pfaffenberger, R., Pforr, J., Phleps, S., Pichon, C., Pieri, M. M., Prada, F., Price-Whelan, A. M., Raddick, M. J., Ramos, B. H. F., Reylé, C., Rich, J., Richards, G. T., Rix, H.-W., Robin, A. C., Rocha-Pinto, H. J., Rockosi, C. M., Roe, N. A., Rollinde, E., Ross, A. J., Ross, N. P., Rossetto, B. M., Sánchez, A. G., Sayres, C., Schlegel, D. J., Schlesinger, K. J., Schmidt, S. J., Schneider, D. P., Sheldon, E., Shu, Y., Simmerer, J., Simmons, A. E., Sivarani, T., Snedden, S. A., Sobeck, J. S., Steinmetz, M., Strauss, M. A., Szalay, A. S., Tanaka, M., Thakar, A. R., Thomas, D., Tinker, J. L., Tofflemire, B. M., Tojeiro, R., Tremonti, C. A., Vandenberg, J., Vargas Magaña, M., Verde, L., Vogt, N. P., Wake, D. A., Wang, J., Weaver, B. A., Weinberg, D. H., White, M., White, S. D. M., Yanny, B., Yasuda, N., Yeche, C., & Zehavi, I. 2011, ApJS, 193, 29

Alvarez, M. A., Busha, M., Abel, T., & Wechsler, R. H. 2009, ApJ, 703, L167

Athanassoula, E. & Beaton, R. L. 2006, MNRAS, 370, 1499

Atkinson, A. M., Abraham, R. G., & Ferguson, A. M. N. 2013, ApJ, 765, 28

Baade, W. 1958, Ricerche Astronomiche, 5, 303

Balser, D. S., Rood, R. T., Bania, T. M., & Anderson, L. D. 2011, ApJ, 738, 27

Barnard, E. E. 1917, AJ, 30, 175

Beaton, R. L., Majewski, S. R., Guhathakurta, P., Skrutskie, M. F., Cutri, R. M., Good, J., Patterson, R. J., Athanassoula, E., & Bureau, M. 2007, ApJ, 658, L91

Beaton, R. L., Martínez-Delgado, D., Majewski, S. R., D'Onghia, E., Zibetti, S., Gabany, R. J., Johnson, K. E., Blanton, M., & Verbiscer, A. 2014, ApJ, 790, 117

Bell, E. F., Slater, C. T., & Martin, N. F. 2011, ApJ, 742, L15

Bell, E. F., Xue, X. X., Rix, H.-W., Ruhland, C., & Hogg, D. W. 2010, AJ, 140, 1850

Berg, D. A., Skillman, E. D., Marble, A. R., van Zee, L., Engelbracht, C. W., Lee, J. C., Kennicutt, Jr., R. C., Calzetti, D., Dale, D. A., & Johnson, B. D. 2012, ApJ, 754, 98

Bertin, E. & Arnouts, S. 1996, A&AS, 117, 393

Bianchi, L. 2011, Ap&SS, 335, 51

Binney, J. & Tremaine, S. 2008, Galactic Dynamics: Second Edition (Princeton University Press)

Blaauw, A. The Calibration of Luminosity Criteria, ed. K. A. Strand (the University of Chicago Press), 383

—. 2004, ARA&A, 42, 1

Blanton, M. R. & Moustakas, J. 2009, ARA&A, 47, 159

Blanton, M. R., Schlegel, D. J., Strauss, M. A., Brinkmann, J., Finkbeiner, D., Fukugita, M., Gunn, J. E., Hogg, D. W., Ivezić, Ž., Knapp, G. R., Lupton, R. H., Munn, J. A., Schneider, D. P., Tegmark, M., & Zehavi, I. 2005, AJ, 129, 2562

Bond, J. R. & Szalay, A. S. 1983, ApJ, 274, 443

Bono, G., Caputo, F., Santolamazza, P., Cassisi, S., & Piersimoni, A. 1997, AJ, 113, 2209

Boyer, M., Barmby, P., Bonanos, A. Z., Gehrz, R. D., Gordon, K. D., Groenewegen, M., Lagadec, E., Lennon, D., Marengo, M., McQuinn, K. B. W., Meixner, M., Skillman, E. D., Sloan, G. C., van Loon, J. T., & Zijlstra, A. 2011a, Spitzer Proposal, 80063

Boyer, M. L., Barmby, P., Bonanos, A. Z., Gehrz, R. D., Gordon, K. D., Groenewegen, M. A. T., Lagadec, E., Lennon, D. J., Marengo, M., McQuinn, K., Meixner, M., Skillman, E. D., Sloan, G. C., van Loon, J. T., & Zijlstra, A. A. 2012, in American Astronomical Society Meeting Abstracts, Vol. 219, American Astronomical Society Meeting Abstracts 219, 244.16

Boyer, M. L., Srinivasan, S., van Loon, J. T., McDonald, I., Meixner, M., Zaritsky, D., Gordon, K. D., Kemper, F., Babler, B., Block, M., Bracker, S., Engelbracht, C. W., Hora, J., Indebetouw, R., Meade, M., Misselt, K., Robitaille, T., Sewiło, M., Shiao, B., & Whitney, B. 2011b, AJ, 142, 103

Boylan-Kolchin, M., Bullock, J. S., & Kaplinghat, M. 2011, MNRAS, 415, L40

—. 2012, MNRAS, 422, 1203

Boylan-Kolchin, M., Bullock, J. S., Sohn, S. T., Besla, G., & van der Marel, R. P. 2013, ApJ, 768, 140

Boylan-Kolchin, M., Springel, V., White, S. D. M., & Jenkins, A. 2010, MNRAS, 406, 896

Brinchmann, J., Charlot, S., White, S. D. M., Tremonti, C., Kauffmann, G., Heckman, T., & Brinkmann, J. 2004, MNRAS, 351, 1151

Brown, A. G. A., Arenou, F., van Leeuwen, F., Lindegren, L., & Luri, X. 1998, Highlights of Astronomy, 11, 547

Brown, T. M., Beaton, R., Chiba, M., Ferguson, H. C., Gilbert, K. M., Guhathakurta, P., Iye, M., Kalirai, J. S., Koch, A., Komiyama, Y., Majewski, S. R., Reitzel, D. B., Renzini, A., Rich, R. M., Smith, E., Sweigart, A. V., & Tanaka, M. 2008, ApJ, 685, L121

Brown, T. M., Smith, E., Ferguson, H. C., Guhathakurta, P., Kalirai, J. S., Kimble, R. A., Renzini, A., Rich, R. M., Sweigart, A. V., & Vanden Berg, D. A. 2009, ApJS, 184, 152

Brown, T. M., Smith, E., Ferguson, H. C., Guhathakurta, P., Kalirai, J. S., Rich, R. M., Renzini, A., Sweigart, A. V., Reitzel, D., Gilbert, K. M., & Geha, M. 2007, ApJ, 658, L95

Brown, T. M., Smith, E., Ferguson, H. C., Rich, R. M., Guhathakurta, P., Renzini, A., Sweigart, A. V., & Kimble, R. A. 2006a, ApJ, 652, 323

Brown, T. M., Smith, E., Guhathakurta, P., Rich, R. M., Ferguson, H. C., Renzini, A., Sweigart, A. V., & Kimble, R. A. 2006b, ApJ, 636, L89

Brunthaler, A., Reid, M. J., Falcke, H., Greenhill, L. J., & Henkel, C. 2005, Science, 307, 1440

Brunthaler, A., Reid, M. J., Falcke, H., Henkel, C., & Menten, K. M. 2007, A&A, 462, 101

Buat, V. & Xu, C. 1996, A&A, 306, 61

Bullock, J. S. 2010, ArXiv e-prints

Bullock, J. S. & Johnston, K. V. 2005, ApJ, 635, 931

Calzetti, D. 2012, ArXiv e-prints

Cappellari, M., Emsellem, E., Krajnović, D., McDermid, R. M., Scott, N., Verdoes Kleijn, G. A., Young, L. M., Alatalo, K., Bacon, R., Blitz, L., Bois, M., Bournaud, F., Bureau, M., Davies, R. L., Davis, T. A., de Zeeuw, P. T., Duc, P.-A., Khochfar,

S., Kuntschner, H., Lablanche, P.-Y., Morganti, R., Naab, T., Oosterloo, T., Sarzi, M., Serra, P., & Weijmans, A.-M. 2011, MNRAS, 413, 813

Caputo, F., Castellani, V., Degl'Innocenti, S., Fiorentino, G., & Marconi, M. 2004, A&A, 424, 927

Cardelli, J. A., Clayton, G. C., & Mathis, J. S. 1989, ApJ, 345, 245

Carollo, D., Beers, T. C., Chiba, M., Norris, J. E., Freeman, K. C., Lee, Y. S., Ivezić, Ž., Rockosi, C. M., & Yanny, B. 2010, ApJ, 712, 692

Carollo, D., Beers, T. C., Lee, Y. S., Chiba, M., Norris, J. E., Wilhelm, R., Sivarani, T., Marsteller, B., Munn, J. A., Bailer-Jones, C. A. L., Fiorentin, P. R., & York, D. G. 2007, Nature, 450, 1020

Carraro, G., Perren, G., Vázquez, R. A., & Moitinho, A. 2014, in Astronomical Society of the Pacific Conference Series, Vol. 480, Structure and Dynamics of Disk Galaxies, ed. M. S. Seigar & P. Treuthardt, 10

Chaboyer, B., Green, E. M., & Liebert, J. 1999, AJ, 117, 1360

Chapman, S. C., Ibata, R., Lewis, G. F., Ferguson, A. M. N., Irwin, M., McConnachie, A., & Tanvir, N. 2006, ApJ, 653, 255

Cheng, L., Guhathakurta, P., Kirby, E., Yang, L., & SPLASH Collaboration. 2012, in American Astronomical Society Meeting Abstracts, Vol. 219, American Astronomical Society Meeting Abstracts 219, 244.18

Chonis, T. S., Martínez-Delgado, D., Gabany, R. J., Majewski, S. R., Hill, G. J., Gralak, R., & Trujillo, I. 2011, AJ, 142, 166

Cioni, M.-R. L. & Habing, H. J. 2003, A&A, 402, 133

Clementini, G., Cignoni, M., Contreras Ramos, R., Federici, L., Ripepi, V., Marconi, M., Tosi, M., & Musella, I. 2012, ApJ, 756, 108

Collins, M. L. M., Chapman, S. C., Rich, R. M., Ibata, R. A., Martin, N. F., Irwin, M. J., Bate, N. F., Lewis, G. F., Peñarrubia, J., Arimoto, N., Casey, C. M., Ferguson, A. M. N., Koch, A., McConnachie, A. W., & Tanvir, N. 2014, ApJ, 783, 7

Condon, J. J. 1992, ARA&A, 30, 575

Conselice, C. J. 2003, ApJS, 147, 1

—. 2014, ARA&A, 52, 291

Cooper, A. P., D'Souza, R., Kauffmann, G., Wang, J., Boylan-Kolchin, M., Guo, Q., Frenk, C. S., & White, S. D. M. 2013, MNRAS, 434, 3348

Cooper, M. C., Newman, J. A., Davis, M., Finkbeiner, D. P., & Gerke, B. F. 2012, spec2d: DEEP2 DEIMOS Spectral Pipeline, astrophysics Source Code Library

Curtis, H. D. 1922, PASP, 34, 33

Darling, J. 2011, ApJ, 732, L2

Davis, M., Faber, S. M., Newman, J., Phillips, A. C., Ellis, R. S., Steidel, C. C., Conselice, C., Coil, A. L., Finkbeiner, D. P., Koo, D. C., Guhathakurta, P., Weiner, B., Schiavon, R., Willmer, C., Kaiser, N., Luppino, G. A., Wirth, G., Connolly, A., Eisenhardt, P., Cooper, M., & Gerke, B. 2003, in Society of Photo-Optical Instrumentation Engineers (SPIE) Conference Series, Vol. 4834, Discoveries and Research Prospects from 6- to 10-Meter-Class Telescopes II, ed. P. Guhathakurta, 161–172

de Jong, J. T. A., Harris, J., Coleman, M. G., Martin, N. F., Bell, E. F., Rix, H.-W., Hill, J. M., Skillman, E. D., Sand, D. J., Olszewski, E. W., Zaritsky, D., Thompson, D., Giallongo, E., Ragazzoni, R., DiPaola, A., Farinato, J., Testa, V., & Bechtold, J. 2008, ApJ, 680, 1112

de Vaucouleurs, G., de Vaucouleurs, A., Corwin, Jr., H. G., Buta, R. J., Paturel, G., & Fouqué, P. 1991, Third Reference Catalogue of Bright Galaxies. Volume I: Explanations and references. Volume II: Data for galaxies between 0^h and 12^h. Volume III: Data for galaxies between 12^h and 24^h.

Deason, A. J., Belokurov, V., Hamren, K. M., Koposov, S. E., Gilbert, K. M., Beaton, R. L., Dorman, C. E., Guhathakurta, P., Majewski, S. R., & Cunningham, E. C. 2014, MNRAS, 444, 3975

Devorkin, D. H. 2006, Journal for the History of Astronomy, 37, 429

Dolphin, A. E., Weisz, D. R., Skillman, E. D., & Holtzman, J. A. 2005, ArXiv Astrophysics e-prints

D'Onghia, E., Besla, G., Cox, T. J., & Hernquist, L. 2009, Nature, 460, 605

D'Onghia, E., Springel, V., Hernquist, L., & Keres, D. 2010a, ApJ, 709, 1138

D'Onghia, E., Vogelsberger, M., Faucher-Giguere, C.-A., & Hernquist, L. 2010b, ApJ, 725, 353

Downes, R. A., Margon, B., Anderson, S. F., Harris, H. C., Knapp, G. R., Schroeder, J., Schneider, D. P., York, D. G., Pier, J. R., & Brinkmann, J. 2004, AJ, 127, 2838

Durrell, P. R., Harris, W. E., & Pritchet, C. J. 2004, AJ, 128, 260

Eggen, O. 1957, AJ, 62, 45

Eggen, O. J. 1955, PASP, 67, 315

—. 1960, MNRAS, 120, 430

—. 1964, AJ, 69, 570

Eggen, O. J., Lynden-Bell, D., & Sandage, A. R. 1962, ApJ, 136, 748

Einasto, J., Saar, E., Kaasik, A., & Chernin, A. D. 1974, Nature, 252, 111

Eisenstein, D. J., Weinberg, D. H., Agol, E., Aihara, H., Allende Prieto, C., Anderson, S. F., Arns, J. A., Aubourg, É., Bailey, S., Balbinot, E., & Co-authors, . 2011, AJ, 142, 72

Faber, S. M., Phillips, A. C., Kibrick, R. I., Alcott, B., Allen, S. L., Burrous, J., Cantrall, T., Clarke, D., Coil, A. L., Cowley, D. J., Davis, M., Deich, W. T. S., Dietsch, K., Gilmore, D. K., Harper, C. A., Hilyard, D. F., Lewis, J. P., McVeigh, M., Newman, J., Osborne, J., Schiavon, R., Stover, R. J., Tucker, D., Wallace, V., Wei, M., Wirth, G., & Wright, C. A. 2003, in Society of Photo-Optical Instrumentation Engineers (SPIE) Conference Series, Vol. 4841, Instrument Design and Performance for Optical/Infrared Ground-based Telescopes, ed. M. Iye & A. F. M. Moorwood, 1657–1669

Fabricant, D., Fata, R., Roll, J., Hertz, E., Caldwell, N., Gauron, T., Geary, J., McLeod, B., Szentgyorgyi, A., Zajac, J., Kurtz, M., Barberis, J., Bergner, H., Brown, W., Conroy, M., Eng, R., Geller, M., Goddard, R., Honsa, M., Mueller, M., Mink, D., Ordway, M., Tokarz, S., Woods, D., Wyatt, W., Epps, H., & Dell'Antonio, I. 2005, PASP, 117, 1411

Fardal, M. A., Babul, A., Guhathakurta, P., Gilbert, K. M., & Dodge, C. 2008, ApJ, 682, L33

Fardal, M. A., Guhathakurta, P., Gilbert, K. M., Tollerud, E. J., Kalirai, J. S., Tanaka, M., Beaton, R., Chiba, M., Komiyama, Y., & Iye, M. 2012, MNRAS, 423, 3134

Feitzinger, J. V., Schmidt-Kaler, T., & Isserstedt, J. 1977, A&A, 57, 265

Ferguson, A. M. N., Irwin, M. J., Ibata, R. A., Lewis, G. F., & Tanvir, N. R. 2002, AJ, 124, 1452

Fiorentino, G., Limongi, M., Caputo, F., & Marconi, M. 2006, A&A, 460, 155

Fiorentino, G. & Monelli, M. 2012, A&A, 540, A102

Font, A. S., Johnston, K. V., Bullock, J. S., & Robertson, B. E. 2006a, ApJ, 638, 585

—. 2006b, ApJ, 646, 886

Font, A. S., Johnston, K. V., Ferguson, A. M. N., Bullock, J. S., Robertson, B. E., Tumlinson, J., & Guhathakurta, P. 2008, ApJ, 673, 215

Francis, C. 2014, MNRAS, 444, L6

Freedman, W. L. & Madore, B. F. 1990, ApJ, 365, 186

Freeman, K. & Bland-Hawthorn, J. 2002, ARA&A, 40, 487

Gallart, C., Aparicio, A., Freedman, W. L., Madore, B. F., Martínez-Delgado, D., & Stetson, P. B. 2004, AJ, 127, 1486

Galleti, S., Federici, L., Bellazzini, M., Fusi Pecci, F., & Macrina, S. 2004, A&A, 416, 917

Geha, M., Blanton, M. R., Yan, R., & Tinker, J. L. 2012, ApJ, 757, 85

Geisler, D. 1990, PASP, 102, 344

Genzel, R. & Downes, D. 1977, A&AS, 30, 145

Gilbert, K. M., Fardal, M., Kalirai, J. S., Guhathakurta, P., Geha, M. C., Isler, J., Majewski, S. R., Ostheimer, J. C., Patterson, R. J., Reitzel, D. B., Kirby, E., & Cooper, M. C. 2007, ApJ, 668, 245

Gilbert, K. M., Font, A. S., Johnston, K. V., & Guhathakurta, P. 2009a, ApJ, 701, 776

Gilbert, K. M., Guhathakurta, P., Beaton, R. L., Bullock, J., Geha, M. C., Kalirai, J. S., Kirby, E. N., Majewski, S. R., Ostheimer, J. C., Patterson, R. J., Tollerud, E. J., Tanaka, M., & Chiba, M. 2012, ApJ, 760, 76

Gilbert, K. M., Guhathakurta, P., Kalirai, J. S., Rich, R. M., Majewski, S. R., Ostheimer, J. C., Reitzel, D. B., Cenarro, A. J., Cooper, M. C., Luine, C., & Patterson, R. J. 2006, ApJ, 652, 1188

Gilbert, K. M., Guhathakurta, P., Kollipara, P., Beaton, R. L., Geha, M. C., Kalirai, J. S., Kirby, E. N., Majewski, S. R., & Patterson, R. J. 2009b, ApJ, 705, 1275

Gilbert, K. M., Kalirai, J. S., Guhathakurta, P., Beaton, R. L., Geha, M. C., Kirby, E. N., Majewski, S. R., Patterson, R. J., Tollerud, E. J., Bullock, J. S., Tanaka, M., & Chiba, M. 2014, ArXiv e-prints

Giovanelli, R., Haynes, M. P., Adams, E. A. K., Cannon, J. M., Rhode, K. L., Salzer, J. J., Skillman, E. D., Bernstein-Cooper, E. Z., & McQuinn, K. B. W. 2013, AJ, 146, 15

Grcevich, J. & Putman, M. E. 2009, ApJ, 696, 385

Grebel, E. K., Gallagher, III, J. S., & Harbeck, D. 2003, AJ, 125, 1926

Green, P. 2013, ApJ, 765, 12

Groenewegen, M. A. T. 2005, ArXiv Astrophysics e-prints

Guhathakurta, P., Dorman, C., Seth, A., Dalcanton, J., Gilbert, K., Howley, K., Johnson, L. C., Kalirai, J., Krause, T., Lang, D., Williams, B., PHAT Team, & SPLASH Collaboration. 2012, in American Astronomical Society Meeting Abstracts, Vol. 219, American Astronomical Society Meeting Abstracts 219, 346.10

Guhathakurta, P., Ostheimer, J. C., Gilbert, K. M., Rich, R. M., Majewski, S. R., Kalirai, J. S., Reitzel, D. B., & Patterson, R. J. 2005, ArXiv Astrophysics e-prints

Guhathakurta, P., Rich, R. M., Reitzel, D. B., Cooper, M. C., Gilbert, K. M., Majewski, S. R., Ostheimer, J. C., Geha, M. C., Johnston, K. V., & Patterson, R. J. 2006, AJ, 131, 2497

Hayward, C. C., Torrey, P., Springel, V., Hernquist, L., & Vogelsberger, M. 2014, MNRAS, 442, 1992

Hernquist, L. 1993, ApJS, 86, 389

Herrnstein, J. R., Moran, J. M., Greenhill, L. J., Diamond, P. J., Inoue, M., Nakai, N., Miyoshi, M., Henkel, C., & Riess, A. 1999, Nature, 400, 539

Hertzsprung, E. 1905, Zeitschrift Fur Wissenschaftliche Photographie, 3, 442

—. 1907, Zeitschrift Fur Wissenschaftliche Photographie, 5, 86

—. 1920, MNRAS, 80, 782

Ho, N., Geha, M., Munoz, R. R., Guhathakurta, P., Kalirai, J., Gilbert, K. M., Tollerud, E., Bullock, J., Beaton, R. L., & Majewski, S. R. 2012, ApJ, 758, 124

Ho, N., Geha, M., Tollerud, E., Zinn, R., Guhathakurta, P., & Vargas, L. 2014, ArXiv e-prints

Hodge, P. W., ed. 1992, Astrophysics and Space Science Library, Vol. 176, The Andromeda galaxy

Hopkins, P. F. 2013, MNRAS, 428, 2840

Hunter, D. A. 1999, in IAU Symposium, Vol. 193, Wolf-Rayet Phenomena in Massive Stars and Starburst Galaxies, ed. K. A. van der Hucht, G. Koenigsberger, & P. R. J. Eenens, 418

Ibata, R., Irwin, M., Lewis, G., Ferguson, A. M. N., & Tanvir, N. 2001, Nature, 412, 49

Ibata, R., Martin, N. F., Irwin, M., Chapman, S., Ferguson, A. M. N., Lewis, G. F., & McConnachie, A. W. 2007, ApJ, 671, 1591

Ibata, R. A., Lewis, G. F., Irwin, M. J., & Cambrésy. 2002, MNRAS, 332, 921

Ibata, R. A., Lewis, G. F., McConnachie, A. W., Martin, N. F., Irwin, M. J., Ferguson, A. M. N., Babul, A., Bernard, E. J., Chapman, S. C., Collins, M., Fardal, M., Mackey, A. D., Navarro, J., Peñarrubia, J., Rich, R. M., Tanvir, N., & Widrow, L. 2014, ApJ, 780, 128

Imai, H., Ishihara, Y., Kameya, O., & Nakai, N. 2001, PASJ, 53, 489

Irwin, M. J., Belokurov, V., Evans, N. W., Ryan-Weber, E. V., de Jong, J. T. A., Koposov, S., Zucker, D. B., Hodgkin, S. T., Gilmore, G., Prema, P., Hebb, L.,

Begum, A., Fellhauer, M., Hewett, P. C., Kennicutt, Jr., R. C., Wilkinson, M. I., Bramich, D. M., Vidrih, S., Rix, H.-W., Beers, T. C., Barentine, J. C., Brewington, H., Harvanek, M., Krzesinski, J., Long, D., Nitta, A., & Snedden, S. A. 2007, ApJ, 656, L13

Irwin, M. J., Ferguson, A. M. N., Ibata, R. A., Lewis, G. F., & Tanvir, N. R. 2005, ApJ, 628, L105

Jarrett, T. H., Chester, T., Cutri, R., Schneider, S. E., & Huchra, J. P. 2003, AJ, 125, 525

Jester, S., Schneider, D. P., Richards, G. T., Green, R. F., Schmidt, M., Hall, P. B., Strauss, M. A., Vanden Berk, D. E., Stoughton, C., Gunn, J. E., Brinkmann, J., Kent, S. M., Smith, J. A., Tucker, D. L., & Yanny, B. 2005, AJ, 130, 873

Johnson, B. D., Weisz, D. R., Dalcanton, J. J., Johnson, L. C., Dale, D. A., Dolphin, A. E., Gil de Paz, A., Kennicutt, Jr., R. C., Lee, J. C., Skillman, E. D., Boquien, M., & Williams, B. F. 2013, ApJ, 772, 8

Johnson, H. L. 1954, ApJ, 120, 325

—. 1966, ARA&A, 4, 193

Johnson, H. L. & Sandage, A. R. 1955, ApJ, 121, 616

Johnston, K. V., Bullock, J. S., Sharma, S., Font, A., Robertson, B. E., & Leitner, S. N. 2008, ApJ, 689, 936

Johnston, K. V., Sackett, P. D., & Bullock, J. S. 2001, ApJ, 557, 137

Junk, V., Walch, S., Heitsch, F., Burkert, A., Wetzstein, M., Schartmann, M., & Price, D. 2010, MNRAS, 407, 1933

Kahn, F. D. & Woltjer, L. 1959, ApJ, 130, 705

Kalirai, J. S., Beaton, R. L., Geha, M. C., Gilbert, K. M., Guhathakurta, P., Kirby, E. N., Majewski, S. R., Ostheimer, J. C., Patterson, R. J., & Wolf, J. 2010, ApJ, 711, 671

Kalirai, J. S., Gilbert, K. M., Guhathakurta, P., Majewski, S. R., Ostheimer, J. C., Rich, R. M., Cooper, M. C., Reitzel, D. B., & Patterson, R. J. 2006, ApJ, 648, 389

Kallivayalil, N., van der Marel, R. P., & Alcock, C. 2006a, ApJ, 652, 1213

Kallivayalil, N., van der Marel, R. P., Alcock, C., Axelrod, T., Cook, K. H., Drake, A. J., & Geha, M. 2006b, ApJ, 638, 772

Kallivayalil, N., van der Marel, R. P., Besla, G., Anderson, J., & Alcock, C. 2013, ApJ, 764, 161

Kaluzny, J. & Rucinski, S. M. 1995, A&AS, 114, 1

Kauffmann, G., Heckman, T. M., White, S. D. M., Charlot, S., Tremonti, C., Brinchmann, J., Bruzual, G., Peng, E. W., Seibert, M., Bernardi, M., Blanton, M., Brinkmann, J., Castander, F., Csábai, I., Fukugita, M., Ivezic, Z., Munn, J. A., Nichol, R. C., Padmanabhan, N., Thakar, A. R., Weinberg, D. H., & York, D. 2003, MNRAS, 341, 33

Kennicutt, Jr., R. C. 1984, ApJ, 287, 116

—. 1998a, ARA&A, 36, 189

—. 1998b, ApJ, 498, 541

Kennicutt, Jr., R. C., Lee, J. C., Funes, José G., S. J., Sakai, S., & Akiyama, S. 2008, ApJS, 178, 247

Kinman, T. D. 1965, ApJ, 142, 655

Kirby, E. N., Boylan-Kolchin, M., Cohen, J. G., Geha, M., Bullock, J. S., & Kaplinghat, M. 2013a, ApJ, 770, 16

Kirby, E. N., Cohen, J. G., Guhathakurta, P., Cheng, L., Bullock, J. S., & Gallazzi, A. 2013b, ApJ, 779, 102

Kirby, E. N., Cohen, J. G., Smith, G. H., Majewski, S. R., Sohn, S. T., & Guhathakurta, P. 2011a, ApJ, 727, 79

Kirby, E. N., Lanfranchi, G. A., Simon, J. D., Cohen, J. G., & Guhathakurta, P. 2011b, ApJ, 727, 78

Kirby, E. N., Simon, J. D., Geha, M., Guhathakurta, P., & Frebel, A. 2008, ApJ, 685, L43

Klypin, A., Kravtsov, A. V., Valenzuela, O., & Prada, F. 1999, ApJ, 522, 82

Kovalevsky, J. 1998, ARA&A, 36, 99

Kroeker, T. L. & Carlberg, R. G. 1991, ApJ, 376, 1

Kundu, A., Majewski, S. R., Rhee, J., Rocha-Pinto, H. J., Polak, A. A., Slesnick, C. L., Kunkel, W. E., Johnston, K. V., Patterson, R. J., Geisler, D., Gieren, W., Seguel, J., Smith, V. V., Palma, C., Arenas, J., Crane, J. D., & Hummels, C. B. 2002, ApJ, 576, L125

Kuo, C. Y., Braatz, J. A., Reid, M. J., Lo, K. Y., Condon, J. J., Impellizzeri, C. M. V., & Henkel, C. 2013, ApJ, 767, 155

Larsen, S. S., Brodie, J. P., Elmegreen, B. G., Efremov, Y. N., Hodge, P. W., & Richtler, T. 2001, ApJ, 556, 801

Law, D. R., Johnston, K. V., & Majewski, S. R. 2005, ApJ, 619, 807

Law, D. R. & Majewski, S. R. 2010, ApJ, 714, 229

Layden, A. C., Bowes, B. T., Ritter, L. A., Welch, D. L., & Webb, T. M. A. 2000, in Astronomical Society of the Pacific Conference Series, Vol. 203, IAU Colloq. 176: The Impact of Large-Scale Surveys on Pulsating Star Research, ed. L. Szabados & D. Kurtz, 264

Lee, J. C., Gil de Paz, A., Kennicutt, Jr., R. C., Bothwell, M., Dalcanton, J., José G. Funes S., J., Johnson, B. D., Sakai, S., Skillman, E., Tremonti, C., & van Zee, L. 2011, ApJS, 192, 6

Lee, J. C., Gil de Paz, A., Tremonti, C., Kennicutt, Jr., R. C., Salim, S., Bothwell, M., Calzetti, D., Dalcanton, J., Dale, D., Engelbracht, C., Funes, S. J. J. G., Johnson, B., Sakai, S., Skillman, E., van Zee, L., Walter, F., & Weisz, D. 2009, ApJ, 706, 599

Leitherer, C., Schaerer, D., Goldader, J. D., González Delgado, R. M., Robert, C., Kune, D. F., de Mello, D. F., Devost, D., & Heckman, T. M. 1999, ApJS, 123, 3

Lemonias, J. J., Schiminovich, D., Thilker, D., Wyder, T. K., Martin, D. C., Seibert, M., Treyer, M. A., Bianchi, L., Heckman, T. M., Madore, B. F., & Rich, R. M. 2011, ApJ, 733, 74

Li, Y.-S. & White, S. D. M. 2008, MNRAS, 384, 1459

Lin, D. N. C. & Lynden-Bell, D. 1982, MNRAS, 198, 707

Loeb, A., Reid, M. J., Brunthaler, A., & Falcke, H. 2005, ApJ, 633, 894

Łokas, E. L., Kazantzidis, S., Klimentowski, J., Mayer, L., & Callegari, S. 2010, ApJ, 708, 1032

Lopez, L. A., Krumholz, M. R., Bolatto, A. D., Prochaska, J. X., Ramirez-Ruiz, E., & Castro, D. 2014, ApJ, 795, 121

Lovell, M. R., Eke, V., Frenk, C. S., Gao, L., Jenkins, A., Theuns, T., Wang, J., White, S. D. M., Boyarsky, A., & Ruchayskiy, O. 2012, MNRAS, 420, 2318

Lovell, M. R., Frenk, C. S., Eke, V. R., Jenkins, A., Gao, L., & Theuns, T. 2014, MNRAS, 439, 300

Lundmark, K. 1932, Handbuch der Astrophysik, 5, 210

Lutz, T. E. & Kelker, D. H. 1973, PASP, 85, 573

Luyten, W. J. 1922, Lick Observatory Bulletin, 10, 135

—. 1928, Proceedings of the National Academy of Science, 14, 241

Majewski, S. R. 2010, in IAU Symposium, Vol. 262, IAU Symposium, ed. G. R. Bruzual & S. Charlot, 99–110

Majewski, S. R., Beaton, R. L., Patterson, R. J., Kalirai, J. S., Geha, M. C., Muñoz, R. R., Seigar, M. S., Guhathakurta, P., Gilbert, K. M., Rich, R. M., Bullock, J. S., & Reitzel, D. B. 2007, ApJ, 670, L9

Majewski, S. R., Frinchaboy, P. M., Kunkel, W. E., Link, R., Muñoz, R. R., Ostheimer, J. C., Palma, C., Patterson, R. J., & Geisler, D. 2005, AJ, 130, 2677

Majewski, S. R., Nidever, D. L., Smith, V. V., Damke, G. J., Kunkel, W. E., Patterson, R. J., Bizyaev, D., & García Pérez, A. E. 2012, ApJ, 747, L37

Majewski, S. R., Ostheimer, J. C., Kunkel, W. E., & Patterson, R. J. 2000, AJ, 120, 2550

Majewski, S. R., Ostheimer, J. C., Rocha-Pinto, H. J., Patterson, R. J., Guhathakurta, P., & Reitzel, D. 2004, ApJ, 615, 738

Majewski, S. R., Skrutskie, M. F., Weinberg, M. D., & Ostheimer, J. C. 2003, ApJ, 599, 1082

Majewski, S. R., Zasowski, G., & Nidever, D. L. 2011, ApJ, 739, 25

Marconi, M., Fiorentino, G., & Caputo, F. 2004, A&A, 417, 1101

Marigo, P., Girardi, L., Bressan, A., Groenewegen, M. A. T., Silva, L., & Granato, G. L. 2008, A&A, 482, 883

Martínez-Delgado, D., Gabany, R. J., Crawford, K., Zibetti, S., Majewski, S. R., Rix, H.-W., Fliri, J., Carballo-Bello, J. A., Bardalez-Gagliuffi, D. C., Peñarrubia, J., Chonis, T. S., Madore, B., Trujillo, I., Schirmer, M., & McDavid, D. A. 2010, AJ, 140, 962

Martínez-Delgado, D., Peñarrubia, J., Gabany, R. J., Trujillo, I., Majewski, S. R., & Pohlen, M. 2008, ApJ, 689, 184

Martínez-Delgado, D., Pohlen, M., Gabany, R. J., Majewski, S. R., Peñarrubia, J., & Palma, C. 2009, ApJ, 692, 955

Martínez-Delgado, D., Romanowsky, A. J., Gabany, R. J., Annibali, F., Arnold, J. A., Fliri, J., Zibetti, S., van der Marel, R. P., Rix, H.-W., Chonis, T. S., Carballo-Bello, J. A., Aloisi, A., Macciò, A. V., Gallego-Laborda, J., Brodie, J. P., & Merrifield, M. R. 2012, ApJ, 748, L24

Mateo, M., Fischer, P., & Krzeminski, W. 1995, AJ, 110, 2166

Mateo, M. L. 1998, ARA&A, 36, 435

Mathewson, D. S., Schwarz, M. P., & Murray, J. D. 1977, ApJ, 217, L5

Mauron, N., Azzopardi, M., Gigoyan, K., & Kendall, T. R. 2004, A&A, 418, 77

McCarthy, I. G., Font, A. S., Crain, R. A., Deason, A. J., Schaye, J., & Theuns, T. 2012, MNRAS, 420, 2245

McCarthy, J. K. & Nemec, J. M. 1997, ApJ, 482, 203

McConnachie, A. W. 2012, AJ, 144, 4

McConnachie, A. W., Irwin, M. J., Ibata, R. A., Dubinski, J., Widrow, L. M., Martin, N. F., Côté, P., Dotter, A. L., Navarro, J. F., Ferguson, A. M. N., Puzia, T. H., Lewis, G. F., Babul, A., Barmby, P., Bienaymé, O., Chapman, S. C., Cockcroft, R., Collins, M. L. M., Fardal, M. A., Harris, W. E., Huxor, A., Mackey, A. D., Peñarrubia, J., Rich, R. M., Richer, H. B., Siebert, A., Tanvir, N., Valls-Gabaud, D., & Venn, K. A. 2009, Nature, 461, 66

Mink, D. J., Wyatt, W. F., Caldwell, N., Conroy, M. A., Furesz, G., & Tokarz, S. P. 2007, in Astronomical Society of the Pacific Conference Series, Vol. 376, Astronomical Data Analysis Software and Systems XVI, ed. R. A. Shaw, F. Hill, & D. J. Bell, 249

Miskolczi, A., Bomans, D. J., & Dettmar, R.-J. 2011, A&A, 536, A66

Mo, H., van den Bosch, F. C., & White, S. 2010, Galaxy Formation and Evolution

Monet, D. G., Levine, S. E., Canzian, B., Ables, H. D., Bird, A. R., Dahn, C. C., Guetter, H. H., Harris, H. C., Henden, A. A., Leggett, S. K., Levison, H. F., Luginbuhl, C. B., Martini, J., Monet, A. K. B., Munn, J. A., Pier, J. R., Rhodes, A. R., Riepe, B., Sell, S., Stone, R. C., Vrba, F. J., Walker, R. L., Westerhout, G., Brucato, R. J., Reid, I. N., Schoening, W., Hartley, M., Read, M. A., & Tritton, S. B. 2003, AJ, 125, 984

Monet, D. G., Levine, S. E., Casian, B., & et al. 2002, VizieR Online Data Catalog, 1284, 0

Moore, B., Ghigna, S., Governato, F., Lake, G., Quinn, T., Stadel, J., & Tozzi, P. 1999, ApJ, 524, L19

Morgan, W. W. 1937, ApJ, 85, 380

Morgan, W. W., Keenan, P. C., & Kellman, E. 1943, An atlas of stellar spectra, with an outline of spectral classification

Morrissey, P., Conrow, T., Barlow, T. A., Small, T., Seibert, M., Wyder, T. K., Budavári, T., Arnouts, S., Friedman, P. G., Forster, K., Martin, D. C., Neff, S. G., Schiminovich, D., Bianchi, L., Donas, J., Heckman, T. M., Lee, Y.-W., Madore, B. F., Milliard, B., Rich, R. M., Szalay, A. S., Welsh, B. Y., & Yi, S. K. 2007, ApJS, 173, 682

Moshir, M. & et al. 1990, in IRAS Faint Source Catalogue, version 2.0 (1990), 0

Mould, J. & Kristian, J. 1986, ApJ, 305, 591

Muñoz, R. R., Carlin, J. L., Frinchaboy, P. M., Nidever, D. L., Majewski, S. R., & Patterson, R. J. 2006a, ApJ, 650, L51

Muñoz, R. R., Frinchaboy, P. M., Majewski, S. R., Kuhn, J. R., Chou, M.-Y., Palma, C., Sohn, S. T., Patterson, R. J., & Siegel, M. H. 2005, ApJ, 631, L137

Muñoz, R. R., Majewski, S. R., Zaggia, S., Kunkel, W. E., Frinchaboy, P. M., Nidever, D. L., Crnojevic, D., Patterson, R. J., Crane, J. D., Johnston, K. V., Sohn, S. T., Bernstein, R., & Shectman, S. 2006b, ApJ, 649, 201

Navarro, J. F. & Benz, W. 1991, ApJ, 380, 320

Navarro, J. F., Frenk, C. S., & White, S. D. M. 1996a, ApJ, 462, 563

—. 1996b, ApJ, 462, 563

—. 1997, ApJ, 490, 493

Navarro, J. F. & White, S. D. M. 1994, MNRAS, 267, 401

Newman, J. A., Cooper, M. C., Davis, M., Faber, S. M., Coil, A. L., Guhathakurta, P., Koo, D. C., Phillips, A. C., Conroy, C., Dutton, A. A., Finkbeiner, D. P., Gerke, B. F., Rosario, D. J., Weiner, B. J., Willmer, C. N. A., Yan, R., Harker, J. J., Kassin, S. A., Konidaris, N. P., Lai, K., Madgwick, D. S., Noeske, K. G., Wirth, G. D., Connolly, A. J., Kaiser, N., Kirby, E. N., Lemaux, B. C., Lin, L., Lotz, J. M., Luppino, G. A., Marinoni, C., Matthews, D. J., Metevier, A., & Schiavon, R. P. 2013, ApJS, 208, 5

Nidever, D. L., Ashley, T., Slater, C. T., Ott, J., Johnson, M., Bell, E. F., Stanimirović, S., Putman, M., Majewski, S. R., Simpson, C. E., Jütte, E., Oosterloo, T. A., & Butler Burton, W. 2013a, ApJ, 779, L15

Nidever, D. L., Majewski, S. R., Butler Burton, W., & Nigra, L. 2010, ApJ, 723, 1618

Nidever, D. L., Monachesi, A., Bell, E. F., Majewski, S. R., Muñoz, R. R., & Beaton, R. L. 2013b, ApJ, 779, 145

Nidever, D. L., Zasowski, G., & Majewski, S. R. 2012, ApJS, 201, 35

Nissen, P. E. & Schuster, W. J. 2010, A&A, 511, L10

—. 2011, A&A, 530, A15

O'Connell, D. J. K. 1958, Ricerche Astronomiche, 5

Oke, J. B. 1957, ApJ, 126, 509

—. 1959, ApJ, 130, 487

Osterbrock, D. E. & Ferland, G. J. 2006, Astrophysics of gaseous nebulae and active galactic nuclei

Ostheimer, Jr., J. C. 2003, PhD thesis, UNIVERSITY OF VIRGINIA

Ostriker, J. P., Peebles, P. J. E., & Yahil, A. 1974, ApJ, 193, L1

Oudmaijer, R. D., Groenewegen, M. A. T., & Schrijver, H. 1998, MNRAS, 294, L41

Palma, C., Majewski, S. R., Siegel, M. H., Patterson, R. J., Ostheimer, J. C., & Link, R. 2003, AJ, 125, 1352

Peacock, J. A. 1999, Cosmological Physics

Peebles, P. J. E. 1994, ApJ, 429, 43

—. 1995, ApJ, 449, 52

Peebles, P. J. E., Phelps, S. D., Shaya, E. J., & Tully, R. B. 2001, ApJ, 554, 104

Perryman, M. A. C., Lindegren, L., Kovalevsky, J., Turon, C., Hoeg, E., Grenon, M., Schrijver, H., Bernacca, P. L., Creze, M., Donati, F., Evans, D. W., Falin, J. L., Froeschle, M., Gomez, A., Grewing, M., van Leeuwen, F., van der Marel, H., Mignard, F., Murray, C. A., Penston, M. J., Petersen, C., Le Poole, R. S., & Walter, H. G. 1995, A&A, 304, 69

Phillips, J. I., Wheeler, C., Boylan-Kolchin, M., Bullock, J. S., Cooper, M. C., & Tollerud, E. J. 2014, MNRAS, 437, 1930

Piatek, S., Pryor, C., Olszewski, E. W., Harris, H. C., Mateo, M., Minniti, D., Monet, D. G., Morrison, H., & Tinney, C. G. 2002, AJ, 124, 3198

Pilyugin, L. S. & Thuan, T. X. 2005, ApJ, 631, 231

Pogge, R. W., Atwood, B., Belville, S. R., Brewer, D. F., Byard, P. L., DePoy, D. L., Derwent, M. A., Eastwood, J., Gonzalez, R., Krygier, A., Marshall, J. R., Martini, P., Mason, J. A., O'Brien, T. P., Osmer, P. S., Pappalardo, D. P., Steinbrecher, D. P., Teiga, E. J., & Weinberg, D. H. 2006, in Society of Photo-Optical Instrumentation Engineers (SPIE) Conference Series, Vol. 6269, Society of Photo-Optical Instrumentation Engineers (SPIE) Conference Series

Press, W. H., Flannery, B. P., & Teukolsky, S. A. 1986, Numerical recipes. The art of scientific computing

Pritchet, C. J. & van den Bergh, S. 1994, AJ, 107, 1730

Pritzl, B. J., Armandroff, T. E., Jacoby, G. H., & Da Costa, G. S. 2002, AJ, 124, 1464

—. 2004, AJ, 127, 318

—. 2005, AJ, 129, 2232

Purcell, C. W., Bullock, J. S., & Kazantzidis, S. 2010, MNRAS, 404, 1711

Putman, M. E., Peek, J. E. G., & Joung, M. R. 2012, ARA&A, 50, 491

Read, J. I., Hayfield, T., & Agertz, O. 2010, MNRAS, 405, 1513

Reid, M. J., Braatz, J. A., Condon, J. J., Lo, K. Y., Kuo, C. Y., Impellizzeri, C. M. V., & Henkel, C. 2013, ApJ, 767, 154

Reid, M. J. & Honma, M. 2014, ARA&A, 52, 339

Reines, A. E., Johnson, K. E., & Goss, W. M. 2008, AJ, 135, 2222

Richardson, J. C., Irwin, M. J., McConnachie, A. W., Martin, N. F., Dotter, A. L., Ferguson, A. M. N., Ibata, R. A., Chapman, S. C., Lewis, G. F., Tanvir, N. R., & Rich, R. M. 2011, ApJ, 732, 76

Roberts, M. S. & Rots, A. H. 1973, A&A, 26, 483

Robertson, B., Bullock, J. S., Font, A. S., Johnston, K. V., & Hernquist, L. 2005, ApJ, 632, 872

Rocha, M., Peter, A. H. G., & Bullock, J. 2012, MNRAS, 425, 231

Rocha-Pinto, H. J., Majewski, S. R., Skrutskie, M. F., Crane, J. D., & Patterson, R. J. 2004, ApJ, 615, 732

Rubin, V. C., Burstein, D., Ford, Jr., W. K., & Thonnard, N. 1985, ApJ, 289, 81

Rubin, V. C. & Ford, Jr., W. K. 1970, ApJ, 159, 379

Rubin, V. C., Ford, W. K. J., & . Thonnard, N. 1980, ApJ, 238, 471

Russell, H. N. 1914, Popular Astronomy, 22, 331

—. 1925a, Scientific American, 133, 241

—. 1925b, Nature, 116, 209

Russell, H. N. & Moore, C. E. 1938, ApJ, 87, 389

—. 1940, ApJ, 92, 354

Ryan-Weber, E. V., Begum, A., Oosterloo, T., Pal, S., Irwin, M. J., Belokurov, V., Evans, N. W., & Zucker, D. B. 2008, MNRAS, 384, 535

Samland, M. & Gerhard, O. E. 2003, A&A, 399, 961

Sanchez-Saavedra, M. L., Battaner, E., & Florido, E. 1990, MNRAS, 246, 458

Sandage, A. 1958a, Ricerche Astronomiche, 5, 41

—. 1958b, Ricerche Astronomiche, 5, 287

—. 1962, ApJ, 135, 333

—. 1986, ARA&A, 24, 421

—. The Malmquist Bias, ed. P. Murdin (Taylor & Francis, Boca Raton)

—. 2004, Centennial History of the Carnegie Institution of Washington, Vol.I; The Mount Wilson Observatory (Cambridge Univ. Cambridge Press)

Sandage, A., Lubin, L. M., & VandenBerg, D. A. 2003, PASP, 115, 1187

Sandage, A. & Saha, A. 2002, AJ, 123, 2047

Sandage, A. & Tammann, G. A. 2006, ARA&A, 44, 93

Sandage, A. R. & Eggen, O. J. 1959, MNRAS, 119, 278

Sarajedini, A., Mancone, C. L., Lauer, T. R., Dressler, A., Freedman, W., Trager, S. C., Grillmair, C., & Mighell, K. J. 2009, AJ, 138, 184

Schiavon, R. P., Barbuy, B., Rossi, S. C. F., Milone, & A. 1997, ApJ, 479, 902

Schlafly, E. F. & Finkbeiner, D. P. 2011, ApJ, 737, 103

Schlegel, D. J., Finkbeiner, D. P., & Davis, M. 1998, ApJ, 500, 525

Schmidt-Kaler, T. 1982, Landolt-Börnstein: Numerical Data and Funcational Relationshipsin Science and Technology, ed. K. Schaifers & H. Voigt (Berlin, Springer-Verlag)

Schönrich, R., Asplund, M., & Casagrande, L. 2011, MNRAS, 415, 3807

Schuster, W. J., Moreno, E., Nissen, P. E., & Pichardo, B. 2012, A&A, 538, A21

Searle, L. & Zinn, R. 1978, ApJ, 225, 357

Shang, Z., Zheng, Z., Brinks, E., Chen, J., Burstein, D., Su, H., Byun, Y.-I., Deng, L., Deng, Z., Fan, X., Jiang, Z., Li, Y., Lin, W., Ma, F., Sun, W.-H., Wills, B., Windhorst, R. A., Wu, H., Xia, X., Xu, W., Xue, S., Yan, H., Zhou, X., Zhu, J., & Zou, Z. 1998, ApJ, 504, L23

Sharma, S., Bland-Hawthorn, J., Johnston, K. V., & Binney, J. 2011, ApJ, 730, 3

Sheffield, A. A., Johnston, K. V., Majewski, S. R., Damke, G., Richardson, W., Beaton, R., & Rocha-Pinto, H. J. 2014, ApJ, 793, 62

Sheffield, A. A., Majewski, S. R., Johnston, K. V., Cunha, K., Smith, V. V., Cheung, A. M., Hampton, C. M., David, T. J., Wagner-Kaiser, R., Johnson, M. C., Kaplan, E., Miller, J., & Patterson, R. J. 2012, ApJ, 761, 161

Siegel, M. H. 2002, PhD thesis, UNIVERSITY OF VIRGINIA

Siegel, M. H., Dotter, A., Majewski, S. R., Sarajedini, A., Chaboyer, B., Nidever, D. L., Anderson, J., Marín-Franch, A., Rosenberg, A., Bedin, L. R., Aparicio, A., King, I., Piotto, G., & Reid, I. N. 2007, ApJ, 667, L57

Sijacki, D., Vogelsberger, M., Kereš, D., Springel, V., & Hernquist, L. 2012, MNRAS, 424, 2999

Simon, J. D. & Geha, M. 2007, ApJ, 670, 313

Skillman, E. D. 1989, ApJ, 347, 883

Slater, C. T., Bell, E. F., & Martin, N. F. 2011, ApJ, 742, L14

Slipher, V. M. 1914, Popular Astronomy, 22, 19

Smith, H. 2003, MNRAS, 338, 891

Sohn, S. T., Anderson, J., & van der Marel, R. P. 2012, ApJ, 753, 7

Sohn, S. T., Majewski, S. R., Muñoz, R. R., Kunkel, W. E., Johnston, K. V., Ostheimer, J. C., Guhathakurta, P., Patterson, R. J., Siegel, M. H., & Cooper, M. C. 2007, ApJ, 663, 960

Spekkens, K., Urbancic, N., Mason, B. S., Willman, B., & Aguirre, J. E. 2014, ApJ, 795, L5

Springel, V. 2000, MNRAS, 312, 859

—. 2005, MNRAS, 364, 1105

Springel, V. & Hernquist, L. 2003, MNRAS, 339, 312

Springob, C. M., Haynes, M. P., Giovanelli, R., & Kent, B. R. 2005, ApJS, 160, 149

Springob, C. M., Masters, K. L., Haynes, M. P., Giovanelli, R., & Marinoni, C. 2007, ApJS, 172, 599

—. 2009, ApJS, 182, 474

Stetson, P. B. 1987, PASP, 99, 191

—. 1994, PASP, 106, 250

Strömberg, G. 1930, ApJ, 71, 175

—. 1932, ApJ, 75, 115

—. 1936, ApJ, 84, 412

Stromberg, G. 1939, ApJ, 89, 10

Strömberg, G. 1940, ApJ, 92, 156

—. 1941, ApJ, 93, 33

Tanaka, M., Chiba, M., Komiyama, Y., Guhathakurta, P., Kalirai, J. S., & Iye, M. 2010, ApJ, 708, 1168

ten Burggencate, P. (Springer Berlin), 137

Teyssier, M., Johnston, K. V., & Kuhlen, M. 2012, MNRAS, 426, 1808

Tollerud, E. J., Beaton, R. L., Geha, M. C., Bullock, J. S., Guhathakurta, P., Kalirai, J. S., Majewski, S. R., Kirby, E. N., Gilbert, K. M., Yniguez, B., Patterson, R. J., Ostheimer, J. C., Cooke, J., Dorman, C. E., Choudhury, A., & Cooper, M. C. 2012, ApJ, 752, 45

Tollerud, E. J., Boylan-Kolchin, M., Barton, E. J., Bullock, J. S., & Trinh, C. Q. 2011, ApJ, 738, 102

Tollerud, E. J., Geha, M. C., Vargas, L. C., & Bullock, J. S. 2013, ApJ, 768, 50

Toomre, A. & Toomre, J. 1972, ApJ, 178, 623

Tremonti, C. A., Heckman, T. M., Kauffmann, G., Brinchmann, J., Charlot, S., White, S. D. M., Seibert, M., Peng, E. W., Schlegel, D. J., Uomoto, A., Fukugita, M., & Brinkmann, J. 2004, ApJ, 613, 898

Trumpler, R. J. & Weaver, H. F. 1953, Statistical astronomy

Turnshek, D. E., Turnshek, D. A., & Craine, E. R. 1985, An atlas of digital spectra of cool stars

Vacca, W. D., Garmany, C. D., & Shull, J. M. 1996, ApJ, 460, 914

van der Marel, R. P. 2001, AJ, 122, 1827

—. 2014, ArXiv e-prints

van der Marel, R. P. & Cioni, M.-R. L. 2001, AJ, 122, 1807

van der Marel, R. P. & Guhathakurta, P. 2008, ApJ, 678, 187

van der Marel, R. P., Kallivayalil, N., & Besla, G. 2009, in IAU Symposium, Vol. 256, IAU Symposium, ed. J. T. Van Loon & J. M. Oliveira, 81–92

van Leeuwen, F., ed. 2007a, Astrophysics and Space Science Library, Vol. 350, Hipparcos, the New Reduction of the Raw Data

van Leeuwen, F. 2007b, A&A, 474, 653

—. 2008, VizieR Online Data Catalog, 1311, 0

van Rhijn, P. J. 1939, Publications of the Kapteyn Astronomical Laboratory Groningen, 49, 1

VandenBerg, D. A., Bergbusch, P. A., & Dowler, P. D. 2006, ApJS, 162, 375

Vargas, L. C., Geha, M., Kirby, E. N., & Simon, J. D. 2013, ApJ, 767, 134

Vargas, L. C., Geha, M. C., & Tollerud, E. J. 2014, ApJ, 790, 73

Veljanoski, J., Mackey, A. D., Ferguson, A. M. N., Huxor, A. P., Côté, P., Irwin, M. J., Tanvir, N. R., Peñarrubia, J., Bernard, E. J., Fardal, M., Martin, N. F., McConnachie, A., Lewis, G. F., Chapman, S. C., Ibata, R. A., & Babul, A. 2014, MNRAS, 442, 2929

Venn, K. A., Irwin, M., Shetrone, M. D., Tout, C. A., Hill, V., & Tolstoy, E. 2004, AJ, 128, 1177

Vogelsberger, M., Sijacki, D., Kereš, D., Springel, V., & Hernquist, L. 2012, MNRAS, 425, 3024

Wakker, B. P. 2001, ApJS, 136, 463

Wallerstein, G. 2002, PASP, 114, 689

Welch, D. L. & Stetson, P. B. 1993, AJ, 105, 1813

Westfall, K. B., Majewski, S. R., Ostheimer, J. C., Frinchaboy, P. M., Kunkel, W. E., Patterson, R. J., & Link, R. 2006, AJ, 131, 375

White, S. D. M., Davis, M., & Frenk, C. S. 1984, MNRAS, 209, 27P

Wilson, O. C. & Vainu Bappu, M. K. 1957, ApJ, 125, 661

Wilson, R. E. 1918, Publications of Lick Observatory, 13, 186

—. 1944a, PASP, 56, 102

—. 1944b, PASP, 56, 203

Wolfe, S. A., Pisano, D. J., Lockman, F. J., McGaugh, S. S., & Shaya, E. J. 2013, Nature, 497, 224

Woo, J., Courteau, S., & Dekel, A. 2008, MNRAS, 390, 1453

Yang, L., Kirby, E. N., Guhathakurta, P., Peng, E. W., & Cheng, L. 2013, ApJ, 768, 4

Zasowski, G., Johnson, J. A., Frinchaboy, P. M., Majewski, S. R., Nidever, D. L., Rocha Pinto, H. J., Girardi, L., Andrews, B., Chojnowski, S. D., Cudworth, K. M., Jackson, K., Munn, J., Skrutskie, M. F., Beaton, R. L., Blake, C. H., Covey, K., Deshpande, R., Epstein, C., Fabbian, D., Fleming, S. W., Garcia Hernandez, D. A., Herrero, A., Mahadevan, S., Mészáros, S., Schultheis, M., Sellgren, K., Terrien, R., van Saders, J., Allende Prieto, C., Bizyaev, D., Burton, A., Cunha, K., da Costa, L. N., Hasselquist, S., Hearty, F., Holtzman, J., García Pérez, A. E., Maia, M. A. G., O'Connell, R. W., O'Donnell, C., Pinsonneault, M., Santiago, B. X., Schiavon, R. P., Shetrone, M., Smith, V., & Wilson, J. C. 2013, AJ, 146, 81

Zheng, Z., Shang, Z., Su, H., Burstein, D., Chen, J., Deng, Z., Byun, Y.-I., Chen, R., Chen, W.-P., Deng, L., Fan, X., Fang, L.-Z., Hester, J. J., Jiang, Z., Li, Y., Lin, W., Sun, W.-H., Tsay, W.-S., Windhorst, R. A., Wu, H., Xia, X., Xu, W., Xue, S., Yan, H., Zheng, Z., Zhou, X., Zhu, J., Zou, Z., & Lu, P. 1999, AJ, 117, 2757

Zibetti, S. 2009, ArXiv e-prints

Zibetti, S., Charlot, S., & Rix, H.-W. 2009, MNRAS, 400, 1181

Zinn, R. & King, C. R. 1982, ApJ, 262, 700

Zolotov, A., Brooks, A. M., Willman, B., Governato, F., Pontzen, A., Christensen, C., Dekel, A., Quinn, T., Shen, S., & Wadsley, J. 2012, ApJ, 761, 71

Zolotov, A., Willman, B., Brooks, A. M., Governato, F., Brook, C. B., Hogg, D. W., Quinn, T., & Stinson, G. 2009, ApJ, 702, 1058

Zolotov, A., Willman, B., Brooks, A. M., Governato, F., Hogg, D. W., Shen, S., & Wadsley, J. 2010, ApJ, 721, 738

Zucker, D. B., Kniazev, A. Y., Martínez-Delgado, D., Bell, E. F., Rix, H.-W., Grebel, E. K., Holtzman, J. A., Walterbos, R. A. M., Rockosi, C. M., York, D. G., Barentine, J. C., Brewington, H., Brinkmann, J., Harvanek, M., Kleinman, S. J., Krzesinski, J., Long, D., Neilsen, Jr., E. H., Nitta, A., & Snedden, S. A. 2007, ApJ, 659, L21

Zwicky, F. 1933, Helvetica Physica Acta, 6, 110